Development of Multifunctional Coatings Combining Anticorrosion and Antibiofouling Properties

Caroline Villardi de Oliveira

Thèse
de doctorat
de l'UTT

Caroline VILLARDI DE OLIVEIRA

Development of Multifunctional Coatings Combining Anticorrosion and Antibiofouling Properties

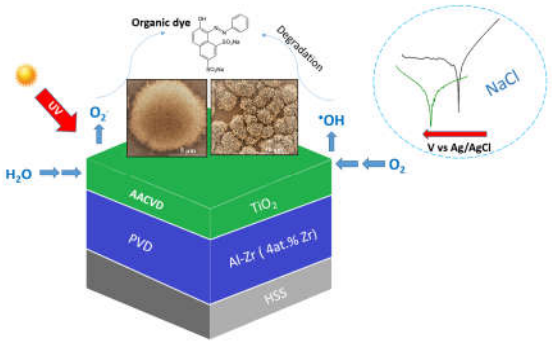

Champ disciplinaire :
Sciences pour l'Ingénieur

2019TROY0034

Année 2019

utt
UNIVERSITÉ DE TECHNOLOGIE
TROYES

THESE

pour l'obtention du grade de

DOCTEUR
de l'UNIVERSITE DE TECHNOLOGIE DE TROYES

EN SCIENCES POUR L'INGENIEUR

Spécialité : MATERIAUX, MECANIQUE, OPTIQUE, NANOTECHNOLOGIE

présentée et soutenue par

Caroline VILLARDI DE OLIVEIRA

le 12 décemebre 2019

Development of Multifunctional Coatings Combining Anticorrosion and Antibiofouling Properties

JURY

M. J. CREUS	PROFESSEUR DES UNIVERSITES	Président
M. A. CAVALEIRO	PROFESSOR CATEDRÁTICO	Rapporteur
M. F. MAURY	DIRECTEUR DE RECHERCHE CNRS	Rapporteur
M. A. BILLARD	PROFESSEUR DES UNIVERSITES	Examinateur
Mme C. JIMÈNEZ	DOCTEURE, INGENIEURE DE RECHERCHE CNRS	Examinatrice
M. F. SCHUSTER	DOCTEUR	Examinateur
M. A. ALHUSSEIN	PROFESSEUR ASSOCIE UTT	Directeur de thèse
M. F. SANCHETTE	PROFESSEUR DES UNIVERSITES	Directeur de thèse

“You will never do anything in this world without courage. It is the greatest quality of the mind next to honor.”

— **Aristotle**

To my parents and brother,

Acknowledgments

During these three years of PhD, I have passed challenging and grateful moments which allowed me to develop both personally and professionally.

First of all, I would like to express my profound gratitude to my three supervisors Prof. Frédéric Sanchette, Prof. Akram Alhussein and Dr. Carmen Jimènez for their patience, motivation and immense knowledge. Their guidance was unquestionably fundamental to overcome all the difficulties during all the time of research and the writing of the thesis. Thank you for giving me a lot of opportunities to visit different laboratories and to attend conferences over the world. Those were extremely useful for extend my vision to a wider research community. Both of you always showed an extraordinary positive attitude, and it was really a great pleasure to work under your supervision.

I would like to particularly thank to Dr. Carmen Jimènez for opening me the door of LMGP and for the hard questions which incented me to widen my research and life from various perspectives. Besides my direct three supervisors, I would like to specially thank Dr. Frédéric Schuster for the support during these last 3 years, I thank you for the words of encouragement and for his implication in my future professional career.

I would like to thanks University of Technology of Troyes (UTT) and doctoral school for this wonderful opportunity to do a PhD. In UTT, I would like to thank Marie Lecomte for all the administrative help and to be always available when I needed. I also want to thank Isabelle Leclercq and Pascale Denis for their administrative help and advices.

I would like to thank prof. Elisabeth Blanquet for all the help and support during my first year of PhD and for giving me the possibility to work in SIMaP lab.

In LMGP, I thank Michele San Martin and Josiane Viboud for the administrative and technical help. I would like to acknowledge Odette Chaix, Hervé Roussel, Laetitia Rapenne and Etienne Pernot for support with the characterization techniques and consequent scientific consultations.

Additionally, I would thank the scientific support and endless discussions with prof. Jean-Luc Deschanvres in the laboratory. Thanks for having always showed an extraordinary positive attitude and to give me lots of valuable suggestions during my thesis work.

I would like to thank Dr. Michel Schlegel for the corrosions tests in CEA and for all the advices which helped me a lot during this PhD. I also want to thank prof. Juan Creus for all the great discussions and for all the scientific support when I needed help.

I would like to thank prof. Claude Guet, Prof. Dong Zhili and Dr. Srikanth Narasimalu for the opportunity to work in Nanyang Technological University. It was a great personal and professional experience.

I also would like to thank Dr. Fabienne Fay for giving me the opportunity to collaborate with her making possible to perform important tests. Thanks for all the support and valuable advices.

I would like to thank Prof. Albano Cavaleiro and Prof. Francis Maury for the honor they gave me by accepting to evaluate my work. I also want to thank Prof. Allain Billard, Prof. Juan Creus and Dr. Frédéric Schuster for accepting to be the members of my PhD examination committee.

My sincere gratitude goes to my LMGP colleagues, Guillaume, Tabassom, Morganne, Fanny, Adria, Soraya, Cesar, Sara, Dorina, Antalya, Maxime, Raquel, Clement, João, Lorenzo, Pierre, Abdou, Mirasbek, Eugene, Getnet, Damir, Klaasjan, Monica, Charlotte, Cécile, Chiara, José, Guislain, Carlos,Viet, Huy... with whom I have shared amazing time. You truly made my lab life enjoyable and unforgettable. Thanks for every good moment shared together.

I express my deepest gratitude to my parents, Marcia and Carlos, and my brother, Pedro, for encouraging me in all of my pursuits and inspiring me to follow my dreams. Even though they miss me, they always encourage me to see the world. I feel very lucky to having you as my parents, always supporting me and encouraging me to do the best I can. I am especially grateful to my mother who makes always herself present motivating myself and giving always the best advices.

Finally, I owe thanks to a very special person, Maxime, for his true love, big support and to making me the happiest person. I am grateful to have you by my side. Thanks for all the advices and to always encourage me.

List of abbreviations

AA-MOCVD: aerosol assisted metal organic chemical vapor deposition

AFM: Atomic force microscopy

APMOCVD*:* atmospheric pressure MOCVD

ASTM: American Society for Testing and Materials

CVD: Chemical Vapor Deposition

DC Magnetron sputtering: Direct current magnetron sputtering

DSSCs: dye-sensitized solar cells

DR: Decomposition rate

EIS: Electrochemical Impedance Spectroscopy

FCC: Face-centered cubic

FTIR: Fourier transform infrared spectroscopy

HSS: High speed steel

OG: Orange G

OCP: Open Circuit Potential

PACVD: plasma assisted chemical vapor deposition

PDMSe: Poly(dimethylsiloxane) elastomers

PVD: Physical Vapor Deposition

REH: Reaction of hydrogen evolution

ROS: Reactive oxygen species

SEM: scanning electron microscopy

SZM: Structure Zone Model

TBT: Tributyltin oxide

TEM: transmission electron microscopy

TM: Transition metals

UV: ultraviolet

VB: valence band

XRD: X-ray diffraction

XPS: X-ray photoelectron spectroscopy

TiO_2: Titanium dioxide

Cu_2O: Copper (I) Oxide or Cuprous Oxide

CuO: Copper (II) Oxide

Table of Contents

General Introduction

Once a metal is submerged into seawater, interactions between metal, living organisms and marine environment result in biofouling and in corrosion of metal components, almost at the same time. The development of micro and macro-organisms is the origin of the biofouling, which causes a significant industrial problem. To develop an antibiofouling coating system, one should take into account the environment, the engineered coating and the substrate.

At the same time that biological changes give rise to biofilm accumulation, a sequence of inorganic changes occurs on the metal surface instantly after submerging it in an aggressive aqueous medium. This consists in the process of metal dissolution and development of corrosion product. While corrosion and corrosion product accumulation develop from the metal surface towards the solution, biofilm development is the result of accumulation processes directed from the bulk towards the metal surface. In this thesis, we propose a novel multi-functional bilayer coating composed of Al-Zr and TiO_2 as an antibiofouling system on steel substrates.

Aluminum-transition metal alloys have demonstrated to be potential candidates for protection of steel parts against galvanic corrosion. The transition metals are added to compensate the weak mechanical characteristics of pure aluminum. An optimized aluminum alloy with a homogeneous microstructure is deposited before the antifouling layer.

The material chosen as antibiofouling is based on titanium dioxide (TiO_2), a promising candidate thanks to its photocatalytic activity and the hydrophilic / hydrophobic behavior in order to slow down the biofouling process in the marine structures.

PVD (Physical Vapor Deposition) and CVD (Chemical Vapor Deposition) processes are suitable industrial technologies for the deposition of functional and protective thin films. Indeed,

the maturity of these techniques allows controlling the deposition parameters of these processes to achieve the best performance according to the application.

Magnetron sputtering and CVD aerosol techniques were selected to deposit Al-Zr and TiO_2 bilayer films, respectively. The bilayers were characterized in terms of morphology, crystallographic structure, texture and roughness, surface wetting, corrosion electrochemical behavior, photocatalytic activity and biofouling behavior.

This thesis is focused on development of Al-Zr films providing cathodic protection for steel parts, TiO_2 films providing photocatalytic and antibiofouling properties, and finally the combination of both films in order to develop a multi-functional coating able to avoid corrosion and biofouling of structures used in marine environment. The thesis manuscript is organized into five chapters:

Chapter I presents the state of the art for the chosen materials and their functionalities, Firstly, the use of aluminium transition metals as sacrificial anodes and the corrosion of aluminium alloys in aqueous solutions are discussed. The choice of Al-Zr coating for corrosion applications is exposed. In a second part, the discussions are based on mechanisms and applications of photocatalysis by titanium dioxide semiconductors. Major aspects of biofouling and corrosion in marine structures are also presented.

Chapter II describes the mechanisms of magnetron sputtering coating process and presents an overview of the magnetron sputtering reactor employed to produce Al-Zr films in LASMIS laboratory. Firstly, optimal processing conditions for depositing Al-Zr films are discussed. In a second part, structural characterizations, nanohardness measurements and electrochemical tests are analyzed in order to choose the Al-Zr alloy providing the best compromise between mechanical reinforcement and electrochemical properties.

Chapter III presents the aerosol assisted metalorganic chemical vapor deposition (AAMOCVD) technique employed to deposit TiO_2 thin films in LMGP laboratory. The choice of TiO_2 precursor, description of AAMOCVD reactor and deposition parameters are discussed in this chapter. Physical and chemical characterizations of TiO_2 films are described in the second part.

Chapter IV presents the functional properties of Al-Zr/TiO_2 bilayer coatings. Structure, electrochemical behavior, photocatalysis properties, hydrophilicity and TEM analysis of the bilayer coatings are developed in this chapter.

Chapter V introduces new Cu-Ti-O films deposited by the AAMOCVD technique using a combination of two precursors in order to improve photocatalytic and antibiofouling properties. Morphological and structural characterizations are firstly analyzed. Photocatalysis and marine biofouling field test were employed in order to check the performance of Cu-Ti-O and TiO_2 films as a new promising solution for biofouling problem.

This manuscript ends with a conclusion summarizing the major results obtained during this thesis and the prospects of this work.

This thesis is a collaboration project between the following research units: Université de Technologie de Troyes (UTT), centre de recherche CEA Saclay, Laboratoire des Matériaux et du Génie Physique (LMGP – Grenoble INP), SIMAP – Grenoble INP, Nanyang Technological University (NTU in Singapore) and LBCM – Université Bretagne Sud.

Magnetron sputtering depositions were carried out in the Laboratory of Life Assessment of Structures, Materials, Mechanics and Integrated Systems (ICD - LASMIS – UTT) in Nogent, and Chemical Vapor depositions were performed in LMGP – Grenoble INP in Grenoble. Electrochemical tests were carried out in CEA, localized in Saclay; Some TEM measurements were performed in NTU and biofouling field tests were executed in collaboration with LBCM – Université Bretagne Sud.

Chapter I: State of the art

In this chapter I the state of the art for the chosen materials and their functionalities are presented. Firstly, the use of aluminium-transition metals as sacrificial anodes and the corrosion of aluminium alloys in aqueous solutions are discussed. The choice of Al-Zr coating for anti-corrosion applications is exposed. In a second part, the discussions are based on mechanisms and applications of photocatalysis by titanium dioxide semiconductors. Major aspects of biofouling and corrosion in marine structures are also presented.

I.1. Corrosion of aluminium and aluminium alloys in aqueous environment

Corrosion of Al alloys is normally presented as a local nature, since there is a separation of anodic and cathodic reactions.

The basic anodic reaction is metal dissolution:

$Al \rightarrow Al^{3+} + 3e^-$ I. 1

Whereas the cathodic reactions are oxygen reduction:

$O_2 + 2H_2O + 4e^- \rightarrow 4OH^-$ I. 2

Or hydrogen reduction in acidified solution being the result of Al ion hydrolysis:

$2H^+ + 2e \rightarrow H_2$ I. 3

So the corrosion of Al can be described as the interaction between local anodes and cathodes and the alloy matrix that leads to all forms of corrosion in Al alloys [1]. It includes pitting corrosion, selective dissolution, trenching and intergranular attack.

Al and its alloys are known to be resistant against corrosion in moderately aggressive aqueous environments. The thermodynamic strength of Al alloys in corrosive environment is due to the protective oxide layer, which acts as a physical barrier and is capable to repair itself in oxidizing environments if damaged [1], although the passive layer breakdown mechanism by chloride ions is still in debate [2] as a result of the complexity of the process [3].

In general, localized attack initiates the adsorption of destructive anions and creation of soluble transitional compounds with the cations at the oxide surface. The passivity aspect that rules the corrosion behavior of Al is summarized by Pourbaix-type analysis. A plot of potential (V_{SCE}) vs. pH in accordance with the electrochemical reaction of the species involved, known as Pourbaix diagram [4], is presented in Figure I- 1.

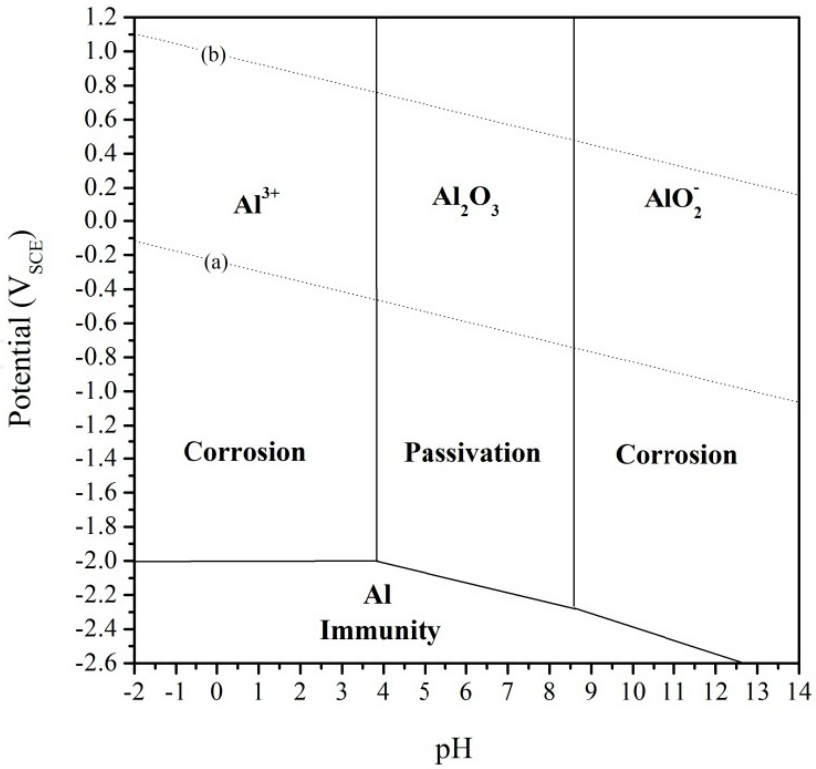

Figure I- 1. Potential-pH diagram for pure Al at 25˚C in aqueous solution (Reproduced from Pourbaix, 1974 [4]). The lines (a) and (b) are the water stability and its decomposed product.

Al is slightly passive in the pH range of ~ 4 to 9 as a result of the existence of an Al_2O_3 film. In environments that diverge from the neutral range, the permanence of Al_2O_3 film can be disrupted. Consequently, the film becomes soluble, making it easier the rapid dissolution of the alloy. In the acidic range, Al is oxidized by creating Al^{3+}, while AlO_2^- happens in alkaline range.

Corrosion prediction can be interpreted as a straightforward process when Pourbaix diagram is taken in account. On the other hand, in actual engineering applications, there are numerous variables that weren't taken into account by Pourbaix. These comprise (i) the existence of alloying elements in the vast majority of engineering metals (ii) the presence of substances, like chloride, in the electrolyte, (iii) the working temperature of the alloy, (iv) the mode of corrosion, and (v) the reaction rate. Gimenez et al.[5] have taken these factors into account and they have created a revised version of a potential (V_{SCE}) vs. pH diagram for 5000 series aluminium alloys in 0.5 M sodium chloride as represented in Figure I- 2.

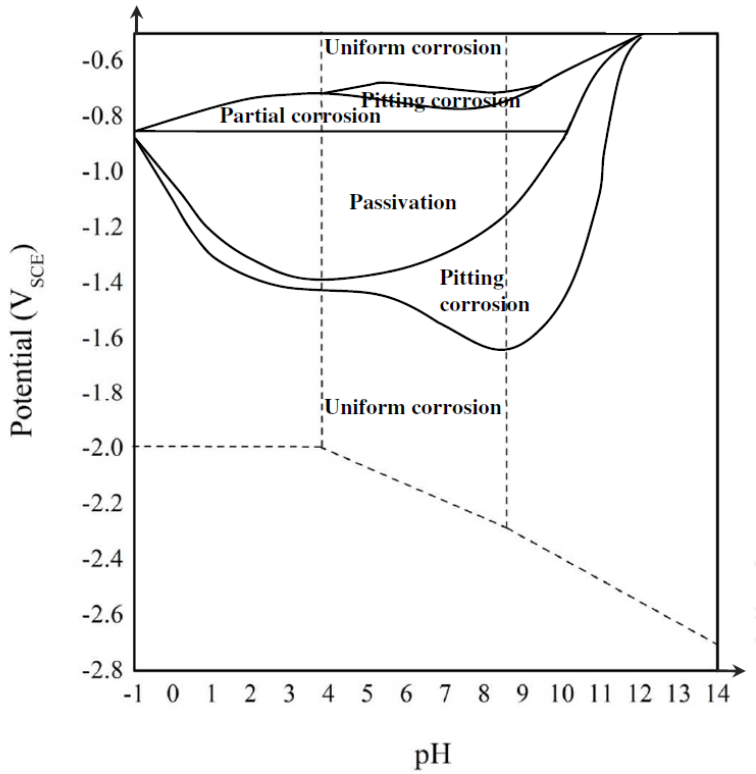

Figure I- 2. Mode of corrosion based on experimental data for AA5086 in saline solution (Reproduced from Gimenez, Rameau et al., 1981[5]).

The conditions where localized attack is strongly possible in the theoretical passive region is shown in Figure I- 2. Gimenez et al.[5] reported that localized attack is possible over the whole range of pH according to the specific potential.

Cathodic polarisation provides alloy degradation in two manners. Primarily, the accumulation of hydroxyl ions at the Al surface induces chemical dissolution of the Al. In the second place, Al is a strong hydride former, and hydrogen from the cathodic reaction at such negative potentials will associate with Al to create hydrides [6].

I.2. Electrochemical basis of corrosion

Corrosion generally takes place at an equilibrium level determined among the different electrochemical reactions. The anodic reaction is one of the reactions, in which a metal is oxidized, releasing electrons inside the metal. The other type is known as the cathodic reaction, in which solution species (usually O_2 or H^+) are reduced, extracting electrons from the metal. When both

reactions are in equilibrium, the flow of electrons from respective reaction is balanced, and there is no electrical current. Both reactions can occur on one metal or on two different metals that are electrically linked.

Figure I- 3 exposes this process. The vertical axis represents the electrical potential and the horizontal axis is the logarithm of absolute current. The straight lines correspond to the theoretical current for the anodic and cathodic reactions. The sharp point in the curve corresponds to the point in which the current reverses polarity as the reaction alters from anodic to cathodic, or vice versa [7].

The open-circuit potential E_{oc} is defined as an equilibrium potential assumed by the metal when there is no electrical connections to the metal. In the majority of electrochemical corrosion tests, the first step is the measurement of E_{oc}. The value of both anodic and cathodic current at E_{oc} is named the corrosion current, I_{corr}. The I_{corr} is used to determine the corrosion rate of the metal. Classic Tafel analysis is carried out by extrapolating the linear portions of a logarithmic current against potential plot back to their intersection, as represented in Figure I- 3. The value of either the anodic or the cathodic current at the intersection is I_{corr}. The measured data are fit to Eq. I.4 by setting the values of E_{corr}, I_{corr}, β_a, and β_c [7].

$$I = I_{Corr}\ \left(e^{\frac{2.303(E-Ecorr)}{\beta a}} - e^{\frac{-2.303(E-Ecorr)}{\beta c}}\right) \quad I.4$$

Where

I is the measured current from the cell in A (amperes).

I_{corr} is the corrosion current in A (amperes).

E is the electrode potential.

E_{corr} is the corrosion potential in V (Volts).

β_a is the anodic β Tafel constant in V/ decade.

B_c is the cathodic β Tafel constant in V/ decade.

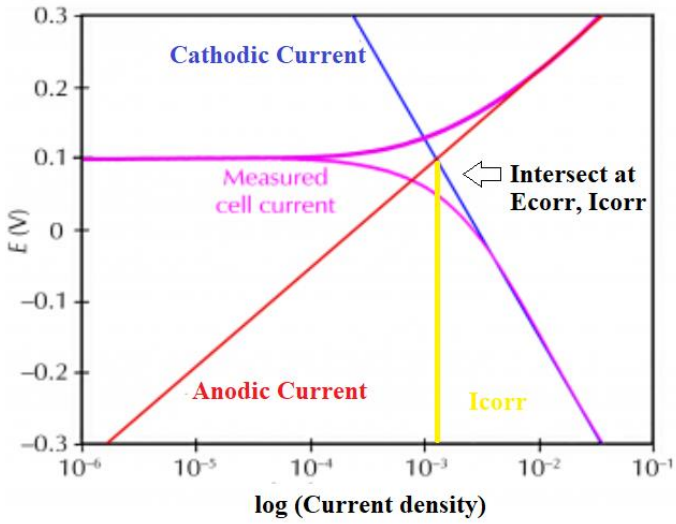

Figure I- 3. Corrosion process presenting anodic and cathodic components of current.

I.2.1. Anodic polarization scan

A schematic view of anodic polarization curve is presented in Figure I- 4. The open circuit potential is situated at point A. At this potential the sum of the anodic and cathodic reaction rates on the electrode surface is equal to zero. When the potential increases, it moves towards the region B, which is the active region. In that zone, metal oxidation is the principal reaction taking place. The passivation potential is represented by the point C, and as long as the applied potential rises over this value the current density decreases with increasing potential (region D) until a low, passive current density is achieved (Passive region - Region E)[8].

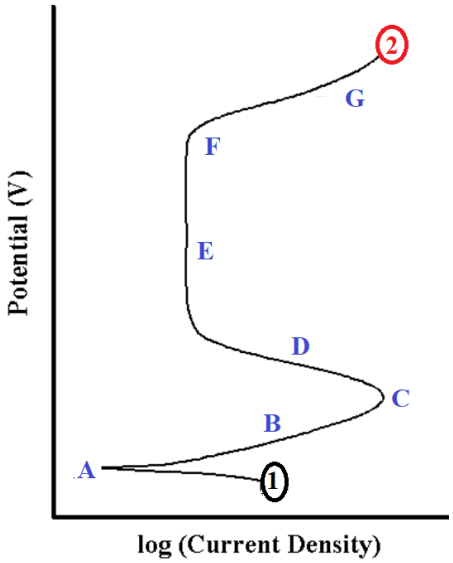

Figure I- 4. Theoretical anodic polarization scan. [8]

When the potential reaches an adequate positive value (Point F) the applied current quickly increases (region G). This increase can be a result of different phenomena, depending on the alloy and environment. For some systems such as aluminium alloys in salt water, this sudden increase in current may be pitting, which means a localized breakdown of passivity, whereas for others it may be transpassive dissolution. Transpassivation occurs when a passivated metal starts rapid dissolution (increase in corrosion rate) if the metal's electrode potential becomes too positive.

I.3. Al-transition metal coatings used as sacrificial anodes

Sacrificial Anodes are highly active metals used to protect a less active material surface from corroding. Sacrificial Anodes are made from a metal alloy with a more negative electrochemical potential than the metal which should be protected: the anode mentioned "sacrificial" will be consumed instead of the protected metal.

Since the sacrificial anode works by introducing another metal surface with a more negative and much more anodic surface, the current will move from the recently introduced anode and the protected metal becomes cathodic forming a galvanic cell. The oxidation reactions are transferred from the metal surface to the galvanic anode and will be sacrificed in favor of the protected metal structure.

Carbon steels are susceptible to corrosion in most environments and will, unless protected, oxidize spontaneously in state of high thermodynamic stability. The integrity of steel structures in marine environments can be ensured by Cathodic Protection (CP) [9]. The cathodic protection links the base metal at risk (steel) to a sacrificial metal that corrodes instead of the base metal. The technique of supplying cathodic protection to steel preserves the metal by providing a highly active metal that can work as an anode and supply free electrons.

In order to ensure a general protection of carbon steel immersed in seawater, a protection potential Ep equal to or less than -850 mV/SCE is needed [10]. Normally, pitting corrosion, stress-corrosion cracking, and intergranular corrosion may be annihilated by maintaining the electrode potential below a given critical value, known as the protection potential [11]. Aluminium and its alloys are extensively used in many industrial applications, mainly in automotive and aerospace industries. Its open circuit potential is more negative than that of steel implying its use as sacrificial materials for protection of steel substrates. It has been demonstrated that nanostructured aluminium alloys show high mechanical properties and corrosion resistance in contrast to their bulk counterparts due to the very great number of crystallizations germs, stable intermetallic compounds and increasing of the germination velocity due to a rapid solidification process [12,13]. The usefulness of pure Al as an anode material in seawater is reduced significantly due to the formation of a protective oxide film, which limits both its current and potential output. In order to improve the efficiency of Al anodes they are typically alloyed with other elements to encourage depassivation (breakdown of the oxide film) and/or shift the operating potential of the metal to a more electronegative direction. The incorporation of alloying elements has been reported as a possible method to improve the corrosion resistance of Al coatings, essentially for limiting the sensitivity to localized corrosion in saline environments [14,15].

The transition metals (TM) have a low solubility in Al, so, when a PVD method is used, it leads to deposition of extended supersaturated solid solutions of TM in Al, which are associated with enhanced mechanical properties. Additionally, TM are characterized by a low diffusivity in Al, leading to a better thermal stability of these metastable alloys. Nevertheless, high TM content in Al alloy conducts also to the detriment of sacrificial properties [16,17]. The ideal solution in terms of steels protection is a compromise between mechanical and corrosion properties.

Over the last decades, a lot of researches focused on the nanocrystalline Al-based coatings reinforced by addition of transition metals (TM) e.g. Al-Cr [18–24] , Al-Mo [25] , Al-Ti [19–21,26]

and Al-Mn [15,27]. Regarding Al-Cr alloys, the best compromise has been achieved for amorphous coatings with approximately 20 at.% Cr [22]. Addition of Mo or Mg in Al led to an improvement of mechanical properties and the pitting resistance of Al-Mo and Al-Mn coatings [16,25] .

I.3.1. Influence of transition metal elements including Zr, Cr, Sc, Ti, W and Sr

As previously explained, alloying elements are added to pure Al for various purposes, mainly for the enhancement of mechanical properties. Alloying elements induce the heterogeneity of microstructure, which is the main cause of localized corrosion starting in the form of pitting.

Zr, Cr, Sc, Ti, W and Sr are normally added individually in small amounts in order to refine grain size, reduce crystallisation and decrease the effect of intermetallic compounds [28].

Intermetallic compounds can be produced at high temperatures in the Al melt with adding Zr and Ti, presenting dispersed particles of Al_3Zr and Al_3Ti inside the solidified matrix. These particles with fine size (i.e << 1 µm) show a minimal impact on corrosion [29]. Al_3X particles where X can be Zr, Ti, Sc, W, Ti and Sr, take the form of fine insoluble dispersoids which are efficient in grain inoculation and refinement.

I.3.2. Kinetic stability of aluminium and its alloys

Kinetics is defined as the reaction during corrosion. Metals tend to stabilize to a value of electrochemical potential, characteristic of the material and its composition for a given electrolyte, when subjected to an aqueous environment. This potential can be described as the potential at which anodic and cathodic reactions over the metal surface are the same, and the value of this potential is strongly influenced by elements that may change the relative rates of anodic or cathodic reaction effectiveness over the metal surface.

Generally, a potentiodynamic polarization test is applied in order to characterize the corrosion performance of an alloy. This technique provides essential kinetic information, for example, current density over a range of potentials, corrosion potential, pitting potential, passive current density, etc. Alloy behavior and dominant reactions can be compared in a quantitative way.

The anodic part of the polarization curve provides information related to the anodic/ dissolution reaction, whereas the cathodic part symbolizes the reduction reaction, known as oxygen reduction, as explained before.

Figure I- 5 presents the potentiodynamic polarization curve for pure Al in aerated aqueous solution containing 0.1 M of NaCl. Aluminium displays a passive region in which current remains unchanged by the modification in applied potential. It is noticed as a current density plateau, as shown in Figure I- 5. Nevertheless, the current density suddenly increased after achieving a specific value of electrode potential which is known as the pitting potential (Epit) [30].

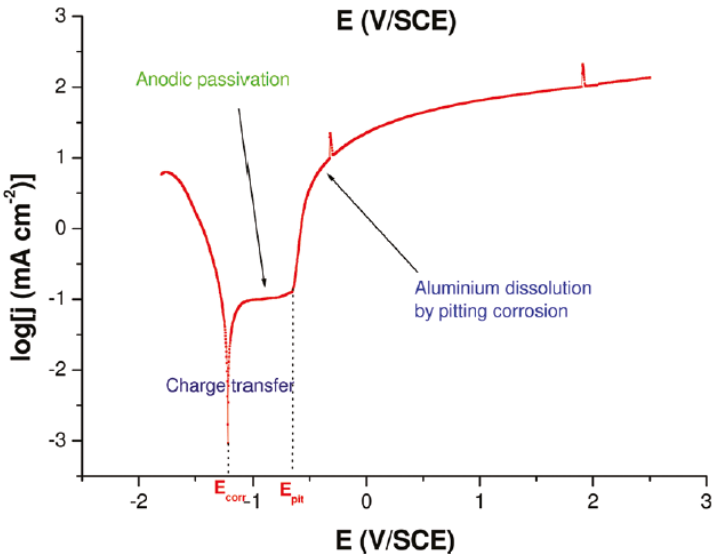

Figure I- 5. Potentiodynamic curve of pure Al in aerated aqueous solution 0.1 M NaCl [30].

Addition of more noble alloying elements normally boosts the corrosion potential to more noble values [31]. This ennoblement is not necessarily correlated to the corrosion rate. Moreover, the major threat for Al alloys is the localized attack, in particular pitting. Therefore, more noble value of pitting potential does not necessarily indicate a better corrosion resistance [32]. Normally, the electrochemical reactions of Al-alloys are greatly influenced by the microstructure and the chemistry. In order to understand better the overall kinetic stability of a metal over the potential-pH space, the staircase potentio-electrochemical impedance spectroscopy (SPEIS) method can be employed to determine kinetic stability diagrams, as demonstrated for pure Al [30].

I.4. Choice of Al-Zr coating for corrosion applications

Zirconium is a transition metal known as a great grain refiner in traditional aluminium alloys [33]. It boosts mechanical properties [33] and improves considerably the corrosion resistance in deaerated borate-boric acid solution containing Cl^- [34]. Contrary to the traditional methods where the Zr solid solubility is very low (maximum solubility is 0.083 at.% in the peritectic reaction [35]), the non-equilibrium processing methods like rapid solidification [36], mechanical alloying [37] and sputtering technique [34,38,39] offer the possibility to achieve an extended supersaturated single solid solution with high Zr contents.

Chaudhury *et al.* [36,40] have shown that rapid solidification and vapour deposition results in an enlargement of the solid solubility of zirconium up to 3 at.%. Ho *et al.* [38] have produced, by alternate sputtering deposition, a face-centered cubic phase supersaturated solution of 7.3 at. % Zr in Al. Yoshioka *et al.* [34] obtained a supersaturated phase with Zr content up to 11 at. % by sputter deposition.

Creus *et al.* presented the open circuit potential classification in saline solution of metals and Al based alloys deposited by PVD as represented in Figure I- 6[14]. The corrosion potentials of Al–Zr coating are more negative than the potential threshold needed to obtain cathodic protection of steels in saline solution. It was reported that the addition of elements such as V, Mn, Cr, Ti, Mo, Si or Zr induces an ennoblement of the corrosion potential compared with pure Al when the alloying element content is increased. The reaction of hydrogen evolution (REH) corresponds to a new cathodic reaction which takes place on the alloy surface for high negative potentials. In fact, very negative corrosion potentials contribute significantly to this cathodic reaction that could degenerate the subjacent substrate. Consequently, it is essential to limit the mass content of these alloying elements.

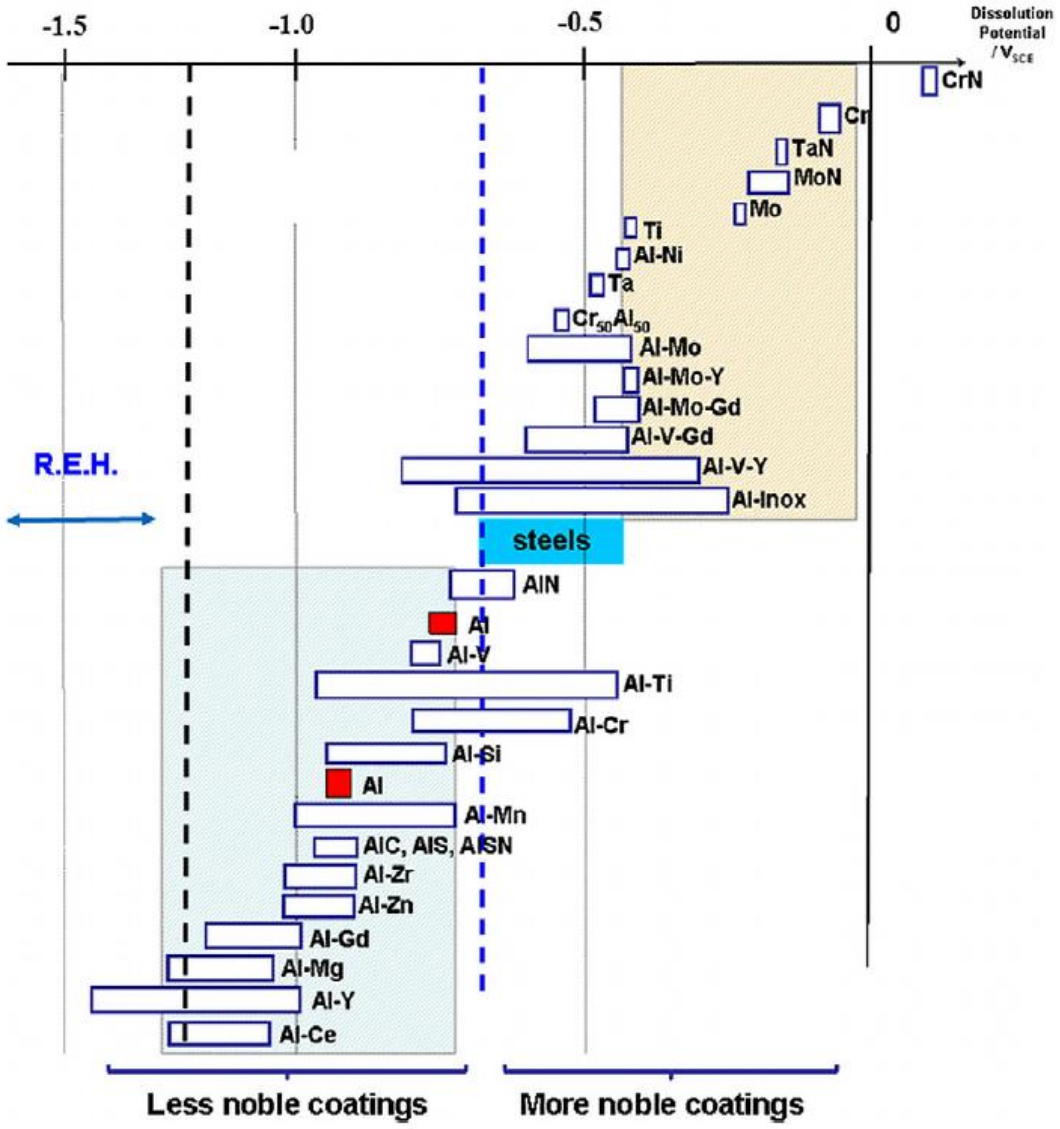

Figure I- 6. Open circuit potential classification in saline solution of binary Electron-beam physical vapor deposition of metals and Al based alloys deposited by PVD(Reproduced from J. Creus et al., 2012 [14]).

The polarization curves for several binary Al–X alloys are represented in Figure I- 7. The shapes of the polarization curves are quite similar in all cases. The presence of a large passivity domain is observed, followed by a brutal increase of anodic current representing the initiation and propagation of pits. The incorporation of these TMs improves the corrosion resistance of material by reinforcing the stability of passive film. Many works in the literature, in particular those of Crossland [41] on the anodization of different binary Al–X alloys showed an improvement of the resistance of passive film in saline medium. This improvement was mainly associated to the

incorporation of more stable oxide in the passive film that is initially mainly composed of aluminium oxide or oxo-hydroxide, and which will permit to modify the net oxide charge in contact with the corrosive medium and will affect the stage of adsorption of the chloride ions during the passive film growth [14].

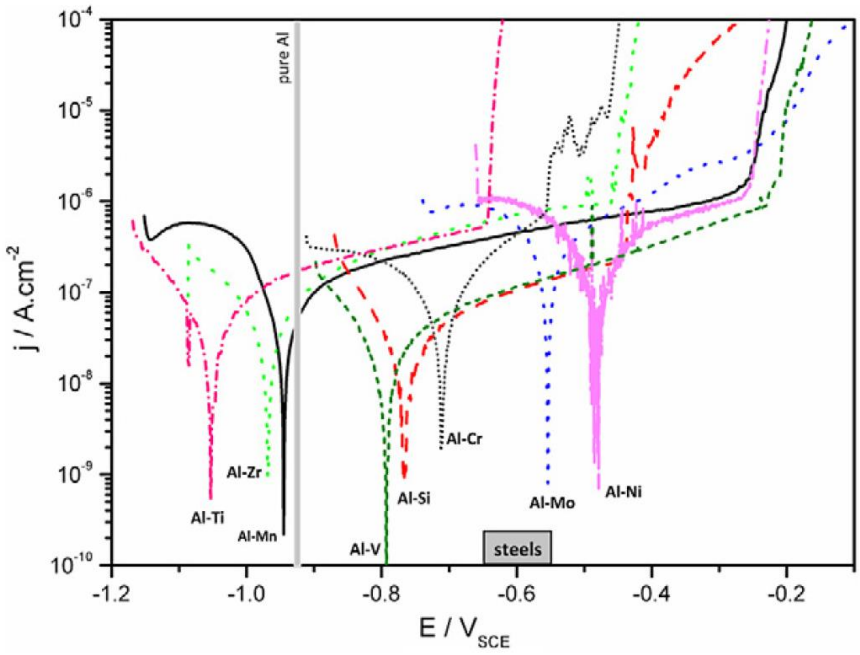

Figure I- 7. Polarization curves after 1 h of immersion in saline solution of binary Electron-beam physical vapor deposition and magnetron sputtering Al–X alloys deposited on glass substrates with concentration close to 20 wt.% (Reproduced from J. Creus et al.,2012 [14]).

Some researchers found that Zr has a tendency to be enriched in the passive film, because of its low electro-negativity and high oxygen affinity compared to Al [42]. Zr addition enhances the protective efficiency of the passive film most likely due to the corrosion products formed on Al alloys [43]. Yoshioka *et al.* have detected, by XPS analysis, the presence of Zr^{4+} species incorporated in the aluminium based passive film when they studied the passive film formed from Al-Zr alloys in deaerated borate-boric solid solution containing chloride ions at pH=8.4. The passive film consists in a solid solution of Al^{3+} and Zr^{4+} ions containing a small amount of OH^- [43].

Sanchette et al. [44] have shown that for Zr content up to 12 at.% in Al, the microstructural characterisation reveals the formation of a fcc supersatured extended solid solution of Zr in Al with a significant decrease of the mean grain size when increasing Zr content. The substitution of Al by

Zr leads to increase the lattice parameter. This increase is related to a gradual refinement of the grain size. For higher Zr contents, the coatings are expected to be a mixture of fcc solid solution of Zr in Al and an amorphous phase. The electrochemical measurements in 5 wt. % NaCl solution performed on Al-Zr films deposited on glass, show an increase of the intrinsic corrosion resistance for Zr alloys and are correlated with microstructures of as-deposited films. The refinement of grain size increases the corrosion resistance and reduces the electrochemical activity of alloys through the development of a dense passive film containing Zr. When Zr is added, the compactness of alloys increases the Cl^- blocking effect and consequently inhibits the pit propagation. The improved pitting corrosion resistance is ascribed to the more compact structure and also to the Zr enrichment in the passive film.

The coupling between Al-Zr and steel was studied by Sanchette et al. [44] in 5 wt.% NaCl solution using potentiodynamic polarisation, linear polarisation resistance and electrochemical impedance spectroscopy (EIS). The results have shown an enhancement of corrosion resistance and a decrease of corrosion kinetics with Zr content. In addition, they reported that the corrosion resistance of Al-Zr coatings is influenced by structure and porosity of coatings [44].
Liu et al. [45] reported that permeable defects like pores or pinholes are prejudicial to the corrosion performance as they afford direct paths to permit the corrosive electrolyte to access to the steel substrate.

I.5. The heterogeneous photocatalysis: principles and generalities

Photocatalysis is employed as an environmentally friendly, versatile and low-cost treatment alternative for water and air purification [46], destruction of microorganisms such as bacteria [47] and viruses [48], nitrogen fixation [49], the inactivation of cancer cells [50], the clean-up of oil spill [51] and the water splitting to generate molecular hydrogen as high-energy and ecologically clean fuel [52]. Palmisano and Sclafani [53] described the heterogeneous photocatalysis as a "catalytic process during which one or more reactions steps occur by means of electron-hole pairs photogenerated on the surface of semiconductor materials illuminated by light of suitable energy". When a photocatalyst is irradiated, it creates excited states that can provide resulting processes such as reduction-oxidation reactions and substrate transformations. The fundamental mechanism of heterogeneous photocatalysis, studied by many researchers [54,55], is presented in Figure I- 8.

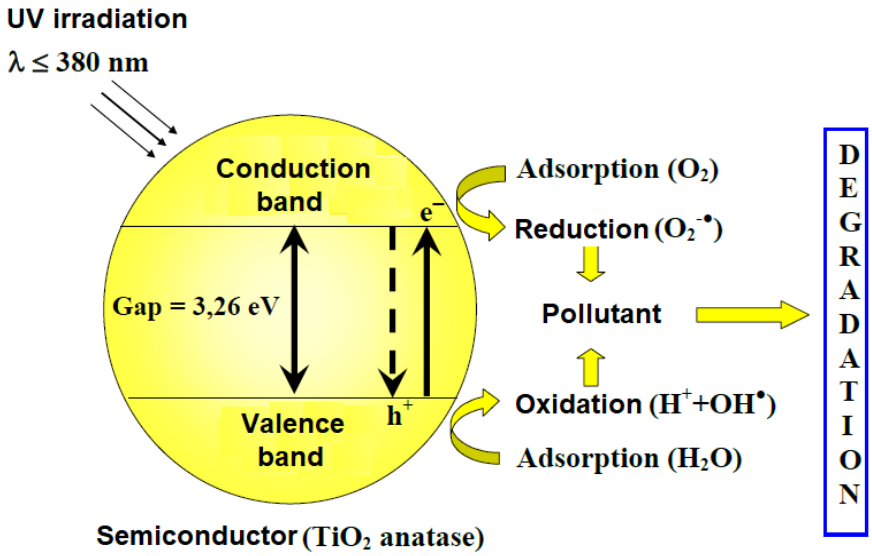

Figure I- 8. Simplified reaction scheme of photocatalysis for TiO_2 anatase.

When a semiconductor is irradiated with light of energy equal or higher than its band gap energy (E_g), electrons (e^-) from the valence band jump to the conduction band, at the same time leaving positive holes (h^+) in the valence band [56]. The photogenerated electron-hole pairs are able to induce oxidation-reduction reactions with electron donor and electron acceptor adsorbed on the catalyst surface. The redox process competes with a potential electrons-holes recombination that takes place during a few nanoseconds. Consequently of electron-hole recombination phenomena, an input energy dissipation is formed. The thermodynamic prerequisite required for the occurrence of this process is a more negative potential of the electron acceptor, and a more positive potential for the holes of the valence band against the oxidation potential of the donor.

An ideal photocatalyst must present the following characteristics [52]:

- High photoactivity.
- Biological and chemical inactivity.
- Stability against corrosion.
- Mechanical robustness.
- Suitability towards visible or near UV light.
- Low cost.
- Lack of toxicity.

A wide range of inorganic semiconductors is used for photocatalytic applications. Band gap energies of the widely used semiconductors are presented in Table I. 1.

Table I. 1. Band gap energies of semiconductors employed in photocatalytic processes [57].

Photocatalyst	Band gap energy [eV]
Si	1.1
WSe_2	1.2
WO_3	2.8
α- Fe_2O_3	2.2
V_2O_5	2.7
Cu_2O	2.2
SiC	3.0
$BaTiO_3$	3.3
CdO	2.1
CdS	2.4
CdSe	1.7
Fe_2O_3	3.1
TiO_2 rutile	3.0
TiO_2 anatase	3.2
$SrTiO_3$	3.4
SnO_2	3.5
GaAs	1.4
ZnS	3.7
ZnO	3.2

Some of the photocatalysts do not guarantee long-term activity within the photocatalytic process. Binary metal sulfides like CdS, CdSe or PbS, with narrow band gap providing the advantage of absorbing the visible light, illustrate an example of unstable semiconductor for catalysis in aqueous media when they experience photo-anodic corrosion. To prevent this drawback, numerous works suggest the addition of sulfide and sulfite to the contacting solution [58]. These materials are worldwide known as toxic compounds.

Hematite ($\alpha - Fe_2O_3$), presenting a band gap of about 2.2 eV, could be a potential photocatalyst in the visible range, but demonstrates much lower activity than TiO_2 or ZnO, certainly because of corrosion or the creation of short-lived metal-to-ligand or ligand-to-metal charge-transfer states as demonstrated by Trillas et al [59]. Both ZnO and TiO_2 anatase have band gap energy of about 3.2 eV, but zinc oxide is known to be more unstable in illuminated aqueous solution, with hydroxide species being created on the particle surface allowing the catalyst deactivation [60]. Wu et al [61] also detected a higher TiO_2 photocatalytic activity in comparison to that of SnO_2.

Heterogeneous photocatalysis based on oxide semiconductors is a promising technique for the inhibition of microbial proliferation and to reduce the growth of microorganisms. Titanium dioxide

is capable to catalyze the degradation of organic substances and it becomes highly hydrophilic under UV illumination, which turns TiO_2 to be an interesting antifouling material [62].

I.6. TiO_2 structures, electronic properties and photocatalysis

Titanium dioxide (TiO_2) presents high photocatalytic activity and chemical stability, non-toxicity and low cost, and consequently it has become the most widely used photocatalyst. TiO_2 has been widely used as white pigment in paints, plastic, paper, cosmetics and foodstuffs.

TiO_2 has three crystalline forms in nature: anatase (tetragonal), rutile (tetragonal) and brookite (orthorhombic) as represented in Figure I- 9. The majority of these phases appear exclusively at high pressure. The unit cells of the TiO_2 crystal structures are presented in Table I. 2 [63].

Rutile is stable and chemically inert. Rutile is able to be excited by both UV and visible light [64]. Anatase can be converted into rutile at high temperatures between 400 and 700 °C, and is able to be excited by UV light. Both phases show a tetragonal, ditetragonal and dipyramidal crystal structure; although they diverge from each by the different space group lattices. Brookite goes through a non-reversible phase transformation into rutile when heated at high temperatures between 700 °C and 900 °C. Additionally, TiO_2 can exist in less common crystal forms, for example, baddeleyite, columbite, ramsdellite, hollandite and monoclinic structures [65].

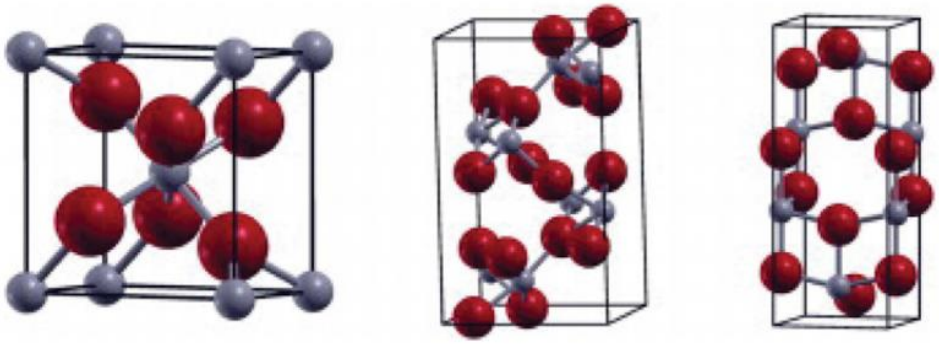

Figure I- 9. Crystal structures of TiO_2 rutile, brookite and anatase , from left to right (Reproduced from Esch et al., 2014 [63]).

Table I. 2. Crystal structure parameters of anatase and rutile TiO_2 [66].

	Anatase	Rutile
Crystal structure	tetragonal	tetragonal
Lattice constants [Å]	$a = 3.784$	$a = 4.5936$
	$c = 9.515$	$c = 2.9587$
Space group	$I4_1/amd$	$P4_2/mnm$
Molecule/cell	4	2
Volume/molecule [$Å^3$]	34.061	31.216
Density [g/cm^3]	3.79	4.13
Ti-O bond length [Å]	1.965(4)	1.949(4)
	1.965(2)	1.980(2)
O-Ti-O bond angle [°]	77.7	81.2
	92.6	90.0

Rutile form presents a more stable thermodynamic behavior and a higher refractive index than anatase, which makes it more suitable for optical applications. In contrast, anatase is the most adequate form for the photocatalytic process, solar cells and gas sensing, as a result of greater charge carrier mobility and its catalytic properties [67]. The crystal structure parameters of the TiO_2 anatase and rutile are given in Table I. 2 [66]. The anatase-rutile phase transformation is affected by several causes, for example, particle size, stress, texture and also pressure. It has been found that the temperature of anatase-rutile transformation increases when the particle size is increased. Li et al. [68] showed that a decrease in the nanoscale particle size, e.g. from 23 to 12 nm, resulted in a higher anatase stability.

TiO_2 presents a band gap energy of approximately 3.2 eV, therefore, its photoactivation demands radiation with light of wavelength less than or equal to approximately 380 nm, having a maximum activation at approximately 340 nm [66]. The valence band of wide-gap rutile and anatase is formed by *O2p* states, whereas the conduction band is made of *Ti 3d* states [69]. The electrical properties are dependent on the crystallographic direction. Titania crystals are considered a wide-gap semiconductor, which present high resistivity (~1015 Ωcm) [70] and present various sorts of ionic imperfections: titanium interstitials, titanium vacancies, bulk oxygen vacancies and reduced crystal surfaces that are considered to create shallow electron donor levels cooperating with the electric conductivity of TiO_2 [71].

I.6.1. Mechanisms of TiO_2 photocatalytic activity

Photocatalyst properties of TiO_2 are strongly based on its hydrophilic character and ability to catalyze the degradation of organic substances. Both of them are induced by UV illumination. The UV radiation provided by a strong daylight presents enough intensity to maintain the strong hydrophilicity and photocatalytic degradation. Photocatalytic decomposition is the major cleaning mechanism in applications such as water and air purification [72]. The photocatalysis performance depends on the quantity of radicals created from the reactions of H_2O and O_2 on defect sites of UV illuminated TiO_2 surfaces. Radicals (such as O_2 −, •OOH, •OH), other active species (H_2O_2), electrons or electron holes of TiO_2 can react with organic matters. Moreover, dissolved oxygen plays a considerable function in the degradation reactions [73]. The end products are predominantly CO_2 and H_2O. Depending on the decomposed compound, numerous intermediate products can be formed during the degradation [74]. TiO_2 being a semiconducting oxide that, under irradiation, behaves as a powerful oxidizing material, reducing the activation energy for the decomposition of organic/inorganic molecules. The necessary energy to promote electrons is influenced by the semiconductor band gap that represents the lowest energy required to transform the material into an electrically conductive material. TiO_2 anatase presents a band gap of about 3.2 eV and rutile phase presents a band gap of approximately 3.0 eV, which corresponds to photons with a wavelength of 388 nm and 413 nm, respectively [75].

The adsorption of organic compounds or water on TiO_2 surface is advantaged by the superhydrophilicity of the TiO_2 surface that leads to a contact angle less than 5° under UV light irradiation. The superhydrophilicity originates from modifications in the chemical configuration of the semiconductor surface [76]. As presented above, the major part of the photogenerated holes produces hydroxyl radicals by reacting with the adsorbed species, whereas the others are grabbed by lattice oxygen vacancies and, reacting with the titania molecules, induce a weakening of the lattice titanium-oxygen ions bonds. The inhibition of these bonds allows water to produce additional hydroxyl groups on the TiO_2 surface under UV light irradiation[77].

The effect of light modifications on the titania photo-induced performance and its structure changes has received considerable attention from researchers, whose objective is to improve the semiconductor performance. It is possible to understand better water and air pollution control, self-cleaning glasses and antifogging by controlling the hydrophilicity phenomenon.

I.6.2. Self-cleaning properties of TiO_2

A photocatalytic material can be considered self-cleaning if the rate of destruction/removal of the surface contaminants is higher than the rate of deposition of the contaminants. If a too thick layer of contaminants is accumulated on the surface, it will eventually impede all the essential UV light and the photocatalytic reactions will finish.

In several situations, photocatalysis alone is not sufficient to provide the surface self-cleaning in practice. TiO_2 surfaces have another property, in addition to photocatalysis, which leads to the self-cleaning ability: the photoinduced superhydrophilicity. This effect was first reported in 1997 by Wang et al. [76]. Many studies have shown that under UV irradiation the surface of TiO_2 becomes highly hydrophilic. The contact angle between a water droplet and the surface approaches zero and instead of forming droplets water forms a thin film on the surface which remains clear and transparent.

Different explanations for the photoinduced superhydrophilic effect have been given in the literature. The first proposed model assumes the ejection of oxygen atoms from the TiO_2 lattice leading to the production of surface oxygen vacancies [76]. These defects are known to induce water splitting which would then lead to increase the number of surface hydroxyl groups and improve the surface hydrophilicity [78]. The second model suggests that an important reconstruction in the surface hydroxyl groups happens under UV irradiation [79]. A more hydrophilic surface is produced when an increased quantity of metastable weakly bound hydroxyl groups are presented after UV irradiation. The third explication, and the most simple, proposes that superhydrophilicity is an intrinsic property of clean TiO_2 surfaces and that decrease in water contact angles under UV irradiation is just created by the photocatalytic oxidation of surface hydrocarbon impurities [78].

Although the ongoing discussion about the current mechanisms, the revelation of the superhydrophilic property resulted in a big interest towards TiO_2 surfaces and many applications began emerging on the market. Photocatalytic TiO_2 thin films can be applied as self-cleaning surfaces to combat fouling problems in many types of environments.

The most famous examples are self-cleaning windows fabricated by Pilkington, PPG and Saint Gobain. Photocatalytic reactions on the surface of TiO_2 decompose the accumulated organic dirt, and consequently clean the surface with the presence of UV light. Superhydrophilicity of the

irradiated TiO_2 facilitates the removal of any dirt on the surface by washing with water. Additionally to the windows, photocatalytic self-cleaning surfaces impede fouling in many other applications like bathroom tiles, lamp covers in highway tunnels, building walls, etc [80].

I.6.3. Structural design and properties of TiO_2 photocatalysts

TiO_2 nanostructures in various shapes are used in multiple applications because of their particular size-related properties. The energy band structure becomes discrete for nanometer-scale TiO_2, and its surface, photochemical, and photophysical properties are rather different from those of the bulk ones as a result of the quantum size effect. For this reason, a lot of works have focused on targeted synthesis of nanocrystalline TiO_2 with a large specific surface area [81,82].

Many aspects have been considered with the maximized surface area. The diffusion of reactants in and out of the surface region must be quick. Since light is necessary for the photocatalytic reactions the piece geometry must allow the light to reach the surface area as more as possible. Thus, photocatalysts having high surface areas have been made by introducing materials with nanoscale geometries. Thin film deposition process can be employed to develop nanostructured photocatalysts but because of large surface areas and complex three-dimensional structures involved, highly conformal film growth is necessary.

The construction of TiO_2 nano- or micro-structures with interesting morphologies and properties has recently attracted considerable attention [83] and many TiO_2 nanostructural materials, such as spheres [84], nanorods [85], fibers [86], tubes [87], sheets [88], and interconnected architectures [89], have been fabricated. Nanostructured TiO_2 materials are widely used not only in photocatalysis, but also in dye-sensitized solar cells (DSSCs) [90], lithium-ion batteries [81], and electrochromic displays [91].

In the different TiO_2 applications, its antimicrobial action has attracted a lot of interest in the last few decades. A lot of works have been published on the efficiency of TiO_2 thin films as antimicrobial systems, for bacteria, viruses, fungi and algae disruption. The TiO_2 unification also allows the reduction of fouling and at the same time highly improves water permeability and self-cleaning ability.

It is widely known that various elements influence significantly the photocatalytic performance of TiO_2, such as the crystallite size, specific surface area, pore volume, pore structure, crystalline

phase, and the exposed surface facets. Consequently, the enhancement of this performance by setting these elements remains the aim of photocatalysis research. Structural dimensionality is also an element that can influence the photocatalytic performance, and presents an important effect on the properties of TiO_2 materials as represented in Figure I- 10. For instance, a sphere with zero dimensionality presents a high specific surface area, leading to a higher rate of photocatalytic decomposition of organic pollutants [92]. One-dimensional fibers or tubes have advantages with respect to less recombination as a result of the short distance for charge carrier diffusion [93], light-scattering properties [94], and fabrication of self-standing nonwoven mats [95].

Two-dimensional nanosheets present high adhesion and smooth surfaces [96], as long as three-dimensional monoliths can have high carrier mobility as a consequence of their interconnecting structure and be used in eco-friendly decontamination. TiO_2 materials with the appropriate dimensionalities allow us to take full advantage of the extraordinary properties provided by TiO_2 materials.

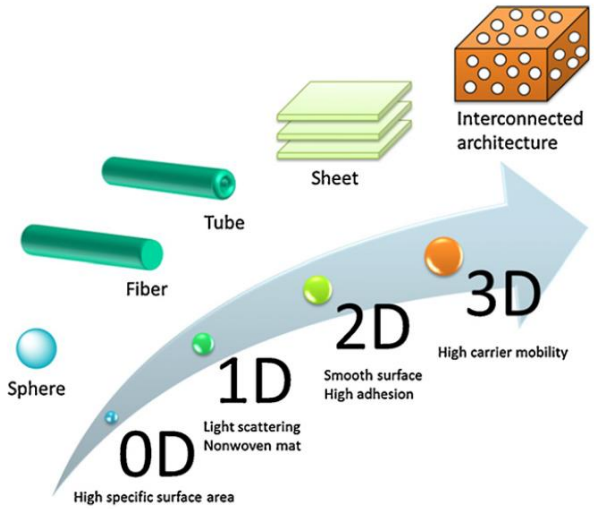

Figure I- 10. Illustration of structural dimensionality of materials with expected properties (Reproduced from K. Nakata and A. Fujishima, 2012 [97]).

I.6.4. Role of crystal size and surface area of TiO_2 on its photoactivity

It has been reported that thin films having a large surface area with high porosity and good transparency to the visible light can be efficient photocatalyst materials [98].

Increasing the light absorption is well-known in small nanocrystals where the surface to volume ratio is very high. The interface improvement of the absorption becomes significant when the particle size is about 20 nm [67]. An extra advantage acquired in nanoparticles in the few nanometer size regimes is that the large surface-to-volume ratio allows the timely usage of photogenerated carriers in interfacial process [99].

As photocatalysis is a surface phenomenon, surface area is crucial in determining the quantity of reacting sites, and charge carriers have to be employed correctly to enhance their ability to launch surface reactions. At the same time, TiO_2 crystallinity must be high to avoid the recombination of charge carriers (e^- and h^+). The energy conversion efficiency on TiO_2 is influenced by many factors, for example, surface area, e^-- h^+ recombination rate, and solar energy spectrum [67]. The surface area and crystallinity of the TiO_2 powder must to be improved in order to have an efficient photocatalysis.

Gerischer [100] created a model based on the mechanistic stages in photocatalysis on TiO_2 that concludes an important increase in quantum yield (defined as the ratio of electron–hole pairs involved in redox reactions at the surface of the titanium dioxide particles to total electron–hole pairs produced) when particle size decreases from 1000 to 10 nm. As long as the performance of light absorption reduces with decreasing the particle size, less electron–hole pairs are generated. The increase in quantum yield predicated by Gerischer's model depends on a large portion of electron–hole pairs participating in redox reactions at the surface when few electron–hole pairs are created inside the particle.

Grela and Colussi [101] created a computer stochastic model that indicates an increase in quantum yield when the particle size increases from 3 to 21 nm. The increasing of quantum yield was also accompanied with a slow rate of electron–hole recombination at the surface [102].

Grela and Colussi model shows that slower electron–hole recombination when particle size increased to 21 nm is a consequence of two hypotheses made in the model: (i) the average initial distance between electron–hole pairs is proportional to the radius of the TiO_2 particle (R), and (ii)

the average number of jumps before a free hole at the surface recombined with a trapped electron is proportional to R^2 [101].

I.6.5. Synthesis of TiO_2 nanomaterials

Nanostructure of TiO_2 can be synthesized through several methods. The most used methods are sol-gel, hydrothermal method, direct oxidation, microwave method, chemical or physical vapor deposition and also atomic layer deposition.

Generally, liquid phase deposition methods take place at low temperature and create amorphous TiO_2; a separate annealing step is essential in order to crystallize the film. TiO_2 thin films made by the sol-gel technique usually require annealing at around 400-500 °C in order to be crystallized [103]. Polycrystalline TiO_2 can be produced directly more easily by vapor phase methods, as crystalline anatase TiO_2 at much lower temperatures, close to 200 °C. Besides, gas phase methods normally ensure high quality thin films with lower impurity and higher film densities.

In the present work, TiO_2 films were synthetized by aerosol assisted chemical vapor deposition method (AACVD).

I.6.6. Synthesis of TiO_2 films by Chemical Vapor Deposition and its photocatalysis properties

Chemical vapor deposition (CVD) is a widely employed material-processing technology, based on a deposition method where chemical precursors are transferred in a vapor state to decompose on a heated substrate to create a film as illustrated in Figure I- 11. The films ca be epitaxial, polycrystalline or amorphous as a function of materials characteristics and reactor conditions. This technology is able to deposit films with a conformal and complex coverage. The CVD can be performed in various environments with improved equipment and different products in order to deposit a large diversity of materials. CVD has become the main method of film deposition for the semiconductor industry as a result of its high capacity, high purity and low cost operation. Moreover, CVD is commonly used for optoelectronics, optical and wear resistant coatings.

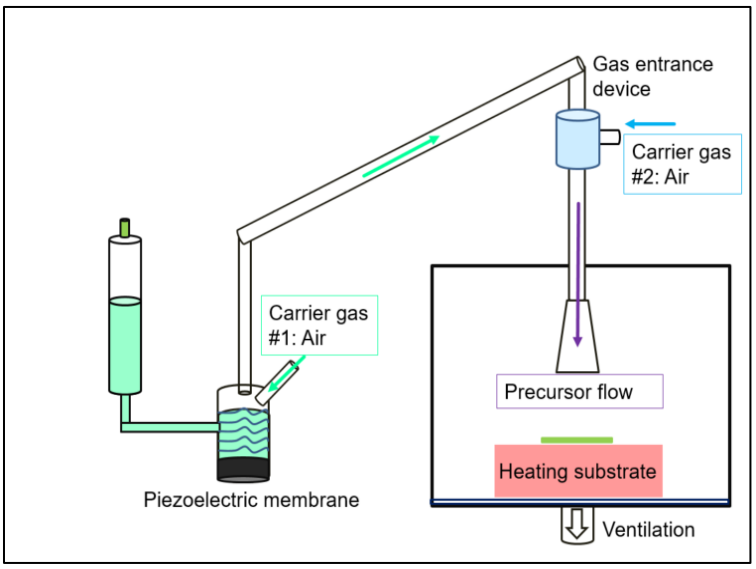

Figure I- 11: Schema of CVD system.

In general, CVD may be conducted in hot-wall or cold-wall reactors usually bellow 10^{-6} Pa and up to atmospheric pressure, with or without carrier gases, and at temperatures normally varying from 200 to 1600°C. The advanced CVD methods include the use of plasma, ions, photons, laser or combustion reactions in order to boost deposition rate and/or decrease deposition temperature. The CVD derivatives involve metal-organic CVD, organo-metallic CVD and inorganic CVD [104]. CVD has been employed in various studies to develop photocatalytic TiO_2 thin films [105] [106]. Generally, CVD reaction is employed where a titanium alkoxide vapor is controllable over the substrate at a defined temperature where the titanium precursor molecules decompose leading to TiO_2 growth [107] [108]. During the chemical reaction, O_2 reacts with the titanium precursor [109]. Plasma enhanced CVD (PECVD) has been applied to deposit photocatalytic TiO_2 thin films using $Ti(iOPr)_4$ and O_2 plasma [110]. A halide precursor, $TiCl_4$, in conjunction with ethyl acetate as the oxygen source can also be employed in the CVD of photocatalytic TiO_2 thin films [106], [111]. The films were photocatalytically active in the degradation of stearic acid by UV light and also become superhydrophilic after irradiation.

It was reported that when the CVD deposition temperature is increased for TiO_2 thin films with about 1- 2 µm of thickness, the layer presents a (112) preferential orientation and it corresponds to an optimum photocatalytic Benzene decomposition rate. As the deposition temperature increases, columnar structure is formed in vertical direction from the interface between the film and substrate that leads to a higher degree of the (112)-preferred orientation [109]. This agrees well with Weinberger and Garber [112] who said that the columnar structure of TiO_2 films grown with

preferred orientation revealed more surface area for photocatalytic reaction (columns with preferred orientation are separated by small voids).

Krumdieck et al [74] reported that the photocatalytic activity of the coatings is greatly dependent on deposition temperature. The films deposited by CVD at 375°C had very low photocatalytic activity and the films deposited at 400°C and 425°C were slightly more active but the film deposited at 450°C presented the highest photocatalytic activity [74]. The high temperature of rod sample presenting very small diameter expands through the film thickness, and leads to high growth rate in the preferred growth direction. Consequently, the surface-to-volume ratio of the samples increases, which according to Manna et al. [113] ensures higher interfacial charge carrier transfer rate and increases the delocalization of carriers in the samples, hence reduces the electron-hole recombination probability. This is consistent with the increasing of methylene blue dye reduction rate for the films deposited at 450 °C [74].

Maury et al. [114] reported that decomposition rate of Orange G by TiO_2 films increases strongly with TiO_2 thickness until approximately 300 nm for coatings deposited by AP-MOCVD on stainless steel. It was reported that when the film is dense and too thick, most of the electron-hole pairs are generated too deeply in the bulk of TiO_2 and they never reach the surface. On the other hand, if the film is too thin, only a small part of the incident light is absorbed by the TiO_2 film and the photocatalysis is low. Maury et al showed that the critical thickness necessary to obtain super-hydrophilic films seems to be the same one found for the maximum photocatalytic activity [114]. They have also reported that TiO_2 film deposited at 400°C containing only anatase phase with (1 0 1) preferred orientation presents a higher decomposition rate of Orange G solution compared to films deposited at higher temperatures containing rutile phase.

Some researchers have compared the photoconductivity between anatase and rutile phases, and they have shown that charge carrier, electrons and positive holes lifetime are higher for anatase. The rate of recombination is significantly higher for rutile. This recombination slows the photodegradation of the pollutants because it limits the formation of oxidizing species necessary for the mineralization of organic matter on the surface [115,116].

Neatu et al reported [117] several important features, which make photocatalysts more efficient, as represented in Table I. 3.

Table I. 3. Desirable properties of a photocatalyst. Adapted from Neatu et al, 2014 [117].

How to accomplish the property	Property	Effect
Small particle size	High surface area	High adsorption
Crystalline material	Single site structure	Homogeneity
Engineering band gap	Light absorption	Higher efficiency
Preferential migration along certain direction	Efficient charge separation	Low recombination
High crystallinity	High mobility of charge carries	More efficient charge separation

I.7. Biofouling and corrosion in marine structures

Biofouling can be clearly defined as the growth of very small organisms (microorganisms) and macroorganisms such as bacteria, fungi, and algae on surfaces. If these organisms provoke an accumulation, it will induce the formation of destructive biofilms that cause problems in a wide range of industrial processes[118]. Different methods are used such as membrane filtration systems, cooling towers in the energy sector, and ship hulls in the marine environment. It menaces food safety, food security, health, safe drinking water, and electricity production.

A lot of research has been made in order to investigate the mechanisms of bacterial attachment to surfaces and biofilm formation leading to biofouling [119].

Biofouling consists in two main aspects: microfouling and macrofouling. Microfouling means the formation of biofilm and adhesion to the surface, and macrofouling is described as the adhesion of organisms like barnacles, diatoms and sea weed to create a fouling community. The growing bacteria and the chemicals produce microfouling, also mentioned as ‘slime’ that expands on objects immersed in water. After few days, macrofouling expands as unicellular eukaryotes, such as protozoa and diatoms that colonize the surface. Multicellular eukaryotes start colonizing the surface during many weeks and include colonization of meroplankton larvae and algal spores.

Marine environment is a hard milieu that causes corrosion and biofouling for marine structures. Biofouling creates large operational losses for the shipping industry. A great extent of fouling on the ship’s hull notably increases the requested drag force, contributing to the drop in the whole

hydrodynamic performance of the vessel and increasing the fuel consumption. For these reasons, ships' owners are concerned with using high-performance coatings that inhibit corrosion and fouling development on the ships' hull. Rigorous environmental legislations and the needs to reduce fuel consumption have led to the development of new antifouling technologies. It has been demonstrated that the increase of roughness made by a heavily fouled ship hull may lead to get a penalty of up to 86 % at cruising speed and rather light fouling by diatom slimes can produce 10 - 16 % of penalty [120].

Marine coating producers are in general careful in adopting new technologies. Nevertheless, more and more strict environmental legislation, accompanied by customer inclination for more eco-friendly solutions, is pushing innovation in the market.

Diverse methods have been employed to minimize and control the accumulation of biofilms on surfaces. The employ of chemical products has been dominating for a long time, although their use is under serious inquiry as a result of injurious effects they have on the environment. Tributyltin oxide (TBT) for example was used as an additive to coatings for more than 40 years and it was very efficient. The use of this chemical agent has been prohibited in almost all countries because of its detrimental effects on the environment causing the toxicity of organisms and marine fauna leading consequently to carcinogenicity in human beings [121]. Physical methods such as manual cleaning are not appropriate for all surfaces and these limit their applicability.

Research over the last two decades was mostly concentrated on surface modification in order to develop self-cleaning surfaces.

Fouling can be divided in four main forms such as scaling, silting, biofouling and organic fouling [122,123], as shown in Figure I- 12. The various types of fouling usually happen at the same time and may interact with each other [124]. For all these types, controlling of biofouling is complicated, which is due to the antimicrobial resistance.

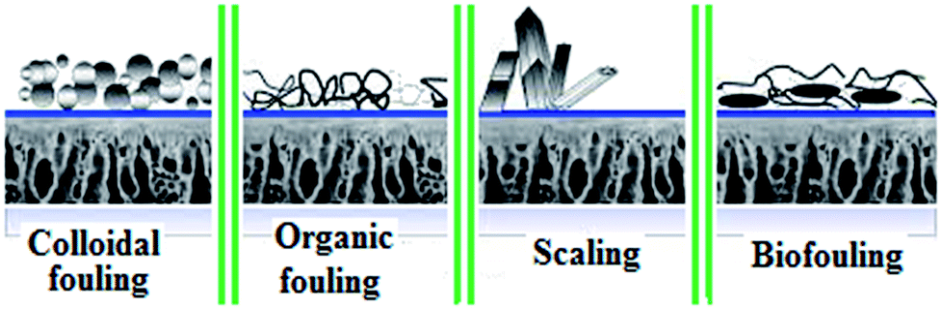

Figure I- 12. Different types of fouling [125].

I.7.1. Biofouling process

Wet environments provide best conditions for the increase of microorganisms. In the natural mediums, the majority of bacterial mass exists in biofilms attached onto surfaces. This can be explained by the fact that nutrients are adsorbed on surfaces. As a biofilm, bacteria are less likely to be swept off to aggressive circumstance and are less susceptible to antibiotics [126]. A lot of environmental parameters, for example, temperature, pH, iron availability and oxygen tension can stimulate the development of microorganisms from planktonic cells (individual microorganisms) to biofilm mode [127].

The consecutive steps of biofilm development seem to be preserved among a large extent of bacteria [128]. As reported by Flemming and Schaule [129], the process of biofouling can be separated in various stages. The processes from first surface settlement to a full biofilm maturation are illustrated in Figure I- 13 [130].

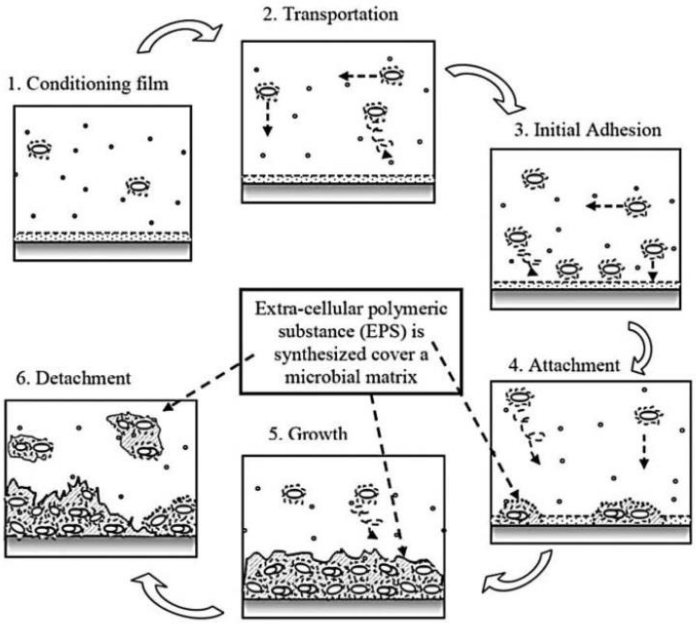

Figure I- 13. Sequential steps in biofilm formation (Reproduced from M. Tiranuntakul, 2011 [130]).

All industrial systems except operating under sterile conditions, are vulnerable to biofilm formation [131]. This generates hygienic and functional issues to several kinds of devices and equipment, resulting in important financial losses. Metals and their alloys are quite susceptible to microbial colonization and this induces biofouling and finally material failure.

I.7.2. Current research in antibiofouling fields

Nowadays, the dominant tendency to resolve the biofouling is to do modifications in the surface characteristics. Developing of self-cleaning surfaces presenting antimicrobial function is the main objective to remove the attached microbial compounds. When the biofilms colonize a surface, they change the surface properties and establish adhesion properties. Consequently, the modification of surfaces to avoid the first steps of biofilm attachment is indispensable for biofouling controlling.

Many researchers develop advanced materials with hydrophilic surfaces as a good method to control fouling [132]. It is generally considered that hydrophilic surfaces present lower fouling potential compared to their hydrophobic counterparts [133]. It is supported by the fact that a hydrophobic material may generate other nonpolar or hydrophobic compounds to be adsorbed onto its surface generating fouling [134].

The principal challenge in developing an active fouling-resistant coating is that the variety of fouling organisms is enormous, as represented in Figure I- 14, and the type of mechanisms applied is diversified. The settlement steps of fouling organisms vary in size from few micrometers to hundreds of micrometers or millimeters [135]. The surface size and topography are important in order to avoid the growth of fouling organisms.

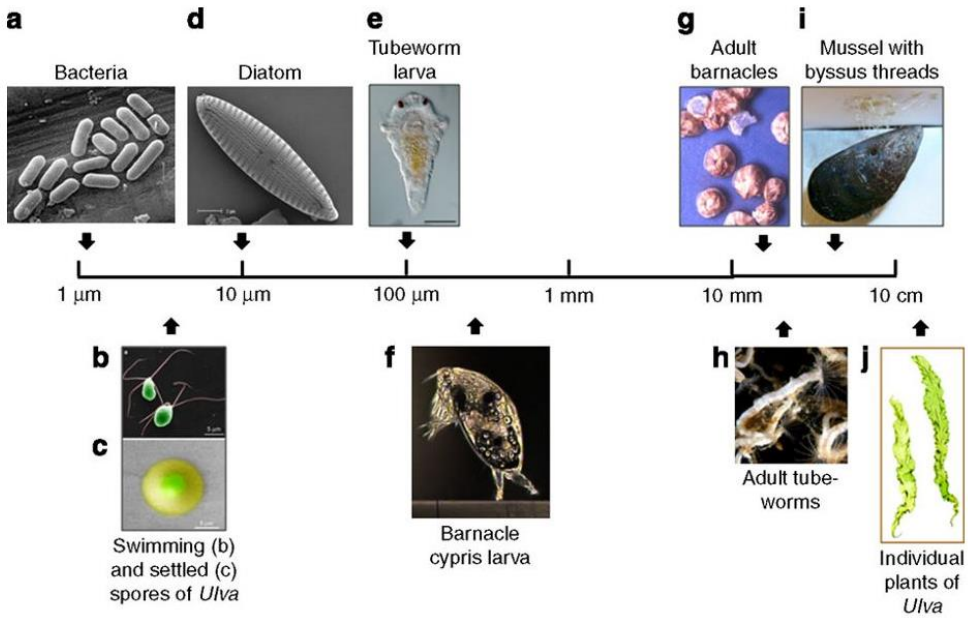

Figure I- 14. Variety and size scale of typical fouling organisms (Reproduced from J.A Callow and M.E Callow, 2011 [135]).

When an organism settles its needs to colonize a surface and grows into adult, its growth in a violent marine environment is influenced by the capacity of the macromolecular adhesive polymers secreted by the settled organisms. This is related to the interfacial molecular interactions that are in turn depend on the properties of the surface or coating at the molecular or nanoscale level [135].

The vast majority of commercial fouling resistant coatings are made with poly (dimethylsiloxane) elastomers (PDMSe). These polymers are hydrophobic, non-polar and present low surface energy (~22 mN m^{-1}) and for this reason they are presumed to have low adhesion of polar molecules because of limited opportunities for H-binding and polar interactions [136].

Despite the fact that PDMSe show the requested association of low surface energy (to reduce the work of adhesion) and low modulus, these types of coatings present some disadvantages. They are complex to bond to a substrate without an adequate tie coat as they present low surface energy. At the same time, they are less durable, more easily broken than other sorts of coatings and they

are not capable to decompose slimes governed by diatoms that bind strongly to hydrophobic surfaces [137].

The antifouling technology is considered potent when employed in high-activity for fast-moving ships (> 15 knot) and is less appropriate for ships that spend long time in a port or that use lower speeds to keep fuel efficiency. For these interests, there are extensive studies to develop antifouling technologies [136].

Field immersion test in natural seawater is required to examine the antifouling property as revealed in laboratory circumstances because there are several environmental conditions that cannot be reproduced in the laboratory [138]. The majority of static field test, not directly affected by high current velocities, and conducted in coastal or port waters is touched by turbulence generated by wind and boat wakes that can influence larval growth [139].

Short-term field tests are commonly employed in field exposures having a duration of not more than one month. This test may be enough to expose the coating to a great number of fouling organisms in the field and investigate the physical integrity of the coating over short period under real conditions. Short-term field testing is mostly employed to collect initial fouling settlements. The best coating performer can be elected after screening quickly the large-scale arrays [134].
Following the first evaluation of activity, the next step would implicate a scale-up and implementation of inspiring coatings onto huge panels composed of thick multi-layered coatings that agree with the ASTM requirements [140]. Promising coatings can be put in normal 10 by 12 inches panels using ASTM [140] rules for coating field characterization. Smaller panels 4 by 8 inches can be employed if dimensions and cost are limited. The effective time of the field immersion tests can differ from one test to another due to the variation in composition and density of fouling communities according to seasonality. Whatever the experiment, it is crucial to compare the results with a controlled coating.

Priyankha et al.[141] reported that ZnO nanorods (nanocoating) synthesized by sol-gel process prevents biofouling by producing reactive oxygen species under visible light irradiation. Other works have also reported that photocatalytic materials like TiO_2 and ZnO are able to degrade an extensive variety of contaminants [142].

It is reported that under irradiation, ZnO generates reactive oxygen species (ROS) which cause microbial cell membrane damage and increase oxidative stress ultimately leading to cell death as represented in Figure I- 15 [141].

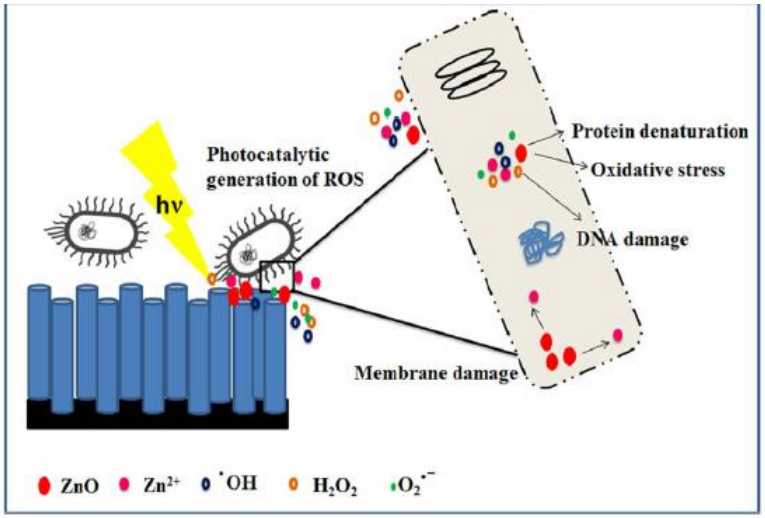

Figure I- 15. Mechanism of antifouling action (Reproduced from S. Priyanka et al., 2017 [141]).

I.8. An additional advantage of TiO_2 on steel substrates: photocathodic protection

TiO_2 films coated on metallic substrates like steel can perform a source of electrons under UV light and can provide a cathodic protection [143].

Yuan et al.[144] reported that the TiO_2 coatings can be applied to cathodic protection of metal upon illumination. It implies that a semiconductor materials as TiO_2 act as a photoanode, which is known as the photocathodic protection. During this process, the photoelectrons created in the conduction band can be moved to the metal to be protected under UV illumination. Consequently, the potential of the metal can be shifted in the negative direction [145]. If the potential is more negative than the potential of the metal to be oxidized, the metal can be protected against corrosion.

Ohko et al. [146] showed that TiO_2 film coated stainless steel produces photoelectrons which are transferred directly to the metal substrate to provide a cathodic protection of the stainless steel substrate under UV irradiation as represented in Figure I- 16.

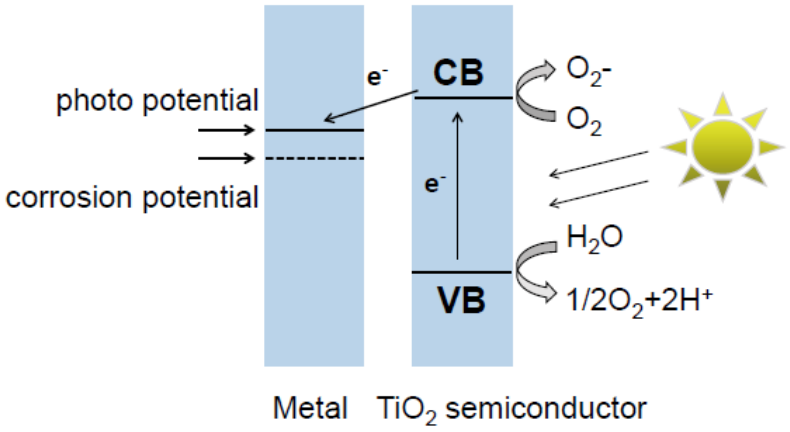

Figure I- 16: Mechanism of the photoelectrochemical anticorrosion effect of TiO2 for metals (Reproduced from Y. Bu and J.P Ao, 2017[143]).

Bamoulid et al.[147] studied the performance of TiO_2 films for improving the anticorrosion properties of a metallic substrate. They combined the use of a conversion coating and a sol-gel TiO_2 top-coat to protect a ferritic stainless steel against corrosion. The TiO_2-coated samples resisted the salt spray test within 500 h whereas the bare samples and the samples coated with a single conversion coating presented clear signs of corrosion.

Gluszek et al. [148] employed plasma assisted chemical vapor deposition (PACVD) to grow TiO_2 coatings on the surface of surgical grade 316L samples. The corrosion resistance of the coated samples was evaluated through polarization curves and EIS (Electrochemical Impedance Spectroscopy) measurements in Ringer's solution. The presence of the TiO_2 layer eliminated pitting corrosion, expanding the passivity region of the 316L samples up to 3 V. The bare alloy presented a breakdown potential at approximately 0.2 V. The corrosion potential was shifted to nobler values and the corrosion current density decreased two orders of magnitude.

Krishna et al.[149] prepared TiO_2 coatings on stainless steel, and they found that the corrosion resistance of stainless steel was improved with TiO_2 coatings.

Shen et al.[150] reported the corrosion protection of 316 L stainless steel by uniform TiO_2 nanoparticulate coatings prepared by sol–gel method. They found that the TiO_2 coatings exhibited very good corrosion resistance by acting as a protective barrier on the steel surface.

Antunes et al.[151] investigated the effect of the deposition temperature on the corrosion performance of the TiO_2 films deposited by MOCVD on Silicon wafers. The TiO_2 films were stable during the polarization tests, independently of the deposition temperature. The current density decreased sharply at the beginning of the test, indicating the passive nature of the TiO_2 films.

I.9. Objective of PhD thesis

The rising demands for eco-friendly materials presenting antibiofouling and anticorrosion properties for marine applications present a challenge to develop advanced coatings. In this context, the main objective of this thesis is to employ high quality DC magnetron sputtering and chemical vapor deposition techniques to deposit Al-Zr/TiO_2 bilayer coatings combining anticorrosion and antibiofouling properties. Al-Zr is known for protection of metallic structures against corrosion and TiO_2 films improve their photocatalytic activity under UV illumination. As well, biofouling field tests in natural seawater, at a depth of 50 cm (Atlantic Ocean, Kernevel Harbour, France) were carried out in order to evaluate the films performance in the real environment. Given the promising characteristics of Al-Zr/TiO_2 films, this work will focus on the elaboration and characterizations of TiO_2 and Al-Zr bilayer films.

References

[1] N.L. Sukiman, X. Zhou, N. Birbilis, A.E. Hughes, J.M.C. Mol, S.J. Garcia, G.E. Thompson, Durability and corrosion of aluminium and its alloys: overview, property space, techniques and developments, in: Alum. Alloy. Trends Fabr. Appl., IntechOpen, 2012.

[2] N. Sato, An overview on the passivity of metals, Corros. Sci. 31 (1990) 1–19. doi:10.1016/0010-938X(90)90086-K.

[3] Z. Szklarska-Smialowska, Mechanism of pit nucleation by electrical breakdown of the passive film, Corros. Sci. 44 (2002) 1143–1149. doi:10.1016/S0010-938X(01)00113-5.

[4] M. Pourbaix, Applications of electrochemistry in corrosion science and in practice, Corros. Sci. 14 (1974) 25–82. doi:10.1016/S0010-938X(74)80006-5.

[5] P. Gimenez, J.J. Rameau, M.C. Reboul, Experimental pH potential diagram of aluminum for sea water, Corrosion. 37 (1981) 673–682.

[6] G.G. Perrault, The role of hydrides in the equilibrium of aluminum in aqueous solutions, J. Electrochem. Soc. 126 (1979) 199–204.

[7] C. Vieillissement, C. Gabrielli, H. Takenouti, Méthodes électrochimiques appliquées à la corrosion - Techniques stationnaires Méthodes électrochimiques appliquées à la corrosion Techniques stationnaires, Ref TIP570WEB - "Corrosion Vieil. 33 (2010). https://www.techniques-ingenieur.fr/base-documentaire/materiaux-th11/essais-et-expertise-en-corrosion-et-vieillissement-42499210/methodes-electrochimiques-appliquees-a-la-corrosion-cor810/.

[8] D.G. Enos, L.L. Scribner, Technical Report on Potentiodynamic Scan, doi:10.1007/978-1-4614-8933-7.

[9] R. Johnsen, B. Nyhus, S. Wastberg, Hydrogen Induced Stress Cracking (HISC) of Stainless

Steels Under Cathodic Protection in Seawater: Presentation of a New Test Method, in: ASME 2009 28th Int. Conf. Ocean. Offshore Arct. Eng., 2009: pp. 55–67.

[10] R.A. Gummow, R.G. Wakelin, S.M. Segall, AC Corrosion: A New Threat to Pipeline Integrity?, (1996) 443–453. http://dx.doi.org/10.1115/IPC1996-1849.

[11] M. Pourbaix, Significance of protection potential in pitting, intergranular corrosion and stress-corrosion cracking, J. Less Common Met. 28 (1972) 51–65. doi:10.1016/0022-5088(72)90168-3.

[12] G. Popescu, L. Vladutiu, V. Soare, I. Surcel, D. Mitrica, I. Carcea, Nanostructure Aluminum Alloys with high physical and Mechanical Properties, Metal. Int. 14 (2009) 35–38.

[13] I. Sabirov, M.Y. Murashkin, R.Z. Valiev, Nanostructured aluminium alloys produced by severe plastic deformation: New horizons in development, Mater. Sci. Eng. A. 560 (2013) 1–24. doi:10.1016/j.msea.2012.09.020.

[14] J. Creus, C. Berziou, S. Cohendoz, A. Perez, C. Rébéré, M. Reffass, S. Touzain, C. Allely, Y. Gachon, C. Héau, F. Sanchette, A. Billard, Reactivity classification in saline solution of magnetron sputtered or EBPVD pure metallic, nitride and Al-based alloy coatings, Corros. Sci. 57 (2012) 162–173. doi:10.1016/j.corsci.2011.12.021.

[15] T.P. Moffat, G.R. Stafford, D.E. Hall, Pitting Corrosion of Electrodeposited Aluminum-Manganese Alloys, J. Electrochem. Soc. 140 (1993) 2779–2786.

[16] M. Reffass, C. Berziou, C. Rébéré, A. Billard, J. Creus, Corrosion behaviour of magnetron-sputtered Al1−x–Mnx coatings in neutral saline solution, Corros. Sci. 52 (2010) 3615–3623. doi:10.1016/J.CORSCI.2010.07.008.

[17] C. Berziou, K. Remy, A. Billard, J. Creus, Corrosion behaviour of dc magnetron sputtered Fe1−xMgx alloy films in 3 wt% NaCl solution, Corros. Sci. 49 (2007) 4276–4295. doi:10.1016/J.CORSCI.2007.04.008.

[18] F. Sanchette, Tran-Huu-Loi, C. Frantz, Deposition of metastable aluminium-chromium alloys by r.f. magnetron sputtering from mixed-powder targets, Surf. Coatings Technol. 57 (1993) 179–182. doi:10.1016/0257-8972(93)90037-O.

[19] F. Sanchette, Tran Huu Loi, A. Billard, C. Frantz, Structure—properties relationship of metastable Al-Cr and Al-Ti alloys deposited by r.f. magnetron sputtering: role of nitrogen, Surf. Coatings Technol. 74–75 (1995) 903–909. doi:10.1016/0257-8972(94)08210-3.

[20] F. Sanchette, A. Billard, C. Frantz, Mechanically reinforced and corrosion-resistant

sputtered amorphous aluminium alloy coatings, Surf. Coatings Technol. 98 (1998) 1162–1168. doi:10.1016/S0257-8972(97)00231-4.

[21] F. Sanchette, A. Billard, Main features of magnetron sputtered aluminium transition metal alloy coatings, Surf. Coatings Technol. (2001) 218–224. doi:10.1016/S0257-8972(01)01197-5.

[22] J. Creus, A. Billard, F. Sanchette, Corrosion behaviour of amorphous Al–Cr and Al–Cr–(N) coatings deposited by dc magnetron sputtering on mild steel substrate, Thin Solid Films. 466 (2004) 1–9. doi:10.1016/J.TSF.2003.11.315.

[23] J. Creus, E.H. Top, C. Savall, P. Refait, C. Ducros, F. Sanchette, Mechanical and corrosion properties of dc magnetron sputtered Al/Cr multilayers, Surf. Coatings Technol. 202 (2008) 4047–4055. doi:10.1016/J.SURFCOAT.2008.02.021.

[24] F. Sanchette, C. Ducros, A. Billard, C. Rébéré, C. Berziou, M. Reffass, J. Creus, Nanostructured aluminium based coatings deposited by electron-beam evaporative PVD, Thin Solid Films. 518 (2009) 1575–1580. doi:10.1016/J.TSF.2009.09.057.

[25] W.C. Moshier, G.D. Davis, J.S. Ahearn, The corrosion and passivity of aluminum exposed to dilute sodium sulfate solutions, Corros. Sci. 27 (1987) 785–801. doi:10.1016/0010-938X(87)90037-0.

[26] J. Creus, H. Idrissi, H. Mazille, F. Sanchette, P. Jacquot, Corrosion behaviour of Al/Ti coating elaborated by cathodic arc PVD process onto mild steel substrate, Thin Solid Films. 346 (1999) 150–154. doi:10.1016/S0040-6090(98)01742-8.

[27] S. Ruan, C.A. Schuh, Electrodeposited Al–Mn alloys with microcrystalline, nanocrystalline, amorphous and nano-quasicrystalline structures, Acta Mater. 57 (2009) 3810–3822. doi:10.1016/J.ACTAMAT.2009.04.030.

[28] J.S. Vetrano, C.H. Henager Jr, S.M. Bruemmer, Y. Ge, C.H. Hamilton, Use of Sc, Zr and Mn for grain size control in Al-Mg alloys, Miner. Met. Mater. Soc. (1998) 89–98. http://www.scopus.com/inward/record.url?eid=2-s2.0-0031702366&partnerID=40&md5=f8338f0f6855394e03b5d73ae14d660b.

[29] J.R. Scully, T.O. Knight, R.G. Buchheit, D.E. Peebles, Electrochemical characteristics of the Al2Cu, Al3Ta and Al3Zr intermetallic phases and their relevancy to the localized corrosion of Al alloys, Corros. Sci. 35 (1993) 185–195. doi:10.1016/0010-938X(93)90148-A.

[30] K. Mansouri, K. Ibrik, N. Bensalah, A. Abdel-Wahab, Anodic dissolution of pure aluminum during electrocoagulation process: Influence of supporting electrolyte, initial pH, and current density, Ind. Eng. Chem. Res. 50 (2011) 13362–13372. doi:10.1021/ie201206d.

[31] J.R. Davis, Corrosion of aluminum and aluminum alloys, Asm International, 1999.

[32] G.S. Frankel, Pitting corrosion of metals a review of the critical factors, J. Electrochem. Soc. 145 (1998) 2186–2198.

[33] I.G. Brodova, D. V Bashlykov, A.B. Manukhin, V. V Stolyarov, E.P. Soshnikova, Formation of nanostructure in rapidly solidified Al-Zr alloy by severe plastic deformation, Scr. Mater. 44 (2001) 1761–1764.

[34] H. Yoshioka, H. Habazaki, A. Kawashima, K. Asami, K. Hashimoto, The corrosion behavior of sputter-deposited Al□Zr alloys in 1 M HCl solution, Corros. Sci. 33 (1992) 425–436. doi:10.1016/0010-938X(92)90071-A.

[35] E. Clouet, J. Sanchez, C. Sigli, E. Clouet, J. Sanchez, C. Sigli, First principles study of the solubility of Zr in Al To cite this version : HAL Id : hal-00001055, (2004).

[36] Z.A. Chaudhury, C. Suryanarayana, A TEM study of decomposition behavior of a melt-quenched Al-Zr alloy, Metallography. 17 (1984) 231–252. doi:10.1016/0026-0800(84)90060-0.

[37] B. Srinivasarao, C. Suryanarayana, K. Oh-ishi, K. Hono, Microstructure and mechanical properties of Al–Zr nanocomposite materials, Mater. Sci. Eng. A. 518 (2009) 100–107. doi:10.1016/J.MSEA.2009.04.032.

[38] J. Ho, K. Lin, The metastable Al-Zr alloy thin films prepared by alternate sputtering deposition, J. Appl. Phys. 75 (1994) 2434–2440. doi:10.1063/1.356267.

[39] M.N. Rittner, Structure-Property Correlations in Nanocrystalline Al-Zr Alloy Composites, 44 (1996) 1271–1286.

[40] Z.A. Chaudhury, C. Suryanarayana, Transmission electron microscopy studies of a vapour-deposited AlZr Alloy, Mater. Sci. Eng. 67 (1984) 47–53. doi:10.1016/0025-5416(84)90030-2.

[41] A.C. Crossland, G.E. Thompson, J. Wan, H. Habazaki, K. Shimizu, P. Skeldon, G.C. Wood, The Composition and Morphology of Anodic Films on Al-Mo Alloys, J. Electrochem. Soc. 144 (1997) 847–855.

[42] H. Yoshioka, H. Habazaki, A. Kawashima, K. Asami, K. Hashimoto, The corrosion behavior

of sputter-deposited AlZr alloys in 1 M HCl solution, Corros. Sci. 33 (1992) 425–436. doi:10.1016/0010-938X(92)90071-A.

[43] H. Yoshioka, H. Habazaki, A. Kawashima, K. Asami, K. Hashimoto, Anodic polarization behaviour of sputter-deposited AlZr alloys in a neutral chloride-containing buffer solution, Electrochim. Acta. 36 (1991) 1227–1233. doi:10.1016/0013-4686(91)85113-L.

[44] M. Reffas, A.Billard, E. Conforto, F.Sanchette, J.Creus, Intrinsic structural, mechanical and corrosion properties of sputtered Al-Zr thin films. In Proceedings of the Presentation B1-3-7 in 42nd International Conference on Metallurgical Coatings and thin Films (ICMCTF), San Diego, CA, USA, 20–24 April 2015.

[45] C. Liu, Q. Bi, A. Leyland, A. Matthews, An electrochemical impedance spectroscopy study of the corrosion behaviour of PVD coated steels in 0.5 N NaCl aqueous solution: Part II.: EIS interpretation of corrosion behaviour, Corros. Sci. 45 (2003) 1257–1273. doi:10.1016/S0010-938X(02)00214-7.

[46] A. Fujishima, K. Honda, Electrochemical Photolysis of Water at a Semiconductor Electrode, Nature. 238 (1972) 37. http://dx.doi.org/10.1038/238037a0.

[47] D. Gumy, A.G. Rincon, R. Hajdu, C. Pulgarin, Solar photocatalysis for detoxification and disinfection of water: Different types of suspended and fixed TiO2 catalysts study, Sol. Energy. 80 (2006) 1376–1381. doi:10.1016/j.solener.2005.04.026.

[48] P. Maness, S. Smolinski, D.M. Blake, Z. Huang, E.J. Wolfrum, W.A. Jacoby, Bactericidal Activity of Photocatalytic TiO2 Reaction : toward an Understanding of Its Killing Mechanism Bactericidal Activity of Photocatalytic TiO2 Reaction : toward an Understanding of Its Killing Mechanism, Appl. Enrironmental Microbiol. 65 (1999) 4094–4098.

[49] G.L Petriconi, H.M Papee, Photocatalytic fixation of nitrogen by aqueous suspensions of silver iodide, Water, Air, and Soil Pollution 20 (1983) 273–274.

[50] E. Kabachkov, E. Kurkin, V. Nadtochenko, A. Terentyev, Research of photocatalytic degradation of HeLa cells at the TiO2 interface by ATR-FTIR and fluorescence microscopy, J. Photochem. Photobiol. A Chem. 217 (2011) 425–429. doi:10.1016/j.jphotochem.2010.11.019.

[51] Y.Y. Hsu, T.L. Hsiung, H. Paul Wang, Y. Fukushima, Y.L. Wei, J.E. Chang, Photocatalytic degradation of spill oils on TiO2 nanotube thin films, Mar. Pollut. Bull. 57 (2008) 873–876.

doi:10.1016/j.marpolbul.2008.03.005.

[52] R. Al-Rasheed, Water Treatment By Heterogeneous Photocatalysis an Overview, 4th SWCC Acquir. Exp. Symp. (2005) 1–14.

[53] C. Mart, G. Solana, V.Ã. Rives, G. Marc, L. Palmisano, A. Sclafani, Physico-chemical properties of WO3/TiO2 systems employed for 4-nitrophenol photodegradation in aqueous medium, Catal. Letters. 49 (1997) 235–243. doi:10.1023/A:1019025926206.

[54] M.R. Hoffmann, S.T. Martin, W. Choi, D.W. Bahnemann, Environmental Applications of Semiconductor Photocatalysis, Chem. Rev. 95 (1995) 69–96. doi:10.1021/cr00033a004.

[55] M.I. Litter, Heterogeneous photocatalysis: Transition metal ions in photocatalytic systems, Appl. Catal. B Environ. 23 (1999) 89–114. doi:10.1016/S0926-3373(99)00069-7.

[56] J. Schneider, M. Matsuoka, M. Takeuchi, J. Zhang, Y. Horiuchi, M. Anpo, D.W. Bahnemann, Understanding TiO_2 Photocatalysis: Mechanisms and Materials, Chem. Rev. 114 (2014) 9919–9986. doi:10.1021/cr5001892.

[57] V. Loddo, L. Palmisano, T. Marino, R. Molinari, Membranes for photocatalysis in water and wastewater treatment, in: Adv. Membr. Sci. Technol. Sustain. Energy Environ. Appl., Elsevier, 2011: pp. 746–768. doi:10.1533/9780857093790.5.746.

[58] D. Beydoun, R. Amal, G. Low, S. McEvoy, Role of Nanoparticles in Photocatalysis, J. Nanoparticle Res. 1 (1999) 439–458. doi:10.1023/a:1010044830871.

[59] M. Trillas, J. Peral, X. Domènech, Photo-oxidation of phenoxyacetic acid by TiO2-illuminated catalyst, Appl. Catal. B Environ. 3 (1993) 45–53. doi:10.1016/0926-3373(93)80067-N.

[60] S. Navaladian, B. Viswanathan, R.P. Viswanath, T.K. Varadarajan, Thermal decomposition as route for silver nanoparticles, Nanoscale Res. Lett. 2 (2006) 44. doi:10.1007/s11671-006-9028-2.

[61] N.-L. Wu, M.-S. Lee, Enhanced TiO2 photocatalysis by Cu in hydrogen production from aqueous methanol solution, Int. J. Hydrogen Energy. 29 (2004) 1601–1605. doi:10.1016/J.IJHYDENE.2004.02.013.

[62] T. Kallio, S. Alajoki, V. Pore, M. Ritala, J. Laine, M. Leskelä, P. Stenius, Antifouling properties of TiO2: Photocatalytic decomposition and adhesion of fatty and rosin acids, sterols and lipophilic wood extractives, Colloids Surfaces A Physicochem. Eng. Asp. 291 (2006) 162–176. doi:10.1016/j.colsurfa.2006.06.044.

[63] T.R. Esch, I. Gadaczek, T. Bredow, Surface structures and thermodynamics of low-index of rutile, brookite and anatase – A comparative DFT study, Appl. Surf. Sci. 288 (2014) 275–287. doi:10.1016/J.APSUSC.2013.10.021.

[64] K. Hashimoto, H. Irie, A. Fujishima, TiO2 Photocatalysis: A Historical Overview and Future Prospects, Jpn. J. Appl. Phys. 44 (2005) 8269. http://stacks.iop.org/1347-4065/44/i=12R/a=8269.

[65] L. Kavan, J.H. Yum, M. Grätzel, Optically Transparent Cathode for Dye-Sensitized Solar Cells Based on Graphene Nanoplatelets, ACS Nano. 5 (2011) 165–172. doi:10.1021/nn102353h.

[66] T. Mathews, R.P. Antony, Titania Nano-architectures for Energy, in: S. Babu Krishna Moorthy (Ed.), Thin Film Struct. Energy Appl., Springer International Publishing, Cham, 2015: pp. 129–165. doi:10.1007/978-3-319-14774-1_5.

[67] A.N. Banerjee, The design, fabrication, and photocatalytic utility of nanostructured semiconductors: Focus on TiO2-based nanostructures, Nanotechnol. Sci. Appl. 4 (2011) 35–65. doi:10.2147/NSA.S9040.

[68] W. Li, C. Ni, H. Lin, C.P. Huang, S.I. Shah, Size dependence of thermal stability of TiO2 nanoparticles, J. Appl. Phys. 96 (2004) 6663–6668. doi:10.1063/1.1807520.

[69] M. Hervieu, The Surface Science of Metal Oxides. By V. E. Henrich and P. A. Cox, Cambridge University Press, Cambridge 1994, XIV, 464 pp., hardcover, £ 55.00, ISBN 0-521-44389-X, Adv. Mater. 7 (1995) 91–92. doi:10.1002/adma.19950070122.

[70] H.K. Ardakani, Electrical and optical properties of in situ “hydrogen-reduced” titanium dioxide thin films deposited by pulsed excimer laser ablation, Thin Solid Films. 248 (1994) 234–239. doi:10.1016/0040-6090(94)90017-5.

[71] A.T. Paxton, L. Thiên-Nga, Electronic structure of reduced titanium dioxide, Phys. Rev. B. 57 (1998) 1579–1584. doi:10.1103/PhysRevB.57.1579.

[72] D.M. Blake, D.M. Blake, Bibliography of Work on the Heterogeneous Photocatalytic Removal of Hazardous Compounds from Water and Air, Update Number 4,October 2001.

[73] J. Schwitzgebel, J.G. Ekerdt, H. Gerischer, A. Heller, Role of the Oxygen Molecule and of the Photogenerated Electron in TiO2-Photocatalyzed Air Oxidation Reactions, J. Phys. Chem. 99 (1995) 5633–5638. doi:10.1021/j100015a055.

[74] S. Krumdieck, R. Gorthy, A.J. Gardecka, D. Lee, S.S. Miya, S. Davies Talwar, M.I.J.

Polson, C. Bishop, Characterization of photocatalytic, wetting and optical properties of TiO2 thin films and demonstration of uniform coating on a 3-D surface in the mass transport controlled regime, (2016). doi:10.1016/j.surfcoat.2016.11.064.

[75] H. Lasa, B. Serrano, M. Salaices, Photocatalytic Reaction Engineering, Photocatalytic React. Eng. 25 (2005) 169–183.

[76] R. Wang, K. Hashimoto, A. Fujishima, M. Chikuni, E. Kojima, A. Kitamura, M. Shimohigoshi, T. Watanabe, Light-induced amphiphilic surfaces, Nature. 388 (1997) 431. http://dx.doi.org/10.1038/41233.

[77] A. Figoli, J. Bundschuh, L. Arockiasamy, C. Chaumette, M. Faccini, M. Boerrigter, T. Marino, Photocatalytic activity and synthesis procedures of TiO2 nanoparticles for potential applications in membranes, in: Appl. Nanotechnol. Membr. Water Treat., CRC Press, 2017: pp. 127–146.

[78] T.L. Thompson, J.T. Yates, Surface Science Studies of the Photoactivation of TiO2 New Photochemical Processes, Chem. Rev. 106 (2006) 4428–4453. doi:10.1021/cr050172k.

[79] N. Sakai, A. Fujishima, T. Watanabe, K. Hashimoto, Quantitative Evaluation of the Photoinduced Hydrophilic Conversion Properties of TiO2 Thin Film Surfaces by the Reciprocal of Contact Angle, J. Phys. Chem. B. 107 (2003) 1028–1035. doi:10.1021/jp022105p.

[80] A. Fujishima, K. Hashimoto, T. Watanabe, TiO2 Photocatalysis: Fundamentals and Applications, BKC, 1999.

[81] S. Ding, J.S. Chen, Z. Wang, Y.L. Cheah, S. Madhavi, X. Hu, X.W. Lou, TiO2 hollow spheres with large amount of exposed (001) facets for fast reversible lithium storage, J. Mater. Chem. 21 (2011) 1677–1680. doi:10.1039/C0JM03650A.

[82] D.S. Kim, S.J. Han, S.-Y. Kwak, Synthesis and photocatalytic activity of mesoporous TiO2 with the surface area, crystallite size, and pore size, J. Colloid Interface Sci. 316 (2007) 85–91. doi:10.1016/J.JCIS.2007.07.037.

[83] X. Chen, Y. Mao, Synthesis of Titanium Dioxide (TiO2) Nanomaterials, J. Nanosci. Nanotechnol. 6 (2006) 906–925.

[84] C. Wang, L. Yin, L. Zhang, Y. Qi, N. Lun, N. Liu, Large Scale Synthesis and Gas-Sensing Properties of Anatase TiO2 Three-Dimensional Hierarchical Nanostructures, Langmuir. 26 (2010) 12841–12848. doi:10.1021/la100910u.

[85] P.D. Cozzoli, A. Kornowski, H. Weller, Low-Temperature Synthesis of Soluble and Processable Organic-Capped Anatase TiO2 Nanorods, J. Am. Chem. Soc. 125 (2003) 14539–14548. doi:10.1021/ja036505h.

[86] H. An, B. Zhu, J. Li, J. Zhou, S. Wang, S. Zhang, S. Wu, W. Huang, Synthesis and Characterization of Thermally Stable Nanotubular TiO2 and Its Photocatalytic Activity, J. Phys. Chem. C. 112 (2008) 18772–18775. doi:10.1021/jp8031258.

[87] K. Nakata, L. Baoshun, Y. Ishikawa, M. Sakai, H. Saito, T. Ochiai, H. Sakai, T. Murakami, M. Abe, K. Takagi, A. Fujishima, Fabrication and Photocatalytic Properties of TiO2 Nanotube Arrays Modified with Phosphate, 2011. doi:10.1246/cl.2011.1107.

[88] Y. Aoyama, Y. Oaki, R. Ise, H. Imai, Mesocrystal nanosheet of rutile TiO2 and its reaction selectivity as a photocatalyst, CrystEngComm. 14 (2012) 1405–1411. doi:10.1039/C1CE05774J.

[89] I.M. Arabatzis, P. Falaras, Synthesis of Porous Nanocrystalline TiO2 Foam, Nano Lett. 3 (2003) 249–251. doi:10.1021/nl0259028.

[90] K. Hou, B. Tian, F. Li, Z. Bian, D. Zhao, C. Huang, Highly crystallized mesoporous TiO2 films and their applications in dye sensitized solar cells, J. Mater. Chem. 15 (2005) 2414–2420. doi:10.1039/B417465H.

[91] P. Periyat, N. Leyland, D.E. McCormack, J. Colreavy, D. Corr, S.C. Pillai, Rapid microwave synthesis of mesoporous TiO2 for electrochromic displays, J. Mater. Chem. 20 (2010) 3650–3655. doi:10.1039/B924341K.

[92] B. Liu, K. Nakata, M. Sakai, H. Saito, T. Ochiai, T. Murakami, K. Takagi, A. Fujishima, Mesoporous TiO2 Core–Shell Spheres Composed of Nanocrystals with Exposed High-Energy Facets: Facile Synthesis and Formation Mechanism, Langmuir. 27 (2011) 8500–8508. doi:10.1021/la201547g.

[93] X. Lu, F. Huang, X. Mou, Y. Wang, F. Xu, A General Preparation Strategy for Hybrid TiO2 Hierarchical Spheres and Their Enhanced Solar Energy Utilization Efficiency, 2010. doi:10.1002/adma.201001008.

[94] L. Yao, T.W. Haas, A. Guiseppi-Elie, G.L. Bowlin, D.G. Simpson, G.E. Wnek, Electrospinning and Stabilization of Fully Hydrolyzed Poly(Vinyl Alcohol) Fibers, Chem. Mater. 15 (2003) 1860–1864. doi:10.1021/cm0210795.

[95] K.H. Lee, H.Y. Kim, M.S. Khil, Y.M. Ra, D.R. Lee, Characterization of nano-structured

poly(ε-caprolactone) nonwoven mats via electrospinning, Polymer (Guildf). 44 (2003) 1287–1294. doi:10.1016/S0032-3861(02)00820-0.

[96] K. Katsumata, S. Okazaki, C.E.J. Cordonier, T. Shichi, T. Sasaki, A. Fujishima, Preparation and Characterization of Self-Cleaning Glass for Vehicle with Niobia Nanosheets, ACS Appl. Mater. Interfaces. 2 (2010) 1236–1241. doi:10.1021/am100091f.

[97] K. Nakata, A. Fujishima, TiO2 photocatalysis: Design and applications, J. Photochem. Photobiol. C Photochem. Rev. 13 (2012) 169–189. doi:10.1016/j.jphotochemrev.2012.06.001.

[98] N. Negishi, K. Takeuchi, Preparation of a transparent thin-film photocatalyst for elimination of VOC, Res. Chem. Intermed. 29 (2003) 861–879. doi:10.1163/156856703322601861.

[99] B. Enright, D. Fitzmaurice, Spectroscopic determination of electron and hole effective masses in a nanocrystalline semiconductor film, J. Phys. Chem. 100 (1996) 1027–1035.

[100] H. Gerischer, Photocatalysis in aqueous solution with small TiO2 particles and the dependence of the quantum yield on particle size and light intensity, Electrochim. Acta. 40 (1995) 1277–1281. doi:10.1016/0013-4686(95)00058-M.

[101] M.A. Grela, A.J. Colussi, Kinetics of Stochastic Charge Transfer and Recombination Events in Semiconductor Colloids. Relevance to Photocatalysis Efficiency, J. Phys. Chem. 100 (1996) 18214–18221. doi:10.1021/jp961936q.

[102] C.-C. Wang, Z. Zhang, J.Y. Ying, Photocatalytic decomposition of halogenated organics over nanocrystalline titania, Nanostructured Mater. 9 (1997) 583–586. doi:10.1016/S0965-9773(97)00130-X.

[103] M. Langlet, S. Permpoon, D. Riassetto, G. Berthomé, E. Pernot, J.C. Joud, Photocatalytic activity and photo-induced superhydrophilicity of sol-gel derived TiO2 films, J. Photochem. Photobiol. A Chem. 181 (2006) 203–214. doi:10.1016/j.jphotochem.2005.11.026.

[104] G. Anthony C. Jones and Michael L. Hitchman.Malandrino, Chemical Vapour Deposition. Precursors, Processes and Applications., Angew. Chemie Int. Ed. 48 (2009) 7478–7479. doi:10.1002/anie.200903570.

[105] I. Justicia, P. Ordejón, G. Canto, J.L. Mozos, J. Fraxedas, G.A. Battiston, R. Gerbasi, A. Figueras, Designed Self-Doped Titanium Oxide Thin Films for Efficient Visible-Light Photocatalysis, Adv. Mater. 14 (2002) 1399–1402. doi:10.1002/1521-4095(20021002)14:19<1399::AID-ADMA1399>3.0.CO;2-C.

[106] A. Mills, N. Elliott, I.P. Parkin, S.A. O'Neill, R.J. Clark, Novel TiO2 CVD films for semiconductor photocatalysis, J. Photochem. Photobiol. A Chem. 151 (2002) 171–179. doi:10.1016/S1010-6030(02)00190-9.

[107] V.G. Bessergenev, M.C. Mateus, D.A. Vasconcelos, J.F.M.L. Mariano, A.M. Botelho Do Rego, R. Lange, E. Burkel, TiO2:(Fe, S) thin films prepared from complex precursors by CVD, physical chemical properties, and photocatalysis, Int. J. Photoenergy. 2012 (2012). doi:10.1155/2012/767054.

[108] V. Bessergenev, R.J.F. Pereira, M.C. Mateus, I. Khmelinskii, D.A. Vasconcelos, R. Nicula, E. Burkel, A.M. Rego, A. Saprykin, Study of physical and photocatalytic properties of titanium dioxide thin films prepared from complex precursors by chemical vapour deposition, Thin Solid Films. 503 (2006) 29–39.

[109] D. Byun, Y. Jin, B. Kim, J. Kee Lee, D. Park, Photocatalytic TiO2 deposition by chemical vapor deposition, J. Hazard. Mater. 73 (2000) 199–206. doi:10.1016/S0304-3894(99)00179-X.

[110] C. Guillard, D. Debayle, A. Gagnaire, H. Jaffrezic, J.M. Herrmann, Physical properties and photocatalytic efficiencies of TiO2films prepared by PECVD and sol-gel methods, Mater. Res. Bull. 39 (2004) 1445–1458. doi:10.1016/j.materresbull.2004.04.028.

[111] S.A. O'Neill, I.P. Parkin, R.J.H. Clark, A. Mills, N. Elliott, Atmospheric pressure chemical vapour deposition of titanium dioxide coatings on glass, J. Mater. Chem. 13 (2003) 56–60. doi:10.1039/B206080A.

[112] D. Byun, Y. Jin, B. Kim, J. Kee Lee, D. Park, Photocatalytic TiO2 deposition by chemical vapor deposition, J. Hazard. Mater. 73 (2000) 199–206. doi:10.1016/S0304-3894(99)00179-X.

[113] L. Manna, E.C. Scher, L.-S. Li, A.P. Alivisatos, Epitaxial Growth and Photochemical Annealing of Graded CdS/ZnS Shells on Colloidal CdSe Nanorods, J. Am. Chem. Soc. 124 (2002) 7136–7145. doi:10.1021/ja025946i.

[114] F.D. Duminica, F. Maury, R. Hausbrand, Growth of TiO2 thin films by AP-MOCVD on stainless steel substrates for photocatalytic applications, Surf. Coatings Technol. 201 (2007) 9304–9308. doi:10.1016/j.surfcoat.2007.04.011.

[115] K.M. Schindler, M. Kunst, Charge-carrier dynamics in titania powders, J. Phys. Chem. 94 (1990) 8222–8226. doi:10.1021/j100384a045.

[116] Y. Ku, R.-M. Leu, K.-C. Lee, Decomposition of 2-chlorophenol in aqueous solution by UV irradiation with the presence of titanium dioxide, Water Res. 30 (1996) 2569–2578. doi:10.1016/S0043-1354(96)00147-9.

[117] Ş. Neaţu, J.A. Maciá-Agulló, H. Garcia, Solar light photocatalytic CO2 reduction: General considerations and selected bench-mark photocatalysts, Int. J. Mol. Sci. 15 (2014) 5246–5262. doi:10.3390/ijms15045246.

[118] M. Al-Ahmad, F. a. Abdul Aleem, a. Mutiri, a. Ubaisy, Biofuoling in RO membrane systems Part 1: Fundamentals and control, Desalination. 132 (2000) 173–179. doi:10.1016/S0011-9164(00)00146-6.

[119] H.-C. Flemming, Biofouling bei Membranprozessen, 1995. doi:10.1007/978-3-642-79371-4.

[120] M.P. Schultz, Effects of coating roughness and biofouling on ship resistance and powering, Biofouling. 23 (2007) 331–341. doi:10.1080/08927010701461974.

[121] M. Champ, Economic and environmental impacts on ports and harbors from the convention to ban harmful marine anti-fouling systems, Mar. Pollut. Bull. 46 (2003) 935–940.

[122] M. Herzberg, M. Elimelech, Biofouling of reverse osmosis membranes: Role of biofilm-enhanced osmotic pressure, J. Memb. Sci. 295 (2007) 11–20. doi:10.1016/j.memsci.2007.02.024.

[123] J.C. Kruithof, J.C. Schippers, P.C. Kamp, H.C. Folmer, J.A.M.H. Hofman, Integrated multi-objective membrane systems for surface water treatment: pretreatment of reverse osmosis by conventional treatment and ultrafiltration, Desalination. 117 (1998) 37–48. doi:10.1016/S0011-9164(98)00065-4.

[124] F. Persson, J. Långmark, G. Heinicke, T. Hedberg, J. Tobiason, T.A. Stenström, M. Hermansson, Characterisation of the behaviour of particles in biofilters for pre-treatment of drinking water, Water Res. 39 (2005) 3791–3800. doi:10.1016/j.watres.2005.07.007.

[125] R.R. Choudhury, J.M. Gohil, S. Mohanty, S.K. Nayak, Antifouling{,} fouling release and antimicrobial materials for surface modification of reverse osmosis and nanofiltration membranes, J. Mater. Chem. A. 6 (2018) 313–333. doi:10.1039/C7TA08627J.

[126] W. Norde, Surface-tethered polymers to influence protein adsorption and microbial adhesion, Zeitschrift Für Phys. Chemie. 221 (2007) 47–63.

[127] N.R. Stanley, B.A. Lazazzera, Environmental signals and regulatory pathways that influence

biofilm formation, Mol. Microbiol. 52 (2004) 917–924. doi:10.1111/j.1365-2958.2004.04036.x.

[128] G.O. Toole, H.B. Kaplan, R. Kolter, Biofilm formation as microbial development, Annu Rev Microbiol, (2000) 49–79.

[129] G. Schaule, Desalination, 70 (1988) 95-119, 70 (1988) 95–119.

[130] M. Tiranuntakul, Evaluation of fouling in a pilot scale membrane bioreactor, Doctoral dissertation, (2011) 256.

[131] P. Bishop, The role of biofilms in water reclamation and reuse, 2007. doi:10.2166/wst.2007.005.

[132] K. Yokwana, N. Gumbi, F. Adams, S. Mhlanga, E. Nxumalo, B. Mamba, Development of functionalized doped carbon nanotube/polysulfone nanofiltration membranes for fouling control, J. Appl. Polym. Sci. 132 (2015) n/a-n/a. doi:10.1002/app.41835.

[133] M. Zhang, B. qiang Liao, X. Zhou, Y. He, H. Hong, H. Lin, J. Chen, Effects of hydrophilicity/hydrophobicity of membrane on membrane fouling in a submerged membrane bioreactor, Bioresour. Technol. 175 (2015) 59–67. doi:10.1016/j.biortech.2014.10.058.

[134] C.S. Lim, S.S.C. Lee, W. Leong, Y.X. NG, S.L.M. Teo, A Short Review of Laboratory and Field Testing of Environmentally Benign Antifouling Coatings, Indian J. Geo-Marine Sci. 43 (2014) 2067–2074.

[135] J.A. Callow, M.E. Callow, Trends in the development of environmentally friendly fouling-resistant marine coatings, Nat. Commun. 2 (2011) 210–244. doi:10.1038/ncomms1251.

[136] A. A. Finnie, D. N. Williams, Paint and Coatings Technology for the Control of Marine Fouling, 2010. doi:10.1002/9781444315462.ch13.

[137] P.J. Molino, E. Campbell, R. Wetherbee, Development of the initial diatom microfouling layer on antifouling and fouling-release surfaces in temperate and tropical Australia, Biofouling. 25 (2009) 685–694. doi:10.1080/08927010903089912.

[138] A.A. Henrikson, J.R. Pawlik, A new antifouling assay method: results from field experiments using extracts of four marine organisms, J. Exp. Mar. Bio. Ecol. 194 (1995) 157–165. doi:10.1016/0022-0981(95)00088-7.

[139] M.R.A. Koehl, Mini review: Hydrodynamics of larval settlement into fouling communities, Biofouling. 23 (2007) 357–368. doi:10.1080/08927010701492250.

[140] W. Conshohocken, Standard Test Method for Testing Antifouling Panels in Shallow Submergence 1, Order A J. Theory Ordered Sets Its Appl. (1998) 1–8. doi:10.1520/D3623-78AR04.2.

[141] P. Sathe, K. Laxman, M.T.Z. Myint, S. Dobretsov, J. Richter, J. Dutta, Bioinspired nanocoatings for biofouling prevention by photocatalytic redox reactions, Sci. Rep. 7 (2017) 3624. doi:10.1038/s41598-017-03636-6.

[142] P. Sathe, J. Richter, M. Myint, S. Dobretsov, J. Dutta, Self-decontaminating photocatalytic zinc oxide nanorod coatings for prevention of marine microfouling: a mesocosm study, Biofouling. 32 (2016) 383–395.

[143] Y. Bu, J.-P. Ao, A review on photoelectrochemical cathodic protection semiconductor thin films for metals, Green Energy Environ. 2 (2017) 331–362. doi:10.1016/j.gee.2017.02.003.

[144] J. Yuan, S. Tsujikawa, Characterization of Sol-Gel-Derived TiO2 Coatings and Their Photoeffects on Copper Substrates, J. Electrochem. Soc. 142 (1995) 3444–3450.

[145] H. Park, K.Y. Kim, W. Choi, A novel photoelectrochemical method of metal corrosion prevention using a TiO2 solar panel, Chem. Commun. (2001) 281–282.

[146] Y. Ohko, S. Saitoh, T. Tatsuma, A. Fujishima, Photoelectrochemical anticorrosion and self-cleaning effects of a TiO2 coating for type 304 stainless steel, J. Electrochem. Soc. 148 (2001) B24--B28.

[147] L. Bamoulid, M.T. Maurette, D. De Caro, A. Guenbour, A. Ben Bachir, L. Aries, S. El Hajjaji, F. Benoît-Marquié, F. Ansart, An efficient protection of stainless steel against corrosion: Combination of a conversion layer and titanium dioxide deposit, Surf. Coatings Technol. 202 (2008) 5020–5026. doi:10.1016/j.surfcoat.2008.05.011.

[148] J. Głuszek, J. Masalski, P. Furman, K. Nitsch, Structural and electrochemical examinations of PACVD TiO2 films in Ringer solution, Biomaterials. 18 (1997) 789–794. doi:10.1016/S0142-9612(96)00210-4.

[149] D.S.R. Krishna, Y. Sun, Thermally oxidised rutile-TiO2 coating on stainless steel for tribological properties and corrosion resistance enhancement, Appl. Surf. Sci. 252 (2005) 1107–1116. doi:10.1016/j.apsusc.2005.02.046.

[150] G.X. Shen, Y.C. Chen, C.J. Lin, Corrosion protection of 316 L stainless steel by a TiO2 nanoparticle coating prepared by sol-gel method, Thin Solid Films. 489 (2005) 130–136. doi:10.1016/j.tsf.2005.05.016.

[151] R. Antunes, Effect of the Deposition Temperature on the Corrosion Stability of TiO2 Films Prepared by Metal Organic Chemical Vapor Deposition., Int. J.Electrochem.Sci, 8 (2013) 1487–1500.

Chapter II: Deposition and Characterization of Al-Zr thin films

Physical Vapor Deposition (PVD) technologies are widely used for the synthesis of thin layers. In PVD processes, the coating is deposited by condensation from a flux of neutral or ionized atoms of metals. The different PVD processes can be distinguished via the type of the transfer of metallic species and the plasma conditions employed during the deposition process [1].

Magnetron sputtering is a PVD technology commonly used because of its high deposition rate and good film performance (reproducibility, homogeneity, etc.). This technique is compatible with the synthesis of films on large surfaces. Sputtering method uses argon ions for bombarding a

cathodically connected target made of the coating material. Sputtered target species are condensed on the cold substrate surface leading to layer growth.

In order to develop new Al-Zr coatings as sacrificial anodes we first studied the effect of the zirconium content on the properties of Al-Zr alloys deposited by DC magnetron sputtering.

The first part of this chapter will be devoted to the description of the production process as well as the deposition conditions for the coating synthesis. The microstructural and physical properties will be discussed in the second part.

II.1. Direct Current Magnetron Sputtering

II.1.1. Principle of magnetron sputtering

Nowadays, sputtering technique is used at industrial scale for many applications. An abnormal glow discharge is produced by applying a voltage in the order of 1 to 3 kV between the cathode (the target) and the anode (the walls of the grounded reactor) in a rarefied atmosphere of argon at a pressure reduced generally between 0.1 and 10 Pa. As a result, partially ionized plasma composed of electrons, ions and neutral species is formed between the two electrodes. Positive ions are accelerated towards the negatively polarized target under the effect of a local electric field and these ions bombard the target's surface. Several mechanisms can be produced on the surface of the target:

- Ejection of an atom from the target by momentum transfer.
- Implantation of the incident ion.
- Reflection of the incident ion neutralized by charge transfer.
- Emission of secondary electrons which ensure the self-maintenance of the discharge.

The ejected atom acquires enough energy to cross the plasma and finally condenses on the first surface encountered. The growth of a thin layer takes place in many stages:

- Adsorption of atoms on the substrate surface.
- Interaction between deposited species and / or those of the substrate forming a stable bond.
- Nucleation.
- Volume growth.
- Diffusion of atoms in volume in the layer and / or in the substrate.

Close to the surface, the incident atom is subjected to a potential energy formed by the atoms of the surface. The interactions involved are Van der Waals interactions. This atom diffuses on the substrate surface during a time that depends on the interactions between the adatoms, the substrate, the temperature and the deposition rate. During its diffusion, it chemically binds with the substrate on a favorable site (Chemisorption). This type of site is called germination site. When the adatom arrives on one of the sites already occupied, it binds to the germ in the course of formation. Nucleation of germs is preferably carried out at the level of the defects present on the substrate surface.

The growth of films can be divided into different stages of germination and growth. These processes are determined by thermodynamic parameters as well as kinetic parameters. The actual growth mode is determined mostly by the conditions such as deposition rate, temperature and pressure.

A thermodynamic criterion developed by Bauer [2] for the growth mode in equilibrium conditions is given by the following equation:

$$\Delta\sigma = \sigma f + \sigma i - \sigma s \quad \textit{II. 1}$$

With:

σs = surface energy of the substrate,

σi = free enthalpy of the film-substrate interface,

σf = free enthalpy of the film surface

It is possible to distinguish three growth modes from this criterion (Figure II- 1).

If $\Delta\sigma \leq 0$, the atoms are bound more strongly to the substrate than the ones to the others and the films tend to extend over the substrate to minimize total energy. In this condition, a full recovery of the substrate by the films is favorable and the growth mode of Frank van der Merwe (layer-by-layer type) is observed.

If $\Delta\sigma \geq 0$, the atoms are bonded to each other more strongly than they are bound to substrate. In this case, the Volmer-Weber growth mode (of the island type) is obtained. There is a third possibility: $\Delta\sigma$ can change from a negative value to a positive one depending on the thickness of the film. This comes from the strain energy, proportional to the thickness of the film, which can bring additional energy to $\Delta\sigma$. In in this case, the growth mode of Stranski-Krastanov (mixed type) is obtained.

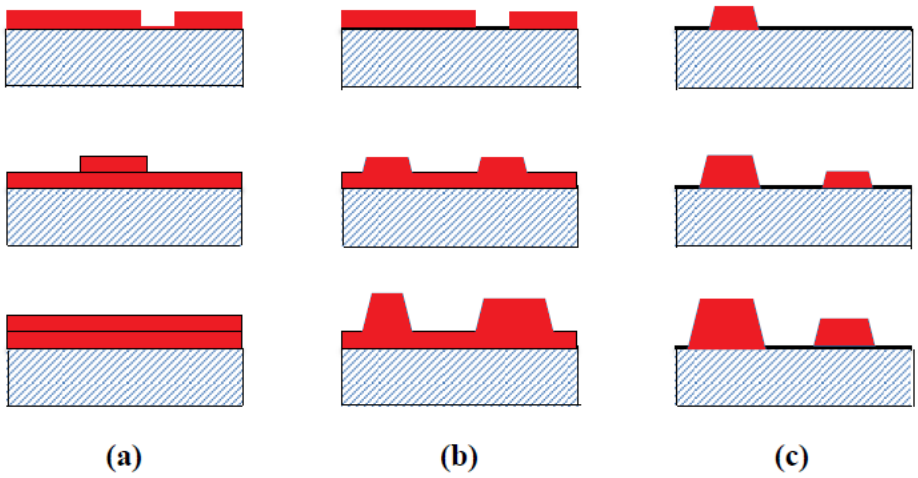

Figure II- 1. Diagram of the three growth modes of thin films: Morphology of a film by the mechanisms of (a) Frank van der Merwe, (b) Stranski-Krastanov and (c) Volmer- Weber.

In most practical cases, the growth of the films takes place in conditions out of thermodynamic equilibrium, and is strongly influenced by kinetic processes. Therefore, the final macroscopic state of the film is not necessarily the most stable thermodynamically but the most favorable from the kinetics point of view. Morphology of thin layers strongly depends on the deposition conditions and is the subject of a so-called structure zone model (the SZMs). The first model of structure zone for metallic thin films was proposed by Thornton in 1977 [3]. In this model, the most important deposition parameters are the working pressure and the homologous temperature (the ratio of the substrate temperature and the melting temperature of the deposited material was used: Ts / Tm). The SZM's concept was extended to a more generalized situation by Anders in 2010 [3] as presented in Figure II- 2. In this model, Anders proposed three axes: the generalized homologous temperature (T *, the homologous temperature as well as the temperature shift caused by the potential energy of particles arriving on the surface), the normalized flow of kinetic energy of the particles arriving on the surface (E *, the initial energy from the plasma as well as the variation related to the acceleration in the reactor), and the thickness of the film (t *).

For magnetron sputtering, T * and E * are mainly influenced by substrate temperature and working pressure. During the deposition, the substrate temperature influences the mobility of the surface adatoms. The increase of the substrate temperature leads to increase the mobility of species adsorbed on the substrate surface and increasing their diffusion in volume leads to densify the deposited layer. The deposition pressure impacts the energy and angles between the normal of the

substrate and the trajectory of the incident particles. Decreasing the deposition pressure has the same effect as increasing the deposition temperature. Anders' model, presented in Figure II- 2, shows four different zones.

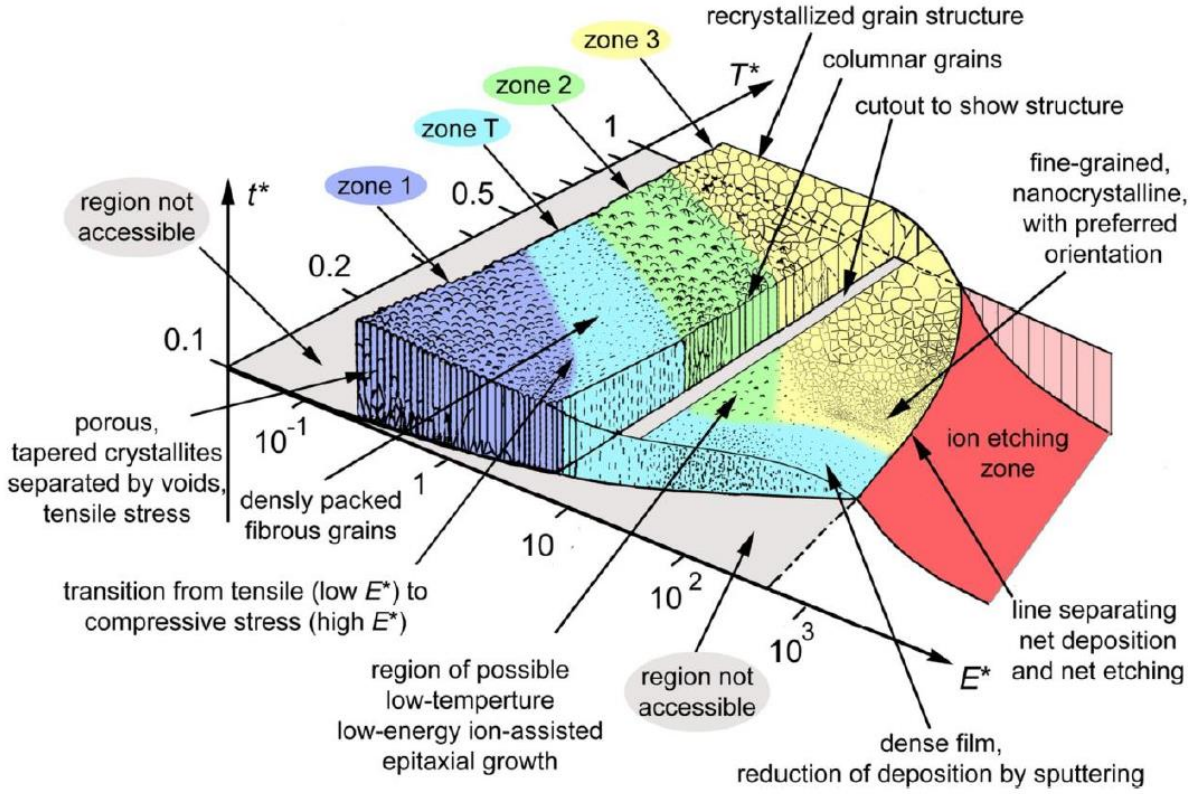

Figure II- 2. Anders's Structure zone diagram.[4]

Zone 1 (T / Tf < 0.25): this zone is composed of grains in the form of porous fibers separated by gaps. This porous morphology is due to the shading effect, which occurs during growth, and at a very limited surface diffusion.

Zone T (transition): the film growth takes place in the form of assembled fibers in a dense morphology, and the shading effects are minimized compared to zone 1. Consequently, the surface appearance is relatively smooth.

Zone 2 (0.25 < T / Tf < 0.5): the width of the columns is fixed on the thickness of the layer and the columns are organized in a dense manner separated by well-defined grain boundaries. Shading effects are very little present in this area where surface diffusion is important.

Zone 3 (T / Tf > 0.5): The volume diffusion is predominant in this zone. Consequently, the recrystallization produces grains that are no longer columnar but equiaxed.

II.1.2. Description of DC magnetron sputtering reactor

The Dephis 4 reactor (Figure II- 3) allows the placement of four targets with a diameter of 200 mm. The targets are placed on the bottom of the chamber. A carbon paper spacer ensures electrical and thermal conduction and provides sufficient mechanical clamping of the target to the cathode. The rotating substrate holder consists in a stainless steel tray with 600 mm in diameter. The distance between the substrate holder and the targets is adjustable and could be varied between 6 and 45 cm. In our study, we kept this distance constant at 10 cm.

A base vacuum of about 10^{-4} Pa is reached through a pumping system consisting of a primary pump and a turbomolecular pump.

The gases are introduced and controlled using brand mass flow meters Tylan. In order to allow stripping and bias of the substrate, the sample holder is connected to a RF power supply. This reactor, equipped with 4 targets, allows deposition of alloys with controlled chemical composition. The working pressure is controlled by either argon flow or a throttle valve.

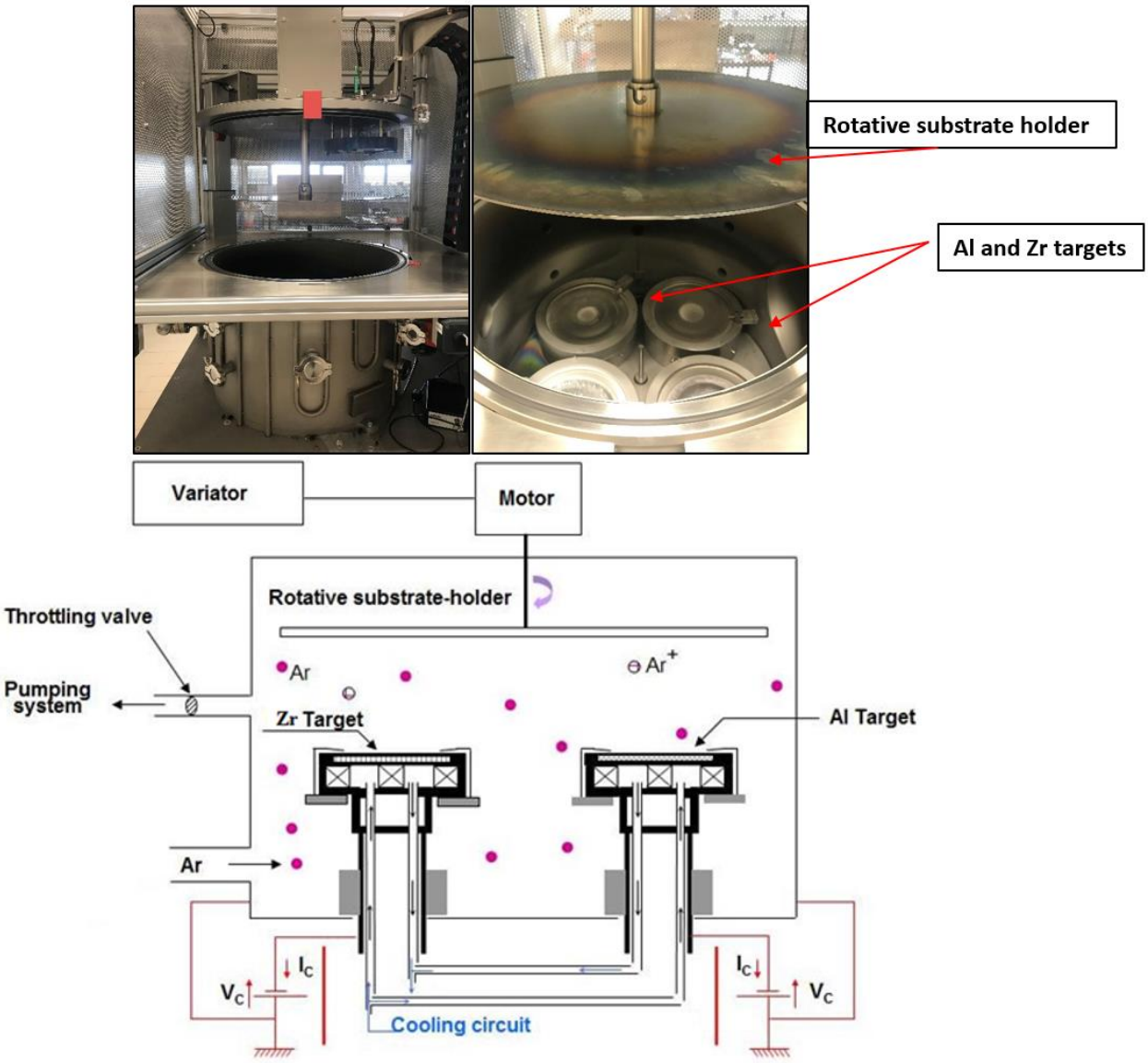

Figure II- 3. View and scheme of the DC magnetron sputtering machine Dephis 4.

II.1.3. Substrates

Al-Zr alloy films were deposited on three types of substrates to be used for performing multi types of characterizations. Glass slides with dimensions 76 × 26 × 1 mm^3 were used for characterizations by XRD and electrochemical measurements. High speed steel disc substrates (Φ 30 mm x 1 mm thick) were polished and used for nanoindentation and electrochemical characterizations. Silicon wafers were also used to perform observations using a scanning electron microscope (SEM).

The substrates were cleaned with ethanol and acetone in an ultrasonic bath and then dried in hot air before ion cleaning and film deposition.

II.2. Al-Zr films deposited by DC magnetron sputtering

Al-Zr alloy films were deposited from pure metallic Al and Zr targets in a pure argon atmosphere at floating temperature (< 80°C). The total mass flow of argon and working pressure were kept constant at 50 sccm and P_{ar} = 0.33 Pa, respectively. The deposition system is shown in Figure II- 3.

The substrates were positioned on a rotating substrate-holder (10 rounds per minute) ensuring a good homogeneity in thickness and composition of coatings.

Bias voltage of the substrate holder allowed an ion etching with applying a power of 500W at an argon pressure of 0.3 Pa for 30 minutes before each deposition stage in order to improve the film adhesion.

Evolution of Zr content was ensured by fixing the aluminium discharge current at 2.0 A and by changing that of the Zr one between 0 and 1.3 A. The deposition conditions of Al-Zr alloys are shown in Table II. 1.

Film thickness was measured using fused quartz substrates by a tactile method using an Altysurf 500 profilometer produced by ALTIMET. This device is equipped with an inductive sensor, allowing a precision of the order of 10 nm.

The chemical composition of Al-Zr alloy films deposited on silicon were evaluated by means of EDS (Figure II- 4).

Table II. 1: Deposition conditions of Al-Zr films.

Samples	I Al (A)	I Zr (A)	Al (V)	Zr (V)	Power Al (W)	Power Zr (W)	Time (min)	Pression (Pa)	Ar (Sccm)
I Al	2.0	-	255	-	515	-	150	0.33	50
II Al-Zr		0.22		180		39			
III Al-Zr		0.35		195		67			
IV Al-Zr		0,5		205		102			
V Al-Zr		1		214		214			
VI Al-Zr		1.3		215		280			

Figure II- 5 shows the variation of film thickness and Zr content as a function of current applied to the Zr target. It is possible to accurately control the zirconium content and confirms that the ratio between the atomic percentages of Zr and Al increases almost linearly with the intensity applied to the zirconium target.

Thickness also increased with the zirconium content, reaching 4.3 μm for a zirconium content greater than 27 at. %. The incorporation of zirconium in aluminium coating increases the deposition rate, which is obviously associated with the increase of the total power dissipated on both targets.

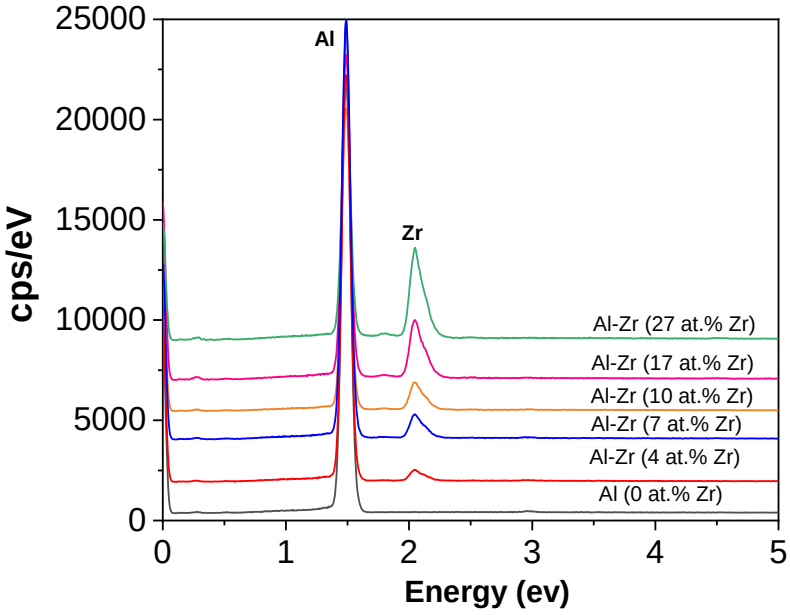

Figure II- 4. EDS analysis of Al-Zr films deposited on silicon substrate.

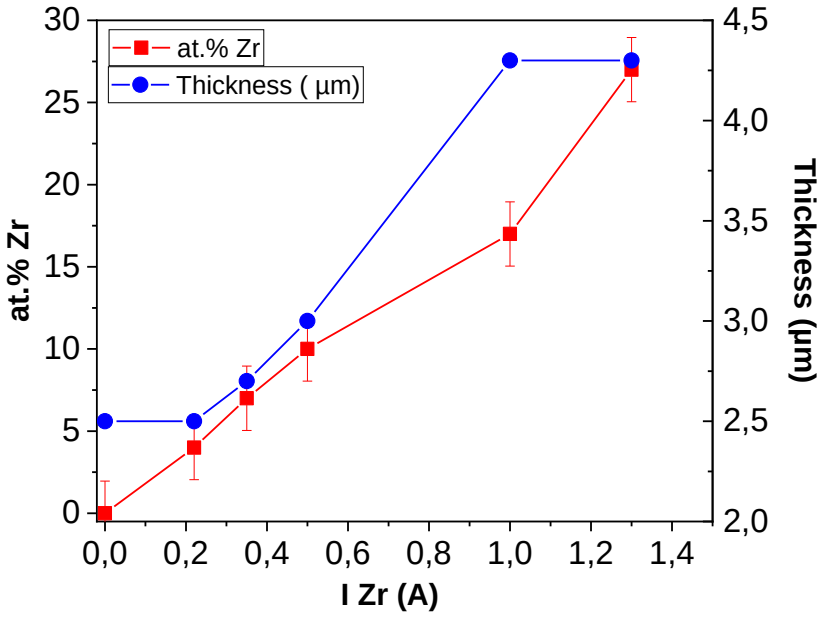

Figure II- 5. Evolution of thickness and Zr content in films as a function of the intensity of current applied to Zr target (I Al = 2 A).

In general, most of coatings presents stresses, which depend on the deposition parameters as well as on the differences in properties between the coating and the substrate. The appearance of compressive and tensile stresses is generally observed in films deposited by PVD[5].

From a qualitative perspective, thin film total stress can be written as follow:

$$\sigma_{tot} = \sigma_{ext} + \sigma_{th} + \sigma_{int} \qquad \text{II. 2}$$

where σ_{ext} means the external stress due to the external loading, σ_{th} the thermally-induced stress and σ_{int} the internal stress[6]. In the case of our coatings σ_{ext} is equal to zero, because no external load was applied and σ_{th} is negligible since our substrates were not heated during deposition.

There are several methods that can be exploited for the determination of internal residual stresses. As part of our study we chose Stoney's formula [6]. The following hypotheses were considered in order to apply this method: homogenous substrate and coating, isotropic and linear elastic behavior, substrate much thick compared to the film thickness, infinitesimal deformations and rotations, constant stress and curvature radius on the whole surface of the sample [6].

The Stoney's formula can be expressed according to the following formula:

$$\sigma = \frac{E_S}{6\,(1-\nu_S)}\,\frac{hs^2}{h_f}\left(\frac{1}{R}-\frac{1}{R_0}\right) \qquad \text{II. 3}$$

Where,

E_S : Young's Modulus of the substrate = 200 Gpa

ν_S : Poisson's ratio of the substrate = 0.3

hs : thickness of the substrate = 220 µm

h_f : thicknesses of the film.

R: Curvature radius of the substrate after deposition.

R_0: Curvature radius of the substrate before deposition.

Iron wires were used a substrate to determine the residual stresses. Before deposition, a heat treatment at 550°C was carried out on these samples, in a Mo device, in order to start from a zero stress state.

The curvature radius was measured by an optical profilometer Altysurf 500 before and after deposition considering the whole surface of the sample. A tensile stress is achieved when the curvature of the sample is concave and a compressive stress is considered when this curvature radius is convex. The positive sign is used respecting the international convention for tensile stress. In the opposite case, a compressive film stress is obtained corresponding to a negative value.

Figure II-6 shows the internal residual stresses calculated by Stoney's formula as a function of zirconium content in Al-Zr alloys. The films containing 4 and 7 at. % Zr present low tensile stress. By increasing the zirconium content above 10 at. %, the internal residual stresses are compressive reaching a value of -260 MPa for Al-Zr film containing 27 at. % of zirconium.

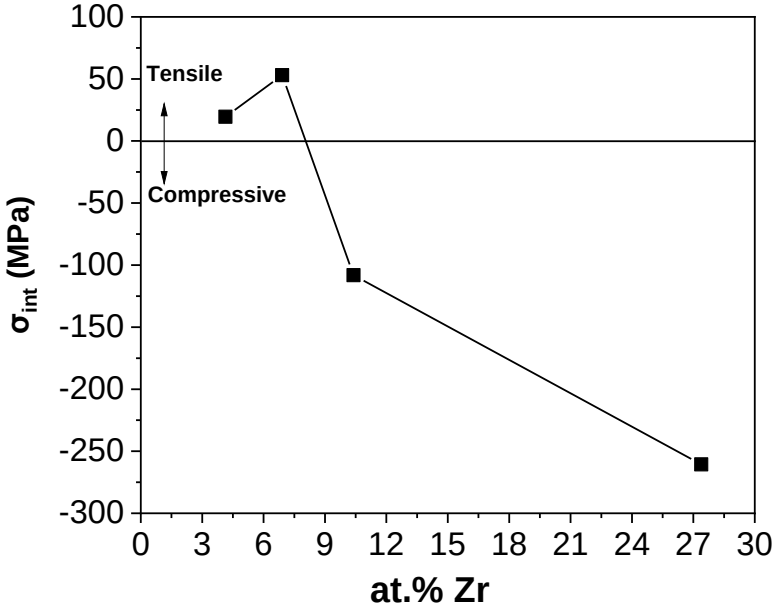

Figure II- 6. Variation of residual stress as a function of zirconium content in Al-Zr alloy films.

Generally, the residual compressive stresses are measured when a growing coating is bombarded by ions having energies between ten and hundreds of eV.

It was noticed that residual stresses take place as a result of a decrease in spacing between growing crystallites [7]. It will be described in more detail in the morphology discussion which follows in section II.3.

II.3. Structural characterization and morphology of Al-Zr thin films

The structure and lattice parameters of the Al-Zr films were studied by standard X-ray diffraction technique using a Bruker AXS D8-Advance diffractometer with Cu K_α (λ_{Cu} = 0.15418 nm) radiation, working at 40 KV and 40 mA. The measurements were carried out with 2θ varying

from 35° to 90°. The acquisition time was 1 s with steps of 0.03° in θ-2θ configuration (Figure II-7).

Films morphology was observed by scanning electron microscopy (SEM) using a FEI Quanta 250 field-emission scanning electron microscope (FESEM) for high-resolution images.

X-ray diffraction patterns of Al-Zr films deposited on glass by magnetron sputtering are shown in Figure II- 6. For Zr contents below 10 at. %, the diffractograms show the well-defined diffraction peaks, which correspond to fcc structure, indicating the growth of a supersaturated solid solution of Zr in Al. When Zr contents are higher than 10 at. % diffraction peaks are broader. The peaks broadening is the result of grain refinement occurred when Zr content increased. Simultaneously, a shift of the diffraction peaks to lower values of 2θ angles was observed, which is due to a progressive increase of lattice parameter. The estimation of average lattice parameter of these Al-Zr alloys from the θ angles corresponding to the (111) planes confirms that the lattice parameter increased from a= 4.050 Å for pure Al to a= 4.060 Å for Al-Zr alloy having 27 at. % Zr. As far as Zr atomic radius (0.218 nm) is greater than that of Al (0.182 nm), the lattice increase is associated to the substitution of aluminium atom by zirconium atom in the fcc lattice.

Above 10 at.% Zr, according to previous results on Al-Transition Metal (TM) coatings, the Al-Zr films are probably a mixture of the solid solution of Zr in fcc-Al and an amorphous phase. This evolution is consistent with binary Al-TM (Transition Metal) alloys deposited by magnetron sputtering [8–12].

The intermetallic compounds like Al_3Zr, stable in Al-Zr alloys made by conventional techniques are not observed in these Al-Zr films, which can be explained by the non-equilibrium character of magnetron sputtering technology [13].

Yang *et al.*[14] have developed a thermodynamic model concerning the structure of Al-Zr alloys deposited by co-sputtering. They showed that Al-Zr alloys having a zirconium content between 23.5 and 67.5 at. % present an amorphous phase thermodynamically more stable compared to the crystalline phases. Co-sputter-deposited Al-Zr alloys containing 7 at. % Zr presents a polycrystalline fcc structure and for films containing a Zr content higher than 22 at. %, an amorphous structure is detected.

The structure of Al-Zr (4 at. % Zr) as-deposited film after annealing at 500 °C was studied by X-ray diffraction in order to check its thermal stability at temperature conditions used for depositing TiO_2 top coating by aerosol CVD.

Figure II- 8 shows the XRD patterns for the high speed steel substrate and Al-Zr (4 at. % Zr) film deposited by DC magnetron sputtering before and after annealing in air at 500°C.

The well-defined diffraction peaks seem to show that there is no effect of annealing of Al-Zr (4 at. % Zr) in air at 500 °C; in both cases, the (111) diffraction peak of aluminum at 38° is observed, suggesting the presence of the α-Al solid solution. Nevertheless, TEM analysis of the Al-Zr layer after TiO_2 deposition shows precipitation of the metastable Al_3Zr phase (see Chapter IV/ Section IV.6).

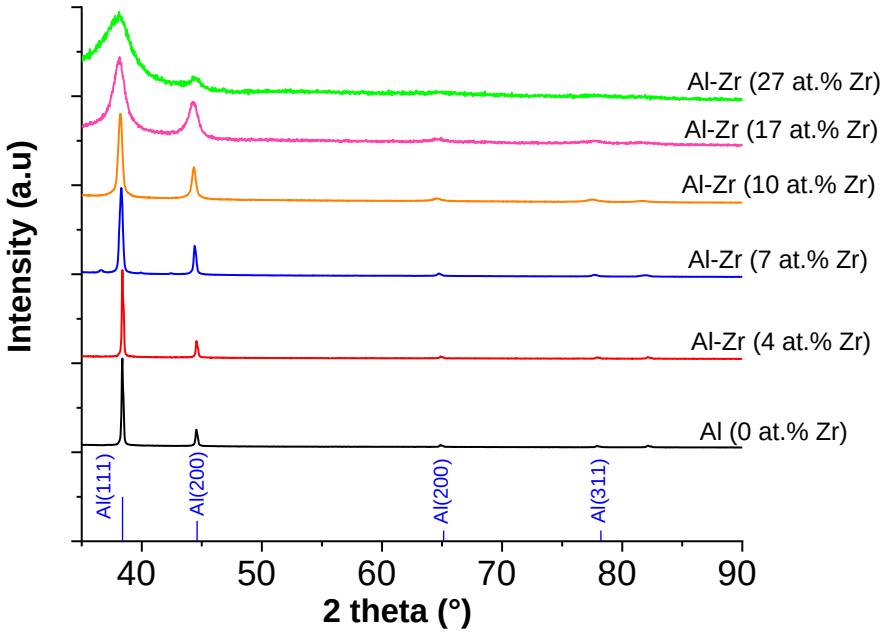

Figure II- 7. XRD patterns of Al-Zr coatings deposited on glass.

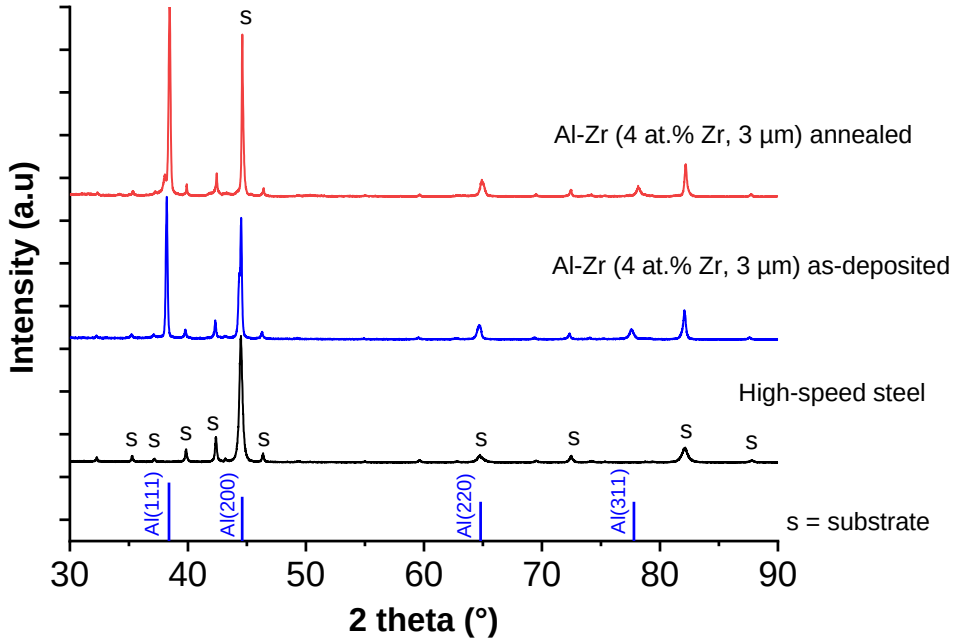

Figure II- 8. XRD patterns of Al-Zr film deposited on high speed steel substrate before and after annealing at 500 °C in air.

The morphology of as-deposited Al-Zr films observed by Scanning Electron Microscopy is presented in Figure II- 9 and Figure II- 10. A clear dependence of the fracture cross-section morphology on Zr content is detected. At low Zr content, the coatings grow with a columnar morphology, while for Al-Zr films with higher Zr contents the films are more compact and the grain refinement is observed.

A low working pressure favors the growth of compact films. In our case the working pressure was about 0.3 Pa, which is considered low for magnetron sputtering technique. In this study, the coatings become more compact as the transition metal content, Zr in our case, increases. Microstructure, morphology and stress evolutions depend on the same mechanisms. The atomic penning, which is the bombarding effect on the growing film surface by an energetic particle-flux of working gas and sputtered species, favors compactness of films, compressive stress and grain size refinement [15].

Flux and energy of neutralized and reflected working gas atoms are proportional to Mt/ Mg ratio where Mt is the atomic mass of the target material and Mg that of the gas, Argon in our case. The transition metal (Zr) is heavier than Al and consequently, increasing the Zr target power is

equivalent to increase the Mt / Mg ratio, which increases the in situ bombardment of the growing film[16]. When Zr discharge current was increased with the objective of adding more Zr, the Mt / Mg ratio raised up and the bombardment of the growing film was enhanced.

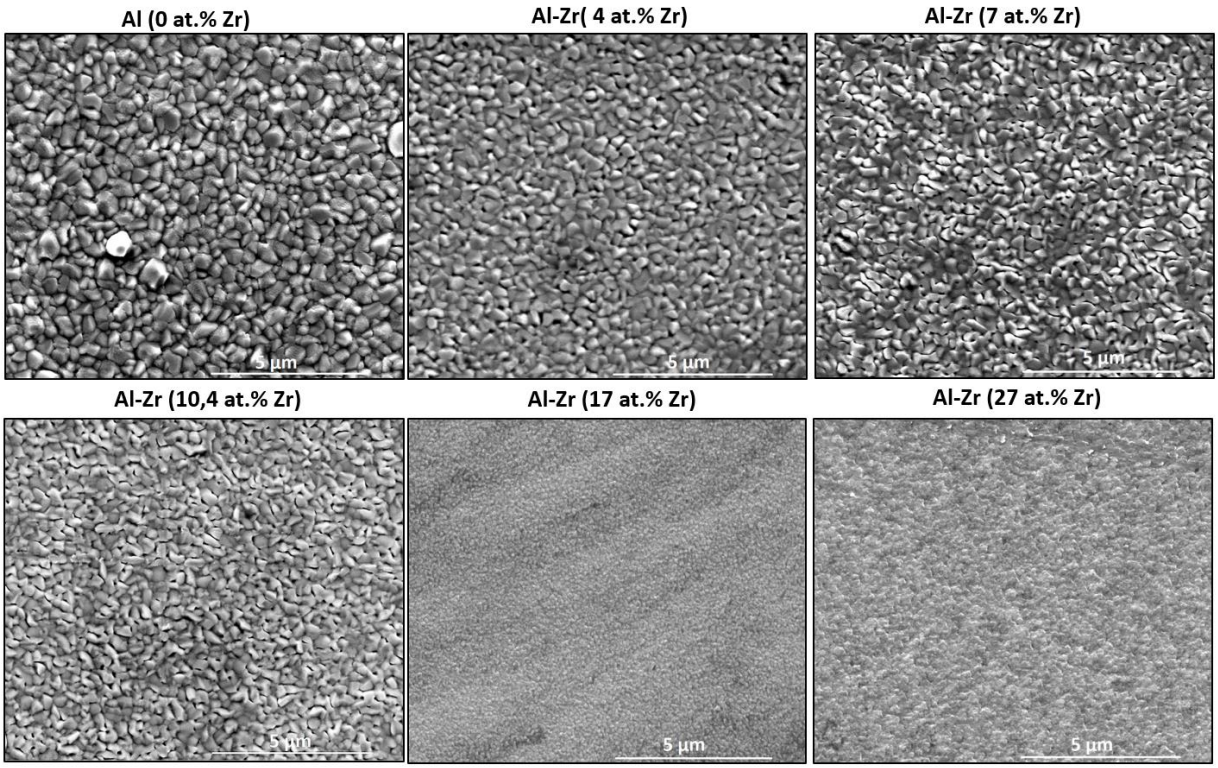

Figure II- 9. Morphology evolution of Al-Zr alloys deposited on silicon substrates.

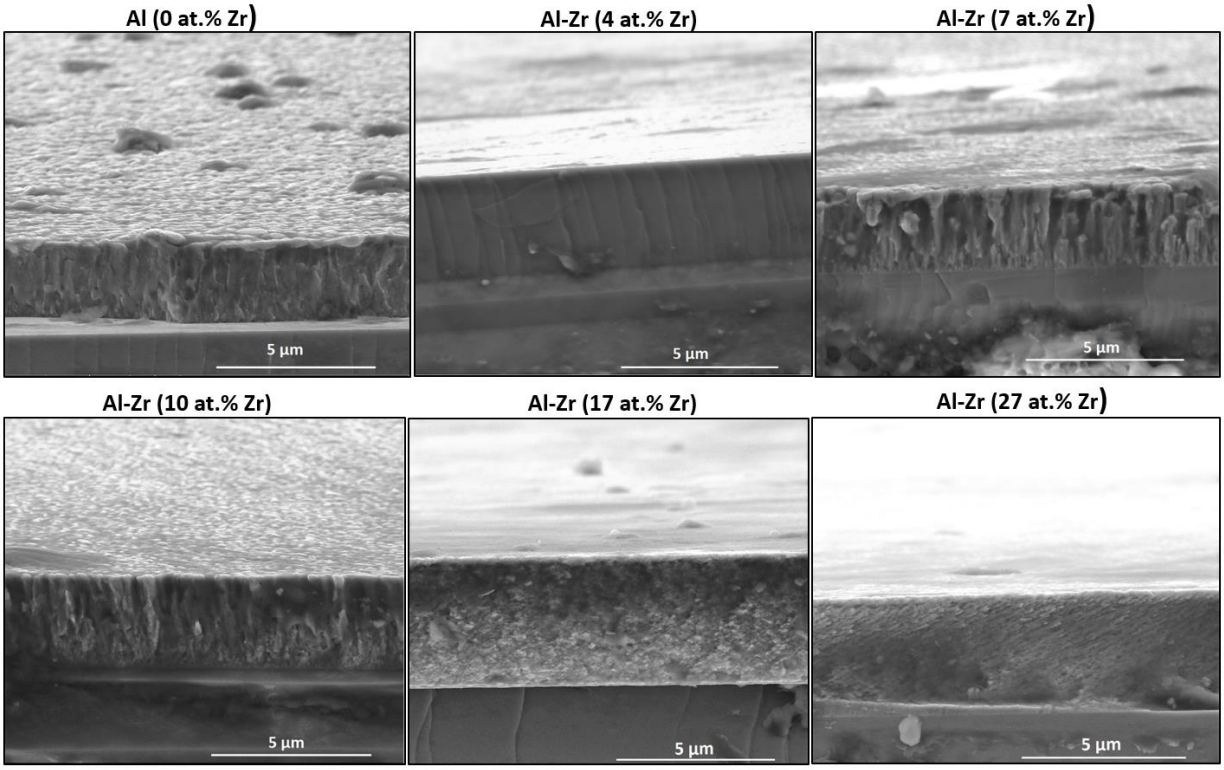

Figure II- 10. Cross-section SEM images of Al-Zr films deposited on silicon wafers.

II.4. Nanohardness measurements of Al-Zr coatings

The nanohardness of Al-Zr as-deposited films were measured by a TI 980 TriboIndenter using dynamic nanoindentation technique to provide a continuous measurement of elastic-plastic properties related to indentation depth. The nanoidentation was performed at an ambient temperature of 20°C with an applied load of 10 mN. Twenty indentations were performed per measurement.

The main constituents in a nanoindentation test are the test material, the sensors used to apply and measure the mechanical load and indenter displacement, and the indenter tip. The indenter tip is made of diamond having a sharp and symmetric shape such as the three-sided Berkovich pyramid. During the nanoindentation test, force and displacement are registered during the time that the indenter tip is penetrated into the test material's surface with a pre-set load. The response of interest is the load-displacement curve [17].

The Hardness of the films is defined as its resistance to plastic deformation and were deduced using the equation II.4.

$$H = \frac{P_{max}}{A} \quad \text{II. 4}$$

Where H is hardness, P_{max} is the peak load, and A is the projected area at peak load.

Evolution of nanohardness with the Zr content is presented in Figure II- 11. It is clear that an increase in Zr content leads to a significant rise of nanohardness. This evolution is due to the combined effect of the diminution of the average grain size (Hall-Petch effect), and also to the solid solution hardening effect.

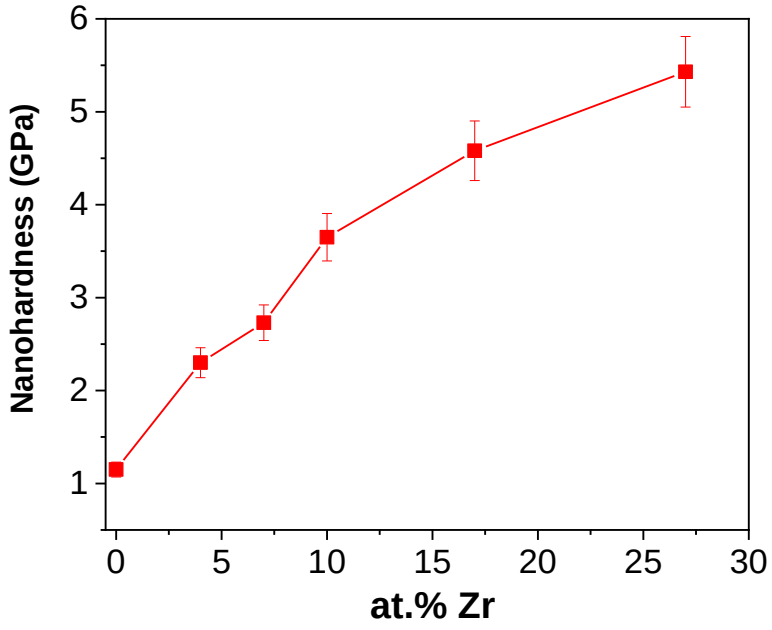

Figure II- 11. Evolution of nanohardness of Al-Zr films as a function of Zr content.

II.5. Electrochemical tests

Samples were degreased in ethanol, rinsed in Mili-QTM water and dried before electrochemical tests. The active surface was delimited using an insulating varnish and the area was 2.25 cm2. The electrochemical measurements were performed in an aerated and stirred chlorine solution, 5 wt.% NaCl, using an EG&EG 273 A potentiostat driven by M352 software. The solution temperature was controlled at 25°C using a Julabo F32 cryothermostat and the pH was fixed at 7 by adding a

dilute NaOH solution. The reference electrode was a saturated calomel electrode (SCE) and the counter electrode was a large platinum grid.

The polarisation curves were registered using a potential range of ± 150 mV around the open circuit potential (OCP) with a scan rate of 0.2 mV/s after 1h of immersion in the saline solution. The corrosion potential E_{corr} and the corrosion current density i_{corr} were predicted using Tafel extrapolation [20]. The evolution of OCP was recorded during 48h.

II.5.1. Electrochemical behaviors of Al-Zr alloys deposited on glass

Al-Zr films deposited on glass were prepared in order to analyze their intrinsic electrochemical behavior.

The electrochemical performances fully depend on zirconium content. Figure II- 12 shows the polarisation curves after 1 h of immersion in saline solution.

The polarisation curves present a stable passive region followed by an abrupt rise in current at the pitting potential, which is correlated with the breakdown of the passive film and the beginning of pitting corrosion. It is clear that the passive region is well defined and the corrosion current density depends on the Zr content.

The ennoblement of the alloys is related to the addition of Zr, which is characterized by an increase of the corrosion potential and also by the decrease of the corrosion current density. When Zr content was increased, an extension of the passive region was observed, which is correlated with an improved pitting resistance. Table II. 2 presents the electrochemical values of Al-Zr films deposited on glass. The corrosion current density decreased from 0.11 $\mu A/cm^2$ for pure Al to 0.06 $\mu A/cm^2$ for Al-Zr with the highest Zr content.

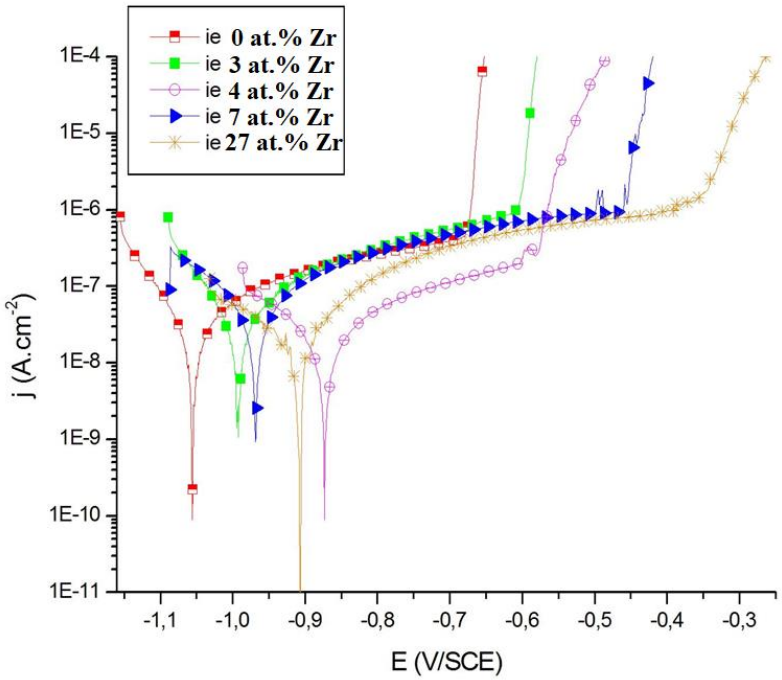

Figure II- 12. Polarisation curves of Al-Zr films deposited on glass after 1h in saline solution (5wt. % NaCl).

Al-Zr alloys Zr (at. %)	E_{ocp} (mV/SCE)	E_{corr} (mV/SCE)	J_{corr} (µA/cm^2)	E_{piq} (mV/SCE)
0	-1013	-1053	0.11	-671
3	-930	-984	0.10	-599
4	-747	-784	0.04	-595
7	-945	-979	0.08	-532
27	-890	-918	0.06	-350

Table II. 2. Electrochemical measurements of Al-Zr films deposited on glass substrates (deduced from polarization curves).

The decrease of the current density seems to be a result of improvement of the quality of passive film formed on Al-Zr alloys. The incorporation of Zr in the passive film reduces films reactivity and, consequently, decreases the corrosion rate.

Yoshioka and al. have shown that Zr has a tendency to be enriched in the passive film as a consequence of its lower electronegativity and higher oxygen affinity compared to Al [21]. Zr also increases the protective efficiency of the passive film since corrosion products are formed on Al

alloys [22]. It was identified by XPS analysis, the existence of Zr^{4+} species integrated in the Al passive film when they analyzed the passive film formed on Al-Zr alloys in deaerated borate-boric solid solution having chloride ions.

The grain size refinement when Zr content increases also contributes to the corrosion resistance improvement. Song and al. have shown the influence of zirconium grain refinement on the corrosion performance of magnesium-rare earth alloy in saline solution. They have noticed a better corrosion resistance of alloy as a result of the increase of the barrier effect of the grain boundary phase [23].

In the present work, Al-Zr film containing 4 atomic percent of Zr shows lower open circuit potential and corrosion current density compared to others Al-Zr alloys. An ennoblement of corrosion potential is also noticed for this film.

II.5.2. Corrosion performance of Al-Zr films deposited on high speed steel (HSS) substrates

The corrosion performance of Al-Zr films deposited on HSS was studied by potentiodynamic polarisation. Figure II- 13 shows the polarisation curves of Al-Zr alloys after 1h of immersion in the 5 wt. % NaCl solution. It is shown that the Al-Zr coatings corrosion is under cathodic control and the general aspect of polarisation curves indicates a passive corrosion. This aspect decreases as Zr content increases.

A significant reduction of cathodic and anodic current takes place when Zr content increases and, consequently, the corrosion current. For Al-Zr alloys having the lowest content of Zr, the corrosion potentials are more negative in comparison with that of high speed steel, which reveals a sacrificial protection of Al-Zr coatings. For Al-Zr alloys having Zr content higher than 10 at. %, the corrosion potential reaches that of high speed steel, and consequently the sacrificial protection is not preserved. The coating becomes progressively nobler than the speed steel substrate when Zr content increases. As a result, the coating depends on the presence of imperfections that locally favors electrolyte penetration on the steel substrate, representing a risk of confinement of corrosion phenomena situated on these defects [24].

The coating ennoblement is followed by decrease of corrosion current densities. The pitting potential of Al-Zr alloys increases with Zr content. Tsuda and al.[25] obtained similar results when

they analyzed the corrosion resistance of the electrodeposited Al-Zr coatings on Cu substrates in deaerated 0.1 mol/L NaCl solutions. They found an increase of pitting potential for coatings having Zr content between 0 and 8 at. %. A stabilization of pitting potential was noticed for Zr content up to 17 at. %.

In order to study the stability of sacrificial behavior in function of time, the OCP potential of Al-Zr alloys was verified for long immersion time. Figure II- 14 presents the evolution of OCP potential versus time in 5 wt. % NaCl during 48 h of immersion.

The OCP potential grows fast for all Al-Zr alloys and remains constant for six hours. The abrupt increase of OCP values can be attributed to the fast growth of a passive film on coatings surface. OCP decreases lightly with immersion time suggesting the dissolution of the passive film. Numerous OCP fluctuations were noticed for pure aluminium coating and Al-Zr coating having 3 atomic percent of Zr. It is due to the fact that these coatings are more porous and the increase of zirconium content leads to a passivation of coatings by the formation of a dense and more stable passive film.

Pores and defects are generally the pitting initiation sites on coatings because when the immersion increases, the pitting corrosion is situated at these pores and propagates by dissolving the steel. The detrimental defects like pores or pinholes are prejudicial to the corrosion performance since they offer paths to allow the corrosive electrolyte to entry to the steel substrate [26].

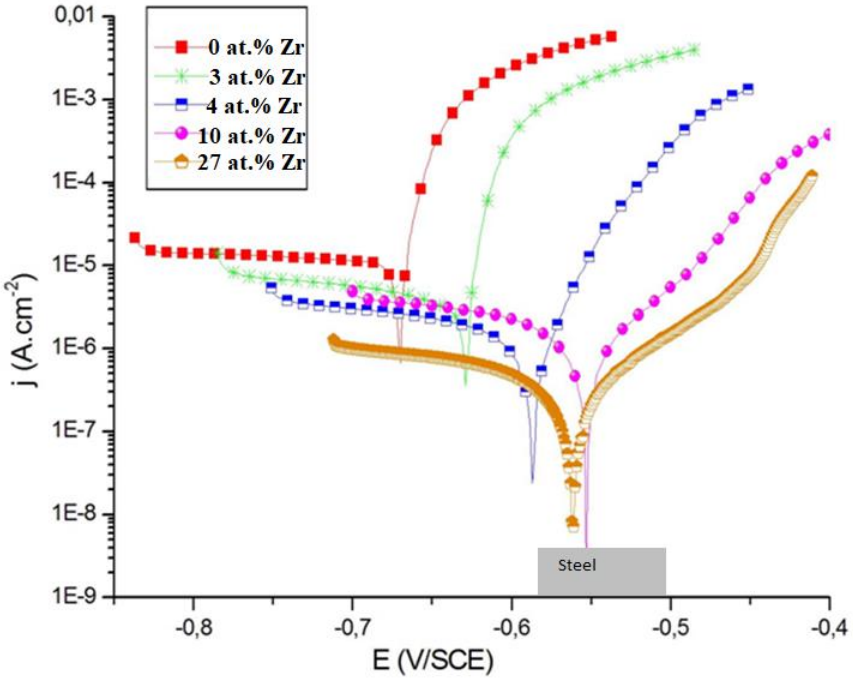

Figure II- 13. Polarisation curves of Al-Zr films deposited on high speed steel after 1h in saline solution (5wt% NaCl).

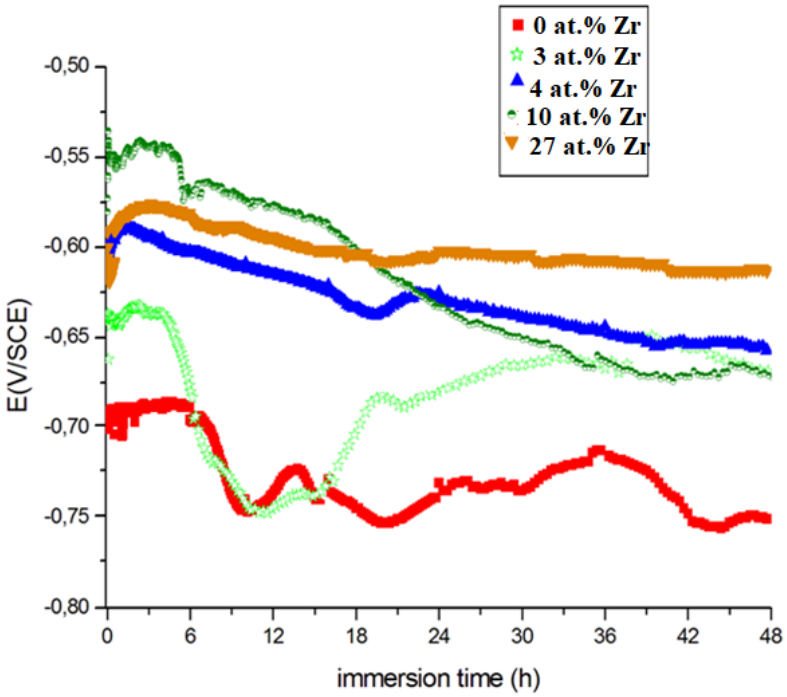

Figure II- 14. Evolution of Open Circuit Potential (OCP) of Al-Zr films deposited on high speed steel in saline solution (5wt/% NaCl).

II.6. Conclusions

Al-Zr films with Zr contents between 0 and 27 at. % were deposited on both glass slides and high speed steel (HSS) substrates by DC magnetron sputtering. Films were deposited from pure metallic Al and Zr targets in a pure argon atmosphere at floating temperature (< 80°C). Evolution of Zr content was ensured by fixing the aluminium discharge current at 2.0 A and by changing that of the Zr one between 0 and 1.3 A.

Al-Zr films having Zr content below 10 at. % present well-defined diffraction peaks, which correspond to fcc structure, indicating the growth of a supersaturated solid solution of Zr in Al. For Zr contents above 10 at. %, the diffraction peaks becomes broader. The peak broadening is the result of a grain refinement occurred when Zr content increases. Above 10 at.% Zr, Al-Zr films are probably a mixture of the solid solution of Zr in fcc-Al and an amorphous phase.

SEM shows that at low Zr content, the coatings grow with a columnar morphology, while for Al-Zr films with higher Zr contents the films are more compact and the grain refinement is observed. A low working pressure favors the growth of compact films. In our case the working pressure was about 0.3 Pa, which is considered low for magnetron sputtering technique. Microstructure, morphology and stress evolutions depend on the same mechanisms.

Evolution of nanohardness with the Zr content is due to a combined effect of the diminution of the average grain size (Hall-Petch effect), and also to the solid solution hardening effect.

The corrosion performance of Al-Zr films deposited on glass and HSS substrates was studied by potentiodynamic polarisation. The ennoblement of the alloys is related to the addition of Zr. For Al-Zr alloys having Zr content higher than 10 at. % deposited on HSS, the corrosion potential reaches that of high speed steel, and consequently the sacrificial protection is not preserved. The coating becomes progressively nobler than the speed steel substrate when Zr content increases.

Besides, Al-Zr film deposited on glass containing a zirconium content of 4 at. % shows an optimal corrosion resistance after 1 hour of immersion in saline water, as it presents lower current density and a higher corrosion potential. As Al–Zr with 4 at.% Zr led to the best compromise between intrinsic corrosion resistance, sacrificial character/ steels, and mechanical reinforcement, it is chosen as the first layer in order to provide anti-corrosion properties.

References

[1] B.J. Hickey, Physical Vapour Deposition PVD techniques, J. Appl. Phys. (2017) 1–5. doi:10.13140/RG.2.1.5063.4964.

[2] E. Bauer, Phänomenologische Theorie der Kristallabscheidung an Oberflächen. I, Zeitschrift Fur Krist. 110 (1958) 372–394. doi:10.1524/zkri.1958.110.1-6.372.

[3] J.A. Thornton, High Rate Thick Film Growth, Annu. Rev. Mater. Sci. 7 (1977) 239–260. doi:10.1146/annurev.ms.07.080177.001323.

[4] A. Anders, A structure zone diagram including plasma-based deposition and ion etching, Thin Solid Films. 518 (2010) 4087–4090. doi:10.1016/j.tsf.2009.10.145.

[5] Y. Pauleau, Generation and evolution of residual stresses in physical vapour-deposited thin films, Vacuum. 61 (2001) 175–181. doi:10.1016/S0042-207X(00)00475-9.

[6] M.R. Ardigo, M. Ahmed, A. Besnard, Stoney Formula: Investigation of Curvature Measurements by Optical Profilometer, Adv. Mater. Res. 996 (2014) 361–366. doi:10.4028/www.scientific.net/amr.996.361.

[7] S.-S. Zhao, H. Du, W.-G. Hua, J. Gong, J.-B. Li, C. Sun, The depth distribution of residual stresses in (Ti,Al)N films: Measurement and analysis, J. Mater. Res. 22 (2007) 2659–2662. doi:10.1557/JMR.2007.0363.

[8] F. Sanchette, Tran Huu Loi, A. Billard, C. Frantz, Structure—properties relationship of metastable Al-Cr and Al-Ti alloys deposited by r.f. magnetron sputtering: role of nitrogen, Surf. Coatings Technol. 74–75 (1995) 903–909. doi:10.1016/0257-8972(94)08210-3.

[9] F. Sanchette, Tran-Huu-Loi, C. Frantz, Deposition of metastable aluminium-chromium alloys by r.f. magnetron sputtering from mixed-powder targets, Surf. Coatings Technol. 57 (1993) 179–182. doi:10.1016/0257-8972(93)90037-O.

[10] F. Sanchette, A. Billard, Main features of magnetron sputtered aluminium-transition metal alloy coatings, Surf. Coatings Technol. 142–144 (2001) 218–224. doi:10.1016/S0257-

8972(01)01197-5.

[11] F. Sanchette, a. Billard, C. Frantz, Mechanically reinforced and corrosion-resistant sputtered amorphous aluminium alloy coatings, Surf. Coatings Technol. 98 (1998) 1162–1168. doi:10.1016/S0257-8972(97)00231-4.

[12] J. Creus, A. Billard, F. Sanchette, Corrosion behaviour of amorphous Al–Cr and Al–Cr–(N) coatings deposited by dc magnetron sputtering on mild steel substrate, Thin Solid Films. 466 (2004) 1–9. doi:10.1016/J.TSF.2003.11.315.

[13] Z.A. Chaudhury, C. Suryanarayana, A TEM study of decomposition behavior of a melt-quenched Al-Zr alloy, Metallography. 17 (1984) 231–252. doi:10.1016/0026-0800(84)90060-0.

[14] Y.Y. Cui, T.L. Wang, J.H. Li, Y. Dai, B.X. Liu, Thermodynamic calculation and interatomic potential to predict the favored composition region for the Cu–Zr–Al metallic glass formation, Phys. Chem. Chem. Phys. 13 (2011) 4103–4108. doi:10.1039/C0CP01722A.

[15] H. Windischmann, Intrinsic stress in sputter-deposited thin films, Crit. Rev. Solid State Mater. Sci. 17 (1992) 547–596. doi:10.1080/10408439208244586.

[16] F. Sanchette, A. Billard, Main features of magnetron sputtered aluminium - transition metal alloy coatings, Surf. Coatings Technol. (2001) 218–224. doi:10.1016/S0257-8972(01)01197-5.

[17] C.A. Schuh, Nanoindentation studies of materials, Mater. Today. 9 (2006) 32–40. doi:10.1016/S1369-7021(06)71495-X.

[18] D. Beegan, S. Chowdhury, M.T. Laugier, Comparison between nanoindentation and scratch test hardness (scratch hardness) values of copper thin films on oxidised silicon substrates, Surf. Coat. Technol. 201 (2007) 5804–5808. doi:10.1016/j.surfcoat.2006.10.031.

[19] A.. Elmustafa, J.. Eastman, M.. Rittner, J.. Weertman, D.. Stone, Indentation size effect: large grained aluminum versus nanocrystalline aluminum-zirconium alloys, Scr. Mater. 43 (2000) 951–955. doi:10.1016/S1359-6462(00)00520-0.

[20] F. El-Taib Heakal, A.M. Fekry, M.Z. Fatayerji, Influence of halides on the dissolution and passivation behavior of AZ91D magnesium alloy in aqueous solutions, Electrochim. Acta. 54 (2009) 1545–1557. doi:10.1016/J.ELECTACTA.2008.09.055.

[21] H. Yoshioka, H. Habazaki, A. Kawashima, K. Asami, K. Hashimoto, The corrosion behavior of sputter-deposited AlZr alloys in 1 M HCl solution, Corros. Sci. 33 (1992) 425–436.

doi:10.1016/0010-938X(92)90071-A.

[22] H. Yoshioka, H. Habazaki, A. Kawashima, K. Asami, K. Hashimoto, Anodic polarization behaviour of sputter-deposited AlZr alloys in a neutral chloride-containing buffer solution, Electrochim. Acta. 36 (1991) 1227–1233. doi:10.1016/0013-4686(91)85113-L.

[23] G. Song, D. StJohn, The effect of zirconium grain refinement on the corrosion behaviour of magnesium-rare earth alloy MEZ, J. Light Met. 2 (2002) 1–16. doi:10.1016/S1471-5317(02)00008-1.

[24] J. Creus, H. Mazille, H. Idrissi, Porosity evaluation of protective coatings onto steel, through electrochemical techniques, Surf. Coatings Technol. 130 (2000) 224–232. doi:10.1016/S0257-8972(99)00659-3.

[25] T. Tsuda, C.L. Hussey, G.R. Stafford, O. Kongstein, Electrodeposition of Al-Zr alloys from lewis acidic aluminum chloride-1-ethyl-3-methylimidazolium chloride melt, J. Electrochem. Soc. 151 (2004) C447--C454.

[26] C. Liu, Q. Bi, A. Leyland, A. Matthews, An electrochemical impedance spectroscopy study of the corrosion behaviour of PVD coated steels in 0.5 N NaCl aqueous solution: Part II.: EIS interpretation of corrosion behaviour, Corros. Sci. 45 (2003) 1257–1273. doi:10.1016/S0010-938X(02)00214-7.

Chapter III: Deposition and characterization of TiO_2 thin films

The chemical vapor deposition technique (Chemical Vapor Deposition or CVD) allows the deposition of a material on a substrate through precursors gases that chemically react under the influence of temperature. The deposition conditions are strongly dependent on the precursor nature and the reactor setup, for instance, the pressure can vary from atmospheric pressure to high vacuum (10^{-7} Pa). In particular, CVD systems working at atmospheric pressure (without vacuum system) are very attractive for industrial applications.

As previously mentioned, CVD is a deposition method based on a chemical reaction that allows to grow films if the reaction takes place in heterogeneous phase vapor-solid at the interface between the heated substrate and the reactive gases. This method can be used to grow different types of materials: metals, nitrides, sulphides, carbides and oxides[1].

In this work we have used an aerosol-assisted metalorganic chemical vapor deposition (AAMOCVD) to synthetize TiO_2 films as photocatalysts top layer. The first part of this chapter will be dedicated to the study of the influence of the deposition parameters on the growth process of TiO_2 films on silicon. The microstructural, physical properties and photocatalytic activity will be discussed in the second part. The objective is to define the deposition parameters to grow TiO_2 films in anatase phase, corresponding to the optimal photocatalyst conditions.

Deposition of TiO_2 films on high speed steel (HSS) substrate is presented at the end of the chapter for comparison with TiO_2 films deposited on silicon.

TiO_2 films were deposited by AAMOCVD technique working at atmospheric pressure in order to develop optimal films presenting a good photocatalytic activity before depositing it on Al-Zr alloy to produce bilayer films, which will be discussed in greater detail in chapter IV.

III.1. Deposition of TiO_2 films by aerosol assisted metalorganic chemical vapor deposition (AAMOCVD)

III.1.1. Principle and reactions of CVD

Metal Organic Chemical Vapor Deposition: One variant of CVD is using Metal organic precursors for the CVD reaction, then the process is named Metal Organic Chemical Vapor Deposition (MOCVD). These precursors are composed of one or more metal atoms connected to organic functional groups by either directly metal-carbon (called organometallics) or through a nitrogen-oxygen coordination.

Implementation: Generally, a CVD reactor is divided in 2 main zones: a pre-treatment precursor zone to generate the precursor vapors (evaporation of liquid precursors, sublimation of solid precursors) and a reaction zone at the substrate. A carrier gas transports the precursor vapors to the reaction zone, while a reactive gas is usually delivered directly in the reaction zone. This area can be heated independently of the evaporation zone to activate the chemical reactions or to achieve a determined crystallographic phase.

Method used at LMGP: Aerosol-assisted CVD (AAMOCVD), also known as aerosol pyrolysis or pyrosol process, is based on the transport of precursor in liquid phase by generating an aerosol from the source solution. These small droplets are transported by a carrier gas to the reaction zone. The reaction zone is heated provoking in a very small region the evaporation of solvent and precursors, and the CVD reaction on the substrate.

As in all CVD process, the process depends on the deposition temperature and the nature of the chemical species. The specific parameters that influence the kinetics of the thin layer growth are the temperature gradient around the substrate and the speed and size of the aerosol droplets.

Figure III- 1 shows the behavior of aerosol according to the temperature:

- In the regime A, at low temperatures, the droplet remains liquid when arriving on the substrate. Solvent evaporates and leaves a dry precursor that can decompose in powder.
- In the B mode, at medium temperature, solvent evaporates before the droplet reaches the area. Precursor arrives on the surface and decomposes there.
- In the regime C, at high temperatures, solvent and precursor vaporize during the course of the droplet to the surface of the substrate. Precursor vapor reacts through a heterogeneous chemical reaction at substrate surface. This process is the CVD itself.
- In the regime D, at higher temperature, the solvent and the precursor vaporize before reaching the surface of the substrate. The chemical reaction takes place in gas or homogeneous phase and results in a non-adherent powdery deposit.

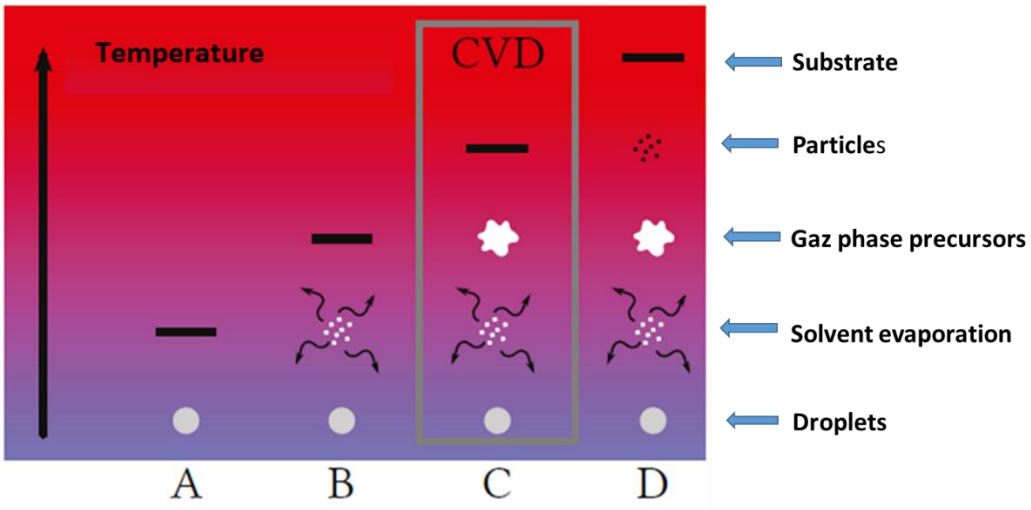

Figure III- 1. Behavior of the aerosol as a function of temperature.

We will seek to place ourselves in the regime C to deposit the TiO_2 layers. This will allow us to obtain adherent layers on the substrate.

Aerosol production: The aerosol can be generated by three techniques [2]:

- Electrostatic spraying; this technique involves charging the solution a narrow duct raised to high potential facing a pierced plate connected to the ground. The effect of electrostatic forces leads to the formation of droplet droplets from the solution. This technique makes it possible to obtain droplets of size controlled.
- Pneumatic spraying; this technique involves passing the solution under pressure through a nozzle. The Venturi effect makes it possible to create and transport the aerosol.
- The ultrasonic spraying (used in this work).

Ultrasonic spray pyrolysis involves generating ultrasound in the precursor solution. It will produce capillary waves at the free surface of the solution. The effect of electrostatic forces leads to the formation of droplets as shown in Figure III- 2. This technique allows to create droplets of controlled size and relatively mono-disperse.

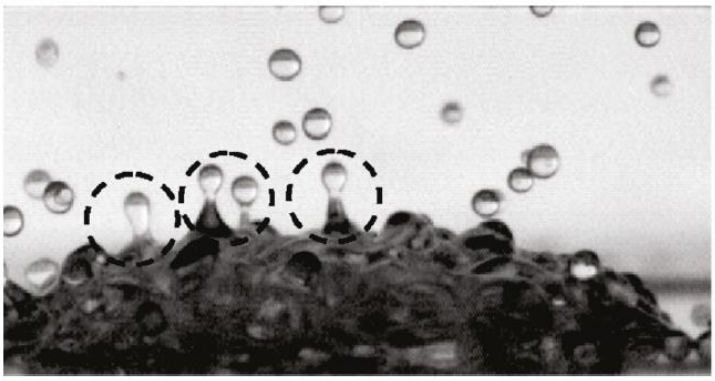

Figure III- 2. Solution atomization[3].

The average diameter of the droplets (d_g) is proportional at the wavelength λc of the capillary wave. The experimental work of E.G Lierke and G. Griesshammer [4] resulted in formula:

$$d_g = 0.34\,\lambda_c = 0.34\left(\frac{8\pi\,\sigma_S}{\rho_S\,f^2}\right)^{1/3} \qquad \text{III. 1}$$

The surface tension of the solution is symbolized by σ_s, its density by ρ_s and the excitation frequency is f. Solution of butanol and ethanol such as used in these works (σ_s = 24.20 mN·m^{-1} and ρ_s = 810kg · m-^{3}) for butanol and (σ_s = 21.82 mN·m^{-1} and ρ_s = 790kg · m-^{3}) for ethanol with a

working frequency of 800 kHz lead to an average diameter of droplets of 3.6 µm if it is assumed that the precursors used have no surfactant effects.

$$\sigma_S = X \frac{4\,\mu s}{\lambda_c\, f\, p_s} \qquad \text{III. 2}$$

Spraying occurs from a certain vibration amplitude of the surface of the piezoelectric transducer. This amplitude α_s can be estimated by empirical formula III-2 [5], where X is a coefficient between 3 and 6, and µs is the viscosity of the solution. For a solution of butanol this amplitude is between 4.55 µm and 9.11 µm in taking the extremal values of the coefficient X.

III.1.2. TiO_2 precursor and substrates

AAMOCVD precursor have to be soluble in the solvent, and stable if other precursors are present in the solution. It must be volatile and should decompose at growth temperatures while being stable at room temperature.

The titanium precursor used in these work is **titanyl (bis) acetylacetonate $(TiOAcAc)_2$,** also known as **Bis(acetylacetonato)titanium(IV) oxide, Bis(2,4-pentanedionato)titanium(IV) oxide, Bis(acetylacetonato)titanium(IV) oxide, or Bis(2,4-pentanedionato)titanium(IV) oxide.**

Its chemical formula is $TiO(CH_3COCHCOCH_3)_2$, (see Figure III- 3), purchased from Strem Chemicals and used without treatment additional. It is a white powder with a melting point at 200°C. It dissolved easily in alcohols.

Solvent must have several specifications to be used in AAMOCVD, it must:

- Dissolve easily the precursors, (in our case, we work with a concentration of $0.03 mol \cdot l^{-1}$).
- Evaporate at a temperature below sublimation or evaporation temperature of the precursors.
- Have a low surface tension to be sprayed by ultrasound.

In this work, we used Butanol or Ethanol. To prepare a precursor solution with a concentration of $0.03\ mol \cdot l^{-1}$, we add 4.71 g of precursor in 600 ml of alcohol solvent (butanol-01 or ethanol). The mixture is stirred until complete dissolution using a magnetic bar with speed 300 cycle/min. The precursor solution becomes clear yellow right after 30 minutes stirring: then the solution is ready for deposition. Once completed, the precursor solution is stable for several months.

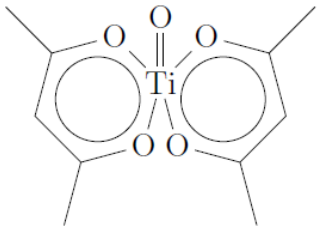

Figure III- 3. Titanyl(bis)acetylacetonate.

Table 1: Precursor properties.

Precursor	Molar mass (g/mol)	Melting temperature (°C)	Purity	CASS Registry number
TiO AcAC	262.08	184	> 95%	14024-64-7

The substrates used for depositing TiO_2 films were (100) Si, corning glass substrates (reference C1737-S111) and polished high speed steel substrates. The substrates were cleaned before deposition through ultrasonication for 10 minutes

III.1.3. Principle and description of AAMOCVD reactor

Aerosol Assisted CVD has the ability to use less volatile metal organic precursors during CVD deposition [2]. Previous works on the TiO_2 deposition confirms the ability to obtain crystalline films [6–8]. In particular, Biswas et al [9] studied the growth of TiO_2 microflowers structures for specific deposition conditions.

We used for this work a homemade AAMOCVD reactor, presented in Figure III- 4. On left, a scheme of the reactor and, on right, a picture of the actual system.

The precursor solution is placed in a vessel. The ultrasounds is generated by a piezoelectric membrane, with a certain power and frequency. As a result, a white mist containing tiny droplets of the precursor solution is created at the surface of the solution. The frequency generator has been provided by the company RBI and allows to provide frequencies between 640 kHz and 870 kHz to the piezoelectric transducer. Two knobs regulate the frequency and power on an arbitrary scale between 0 and 10 units. The optimal frequency is settled by observing the surface of the solution while changing the potentiometer. When we approach the resonance frequency, the surface is covered by concentric waves of maximum intensity in the center of the pot. The optimal frequency

is achieved at the maximum deformation of the surface. In the standard parameters of these works the potentiometer is set at 2.0 which coincides to a frequency of 800 kHz. The mist is then carried by a gas flow used as the carrier gas (**CG#1**) towards the reaction chamber. In our case, the carrier gas is an oxidizing gas flow consisting in 3 L min^{-1} of air (12% of O_2). Before entering in the reaction zone, a process gas consisting in 3 L min^{-1} (**CG#2**) of air is added to the precursor flow. This second flow is introduced from the middle part for sake of security, and accelerates the precursor onto the top heating plate, where the reaction takes place. A funnel at the top the substrate allows to spread the precursor aerosol in a bigger surface. The heating plate of 20 x 20 cm^2 allows to heat up to 550°C.

The decomposed precursor wastes and evaporated solvent are ventilated from the bottom, going through a liquid nitrogen cooled solvent trap.

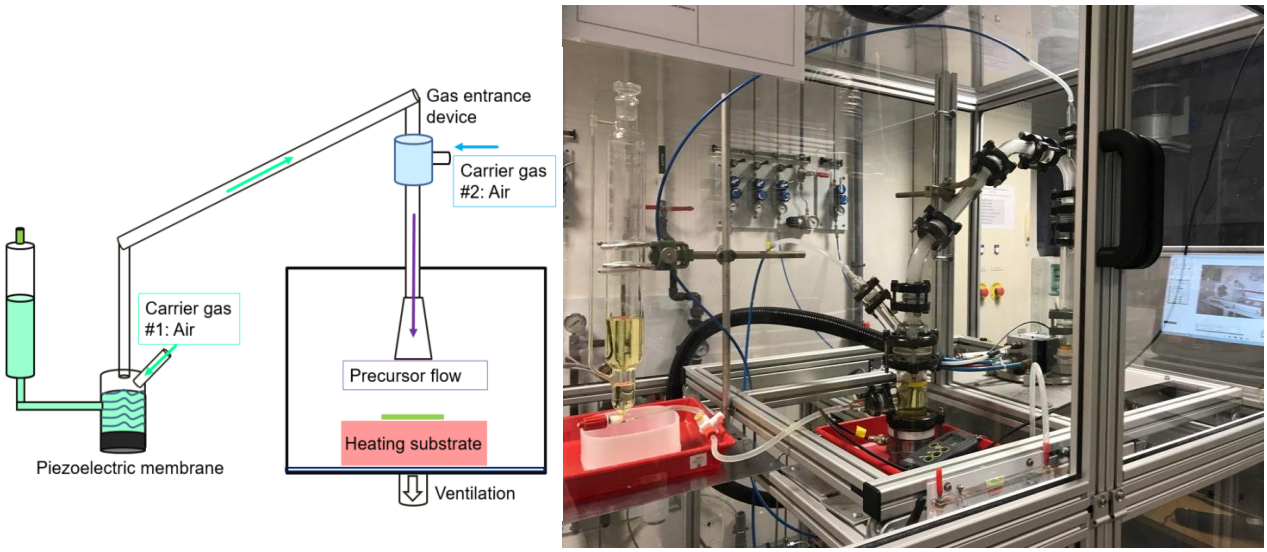

Figure III- 4. Details of AACVD configuration.

A ventilation system exhaust is placed at the bottom right below the hot plate. In our working conditions, an extraction pressure of 3 mm.H_2O is used for all the depositions.

III.2. Effect of deposition temperature on the TiO_2 films deposited on silicon

The goal of this study was to evaluate the effect of the deposition temperature on TiO_2 films grown on silicon substrate as a first step to evaluate the best conditions for the deposition on

metallic substrates. We will present here the results obtained by different characterization techniques.

The deposition temperature was varied between 350 °C and 550 °C, the other deposition parameters are represented in Table III. 1.

Table III. 1. AAMOCVD deposition parameters used in this work.

Precursor Concentration ($mol \cdot l^{-1}$)	T Surface Holder (°C)	Total carrier gas flow rate ($Lmin^{-1}$)	Extraction pressure ($mm.H_2O$)	Deposition Duration (min)	Vibration Frequency (kHz)	Power (a.u)
0.03	350-550	6	3	40	800	5-6

III.2.1. Scanning Electron Microscopy (SEM)

Analysis of the microstructure of the samples and the evaluation of their thickness were acquired by means of a scanning electron microscope (SEM). The SEM was performed in a FEI Quanta 250 MEB FEG ESEM tool.

Biswas et al. [9] previously proved that AAMOCVD employing Titanium($_{IV}$) oxide bis-acetylacetonate as the precursor allows the deposition of TiO_2 films crystallized in the anatase phase and containing hierarchical microflowers on the surface by adjusting the deposition conditions.

As this microstructure can be interesting for our application because it presents a very large active surface, optimal deposition parameters are needed to tune the morphology and density of the microflowers. The deposition temperature was determined to be the main parameter providing the development of TiO_2 microflowers, maintaining all the other parameters constant, such as a solution feeding rate of 3 ml min^{-1}, a precursor solution concentration of 0.03 mol L^{-1} and a deposition time of 40 min. Microflowers characteristics revealed to be definitely sensitive to the temperature. SEM images of the deposited TiO_2 films (Figure III- 5) demonstrate that, at lower temperatures, such as 400°C, no flower is created. At 500 °C, some flowers can be observed, but

much smaller and in smaller quantity than those developed at 550°C. At 550 °C, TiO_2 microflowers of about 7-8 µm in diameter are clearly detected. Finally, at temperatures higher than 570 °C (not shown) bigger nanoparticles agglomerates are formed instead of flowers.

Biswas et at.[9] also demonstrated that a feeding rate higher than 3 ml min^{-1} is crucial to the development of microflowers.

Figure III- 5 presents SEM images of TiO_2 films deposited at a range of temperature from 400°C to 550° that mostly comprise of two parts: one is a thin layer immediately over the substrate and the other is composed of the microflowers that are dispersed at the top of the layer. The flowers having an average diameter of about 7 µm are characterized by a homocentric association of TiO_2 nanopetals forming a corolla as if growing from the receptacle of a flower (Figure III- 5b). Figure III- 5a) presents de cross-section of TiO_2 film containing microflowers. It is noticed that microflowers rise from the layer, at first as single nanopetals to develop subsequently into a bundle of interconnected petals. The principal characteristics of these microstructure is that petal have a nanometric thickness (~ 5 nm) and are formed by nanocrystal of anatase phase [9].

ImageJ was used to quantify the density of the flowers by calculating the area fraction coverage of the substrate covered by the flowers (in percentage) from the images. The area fraction coverage by microflowers is about 40 % for TiO_2 thin films samples obtained deposited at 550°C.

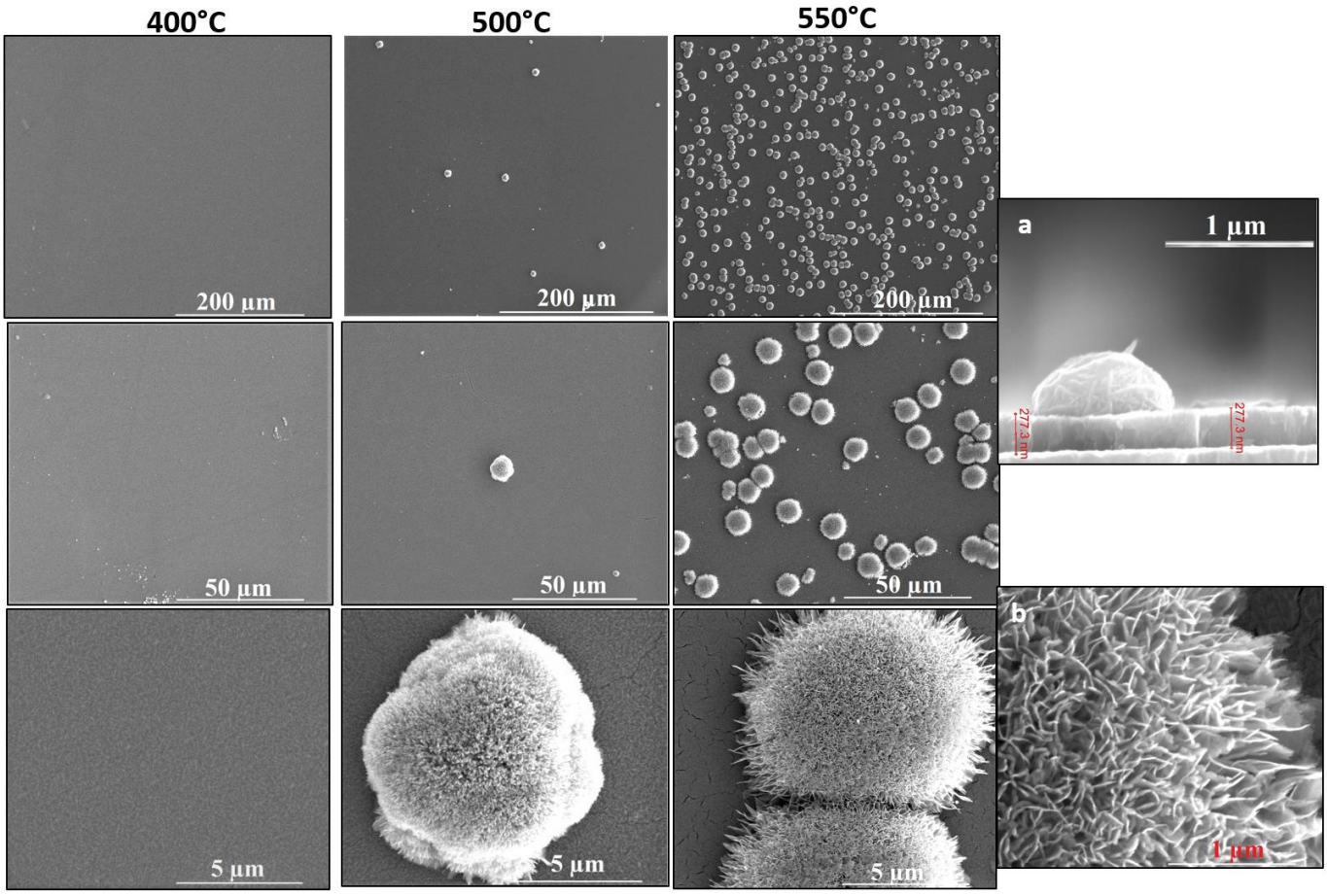

Figure III- 5. SEM images of microstructured TiO_2 thin films deposited by AA-MOCVD at 400°C, 500°C and 550°C on silicon substrate a) cross section showing the interfaces between the substrate, TiO_2 film and microflowers and b) zoomed in image of petals to show their nanometric thickness.

The creation of TiO_2 nanopetals is associated to the metastable conditions that take place at the surface when the aerosol evaporates developing supersaturation circumstances, which perform as a leading force for TiO_2 crystallization. During the evaporation of the solvent, the precursor is under supersaturation conditions in the droplet. The excess of the precursor can result in a spontaneous agglomeration process or a reaction in the homogeneous phase by reacting with oxygen and consequently crystallizing in a very thin structure. The petal thickness seems to be independent of the deposition parameters and it is not preferentially oriented; it have changed only when a second deposition on the microflowers is made [10].

Following the evaporation of the solvent, the precursor has a tendency to precipitate in the created petals in place of keeping moving in the gas phase. When a long deposition time is carried out, the precursor provides a growth of microflowers in the density and also the height. However,

supersaturation happens far away from the surface, rendering impossible the creation of new nucleation sites.

The influence of deposition temperature on deposition rate of TiO_2 films deposited by AACVD is shown in Figure III- 6. Since our films are not homogenous in thickness, an average thickness is calculated using cross section SEM images for all the films deposited on silicon presenting a percentage error of +- 5 %.

An evolution is observed as the deposition rate increases from 5.5 nm/min for films deposited at 350 °C to about 8 nm/min for films deposited at temperatures higher than 450 °C. It should be noticed that surface reaction phenomena are thermally-activated processes that have an visible dependence on temperature only at low values (the lower the T values, the lower the rate of the process), but at higher temperatures there is enough energy for any surface reaction to be achieved, and the dependence on T decreases.

The deposition rate is often an important processing variable in CVD processing. Not only can the rate affect the film growth; along with the deposition time, it is often used to control the total amount of material deposited.

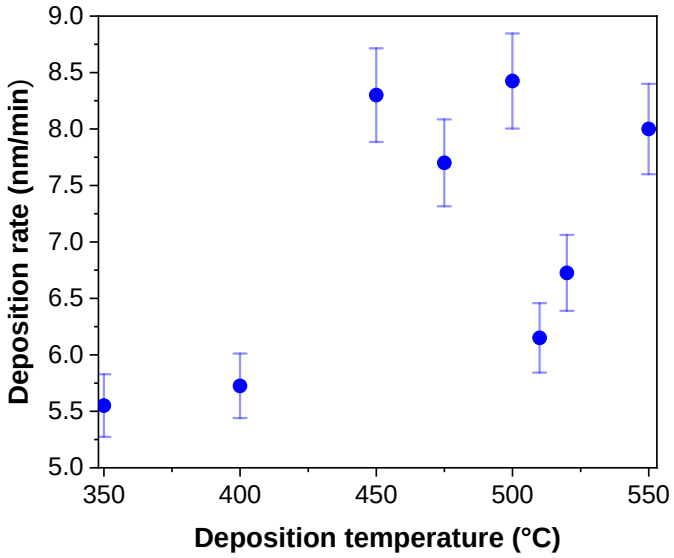

Figure III- 6. Evolution of deposition rate over deposition temperature for TiO_2 films deposited by AACVD.

III.2.2. Fourier transform infrared spectroscopy (FTIR)

Fourier transform infrared spectroscopy (FTIR) is a technique that allows the identification of chemical bounds in the films as a consequence of the absorption of infrared light. In this context, an infrared beam consisting of various wavelengths goes over the film, interacting with the chemical species. In the case of one specific chemical bond presents the same energy of the infrared light, it will be absorbed. The light beam is divided in two distinct beams, using a Michelson Interferometer that will goes through the sample and produce an interferogram (interference pattern) in the detector. The Fourier transform of the generated pattern will produce an infrared spectrum, employed for the identification of chemical bonds.

In the analysis of TiO_2 films, this technique is interesting for the detection of Ti–O and Ti–O–Ti bonds. In case of incomplete decomposition of the precursor, residual organic substances can indeed be present in the film, which can lead to meagre physical properties. Fourier-transform infrared (FTIR) measurements were conducted in a Bruker Vertex 70V spectrometer, equipped with a CsI beamsplitter and working under vacuum. Spectra were recorded with a resolution of 4 cm^{-1} by accumulating 64 scans in transmission mode using silicon substrates, transparent to infrared light.

The FTIR spectrum was used to identify various functional groups present in the TiO_2 thin films deposited at a substrate temperatures *range* from 400 °C to 550 °C as represented in Figure III- 7. The scanning range was 200–4000 cm^{-1}, but no absorption peak was noticed in the range of 2000–4000 cm^{-1}. Only small peaks in the region of 1200 to 1800 cm^{-1} were visible, mainly at 1425, 1600, 1718 cm^{-1} and with a lower intensity at 1250 cm^{-1}. These peaks correspond to characteristic absorption bands of acetylacetonate [11,12]. Also C-O-C stretch is detected at 1150 cm^{-1}.The bands for the Ti–O and Ti–O–Ti bonds are present in the 800–400 cm^{-1} region. These infrared bands are detected at 440 cm^{-1} and 265 cm^{-1} with a small shoulder at 660 cm^{-1}. These absorptions are related to the stretching vibration of Ti–O–Ti in anatase [9].

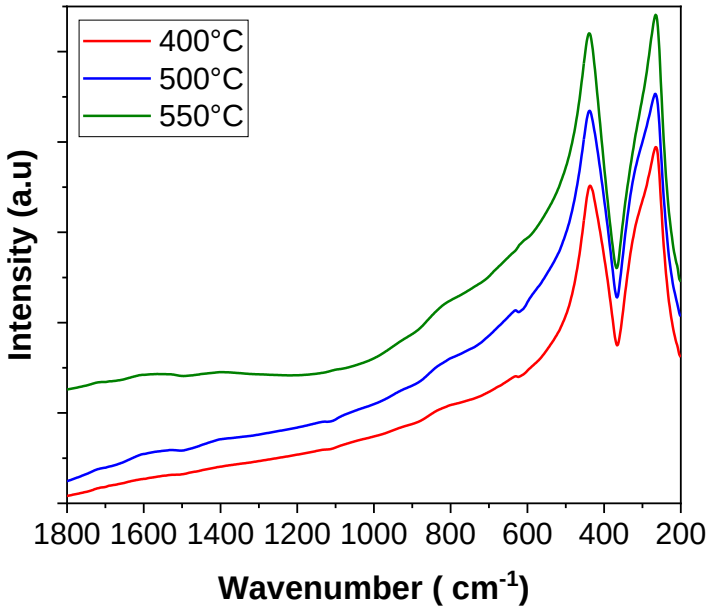

Figure III- 7. FTIR spectra of thin film samples on the Si substrate.

III.2.3. X-Ray diffraction (XRD)

The crystallinity and phase identification of the samples were studied by X-ray diffraction (XRD) in θ–2θ scanning mode using a Bragg–Brentano configuration between 10° and 80° at 0.011° intervals with an acquisition time of 2 s using a Bruker D8 Advance diffractometer with monochromatic CuKα1 radiation (λ = 0.15406 nm).

Figure III- 8 shows the diffraction patterns obtained for as-deposited films deposited at a range from 400 °C to 550 °C on silicon substrate with a deposition time of 40 min. The XRD patterns show that the obtained films are crystalline and consisted of pure anatase phase.

The diffraction peaks were observed at 25.5°, 37.5°, 48° and 55.3° 2θ degrees, corresponding to the anatase (101), (004), (200) and (211) planes (JCPDS- 21-1272). No evidence for rutile phase was found by XRD, even for TiO_2 films deposited at 550 °C.

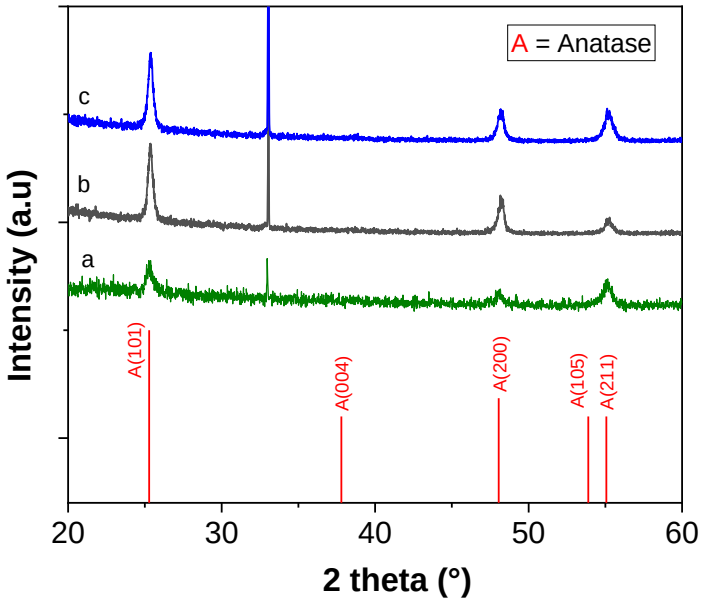

Figure III- 8. XRD of TiO_2 films deposited at silicon substrate at a) 400 °C b) 500 °C and c) 550 °C.

III.2.4. Raman Spectroscopy analysis

Regarding the chemical composition of the films, Raman spectroscopy is an effective tool to cover vibrational, rotational, and diverse low-frequency modes in a material. This type of spectroscopy technique is based on the Raman scattering (inelastic) taking place inside the samples over illumination with a monochromatic light source. Once a high intensity monochromatic light, in this matter a laser, strikes a material, the majority of photons are scattered with the same energy as the incident light. This elastically scattering technique is named Rayleigh scattering. Nevertheless, a certain number of the scattered photons, around 1 in 10 millions, present a shift of energy compared to the original energy. In the case of a lower or higher energy, this inelastic technique is named Raman scattering. In this technique, it is normal to employ wavenumber, cm^{-1}, in place of wavelength, as long as we always present the shift from the original light source. Concerning TiO_2 thin films, this technique was important for the detection of the anatase phase.

Raman spectra were collected using a Jobin-Yvon/Horiba LabRam multichannel spectrometer equipped with a liquid N_2 cooled CCD detector. Experiments were carried out in the micro-Raman mode at room temperature in a backscattering geometry. The 514.5 nm line of an Ar^+ laser (2.6 mW) was focused giving a spot size of about 1 μm. The recorded spectra were calibrated using Si

spectra at room temperature. The integration times were adjusted in order to obtain a high signal-to-noise ratio.

Many works have been reported in the literature about the Raman signature of the different TiO_2 phases [13]. Moreover, this technique is more sensitive to anatase, rutile and amorphous phases of TiO_2 films than XRD [14]. In addition, this technique is used to perform local measurements, allowing to probe the different microstructure phases of the sample surface.

Figure III- 9 shows the Raman spectra of TiO_2 films deposited on silicon at different temperatures ranging between 400 °C and 550 °C. The Raman spectra of the films show characteristic modes of the TiO_2 anatase phase [15]: two E_g modes at 141 cm^{-1} and 635 cm^{-1}, one A_{1g} mode at 513 cm^{-1} and one B_{1g} mode at 397.5 cm^{-1}. The sharp peak at 144 cm^{-1} clearly identifies the anatase phase of TiO_2. Smaller peaks at 398 and 639 cm^{-1} can also be assigned to the anatase phase. No band corresponding to the rutile phase of TiO_2 was observed. Moreover, the absence of a broad band background in the Raman spectra allows to discard the growth of amorphous TiO_2.

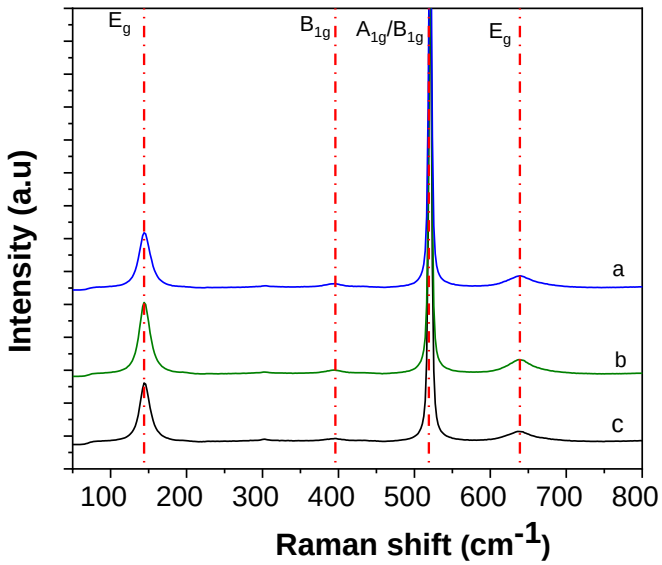

Figure III- 9. Raman spectra for TiO_2 films deposited on silicon by aerosol CVD at a) 550 °C, b) 500 °C and c) 400 °C.

III.2.5. X-ray Photoelectron Spectroscopy (XPS)

XPS is a non-destructive surface analysis method that characterize the binding energy between atoms. The analyzed depth is about 10 nm.

A monochromatic beam of X-Ray bombards the sample, causing the ionization of the atoms. By absorbing an X-ray photon of energy *hv*, a core electron is ejected: it is called a photoelectron. To return to its initial stable state, the electronic levels are rearranged: a higher energy electron replace the vacant core electron. To do so, the atom gets rid of an excess of energy via the emission of an X-ray photon (X-ray fluorescence) or of high energy level electron (Auger electron).

The XPS spectra acquired represent the number of photoelectrons collected per unit of time depending on their binding energy. These energies are a characteristic of an element and are computed with the equation III. 3.

$$E_{binding} = hv - E_C \qquad \text{III. 3}$$

where *hv* is the energy of the photon, $E_{binding}$ *is* the binding energy of the electron and E_c the kinetic energy measured by the detector. Integrating the electrons at different binding energy generates a spectrum where the peaks correspond to characteristic orbitals of each element. In the context of this study, XPS was fundamental to detect alterations in titanium oxidation state, in order to identify the presence of Ti^{+4} in the films.

The analysis was conducted in Vacuum Generator XR3E2 device at SIMAP – Grenoble INP using Al Kα radiation (energy 1486.6.6 eV) as an X-ray source. Before acquisition, the samples are placed during 12 hours in an introduction chamber at the pressure of 10^{-8} mbar in order to obtain a state desorption equilibrium, then introduced into the analysis chamber whose pressure is 10^{-10} mbar.

XPS spectra were made between 100 and 1100 eV with a resolution of 0.5 eV allowing to determine all the elements present.

Figure III- 10 shows high resolution XPS spectrum of a TiO_2 film deposited at 550°C on silicon substrate after rising with ethanol and distilled water.

The peak at binding energy 530.3 eV imply that the oxygen atoms exist as crystal lattice oxygen in Ti-O-Ti. Secondly, the peak at 531.9 eV is attributed to hydroxyl groups chemisorbed on the surface [16].

The Ti2p peaks are constituted of a doublet that arises from spin orbit-splitting. The doublet $Ti2p_{3/2}$ presents a binding energy of 459.2 eV and $Ti2p_{1/2}$ presents a binding energy of 464.9 eV. The literature shows that these peaks are consistent with Ti^{4+} in TiO_2 lattice, since $Ti2p_{3/2}$ shows a binding energy of 458.6 eV and $Ti2p_{1/2}$ shows a binding energy of 464.4 eV [17]. In our case, the contributions $Ti2p_{3/2}$ and $Ti2p_{1/2}$ with a splitting energy of 5.7 eV confirms a normal state of Ti^{4+}ion in the sample [18]. XPS proves that Ti^{3+} is not presented in the film.

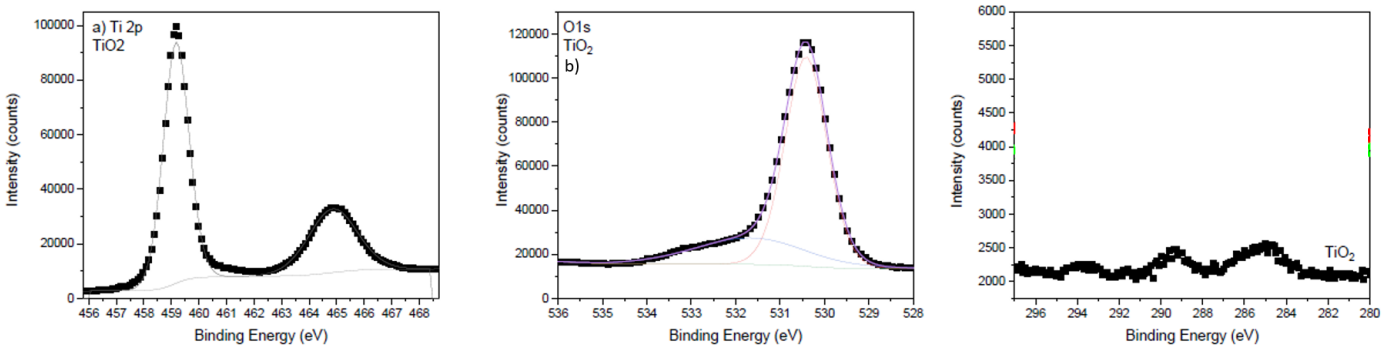

Figure III- 10. XPS for a) Ti2p configuration, b) O1s configuration and c) C1s configuration for TiO_2 film deposited at 540°C on silicon substrate.

III.2.6. UV-VIS-IR transmittance

The optical characterization of the TiO_2 layers consisting in measuring the total transmittance thanks to an integrated sphere of a diameter of 150 mm. The measurements from Ultraviolet to near-infrared were carried out in a Lambda 950 spectrophotometer from Perkin Elmer in the range of 250 nm to 2500 nm, displaying a wavelength step of 5 nm. The spectra were employed to calculate the band gap by tracing the Tauc plot using the equation III. 4 [19].

The transmittance of the films was measured on samples deposited on corning glass, and the bandgap of TiO_2 films was determined by extrapolating the slope of the curve to the photon energy axis.

$$(\alpha h\nu)^n = A(h\nu - E_g) \qquad \text{III. 4}$$

where α is the absorption coefficient, hv is the photon energy (eV), A is the proportionality constant, Eg (band gap energy) while n stands for the type of transition, which may be direct or indirect. In this case, the transition was indirect and as such n = 2.

The total optical transmittance and optical band gap calculated using Tauc plot of $(\alpha h\nu)^2$ versus photon energy of TiO_2 deposited on corning glass at different temperatures are shown in Figure III- 11 a) and Figure III- 11 b).

Figure III- 11 a) shows that TiO_2 films presents a high transmission (> 60 – 80 %) in the visible range, films are highly transparent in the visible. The oscillation observed are the result of interferences with the interfaces air – film and film – substrate.

The band gap energies of TiO_2 films are higher than the bulk value (3.2 eV) [20] of anatase. Moses et al. [21] obtained a band gap of 3.65 eV for TiO_2 films deposited at 450 °C by spray pyrolysis using titanyl (bis) acetylacetonate as precursor and it was explained that the band gap is larger than the bulk TiO_2 (3.2 eV) due to the presence of nano-sized grains.

It is noticed that the optical band gap of TiO_2 films varies from 3.78 eV to 3.55 eV when the deposition temperature increases from 400 °C to 550 °C .This can be explained by an increase of the crystallinity with deposition temperatures, which is supported by the XRD patterns of TiO_2 films deposited at different temperatures. The optical absorption of samples demonstrates that absorption is located mainly in UV region as a consequence of its wide band gap. The strong UV absorption of TiO_2 sample is due to electronic transition of an electron from valence band to the conduction band.

Fan Zhang et al [22] demonstrated that electron life time τ and band gap Eg decrease at elevated temperature. It is due to the thermal expansion of the lattice and renormalization of the band structure by electron-phonon interaction [23].

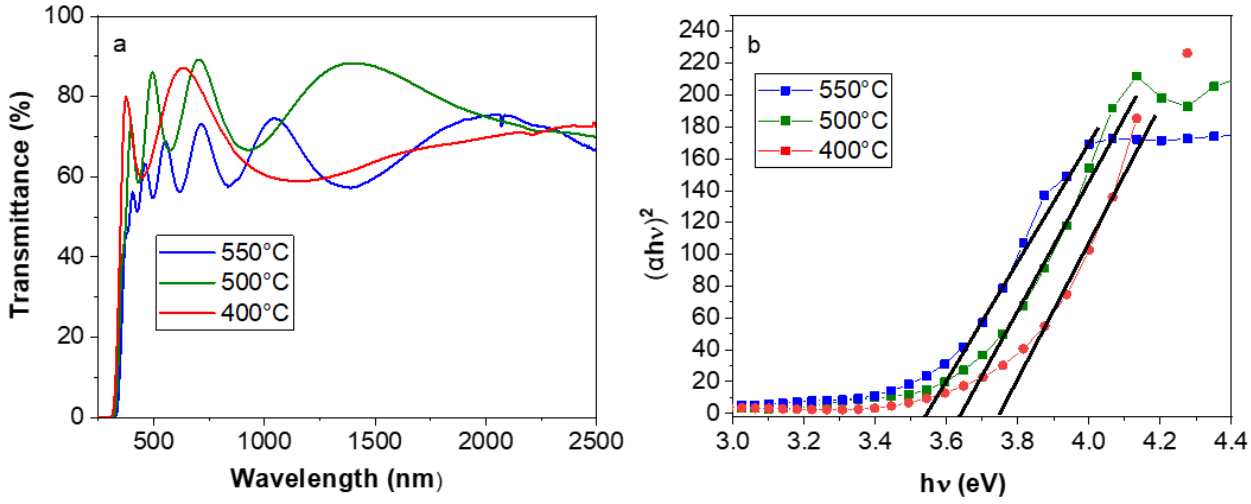

Figure III- 11. a) Total transmittance of TiO_2 films deposited at different temperatures. b) Optical band gap calculated using Tauc plot of TiO_2 films deposited at different temperatures.

III.3. Photocatalytic characterization

Photocatalysis is based on photo-induced oxidation-reduction mechanisms leading to the decomposition (e.g. mineralization) of organic molecules adsorbed on the surface of a semiconductor. The kinetics of photocatalytic decomposition of molecules in aqueous solution generally follow a Langmuir-Hinshelwood mechanism, modified to account for the reactions taking place at the interface between the solid photocatalyst and the liquid, assimilating the liquid to a gas under strong pressure. Under these conditions, the rate of degradation of the reactant (r) is written:

$$r = -\frac{dC}{dt} = k_c . \frac{K_{ads} . C}{1 + K_{ads} . C} \qquad \text{III. 5}$$

where k_c is the kinetic constant of the reaction, K_{ads} is the adsorption constant of the reactant, and C the reactant concentration at time t. The ability to photocatalytic degradation (photocatalytic activity) of different materials can be quantified comparatively according to the degradation rate of the same model molecule.

The model molecule studied in this work is an azo dye named orange G (OG, marketed by Aldrich and of empirical formula: $C_{16}H_{10}N_2Na_2O_7S_2$) whose chemical structure is illustrated in Figure III- 12. Studies published by other authors showed that the OG is not only decolorized by photocatalytic reactions but fully mineralized [24]. The mineralization is a set of chemical reactions including the dissociation of the central azo group and its elimination in the form of dediazote gas, as well as the multi-stage reduction of aromatic rings in carboxylic species, then CO_2.

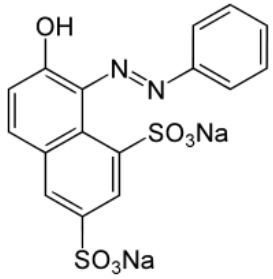

Figure III- 12. The molecular structure of orange G.

It is important to fix two geometrical parameters to ensure the comparison of results from one sample to other. One parameter is the exposed area of the sample has to be the same for all the experiments. In our work the area was of 7.06 cm^2 for films deposited on round high speed steel substrate (d=3 cm) and 9 cm^2 for films deposited on silicon substrate. The second parameter is the distance of the layer to the bottom of the beaker. This distance fixes the volume of the solution in contact with the layer, and the distance to the UV lamps. We use a polymeric holder imposing a distance of 8 mm from the sample to the beaker bottom, which is placed at 20 mm of the UV lamps. We insert the sample in the holder and then the sample and its support are placed at the bottom of the beaker. The face covered by the layer TiO_2 (active face) is directed towards the bottom of the beaker as represented in Figure III- 13. The whole is placed in an oven regulated in humidity (RH = 40 %) and temperature (T = 20 °C). In order to homogenize the solution and maintain constant adsorption/desorption conditions during UV exposure, the solution is stirred constantly during irradiation via a magnetic bar and a magnetic stirrer set at 500 rpm.

For our measurements of photocatalytic activity, 50 ml of an aqueous solution of OG (concentration 5.10^{-5} M) are poured into a beaker. The beaker is then positioned on a support allowing it to be held an above three UV lamps (Philips PLS 11W). These lamps emit a continuous spectrum in the UV-A range (negligible UV-B and UV-C emission), with a maximum emission at 365 nm, and provide a light intensity at the sample level of approximately 5 mW/cm^2.

Before irradiation, the system is kept in the dark for one hour in order to obtain a balance of adsorption of the OG on the surface of the photocatalyst. However, no significant variation in the concentration of OG in solution was observed during this preliminary stabilization step, regardless of the nature of the samples analyzed. It can be inferred that, under our conditions, not only the amount of GO adsorbed on the surface of the thin film photocatalyst is extremely weak but also that OG is chemically stable in the absence of UV and photocatalyst. After this step, the whole is irradiated for three hours via the device described above. A small amount of solution (approximately 3 ml) is taken every thirty minutes in order to measure the evolution of the concentration of OG by UV-Vis spectrometry and then reinjected into the solution.

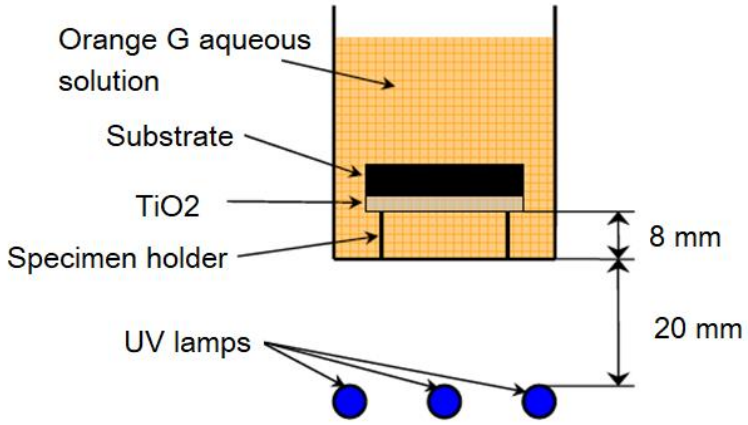

Figure III- 13. Diagram of the device used for the measurement of photocatalytic activity.

We used UV-visible spectrophotometer (Lambda 950 from Perkin Elmer) in order to obtain the measured absorbance of the orange G dye, as represented in Figure III- 14. The UV-vis measurements were carried out using a wavelength range from 400 to 600 nm with a scan speed of 480 nm/min.

According to the Beer-Lambert law, the concentration of OG (C) is a function of the measured absorbance A (equation III. 6):

$$A = \alpha . l . C \qquad \text{III. 6}$$

where α is the molar absorption coefficient at the measured wavelength and l the light path in the solution (1 cm in our case). In this study, the measurement of A is performed at 480 nm, which corresponds to the maximum absorption of the Orange G dye (and confers its orange color to this compound). Under our conditions, the parameters l and α are constant, which means that A is directly proportional to C.

Calibration measurements under irradiation carried out in the presence of the substrate alone have shown that the concentration of Orange G in the solution increases slightly during the time due to slow evaporation of the water as a dilution medium (reconcentration mechanism). A reconcentration correction has therefore been done in order to determine the changes in Orange G concentration actually induced by the photocatalytic decomposition (Figure III- 15).

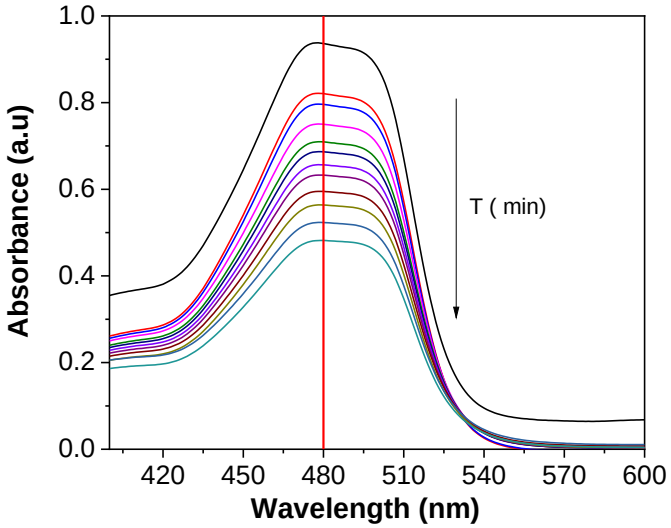

Figure III- 14. UV-visible absorbance spectra of decomposed Orange G-dye solution over TiO_2 film deposited at 550 °C on silicon under UV light illumination.

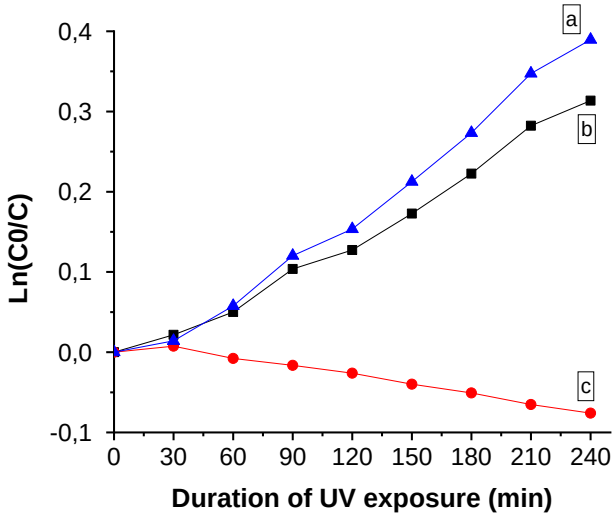

Figure III- 15. Kinetics of photocatalytic decomposition of OG on the surface of a thin layer of TiO_2 after reconcentration correction (a). Kinetics in the presence (b) and in the absence (c) of the photocatalyst.

Monitoring the photocatalytic decomposition of the OG over three hours makes it possible to deduce the photocatalytic activity according to the relationship. Given the low concentration of OG of the aqueous solutions used during this work (5.10 M^{-5}), the term K_{ads}. C is much lower than 1 and can be neglected in this equation, which becomes:

$$r = -\frac{dC}{dt} = k_c \,.\, K_{ads} \,.\, C = k.C \qquad \text{III. 7}$$

Where k describes an apparent kinetic constant of the system. By integrating the equation III. 7, we obtain:

$$ln\left(\frac{A_0}{A}\right) = \left(\frac{C_0}{C}\right) = k.t_{UV} \qquad \text{III. 8}$$

where C_0 represents the OG concentration deduced from a measurement of absorbance A_0 at 480 nm at the start of irradiation and C is the concentration measured from the absorbance A after an exposure of duration t_{UV}. The representation of ln (A_0/A) = f (t_{UV}) must therefore give a straight line passing through the origin whose slope makes it possible to determine the kinetic constant k. The constant k will be used to compare the photocatalytic activity of the different samples studied in this work. It should be noted that the linearity predicted by equation III. 8 has been systematically verified after reconcentration correction in the general case of TiO_2 thin layers (Figure III- 15).

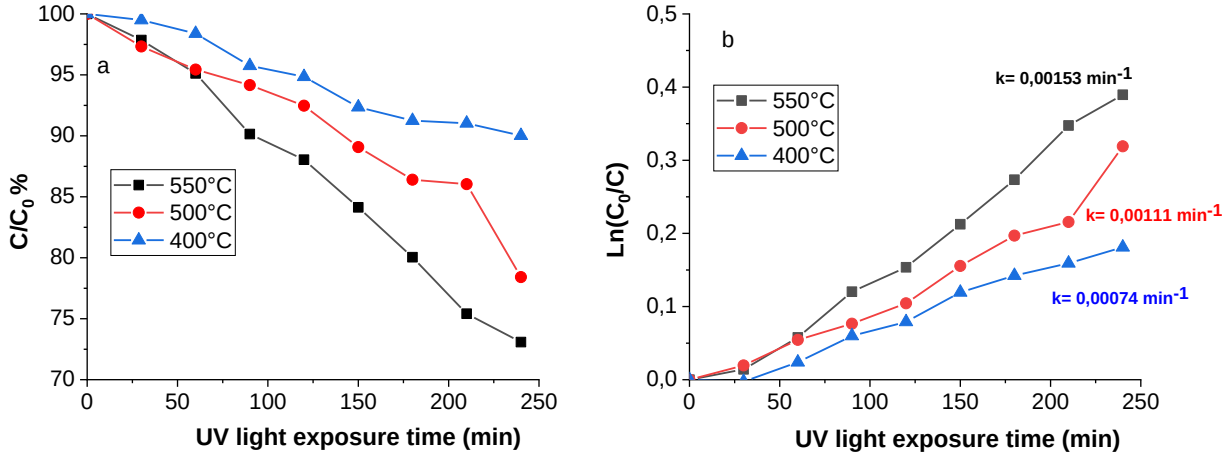

Figure III- 16.a) Relative photocatalytic activity of different TiO_2 films deposited on silicon (about 250 nm thick) as deposited. b) Kinetics of photocatalytic decomposition of orange G measured for different TiO_2 films.

The evolution of the absorption band at 480 nm corresponding to Orange G allowed to quantify the concentration variation with UV exposure time. The concentration of orange G decreases when exposed to TiO_2 films as represented in Figure III- 16 a). Figure III- 16 b) shows plots of Ln(C/C_0) as a function of UV light irradiation time. The photocatalytic activity of three different TiO_2 films deposited at 400 °C, 500 °C and 550 °C on silicon was analysed in order to evaluate the films performance. For films containing TiO_2 microflowers, deposition temperature presents an influence on the degradation rate, with a maximum value in the case of the film deposited at 550 °C, which shows almost 30 % of mineralization after 240 min of UV light exposure. For the film

deposited at 500 °C the value is 20 % of mineralization for the same exposition time, and only of 10% for the film deposited at 400°C.

The k constant for Orange G degradation calculated from the slope with formula III.8 is presented in Figure III- 16 b). It is important to notice that microflowers structure were mainly present in samples deposited ant 550 °C, creating a higher roughness and a higher surface area for chemical exchange or reaction. For films without microflowers deposited at 400°C the k constant is one order of magnitude lower than films containing microflowers deposited at the same range of temperature.

It can be also explained by the fact that the band gap shift in the absorption band edge for TiO_2 film deposited at 550 °C is attributed to the higher rate of electron-hole pairs on the photocatalyst surface, leading to higher photocatalytic activity [25].

The photocatalytic activity of Al-Zr/TiO_2 bilayer films deposited at different temperatures with different deposition feeding rates (mL/min) will be presented and further analysed in chapter IV.

III.4. Reproducibility of TiO_2 films on high speed steel substrates

Since TiO_2 films is used as a top layer on Al-Zr coated High Speed Steel (see chapter IV) it is important to evaluate the reproducibility of TiO_2 films presenting hierarchical microflowers on the surface when deposited on high speed steel substrates. Indeed, the presence of microflowers on the surface is important to improve the photocatalytic activity.

Deposition was carried out on different substrates like high speed steel, FTO and ITO-coated substrates. The same microstructure is obtained in all the cases as represented in Figure III- 17.

XRD measurements were also performed in order to confirm the same crystalline structure for films deposited on high speed steel.

Figure III- 18 shows the diffraction patterns obtained for as-deposited films deposited at a range from 500 °C to 550 °C on high speed steel with a deposition time of 40 min.

The XRD patterns show that the obtained films are crystalline and anatase single phased. For films deposited on high speed steel at 540 °C and 550 °C, we observed a much higher intensity of the diffraction peaks compared to film deposited at 500 °C. The effect of temperature and presence of microflowers on the surface with regard to crystallite size is discussed in chapter IV.

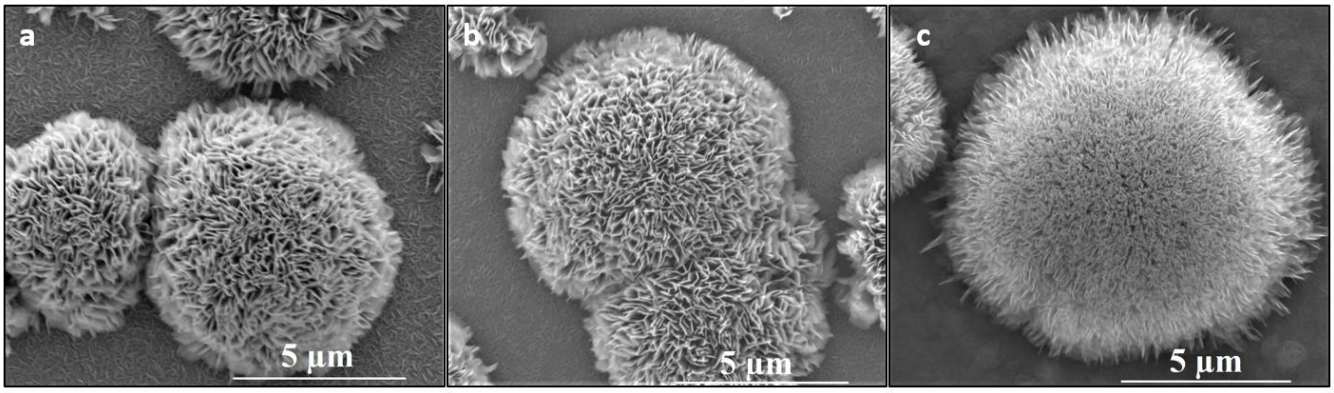

Figure III- 17. a) SEM image of TiO_2 microflowers on films deposited at 550 °C on a) FTO-coated glass b) ITO-coated glass and c) high speed steel substrate.

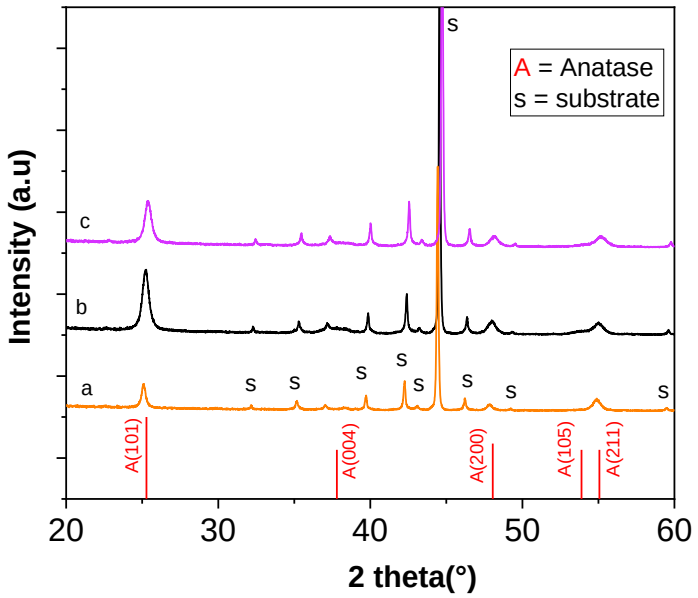

Figure III- 18. XRD of TiO_2 films at deposited at high speed steel substrate at a) 500 °C, B) 540 °C and C) 550 °C.

III.5. Conclusions

AA-MOCVD using titanyl (bis) acetylacetonate as precursor and working at atmospheric pressure allows the direct synthesis of TiO_2 microflowers dispersed at the top of a thin film of TiO_2. Optimum growth conditions are acquired by the combining the deposition temperature, precursor concentration and precursor feeding rate. The formation of the microstructure occurs at a specific thermal window that depends on the precursor concentration; more precisely when working with a 0.03 mol L^{-1} concentration solution and an aerosol feeding rate of 3 ml min^{-1}, flower-like structures are generated at 550 °C. At this temperature, the maximum flower density is about 40 %, in terms

of area fraction coverage. The development of microflowers is definitely sensitive to the temperature. At lower temperatures, such as 400 °C, no flower is created. At 500 °C, some flowers can be observed and at 550 °C, TiO_2 microflowers of about 7-8 µm diameter are clearly detected.

XRD and Raman Spectroscopy confirm the flowers and the thin film to be in the anatase phase.

TiO_2 samples deposited at 550 °C shows better photocatalytic with a higher k (0.00153 min^{-1}) and 30 % of mineralization of Orange G dye after 240 min under UV light when compared to others films deposited at lower deposition temperatures (500 and 400 °C). This chapter confirms the fundamental role of microflowers with an average size of 7 µm and its density on the surface layer on the photocatalysis process.

The optical band gap of TiO_2 films decreases from 3.78 eV to 3.55 eV when the deposition temperature increases from 400 °C to 550 °C. It is related to the band gap shift in the absorption band edge for TiO_2 film deposited at 550 °C, which is attributed to a higher rate of electron-hole pairs on the surface of the film, leading to higher photocatalytic activity.

References

[1] H.O. Pierson, Handbook of chemical vapor deposition: principles, technology and applications, William Andrew, 1999.

[2] P. Marchand, I.A. Hassan, I.P. Parkin, C.J. Carmalt, Aerosol-assisted delivery of precursors for chemical vapour deposition: expanding the scope of CVD for materials fabrication., Dalton Trans. 42 (2013) 9406–22. doi:10.1039/c3dt50607j.

[3] J.C. Viguie, J. Spitz, Chemical vapor deposition at low temperatures, J. Electrochem. Soc. 122 (1975) 585–588.

[4] R.J. Lang, Ultrasonic atomization of liquids, J. Acoust. Soc. Am. 34 (1962) 6–8.

[5] E.G. Lierke, G. Griesshammer, The formation of metal powders by ultrasonic atomization of molten metals, Ultrasonics. 5 (1967) 224–228.

[6] F.D. Duminica, F. Maury, R. Hausbrand, Growth of TiO_2 thin films by AP-MOCVD on stainless steel substrates for photocatalytic applications, Surf. Coatings Technol. 201 (2007) 9304–9308. doi:10.1016/j.surfcoat.2007.04.011.

[7] J. Mungkalasiri, L. Bedel, F. Emieux, J. Doré, F.N.R. Renaud, C. Sarantopoulos, F. Maury, CVD elaboration of nanostructured TiO_2-Ag thin films with efficient antibacterial properties, Chem. Vap. Depos. 16 (2010) 35–41. doi:10.1002/cvde.200906764.

[8] J. Mungkalasiri, L. Bedel, F. Emieux, J. Doré, F.N.R. Renaud, F. Maury, DLI-CVD of TiO_2-

Cu antibacterial thin films: Growth and characterization, Surf. Coatings Technol. 204 (2009) 887–892. doi:10.1016/j.surfcoat.2009.07.015.

[9] S. Biswas, C. Jiménez, A. Khan, S. Forissier, A.K. Kar, D. Muñoz-Rojas, J.-L. Deschanvres, Structural study of TiO_2 hierarchical microflowers grown by aerosol-assisted MOCVD, CrystEngComm. 19 (2017) 1535–1544. doi:10.1039/C6CE02648F.

[10] C.V. De Oliveira, A. Alhussein, J. Creus, F. Schuster, Bifunctional TiO_2 /AlZr Thin Films on Steel Substrate Combining Corrosion Resistance and Photocatalytic Properties, (2019) 1–16. doi:10.3390/coatings9090564.

[11] S.F. Tayyari, F. Milani-nejad, Vibrational assignment of acetylacetone, Spectrochim. Acta - Part A Mol. Biomol. Spectrosc. 56 (2000) 2679–2691. doi:10.1016/S1386-1425(00)00304-8.

[12] D.C.L. Vasconcelos, V.C. Costa, E.H.M. Nunes, A.C.S. Sabioni, M. Gasparon, W.L. Vasconcelos, Infrared Spectroscopy of Titania Sol-Gel Coatings on 316L Stainless Steel, Mater. Sci. Appl. 02 (2011) 1375–1382. doi:10.4236/msa.2011.210186.

[13] S. Boukrouh, R. Bensaha, S. Bourgeois, E. Finot, M.C. Marco de Lucas, Reactive direct current magnetron sputtered TiO2 thin films with amorphous to crystalline structures, Thin Solid Films. 516 (2008) 6353–6358. doi:10.1016/J.TSF.2007.12.150.

[14] A. Brevet, F. Fabreguette, L. Imhoff, M.C. Marco de Lucas, O. Heintz, L. Saviot, M. Sacilotti, S. Bourgeois, Thermal effects on the growth by metal organic chemical vapour deposition of TiO2 thin films on (100) GaAs substrates, Surf. Coatings Technol. 151–152 (2002) 36–41. doi:10.1016/S0257-8972(01)01586-9.

[15] G. Busca, G. Ramis, J.M.G. Amores, V.S. Escribano, P. Piaggio, FT Raman and FTIR studies of titanias and metatitanate powders, J. Chem. Soc.{,} Faraday Trans. 90 (1994) 3181–3190. doi:10.1039/FT9949003181.

[16] G. Colón, M.C. Hidalgo, G. Munuera, I. Ferino, M.G. Cutrufello, J.A. Navío, Structural and surface approach to the enhanced photocatalytic activity of sulfated TiO_2 photocatalyst, Appl. Catal. B Environ. 63 (2006) 45–59. doi:10.1016/j.apcatb.2005.09.008.

[17] B. Bharti, S. Kumar, H.N. Lee, R. Kumar, Formation of oxygen vacancies and Ti3+ state in TiO_2 thin film and enhanced optical properties by air plasma treatment, Sci. Rep. 6 (2016) 1–12. doi:10.1038/srep32355.

[18] C.D. Wagner, W.M. Riggs, L.E. Davis, J.F. Moulder, G.E. Muilenberg, Handbook of X-ray

Photoelectron Spectroscopy, Perkin-Elmer Corp, Eden Prairie, MN. (1979) 38.

[19] J. Tauc, A. Menth, States in the gap, J. Non. Cryst. Solids. 8–10 (1972) 569–585. doi:10.1016/0022-3093(72)90194-9.

[20] C. Dette, M.A. Pérez-Osorio, C.S. Kley, P. Punke, C.E. Patrick, P. Jacobson, F. Giustino, S.J. Jung, K. Kern, TiO_2 anatase with a bandgap in the visible region, Nano Lett. 14 (2014) 6533–6538.

[21] A. Moses Ezhil Raj, V. Agnes, V. Bena Jothy, C. Ravidhas, J. Wollschläger, M. Suendorf, M. Neumann, M. Jayachandran, C. Sanjeeviraja, Spray deposition and property analysis of anatase phase titania (TiO_2) nanostructures, Thin Solid Films. 519 (2010) 129–135. doi:10.1016/j.tsf.2010.07.073.

[22] Z. Fan, Z. Rong-Jun, Z. Dong-Xu, W. Zi-Yi, X. Ji-Ping, Z. Yu-Xiang, C. Liang-Yao, H. Ren-Zhong, S. Yan, C. Xin, M. Xiang-Jian, D. Ning, Temperature-Dependent Optical Properties of Titanium Oxide Thin Films Studied by Spectroscopic Ellipsometry, Appl. Phys. Express. 6 (2013) 121101. http://stacks.iop.org/1882-0786/6/i=12/a=121101.

[23] J.J. Zhu, W.W. Li, G.S. Xu, K. Jiang, Z.G. Hu, J.H. Chu, A phenomenological model of electronic band structure in ferroelectric Pb(In1/2Nb1/2)O3–Pb(Mg1/3Nb2/3)O3–PbTiO3 single crystals around the morphotropic phase boundary determined by temperature-dependent transmittance spectra, Acta Mater. 59 (2011) 6684–6690. doi:10.1016/J.ACTAMAT.2011.07.025.

[24] H. Lachheb, E. Puzenat, A. Houas, M. Ksibi, E. Elaloui, C. Guillard, J.M. Herrmann, Photocatalytic degradation of various types of dyes (Alizarin S, Crocein Orange G, Methyl Red, Congo Red, Methylene Blue) in water by UV-irradiated titania, Appl. Catal. B Environ. 39 (2002) 75–90. doi:10.1016/S0926-3373(02)00078-4.

[25] S. Danwittayakul, M. Jaisai, T. Koottatep, J. Dutta, Enhancement of photocatalytic degradation of methyl orange by supported zinc oxide nanorods/zinc stannate (ZnO/ZTO) on porous substrates, Ind. Eng. Chem. Res. 52 (2013) 13629–13636.

Chapter IV: Characterizations of Al-Zr/TiO_2 bilayer thin films

The corrosion of metals in natural seawater is a consequence of interactions between the metal, living organisms and seawater composition [1]. When a metal is submerged into seawater, corrosion and biofouling take place simultaneously [2]. This is usually pursued by the development of biofilm within some days after submersion [3] and after a continuous exposure, macrobiota like invertebrate larvae may combine with the biofilm and settle on the surface [4]. In order to solve this problem we focus on two different functional properties: photocatalysis, which is related to the

surface properties to avoid initial step of attachment, and corrosion, to protect the steel used in the mechanical system.

This chapter presents the physico-chemical and functional properties of a multi-functional bilayer coating combining Al-Zr (4 at.% Zr) alloy deposited by DC Magnetron Sputtering on high speed steel substrates and TiO_2 deposited on the top by AAMOCVD. Al-Zr (4 at.% Zr) film was used to provide sacrificial corrosion resistance of steels as presented in chapter II and, TiO_2 was added as a top layer to induce photocatalytic activity and hydrophilic behavior which can generate antifouling properties in order to slow down the biofouling process.

The first part of this chapter will be dedicated to the microstructural and physical properties of the bilayer films. The functional properties such as the electrochemical behavior and the photocatalytic properties of bilayer films will be treated in the second part.

IV.1. Deposition conditions

Polished round High Speed Steel (HSS) substrates with 30 mm in diameter and 1 mm thick were systematically covered with a previously optimised composition of Al-Zr coating having 4 atomic percent of zirconium and a thickness of 3 microns, as explained in chapter I. Then, TiO_2 films were deposited at different temperatures in order to achieve the optimal deposition conditions allowing the formation of flower-like microstructures as described in chapter III. Figure IV-1 presents HSS substrates coated with Al-Zr alloy and Al-Zr/TiO_2 bilayer film.

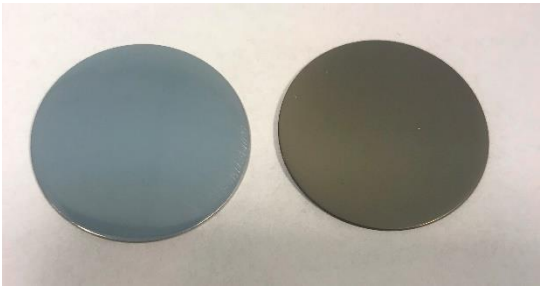

Figure IV- 1. Al-Zr (4 at. % Zr) alloy, on the left, and Al-Zr/TiO_2 bilayer film on the right.

As presented in chapter III, the titanium precursor (titanyl (bis) acetylacetonate) was dissolved in ethanol with a concentration of 0.03 mol L^{-1} and the solution consumption was around 3mL min^{-1} in order to develop microflowers in the TiO_2 layer. A solution consumption between 3 and 4mL min^{-1} allows the formation of hierarchical microflowers. However, less than 3mL min^{-1}

microflowers are not developed. The oxidizing gas flow rate was obtained by using 6 L min^{-1} of air (12% of O_2) and the deposition temperature was varied between 500 °C and 550 °C for a deposition time of 40 minutes. The substrates used were Al-Zr coated HSS substrates.

IV.2. Morphology and roughness of HSS/Al-Zr/TiO_2films

The morphology of as-deposited Al-Zr films observed by a SEM is shown in Figure IV- 2 (a-b) for low and high magnification conditions in the upper and lower pictures respectively, and in cross section represented in Figure IV- 2 c). For low Zr content like in our case and in our deposition conditions, the coatings grow with a columnar morphology forming big grains of around 500 nm of diameter, as explained in chapter II. The Al-Zr thickness is 3 µm. When TiO_2 was deposited by AACVD as a second layer on the Al-Zr coating, two kinds of features appeared. On one hand, a film consisting in small needle-like (dendritic microspheres) grains of 50 nm covered the Al-Zr grains in a very conformal way. This morphology can be observed in Figure IV- 2 (e-h-k), for the three deposition temperatures used. We cannot see any difference or significant changes between these morphologies. The Al-Zr grains can be still identified even if TiO_2 film thickness is around 400 nm. On the other hand, microflowers started to grow at deposition temperature higher than 500 °C, as explained before in chapter III. At 500 °C, represented in Figure IV- 2 (d-f), some sparse flowers can be observed but much smaller than those shown in Figure IV- 2 (g-i) and (j-l) for films deposited at 540 °C and 550 °C, respectively. For films deposited at 540 °C and 550 °C, the flowers density increases and a quite high density of microflowers is observed on the surface. Flowers having an average diameter of about 7 µm can be described by a homocentric association of TiO_2 nanopetals forming a corolla as if growing from the receptacle of a flower. The main characteristics of these microstructures are that petals have a nanometric thickness (~ 5 nm) and are formed by nanocrystal of anatase phase as shown in the next section.

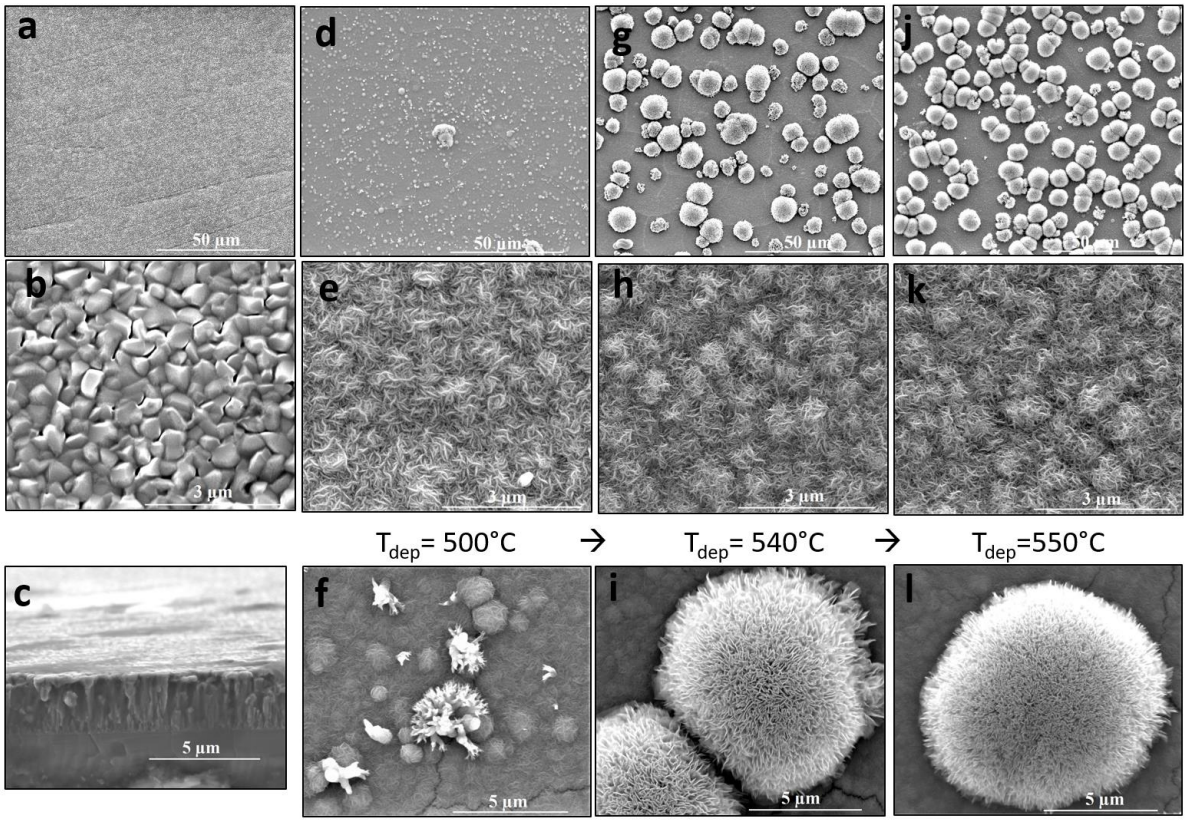

Figure IV- 2. SEM images of samples: a-b-c) Al-Zr (4 at.% Zr) coating and TiO_2 deposited at d-e-f) 500 °C, g-h-i) 540 °C and j-k-l) 550 °C.

Images d, g and j were used to quantify the density of the flowers by calculating the area fraction covering the sample by the flowers (in percentage) as shown in Figure IV- 3. The area fraction covered by microflowers was about 43 % for TiO_2 thin films samples deposited at 550°C, 23 % for films deposited at 540°C and 8 % for TiO_2 films deposited at 500°C.

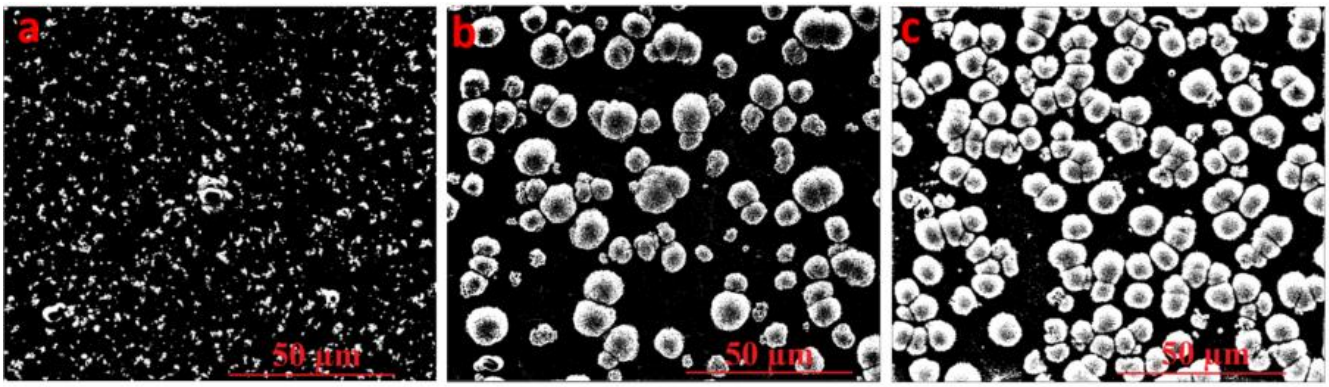

Figure IV- 3. SEM images processed by ImageJ for TiO_2 films deposited at a) 500 °C, b) 540 °C and c) 550 °C.

Surface roughness profiles of samples were obtained using a Form Talysurf 50 (Taylor Hobson Co Ltd) surface Profilometer and measured 25 mm crossing the centre along the surface of the sample. For these measurements, the pre-race length used was 0.30 mm, the spacing (y) was 0.1 mm, the measuring speed was 1 mm/ s and the number of points was 5000. As described in ASME B46.1, Ra is the arithmetic average of the absolute values of the profile height deviations from the mean line, recorded within the evaluation length. Ra is the average of a set of individual measurements of surface peaks and valleys[5].

Figure IV- 4 presents the surface roughness profiles for the HSS/Al-Zr film and for the HSS/Al-Zr/ TiO_2 bilayer films deposited at 500 °C and 550 °C. R_a values were measured using contact mode, where the measuring instrument was in direct contact with the surface.

Al-Zr monolayer film presents a surface with a R_a value of 87 nm. The roughness increases when TiO_2 layer is added and also when the deposition temperature increases. The TiO_2 film deposited at 500°C, reproduces the Al-Zr baseline, with sparse peaks corresponding to the presence of microflowers. For TiO_2 deposited at 550 °C, the density of microflowers is so high that causes a high roughness with an average Ra= 524 nm. The highest peaks correspond to the height of the biggest microflowers dispersed at the top of the layer (about 7 µm in size).

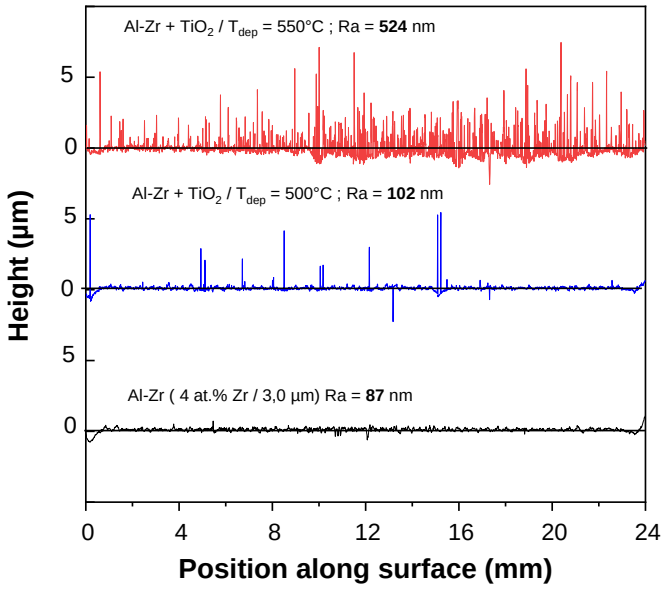

Figure IV- 4. Surface roughness profiles measured 25 mm along the surface.

IV.3. Structural properties

IV.3.1. X-Ray Diffraction (XRD) analysis

The crystallinity and phase identification of the samples were studied by X-ray diffraction (XRD) in θ–2θ scanning mode using a Bragg–Brentano configuration between 10° and 80° at 0.011° intervals with an acquisition time of 2 s using a Bruker D8 Advance diffractometer equipped with monochromatic CuKα1 radiation (λ = 0.15406 nm).

The crystallite size was determined using the Scherer's formula based on the FWHM (Full Width At half Maximum) of (101), (200) and (211) anatase peaks in XRD patterns (Eq. IV.1):

$$Dp = (K \times \lambda) / (\beta \times \cos\theta) \qquad \text{IV. 1}$$

where D_P is the crystallite size in nanometers, λ_{Cu} = 0.15418 nm is the X-ray wavelength, θ is the diffraction angle of the (101), (200) and (211) peaks and β is defined as the peak width of the diffraction peak profile at half maximum height resulting from small crystallite size in radians and K is Scherrer's constant related to crystallite shape (in our study, K = 0.9). To determine the evolution of crystallite size with temperature on the dense TiO_2 film without flowers, we performed XRD analysis on HSS/Al-Zr/TiO_2 films deposited on polished HSS substrates. In this case, the grain size values obtained by Scherer's method given by formula IV.1 were 44 nm for film deposited at 500°C and 53 nm for films deposited at 550°C. However, if we calculate crystallite size from the samples containing flowers, these values are 18 nm and 20 nm for films deposited at 500 and 550°C respectively. As the mean value includes the crystallites size from the film that should be equivalent to previous values in TiO_2 films, we can infer that crystallites size contained in the microflowers are rather smaller to 18 nm. The crystallite size values for TiO_2/Al-Zr coatings deposited at 500°C and 550°C are resumed in Table IV- 1.

Table IV- 1: Effect of presence of microflowers on the crystallite size in TiO_2 coatings deposited at 500°C and 550°C.

Samples with microflowers	
Bilayer films	Crystallite Size (nm)
HSS/Al-Zr/TiO_2 T_{dep}=500°C	18
HSS/Al-Zr/TiO_2 T_{dep}=550°C	20
Samples without microflowers	
HSS/Al-Zr/TiO_2 T_{dep}=500°C	44
HSS/Al-Zr/TiO_2 T_{dep}=550°C	53

XRD characterisation was also performed after deposition of TiO_2 at 500, 540 and 550°C on HSS/Al-Zr substrates. The XRD patterns of these TiO_2 coatings with and without microflowers are shown in Figure IV- 5 and Figure IV- 6, respectively. They reveal only anatase phase in all cases, mainly detected by the (101) and (200) diffraction peaks at 25° and 48° respectively. The XRD pattern of TiO_2 thin film is also dominated by anatase phase with a preferential orientation of (101), without presence of rutile phase, even for the highest deposition temperature of 550 °C. This is favourable because rutile has a lower charge-transfer rate and higher recombination rate of photogenerated electron–hole pairs than anatase [6].

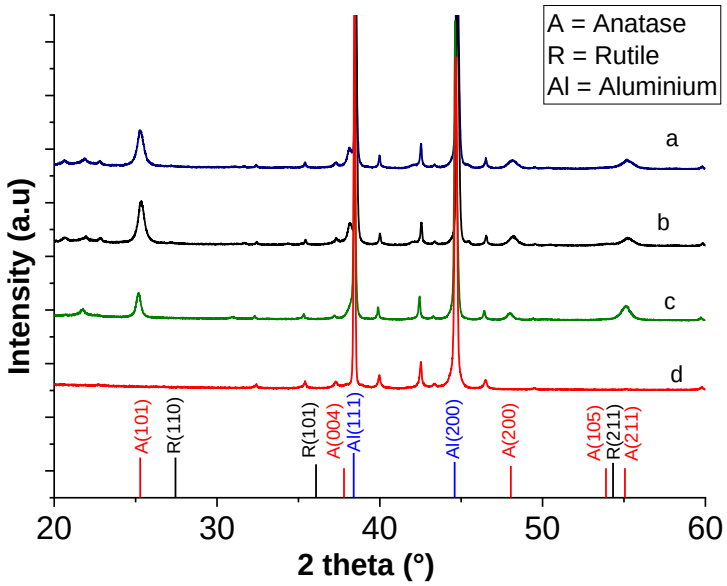

Figure IV- 5. XRD patterns for Al-Zr/TiO_2 films with microflowers deposited at a) 550°C, b) 540°C and c) 500°C on d) Al-Zr.

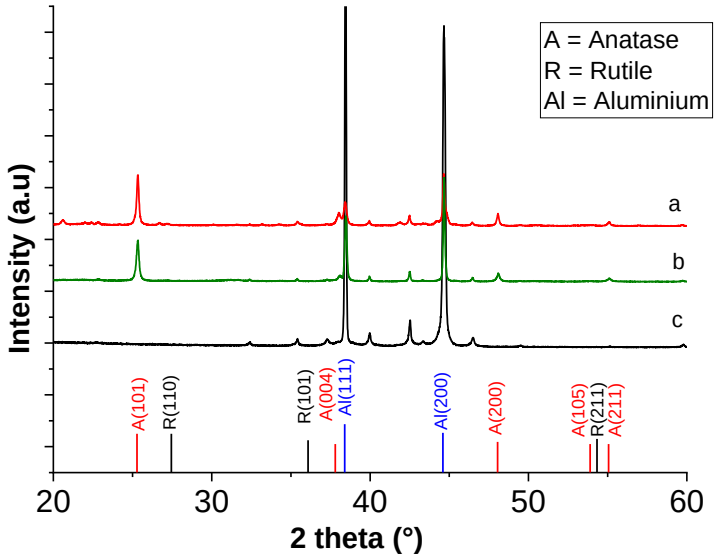

Figure IV- 6. XRD Patterns for Al-Zr/TiO_2 thin films without microflowers deposited at a) 500°C, b) 550°C on c) Al-Zr.

IV.3.2. Raman Spectroscopy analysis

Figure IV- 7 shows the Raman spectra of HSS/Al-Zr/TiO_2 bilayer films deposited at different temperatures ranging between 500 and 550°C. The Raman spectra of the films containing microflowers on the surface show characteristic modes of the TiO_2 anatase phase[7]: two E_g modes at 141 cm^{-1} and 635 cm^{-1}, one A_{1g} mode at 513 cm^{-1} and one B_{1g} mode at 397.5 cm^{-1}. The sharp peak at 144 cm^{-1} clearly identifies the anatase phase of TiO_2. Smaller peaks at 398 and 639 cm^{-1} can also be assigned to the anatase phase. No band corresponding to the rutile phase of TiO_2 was observed. Moreover, the absence of a broad band background in the Raman spectra allows to discard the growth of amorphous TiO_2.

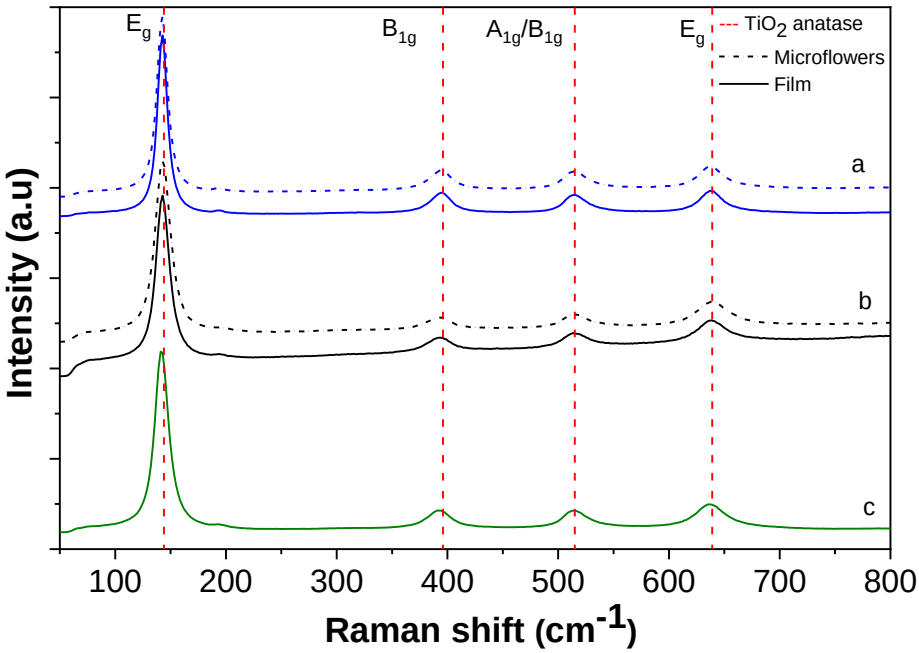

Figure IV- 7. Raman spectra for HSS/Al-Zr/TiO2 films deposited by aerosol CVD at a) 550°C, b) 540°C and c) 500°C.

IV.4. Photocatalytic properties of HSS/Al-Zr/TiO2 bilayer films

Evolution of the absorption band at 480 nm corresponding to Orange G allowed to quantify the variation of its concentration under UV light. Figure IV- 8 shows plots of $Ln(C/C_0)$ as a function of UV light irradiation time.

$$\ln(C_0/C) = k_c . K_{ads} .t = K_{appt} \qquad \text{IV. 2}$$

where C_0 is the concentration of Orange G after the adsorption – desorption equilibrium, K_{app} is the apparent first-order rate constant (h^{-1}).

The constant k was used to compare the photocatalytic activities of the different samples. k describes an apparent kinetic constant of the system as explained before in chapter III.

Al-Zr coating was tested for verification and, as expected, this layer did not present any photocatalytic activity as indicated in Figure IV- 8. On the contrary, the concentration of orange G decreased when exposed to TiO_2 films. Two kinds of TiO_2 films were deposited to highlight the influence of microflowers on phtotocatalytic properties. Using the same deposition temperature, the solution consumption is decreased to less than $3L.min^{-1}$ by decreasing the frequency of the

piezoelectric ceramic, which allows to deposit TiO_2 films without flowers. These layers present the same morphology and crystallised also in anatase phase.

The photocatalytic activities of these two series are represented in Figure IV- 8. For films containing TiO_2 microflowers, deposition temperature has an influence on the degradation rate, with a maximum value in the case of the film deposited at 550 °C, which shows 50 % of mineralization after 400 min of UV light exposure. For the film deposited at 540 °C the value is 30 % of mineralization for the same exposition time, and only of 20 % for the film deposited at 500 °C. The k constant for Orange G degradation calculated from the slope with formula IV.2 is given in Table IV- 2. It is important to notice that microflowers were mainly present in samples deposited ant 540 and 550 °C, creating a higher roughness and a higher active surface for chemical exchange or reaction. For films without microflowers deposited at 500 °C and 550 °C, as represented in Figure IV- 8 (2) and table IV-2, the k constant is one order of magnitude lower than films containing microflowers deposited at the same range of temperature.

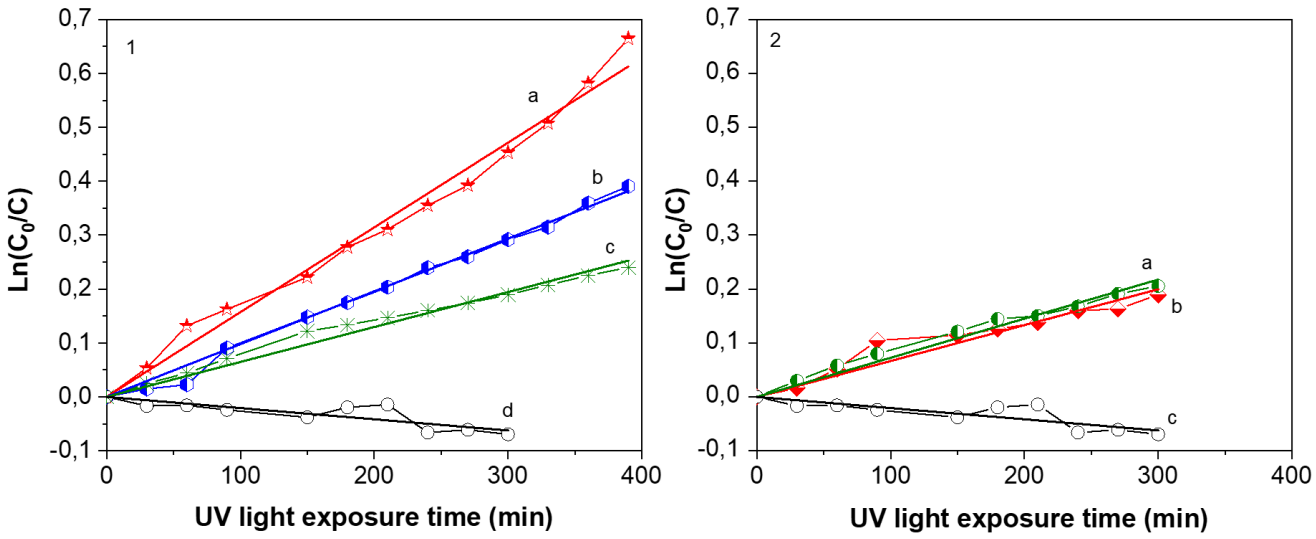

Figure IV- 8. Linear regression of kinetics of orange G degradation by the HSS/Al-Zr/TiO_2 thin films under UV light (371 nm) irradiation: On left, films with microflowers deposited at 1a) 550 °C, 1b) 540 °C, 1c) 500 °C; films without microflowers (on right) deposited at 2a) 500 °C and 2b) 550 °C; and (1d and 2c) Al-Zr films.

Table IV- 2. Constant k (kinetic constant of the system) for HSS/ Al-Zr/ TiO_2 coatings deposited at different temperatures.

Samples with microflowers	Constant k (min^{-1})
Al-Zr/TiO_2 T_{dep}=500°C	0.00063
Al-Zr/TiO_2 T_{dep}=540°C	0.00102
Al-Zr/TiO_2 T_{dep}=550°C	0.00156
Samples without microflowers	Constant k (min^{-1})
Al-Zr/TiO_2 T_{dep}=500°C	0.00066
Al-Zr/TiO_2 T_{dep}=550°C	0.00059

The decomposition rate (DR) was calculated by multiplying the initial concentration of Orange G ($C_0 = 5x10^{-5}$ M) by the constant k. These values are also shown in Table IV- 3 for the Al-Zr/TiO_2 coatings deposited at 500 °C and 550 °C.

Table IV- 3. Effect of presence of microflowers on the decomposition rate of orange G and crystallite size for the TiO_2/Al-Zr coatings deposited at 500°C and 550°C.

Samples with microflowers		
Bilayer films	DR (10^{-10} mol L^{-1} min^{-1})	Crystallite Size (nm)
Al-Zr/TiO_2 T_{dep}=500°C	510	18
Al-Zr/TiO_2 T_{dep}=550°C	780	20
Samples without microflowers		
Al-Zr/TiO_2 T_{dep}=500°C	332	44
Al-Zr/TiO_2 T_{dep}=550°C	297	53

F. Maury et al.[8] reported a maximum DR of Orange G solution (10 ppm) of about 280 X 10^{-10}mol L^{-1} min^{-1} for TiO_2 films deposited at 400 °C by AAMOCVD containing pure anatase phase.

In our work, the increase in decomposition rate from 510 X 10^{-10}mol L^{-1} min^{-1} for the TiO_2/Al-Zr film deposited at 500 °C to 780 X 10^{-10}mol L^{-1} min^{-1} for the sample deposited at 550 °C was observed only for films with microflowers. For samples without flowers, the DR was similar or even lower for the film deposited at the highest temperature 550 °C (297-332 X 10^{-10}mol L^{-1} min^{-1}).

The presence of microflowers and small crystallite size contribute to a large specific surface, which enhances the photocatalytic activity and improves the degradation rate of organic pollutants by multiplying the active sites for absorption in TiO_2 [9,10]. By increasing the surface area, adsorption of the reactants upon the photocatalyst and absorption of the light will increase. This is the double interest of the microflowers activity [11].

IV.5. Wettability of HSS/Al-Zr/TiO_2 bilayer films

The film wettability was evaluated by measuring the contact angle and surface energy with water droplets. These measurements were performed with a goniometer KRÜSS G10 equipped with an image analysis system consisting of a CCD video camera, a card of acquisition connected to a PC computer and DROP SHAPE image processing software ANALYSIS (DSA), represented in Figure IV- 9. This software first determines the baseline of the drop using its reflected mirror image on the surface of the sample, then measures the contact angles of the drop at the intersection with the baseline via the 'Circle fitting' method (Figure IV- 10).

A droplet of distilled water of 0.5 µl volume was placed on the film surface and the first contact angle was measured immediately. The contact angle was measured before and after the incidence of light in the UV-C region used for the evaluation of photocatalytic activities. Each value was an average of 3 measurements on different areas of the sample surface.

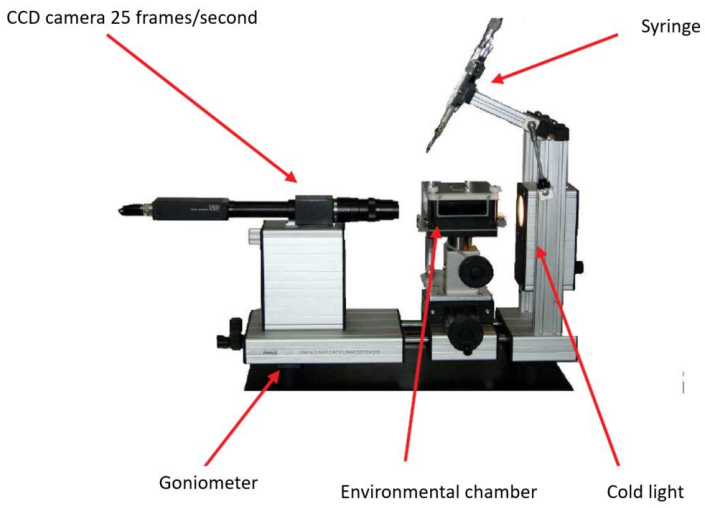

Figure IV- 9. Schematic representation of the contact angle measuring device.

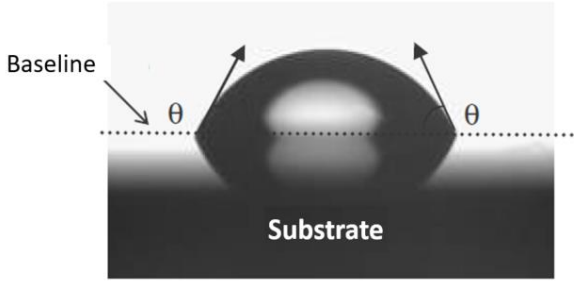

Figure IV- 10. Determination of the contact angle using the DSA software.

Hydrophilicity is usually associated with photocatalytic activity [12]. This property can be enhanced, and even restored, by UV light. The self-cleaning property is directly related to this material ferature[12]. Al-Zr/TiO_2 thin films were irradiated with UV light during 4 hours and the water contact angle was measured at different exposure times. The results are presented in Figure IV- 11. For all samples, the contact angle decreased sharply with the time from about 60° to 0° after 4 hours indicating a photoinduced superhydrophilicity. After six months in the absence of UV irradiation, the samples remained superhydrophilic presenting a contact angle of about 5°, as shown in Figure IV- 12.

For a sample in contact with water, its high photoactivity means that the photogenerated holes attract hydroxyl groups from water and produce hydroxyl radicals (•OH). The higher the number of hydroxyl molecules on the surface, the higher its hydrophilicity is. This is presented as a small contact angle between the water droplet and the TiO_2 surface.

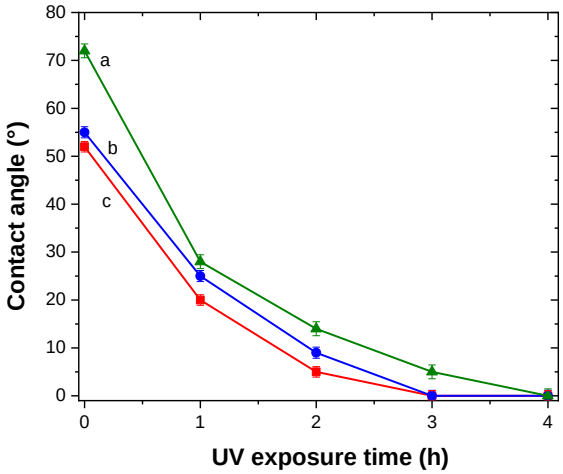

Figure IV- 11. Variation of water contact angles under UV illumination for HSS/Al-Zr/TiO_2 bilayer films with TiO_2 deposited at a) 500°C, b) 540°C and c) 550°C.

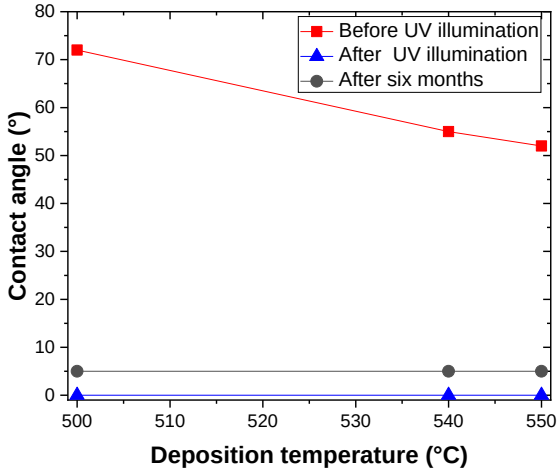

Figure IV- 12. Water contact angles as a function of TiO_2 deposition temperature for HSS/Al-Zr/TiO_2 bilayer films before UV illumination, after UV illumination and after six months without UV illumination.

IV.6. TEM Analysis of HSS/Al-Zr/TiO_2 bilayer films

The equipment used for TEM imaging was a JEM - ARM 200F Cold FEG TEM/STEM operating at 200 kV and equipped with a spherical aberration (Cs) probe and image correctors (point resolution 0.12 nm in TEM mode and 0.078 nm in STEM mode).

Figure IV- 13 shows the microstructure of the TiO_2 layer deposited by AA-MOCVD. The composition appears to be homogeneous (Elemental X-ray X-maps, Figure IV- 14). The electron diffraction pattern confirms that TiO_2 grows with the anatase structure.

X-ray diffraction patterns of as-deposited Al-Zr coatings (4 at.% Zr) and annealed at a temperature of about 550 °C during TiO_2 deposition (Figure II-8 in chapter II) do not show significant change. So, it seems that the structure and microstructure of the Al-Zr layer are stable up to this temperature.

Before the AA-MOCVD process step, the Al-Zr alloy has a columnar microstructure (Figure IV- 15). EDS analysis has shown that zirconium is homogeneously distributed throughout the layer. The columns are approximately 450 nm wide and the growth is not systematically from the interface to the surface of the film. This coating is clearly single-phased; it is an extended supersaturated solid solution of zirconium in aluminum. This solid solution grows without preferential orientation, which is not surprising for an aluminum coating deposited at low temperature without bias.

After the AA-MOCVD process step at substrates temperature of about 550 °C, the Al-Zr coating has a different microstructure (Figure IV- 14a, b). Indeed, dark precipitates appear clearly in the Bright field scanning transmission electron microscopy (STEM BF, Figure IV- 14 a)

Scanning-mode transmission electron microscopy coupled to a High-Angle Annular Dark-Field Detector (STEM-HAADF), due to the dependence of signal strength with Z, increases the contrast between phases with different atomic numbers. Figure IV- 14a, b confirm that these precipitates are richer in zirconium than the matrix. These precipitates have essentially two morphologies; rod and spherical. The spherical ones crystallize mainly at the solid solution grains boundaries. EDS analyzes have shown that the zirconium content of these precipitates is in the range 15.0 to 17.5 at. %. The compound with the highest aluminum content in the phase diagram is Al_3Zr. Its stable structure is of type DO_{23} (Figure IV- 16).

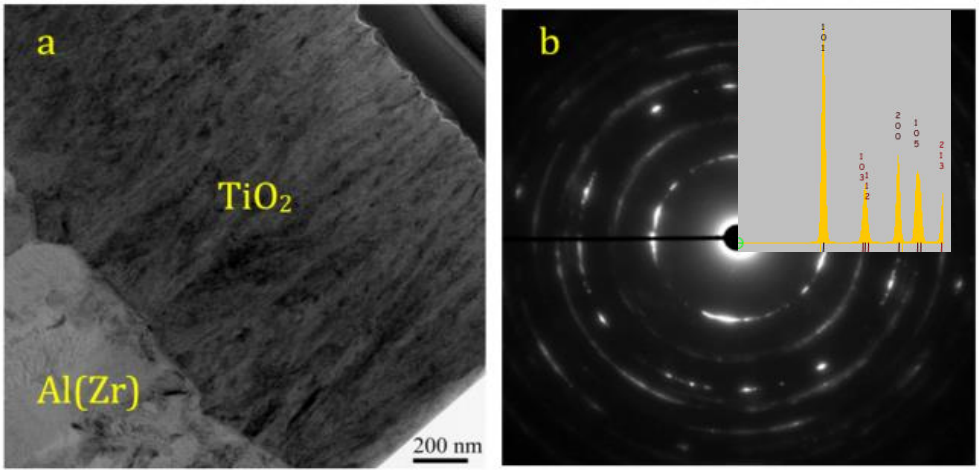

Figure IV- 13.TEM Bright field (a) and SAED (b, anatase TiO_2) of TiO_2 layer deposited on the Al-Zr coating.

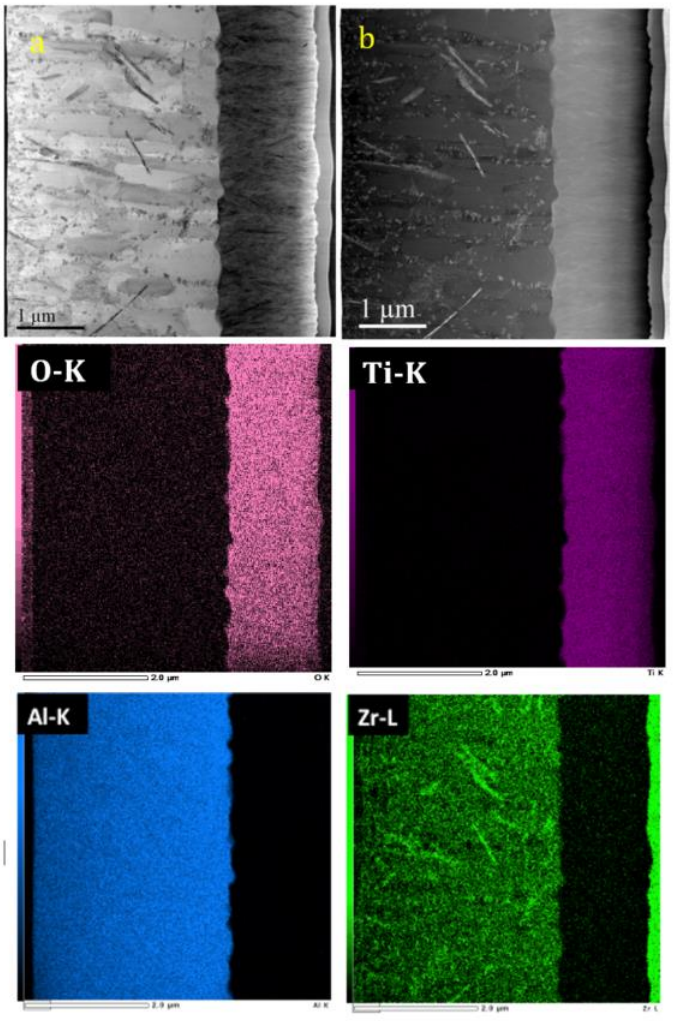

Figure IV- 14. STEM bright field (a); STEM HAADF (b) images and associated X-maps of HSS/Al-Zr /TiO_2 bilayer.

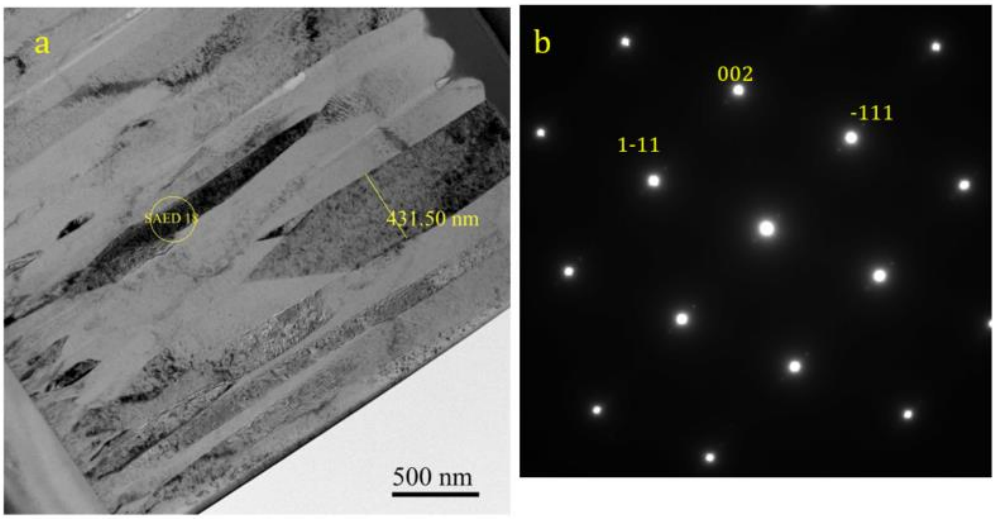

Figure IV- 15. TEM Bright field (a) and SAED (b, [110] zone axis) of Al-Zr layer deposited before AA-MOCVD process (before annealing).

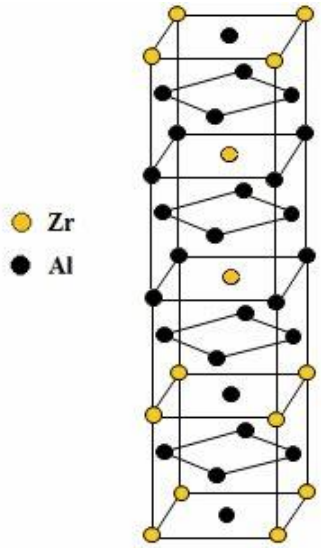

Figure IV- 16. Unit cell of $D0_{23}$ type for Al_3Zr.

The DO_{23} structure has a parameter a = 4.001 Å [13] to be compared with a = 4.032 Å for Al and a ratio of tetragonality c/a = 4.31. Because of this ratio c/a significantly higher than 4, such an Al_3Zr coherent precipitate with the aluminum matrix will therefore be subjected to high elastic stresses. This makes it unlikely to precipitate this structure in the Al-Zr coating.

The Al_3Zr compound also has an ordered metastable structure based on FCC cell but which has the symmetries of a simple cubic; the $L1_2$ type structure (Figure IV- 17). The parameter of this phase is very close to that of aluminum; a = 4.093 Å. The elastic effects related to the coherence

of the small precipitates with the low zirconium-loaded matrix are therefore weak and we should rather expect the precipitation of metastable Al_3Zr.

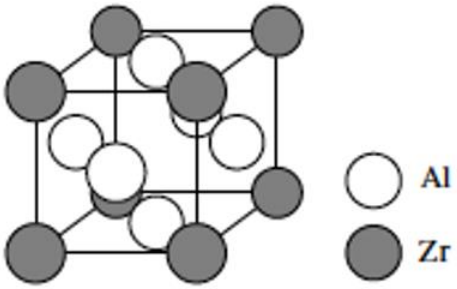

Figure IV- 17. Unit cell of $L1_2$ type for Al_3Zr.

Figure IV- 18 shows the TEM bright field images and selected area electron diffraction (SAED) patterns corresponding to zone axis [110]. The structure is clearly biphased; an FCC solid solution of zirconium in aluminum and an ordered Al_3Zr compound of $L1_2$ type, which confirms the hypothesis of the precipitation of this ordered metastable phase.

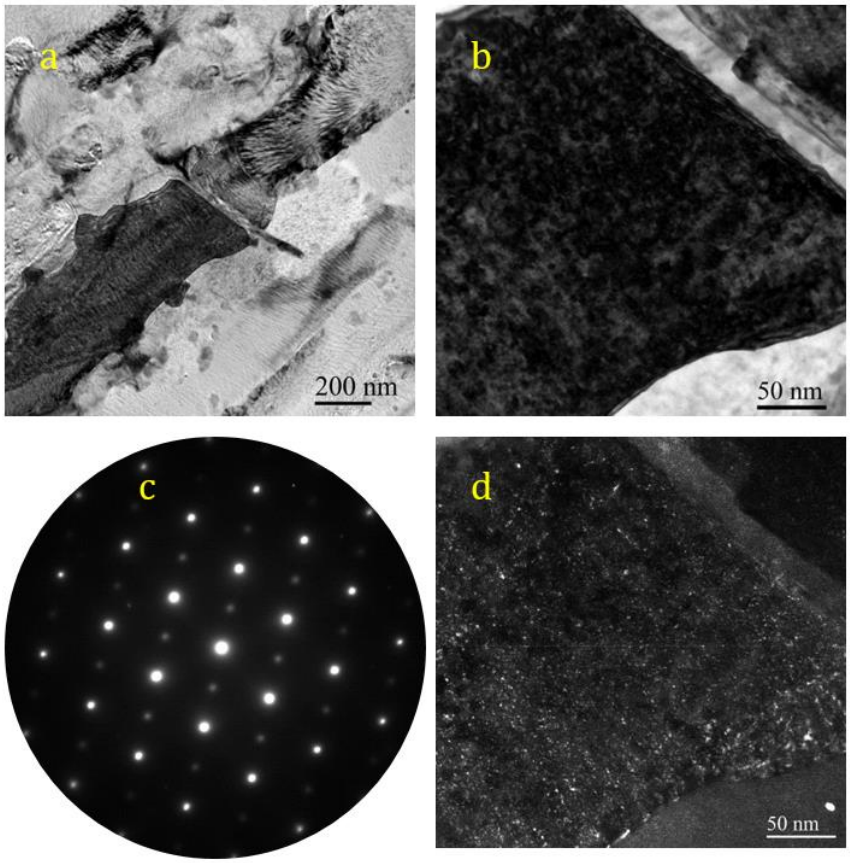

Figure IV- 18. TEM bright field (a, b zoomed) images, associated SAED pattern with the [110] zone axis (c) and darkfield (d) obtained from sport corresponding to Al_3Zr precipitates.

Figure IV- 19 clearly confirms that $L1_2$ type ordered Al_3Zr precipitates are fine coherency with the Al(Zr) solid solution matrix in cube on cube relationship with $[100]_{Al3Zr}$ // $[100]_{Al(Zr)}$, $[010]_{Al3Zr}$ // $[010]_{Al(Zr)}$ and $[001]_{Al3Zr}$ // $[001]_{Al(Zr)}$.

Precipitation of this metastable phase has already been observed in conventional alloys after annealing at temperatures below 500 °C[14–16] while annealing at higher temperatures can lead to the precipitation of the stable phase [17,18]. These precipitates have either a spherical or rod shape. Image obtained by high resolution STEM-HAADF (Figure IV- 20) shows the coherent interfaces, with adaptation of the parameter between the supersaturated solid solution matrix of Zr in Al, and the Al_3Zr precipitates with higher zirconium content. There is a very small difference in the parameter between the f.c.c. aluminum matrix and the f.c.c. L12-type Al_3Zr compound; and since the mismatch is slight, the $L1_2$-type compounds form coherent precipitates [19].

Scully et al. reported that these particles is an important grain refiner in commercial structural Al base alloys and presents a minimal impact on corrosion properties [20].

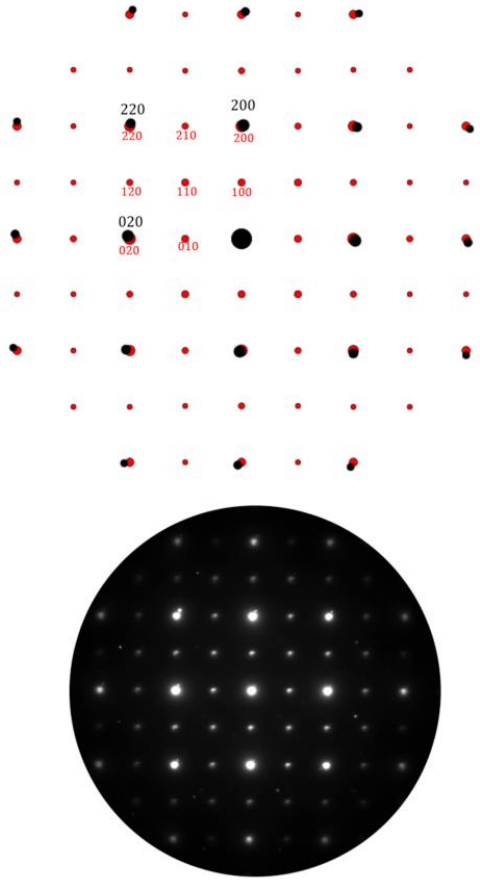

Figure IV- 19. Model (red: Al_3Zr and black: Al(Zr)) and SAED diffraction pattern of Al-Zr after AA-MOCVD process for TiO_2 deposition (after annealing). $[001]_{Al3Zr}$ // $[001]_{Al(Zr)}$.

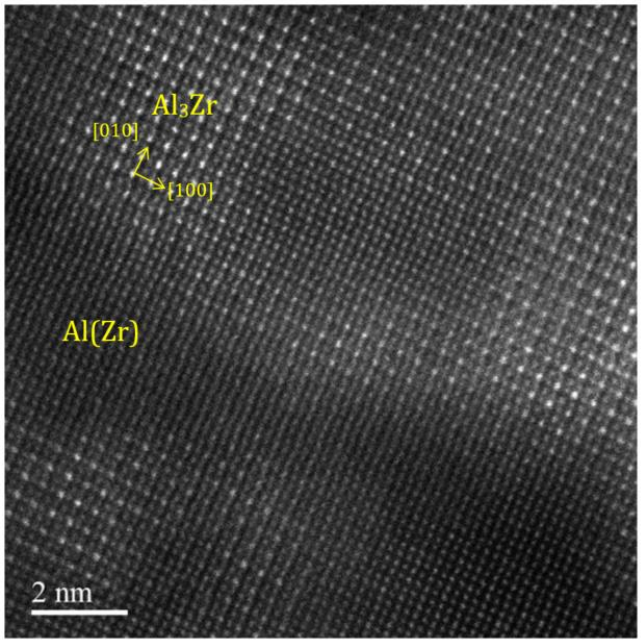

Figure IV- 20. High resolution STEM-HAADF of Al-Zr coating after AA-MOCVD process for TiO_2 deposition (after annealing).

IV.7. Electrochemical tests

The electrochemical measurements were carried out in an aerated and stirred chlorine solution (5 wt. % NaCl solution) in a polarization cell with a total volume of 200 mL, as represented in Figure IV- 21. The measurements were made using an Autolab potentiostat driven by NOVA 2.0 software.

A polarization cell was composed of an electrolyte solution, a reference electrode, a counter electrode and the metallic sample placed with a sample holder. The sample presented the working electrode and the other electrodes were connected to an electronic instrument named a potentiostat. The working reference and counting electrodes were located in the electrolyte solution, normally a solution that most closely represents the real application environment of the material being analysed. In the solution, an electrochemical potential (voltage) was produced between the various electrodes.

In this work, the pH of the solution was adjusted to 6 by addition of 0.5 M HCl solution and each measurement was performed at room temperature. The potentials were referenced against an Ag/AgCl electrode and the counter electrode was a large platinum grid. The effective area of

working electrode was 1.327 cm2. The polarisation curves were recorded in the potential range of ±150 mV around the open circuit potential (OCP) with a scan rate of 0.2 mV/s after 1 h of immersion in the saline solution. The corrosion potential E_{corr} and corrosion current density I_{corr} were estimated from the cross-over point of the two tangents drawn on linear portion of anodic and cathodic polarization curves. The evolution of Open Circuit Potential was recorded during 1 h.

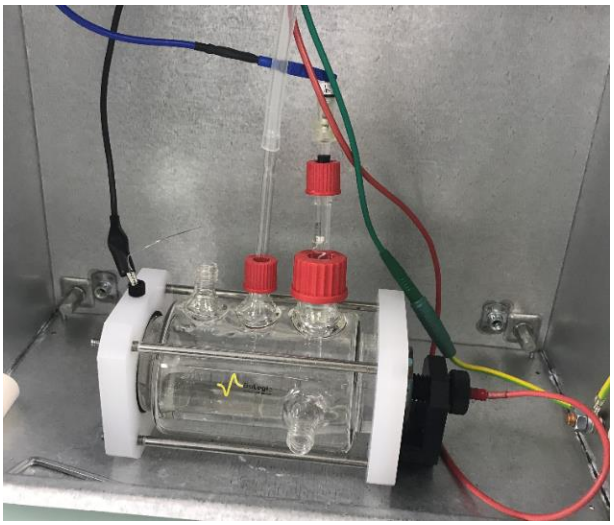

Figure IV- 21. Schema of polarization cell used for electrochemical measurements.

In this work, Al-Zr films containing 4 at. % Zr were deposited on HSS substrate where this composition has shown the best compromise between mechanical properties, electrochemical behavior and sacrificial character, as explained before in chapter II.

Figure IV- 22 shows the evolution of the open circuit potential (*OCP*) versus time during 1h of immersion in 5 wt.% NaCl for different samples: HSS, HSS/Al-Zr, HSS/TiO_2, and the HSS/Al-Zr/TiO_2. The steel OCP was reported as a reference. The steel OCP rapidly decreased and then stabilized at around -0.55 V/Ag-AgCl. This evolution is typical for the progressive formation of iron based corrosion products on the steel surface[21]. The TiO_2 coated steel presents a quite similar *OCP* evolution during the immersion suggesting that this evolution is directly related to the steel degradation through the open defects of the oxide film. However, the OCP values are nobler in presence of the titanium oxide layer. Ramaprakash et al.[22] also observed a slight ennoblement of the steel corrosion potential when is covered with TiO_2 in 3.5% NaCl solution. This ennoblement

was attributed to the modification of the electronic charge transfer during the steel dissolution due to the presence of the oxide film.

The OCP of the Al-Zr coating is quite constant during the immersion at around -0.62 V/Ag-AgCl, which seems to be closed to the pitting potential as mentioned in [23] for similar Al based coatings in saline solution. The OCP of HSS/Al-Zr/TiO_2 bilayer coating is also quite constant during the immersion at around – 0.69 V/Ag-AgCl, which is slightly more negative compared with the Al-Zr coating. The shift of the OCP towards more negative values was also reported by Dias et al. on TiO_2 thin films deposited by atomic layer deposition on Al-Mn alloys[24].

The OCP measurements prove that Al-Zr and HSS/Al-Zr/TiO_2 bilayer coatings keep the sacrificial character. It seems that the presence of the TiO_2 coatings acts differently when is deposited on steel or aluminium based materials. This could be due to the intrinsic properties of the titanium oxide film [11].

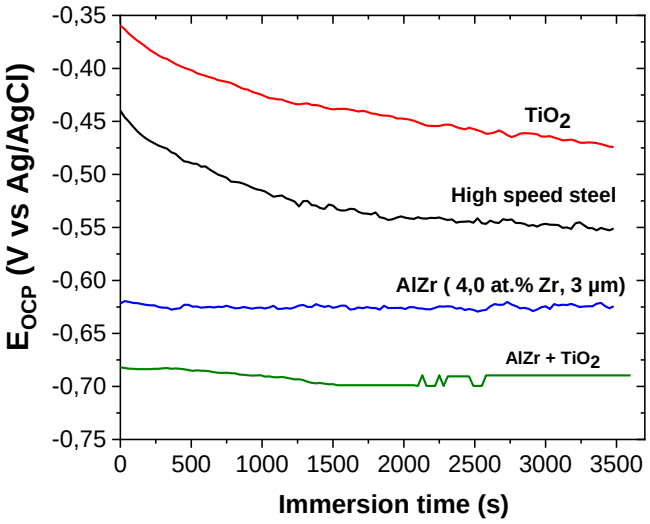

Figure IV- 22. OCP evolution of steel coated with Al-Zr (4 at. % Zr), TiO_2 and Al-Zr/TiO_2 bilayer films vs immersion time in 5 wt.% NaCl.

The polarization curves of the coated steels with Al-Zr, TiO_2 and Al-Zr/TiO_2 are presented in Figure IV- 23 and compared with the bare steel. Corrosion potential (E_{corr}) and corrosion current density (I_{corr}) were determined from the polarization curves by imposing a straight line along the linear portion of the anodic and cathodic curve and extrapolate it through E_{corr}. Table IV. 4 presents the corrosion current density and corrosion potential values extracted from the potentiodynamic test for all the samples.

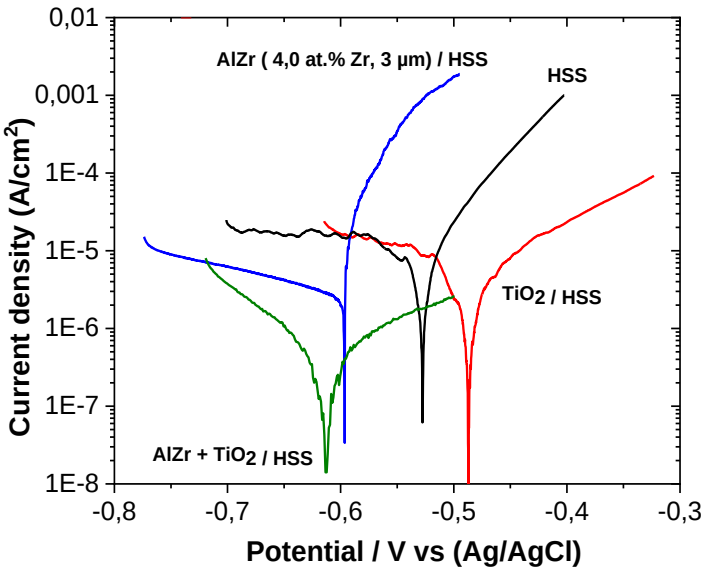

Figure IV- 23. Polarisation curves of Al-Zr (4 at. % Zr), TiO_2 and Al-Zr/TiO_2 bilayer films deposited on HSS after 1h of immersion in 5 wt. % NaCl.

Table IV. 4. I_{corr} and E_{corr} values for Al-Zr, TiO_2, Al-Zr/TiO_2 films and HSS substrate.

Samples	I_{corr} (µA/cm^2)	E_{corr} (V /(Ag/AgCl))
HSS substrate	18	-0.52
HSS/TiO_2	9.25	-0.48
HSS/Al-Zr (4 at.% Zr)	2.49	- 0.59
HSS/Al-Zr/TiO_2	0.41	-0.61

The corrosion potential of the bare steel after one hour of immersion in stirred saline solution was around -0.52 V vs Ag/AgCl. A diffusional plateau is observed in the cathodic domain corresponding to the dioxygen reduction and a uniform corrosion is observed in the anodic domain. The TiO_2 film induces a shift of the corrosion potential towards more positive values as observed by Ramaprakash et al. [22]. The cathodic branch is not affected by the presence of the titanium oxide film, whereas the steel dissolution mechanism is modified. The anodic slope is decreased suggesting that the oxide film affect the charge transfer reactions during the steel dissolution.

Al-Zr coating presents a corrosion potential at around -0.59V vs Ag/AgCl which is slightly more negative compared to the HSS substrate. The anodic polarisation curve presents a sudden rise in

current close to the corrosion potential corresponding to the initiation of pitting corrosion as presented by Juan Creus et al. [23]. We can notice that the initiation of the pitting corrosion occurs at a potential value that is close to the corrosion potential.

The polarization curve for the bilayer coated sample (HSS/Al-Zr/TiO_2) is quite different from the other configurations. The influence of the TiO_2 film on the corrosion behavior is different from HSS and Al-Zr material, probably due to the fact that steel suffers from a uniform corrosion whereas pitting corrosion is the main degradation observed on Al-Zr coating. The oxide film affects the cathodic domain with an increase of the cathodic reaction slope associated to the dioxygen reduction suggesting that the charge transfer reaction is slow down. The TiO_2 film permits to reduce the contribution of the cathodic reactions leading to the decrease of the corrosion current density, down to 4.1 X 10^{-7} A/cm^2. As observed for the Al-Zr coating, the pitting corrosion occurs at potential values very close to the corrosion potential, but in the bilayer coating, we can suppose that the pit initiation is mainly localised at the oxide film defects. An important decrease of the anodic reaction kinetics is observed and probably due to the increase of the surface impedance associated to the TiO_2 layer. So the pit propagation seems to be reduced in presence of the oxide film.

The optical observations of the corroded surfaces of the coated samples after the potentiodynamic polarization tests are presented in Figure IV- 24. It shows that the mean pit diameter decreases when TiO_2 is added as a second layer. It suggests that the TiO_2 coating impedes the growth of pits. It seems that the TiO_2 layer is able to increase the pitting resistance because of the low cathodic reaction kinetics.

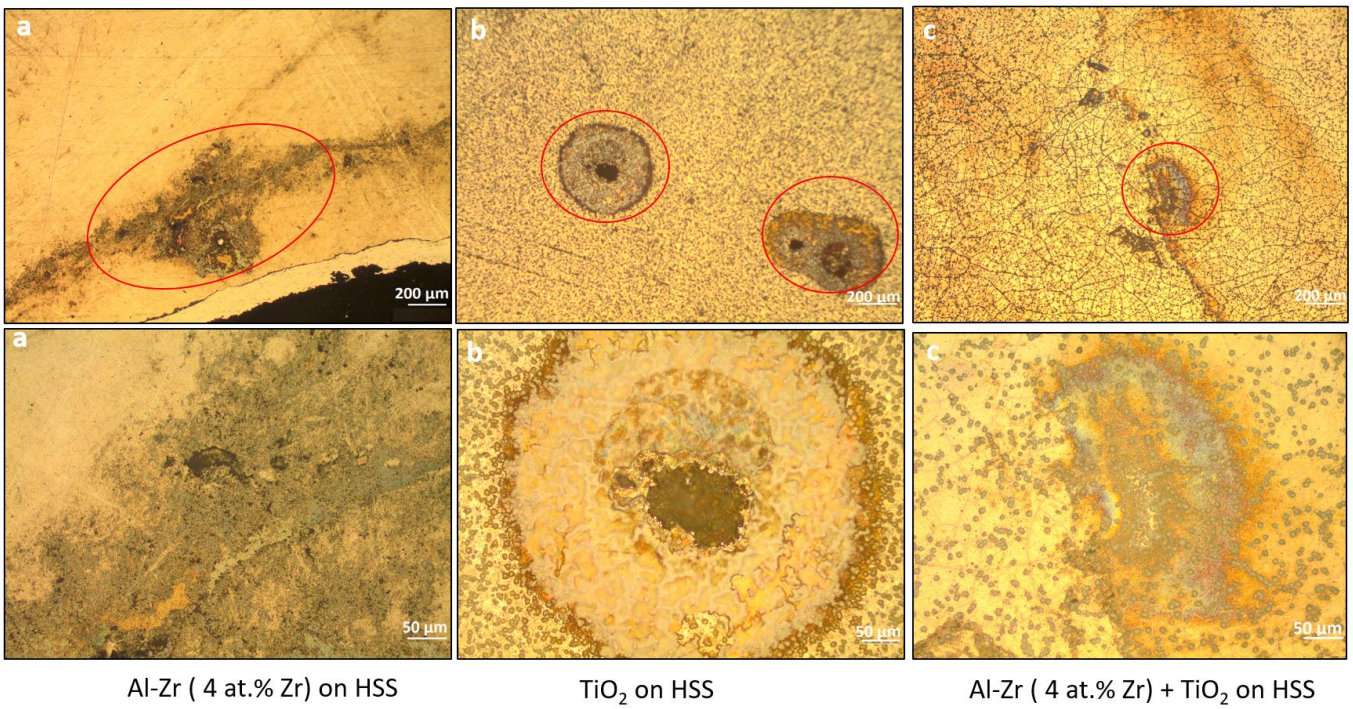

Figure IV- 24. Optical micrographs of pits formed on a) Al-Zr (4 at.% Zr), b) TiO_2 and c) Al-Zr/TiO_2 bilayer films deposited on HSS after 1h of immersion in 5 wt.% NaCl.

IV.8. Conclusions

The potential functionality of HSS/Al-Zr/TiO_2 bilayer coating combining anticorrosion and photocatalysis properties was tested using High speed steel (HSS) substrates. The Al-Zr thin films containing a saturated solid solution with 4 at. % Zr were deposited on HSS substrates by DC magnetron sputtering. Then, TiO_2 coatings were deposited by Aerosol Assisted CVD in optimised conditions to grow a microstructure characterised by the presence of TiO_2 microflowers physically attached to the TiO_2 thin film. Optimal growth conditions were obtained by the combination of deposition temperature, precursor concentration and precursor feeding rate. XRD and Raman spectroscopy confirm that TiO_2 microflowers and thin film reveal anatase phase. The presence of TiO_2 microflowers having a size of about 7 µm and a crystallite size of 20 nm plays a crucial role in photocalysis of Orange G compound. This behaviour was enhanced on TiO_2 samples deposited at 550 °C, showing a higher decomposition rate of Orange G (780 X 10^{-10} mol L^{-1} min^{-1}) under UV light when compared to other films deposited at lower deposition temperatures (500 and 540 °C). This study confirms the fundamental role of roughness and superhydrophilicity on the

photocatalysis process and encourage the application of TiO_2 nano-coatings for the fabrication of components to avoid algal adhesion on underwater structures.

TEM analysis revealed that after the AA-MOCVD process step at 550 °C, Al-Zr (4 at.% Zr) presented precipitates, which are richer in zirconium than the matrix. EDS analyzes have shown that the zirconium content of these precipitates is in the range 15.0 to 17.5 at. %. The structure formed after deposition at 550°C is clearly biphased ; an FCC solid solution of zirconium in aluminum and an ordered metastable Al_3Zr compound.

Finally, HSS/Al-Zr/TiO_2 bilayer coatings were found to be an interesting alternative to preserve sacrificial character for the protection of steel structures in saline environment, showing a corrosion potential of – 0.61 V vs Ag/AgCl. Al-Zr/TiO_2 bilayer coatings deposited on steel substrates offer good protection through the preferential oxidation of the bilayer presenting a lower corrosion current density of 4.01 X 10^{-7} A/cm^2. TiO_2 as a second layer reduces the electrochemical activity of the films through the formation of a dense passive film, and also increases the pitting resistance when the cathodic reaction kinetics is lower.

References

[1] S.M. Gerchakov, B. Sallman, Biofouling and Effects of Organic Compounds and Microorganisms on Corrosion Processes., 1977.

[2] A. Mollica, Biofilm and corrosion on active-passive alloys in seawater, Int. Biodeterior. Biodegrad. 29 (1992) 213–229. doi:10.1016/0964-8305(92)90045-P.

[3] C.E. Zobell, E.C. Allen, The Significance of Marine Bacteria in the Fouling of Submerged Surfaces., J. Bacteriol. 29 (1935) 239–51.

[4] M.E. Callow, R.L. Fletcher, The influence of low surface energy materials on bioadhesion — a review, Int. Biodeterior. Biodegradation. 34 (1994) 333–348. doi:10.1016/0964-8305(94)90092-2.

[5] B46.1-1995 Surface Texture—Surface Roughness, Waviness, and Lay; The American Society of Mechanical Engineers: New York, NY, USA, 1995.

[6] Y.-S. Jung, K.-H. Kim, T.-Y. Jang, Y. Tak, S.-H. Baeck, Enhancement of photocatalytic properties of Cr2O3–TiO2 mixed oxides prepared by sol–gel method, Curr. Appl. Phys. 11 (2011) 358–361. doi:10.1016/J.CAP.2010.08.001.

[7] G. Busca, G. Ramis, J.M.G. Amores, V.S. Escribano, P. Piaggio, FT Raman and FTIR studies of titanias and metatitanate powders, J. Chem. Soc.{,} Faraday Trans. 90 (1994) 3181–3190. doi:10.1039/FT9949003181.

[8] F. Duminica, F. Maury, R. Hausbrand, Growth of TiO2 thin films by AP-MOCVD on stainless steel substrates for photocatalytic applications, 201 (2007) 9304–9308. doi:10.1016/j.surfcoat.2007.04.011.

[9] D.S. Kim, S.J. Han, S.-Y. Kwak, Synthesis and photocatalytic activity of mesoporous TiO2 with the surface area, crystallite size, and pore size, J. Colloid Interface Sci. 316 (2007) 85–91. doi:10.1016/J.JCIS.2007.07.037.

[10] A.R. Liu, S.M. Wang, Y.R. Zhao, Z. Zheng, Low-temperature preparation of nanocrystalline TiO2 photocatalyst with a very large specific surface area, Mater. Chem. Phys. 99 (2006) 131–134. doi:10.1016/J.MATCHEMPHYS.2005.10.003.

[11] C.V. De Oliveira, A. Alhussein, J. Creus, F. Schuster, Bifunctional TiO2 / AlZr Thin Films on Steel Substrate Combining Corrosion Resistance and Photocatalytic Properties, (2019) 1–16. doi:10.3390/coatings9090564.

[12] S. Anandan, T. Narasinga Rao, M. Sathish, D. Rangappa, I. Honma, M. Miyauchi, c, ACS Appl. Mater. Interfaces. 5 (2013) 207–212. doi:10.1021/am302557z.

[13] C. Amador, J.J. Hoyt, B.C. Chakoumakos, D. De Fontaine, Theoretical and Experimental Study of Relaxations in Al3Ti and Al3Zr Ordered Phases, Phys. Rev. Lett. 74 (1995) 4955.

[14] E.T. Recristallisation, U.N. Alliage, I.N. Einer, Precipitation and recrystallization, (1969).

[15] K.S. Vecchio, D.B Williams, Convergent beam electron diffraction study of Al3Zr in Al-Zr and Al-Li-Zr alloys, Acta metallurgica 35 (1987).

[16] E. Clouet, Séparation de phase dans les alliages Al-Zr-Sc: du saut des atomes à la croissance de précipités ordonnés, Ecole Centrale Paris, 2004.

[17] K.E. Knipling, D.C. Dunand, D.N. Seidman, Precipitation evolution in Al-Zr and Al-Zr-Ti alloys during aging at 450-600°C, Acta Mater. 56 (2008) 1182–1195. doi:10.1016/j.actamat.2007.11.011.

[18] K.E. Knipling, D.C. Dunand, D.N. Seidman, Precipitation evolution in Al-Zr and Al-Zr-Ti alloys during isothermal aging at 375-425 °C, Acta Mater. 56 (2008) 114–127. doi:10.1016/j.actamat.2007.09.004.

[19] A. V. Mikhaylovskaya, A.G. Mochugovskiy, V.S. Levchenko, N.Y. Tabachkova, W. Mufalo, V.K. Portnoy, Precipitation behavior of L12 Al3Zr phase in Al-Mg-Zr alloy, Mater. Charact. 139 (2018) 30–37. doi:10.1016/j.matchar.2018.02.030.

[20] J.R. Scully, T.O. Knight, R.G. Buchheit, D.E. Peebles, Electrochemical characteristics of

the Al2Cu, Al3Ta and Al3Zr intermetallic phases and their relevancy to the localized corrosion of Al alloys, Corros. Sci. 35 (1993) 185–195. doi:10.1016/0010-938X(93)90148-A.

[21] J. Creus, H. Idrissi, H. Mazille, Galvanic corrosion behaviour of mild steel, Al, and Ti in 3%NaCl solution: application to PVD coatings on steel substrate, Surf. Eng. 13 (1997) 415–419. doi:10.1179/sur.1997.13.5.415.

[22] M. Ramaprakash, G. Sreedhar, S. Mohan, S.K. Panda, Corrosion protection studies of CeO2–TiO2 nanocomposite coatings on mild steel, Trans. IMF. 94 (2016) 254–258. doi:10.1080/00202967.2016.1209892.

[23] J. Creus, C. Berziou, S. Cohendoz, A. Perez, C. Rébéré, M. Reffass, S. Touzain, C. Allely, Y. Gachon, C. Héau, F. Sanchette, A. Billard, Reactivity classification in saline solution of magnetron sputtered or EBPVD pure metallic, nitride and Al-based alloy coatings, Corros. Sci. 57 (2012) 162–173. doi:10.1016/j.corsci.2011.12.021.

[24] V. Dias, H. Maciel, M. Fraga, A.O. Lobo, R. Pessoa, F.R. Marciano, Atomic layer deposited TiO2 and Al2O3 thin films as coatings for aluminum food packaging application, Materials (Basel). 12 (2019). doi:10.3390/ma12040682.

Chapter V: New Cu-Ti-O films for photocatalysis and antibiofouling applications

In order to improve the characteristic properties of wide band gap semiconductor, the incorporation of transition metals is an efficient method. Consequently, several studies have been directly concerned in doping with the transition metals (Mn, Ni, Cu, Fe) to improve and control the characteristic properties of TiO_2 films [1,2].

Zhang et al. [3] reported that the substitution of Ti^{4+} by Cu^{2+}/Cu^{1+} in the TiO_2 lattice induces the creation of oxygen vacancies and additional impurity band that results in a significant reduction of both band gap and recombination rate of photo electron-hole pair. Thus, photocatalytic performance and the ability of visible light absorption of TiO_2 have been improved.

Indeed, most single phase materials do not meet all the requirements to be an efficient visible-light-active photocatalysts, comprising high surface area for adsorption of targeted species, high conductivity, long-charge lifetimes, direct pathways to carry photogenerated charge, and good chemical stability in water. Mixed phase or doped materials, tough, present higher charge separation at the interfaces leading to higher photocatalytic activities and have begun to attract greater attention as visible light-active photocatalysts [4][5].

For environmental recovery and solar-energy conversion applications, TiO_2 and Cu_xO mixtures reveal great potential, in part as a result of their low toxicity but also in lieu of their suitable energy band positions [6].

In this chapter the influence of incorporation of high contents of copper into TiO_2 thin films on structural, optical, photocatalytic activity and antibiofouling properties of TiO_2 thin films is proposed as new Cu-Ti-O films. Cu-Ti-O films with different Cu contents were deposited by aerosol-assisted metalorganic chemical vapor deposition using the same parameters used for depositing pure TiO_2 films as presented in chapter III.

The properties of the compounds obtained were evaluated by measurements of X-ray diffraction (XRD), Raman spectroscopy, X-ray Photoelectron Spectroscopy, UV-vis spectrometry, Transmission and Scanning Electron Microscopy, and Photocatalytic degradation of Orange G. Marine biofouling field test were carried out in Lorient's Harbor in France in order to evaluate the antifouling performance of the coatings.

V.1. AAMOCVD parameters and preparation of starting precursor solutions

V.1.1. Preparation of starting precursor solutions

The preliminary step in the deposition process is the preparation of the solution. The precursor chosen for copper deposition was Cu(II) acetylacetonate (Cu(AcAc)2) (98%, STREM Chemicals). This precursor has been already used in LMGP for Cu_2O films deposition by AACVD [7]. Starting

solutions with a concentration of 0.01 M and 0.03 M were prepared by adding 1.3 g and 3.9 g of precursor respectively, in 500 ml of absolute ethanol followed by a constant stirring. Since $Cu(AcAc)_2$ has low solubility in alcohol solvents, ethylendiamine was added to increase the solubility, at a double concentration in relation with the total molar concentration of precursors[8]. In our case, at least 0.01 M ethylene diamine (99%, Sigma Aldrich) was added as dispersant (2.5 ml of ethylene diamine for 500 ml of 0.01 M solution). The solution became dark blue right after addition the dispersant, as represented in Figure V- 1. After adding ethylendiamine, the solution was stirred with speed of 300 cycle/min until complete dissolution. The temperature of the solution is also increased to 50 ºC to promote the precursor dissolution. The stirring lasted 15 hours until a homogenously solution was obtained.

The precursor molecule structure is shown below:

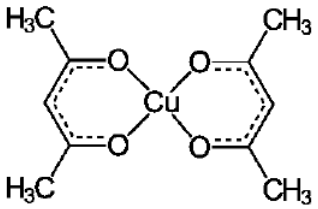

The $Cu(II)(AcAc)_2$ prepared solutions was then mixed with a $Ti(IV)O(AcAc)_2$ solutions at a concentration of 0.03 M in ethanol, prepared as explained in chapter III. In this way, we obtained two different cation concentration starting solutions in ethanol: Solution I) a solution of 0.01M of Cu and 0.03 M of Ti, Solution II) 0.03 M of Cu and 0.03 M of Ti. The mixture was stirred until complete mixing using a magnetic bar with speed 300 cycle/min at room temperature. After 3 hours the solution was ready for deposition.

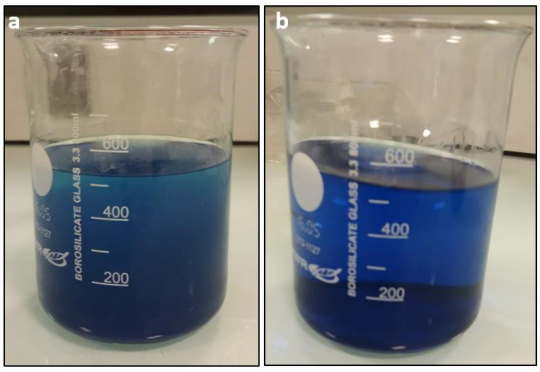

Figure V- 1 Effect of the addition of the dispersant in the $Cu(acac)_2$ solution a) before and b) after addition.

V.1.2. Deposition conditions

The substrates used for depositing copper-titanium oxide films were (100)-oriented silicon single crystal and alkaline earth boroaluminosilicate glass (reference Corning C1737-S111). In some experiments, Al-Zr on HSS (d= 30 mm) were also used as substrates. Substrates were cut with a diamond pen into squares with size of about 1.5 x 5 cm^2 and 5 x 5 cm^2 and washed in an ethanol solution with ultrasounds for 10 minutes, rinsed with deionized water and dried with N_2 flow.

The substrate deposition temperature was fixed at 550 °C with a deposition time of 40 minutes. In this work, an extraction pressure of 3mm of H_2O was used in order to homogenize the air in the deposition chamber. As explained in chapter III, air as carrier gas #2 was introduced with flow rate of 3 L/min and, consequently, when temperature reaches the set point, air as carrier gas #1 was introduced with flow rate 3 L/ min. Once precursor flow achieves the heating place the timer can be set.

The analysis of the microstructure and chemical composition of Cu-Ti-O films deposited by aerosol-assisted CVD using the two starting solutions were performed by scanning electron microscope SEM in a FEI Quanta 250 MEB FEG ESEM tool. Energy dispersive spectroscopy (EDS) analysis was conducted in order to investigate the chemical composition of the sample at the microscopic scale.

Table V. 1 shows the at.% Cu in film measured by EDS for films deposited on silicon, corning glass and Al-Zr coated high speed steel using the two different solutions.

One mean value of Cu content is given in Table V. 1 for each substrate for samples deposited using solution 1 and solution 2.

For Cu-Ti-O films deposited using the lowest Cu concentration (solution 1), the Cu content in film is 16 at.% Cu for films deposited on Si and corning glass substrates. This solution leads to reproducible films from run to run.

For Cu-Ti-O films deposited using the highest Cu concentration (solution 2), the film composition are less reproducible. Three runs were performed from the same solution and films present a Cu content that varies between 50 and 66 at.% Cu for films deposited on silicon, between 50 and 75 at.% Cu for films deposited on corning glass and between 25 and 50 at.% Cu for Al-Zr coated high speed steel (HSS). Figure V- 2 a) presents the evolution of the amount of copper on

the film with the percentage of copper in solution. Figure V- 2 b) exhibits the evolution of film thickness when the concentration of copper increases. The evolution is clearly not linear.

Table V. 1. Cu-Ti-O films deposited on silicon, corning glass and Al-Zr coated high speed steel measured by EDS for $Ti(AcAc)_2$ solutions mixed with $Cu(AcAc)_2$ at a concentration of 0.01M or 0.03 M.

Solutions	% Cu in solution	Cu/(Cu/Ti) for films deposited on Si (at.%)	Cu/(Cu/Ti) for films deposited on Corning glass (at.%)	Cu/(Cu/Ti)for films deposited on Al-Zr coated HSS (at.%)
Solution 1 Ti(AcAc)2 **0.03 M** + Cu(AcAc)2 **0.01 M**	33	16	16	-
		Name:CuTiO16S	**Name:CuTiO16C**	
Solution 2 Ti(AcAc)2 **0.03 M** + Cu(AcAc)2 **0.03 M**	50	50	50	25
		Name:CuTiO50S	**Name:CuTiO50C**	**Name:CuTiO25A**
		55	58	50
		Name:CuTiO55S	**Name:CuTiO58C**	**Name:CuTiO50A**
		66	75	-
		Name:CuTiO66S	**Name:CuTiO75C**	

Since our films are not homogenous in thickness, an average thickness is calculated using cross section SEM images for all the films deposited on silicon presenting a percentage error of +- 10 %. Films containing 55 at.% Cu shows the maximum thickness of 500 nm for a deposition time of 40 minutes. Secondly, pure TiO_2 films presented the smallest thickness presenting an average thickness of about 300 nm. This can be explained because the Ti solution has a molar concentration of 0.03 M, lower than mixed solutions.

It is important to emphasise that the molar concentration is not the same in the two mixed solutions since solution 1 has a total of 0.04 M and solution 2 has a total of 0.06 M. The total molar concentration does not seem to have influence on the deposition rate of films.

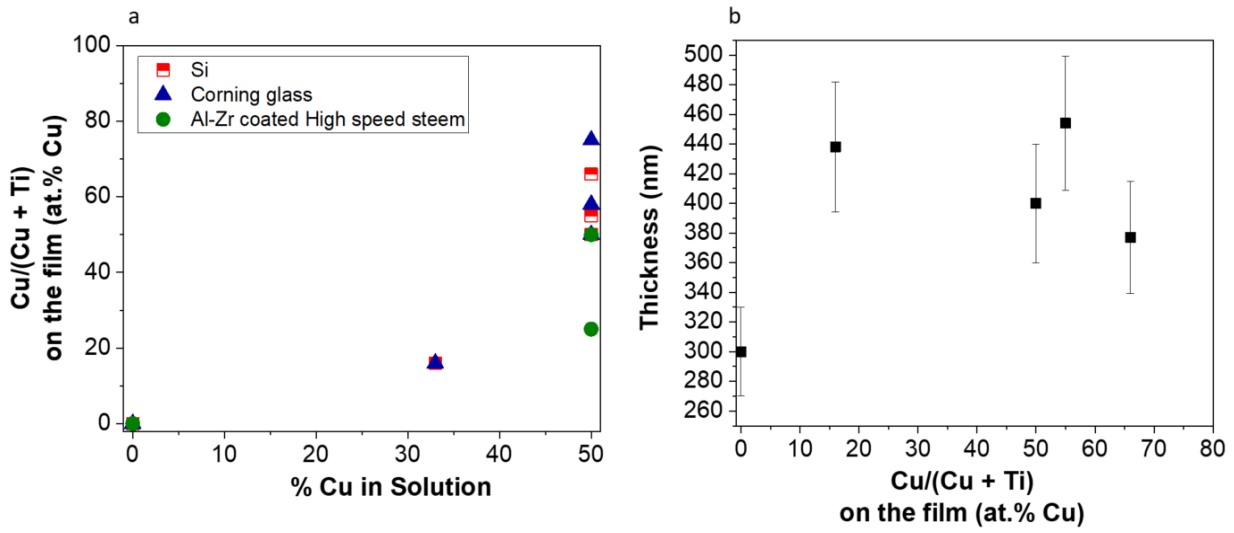

Figure V- 2. a) Evolution of at.% Cu on the film with the % of Cu in solution for the three substrates. b) Evolution of film thickness measured on silicon with at.% Cu.

V.2. Morphological characterization

The microstructure morphology of Cu-Ti-O films deposited on silicon and glass observed by SEM is shown in Figure V- 3. Figure V- 3 a) presents pure TiO_2 films containing the typical microflowers. Morphology is rather different for films containing copper in their composition and microflowers are no longer presented. When at.% Cu increases, the morphology becomes granular and rough as represent in Figure V- 3 b, c, d, e and f. The same feature is noticed for Cu-Ti-O films deposited on silicon, corning glass and on Al-Zr coated high speed steel substrate (Figure V- 4). No significant influence of the substrate was found on the morphology of these Cu-Ti-O films.

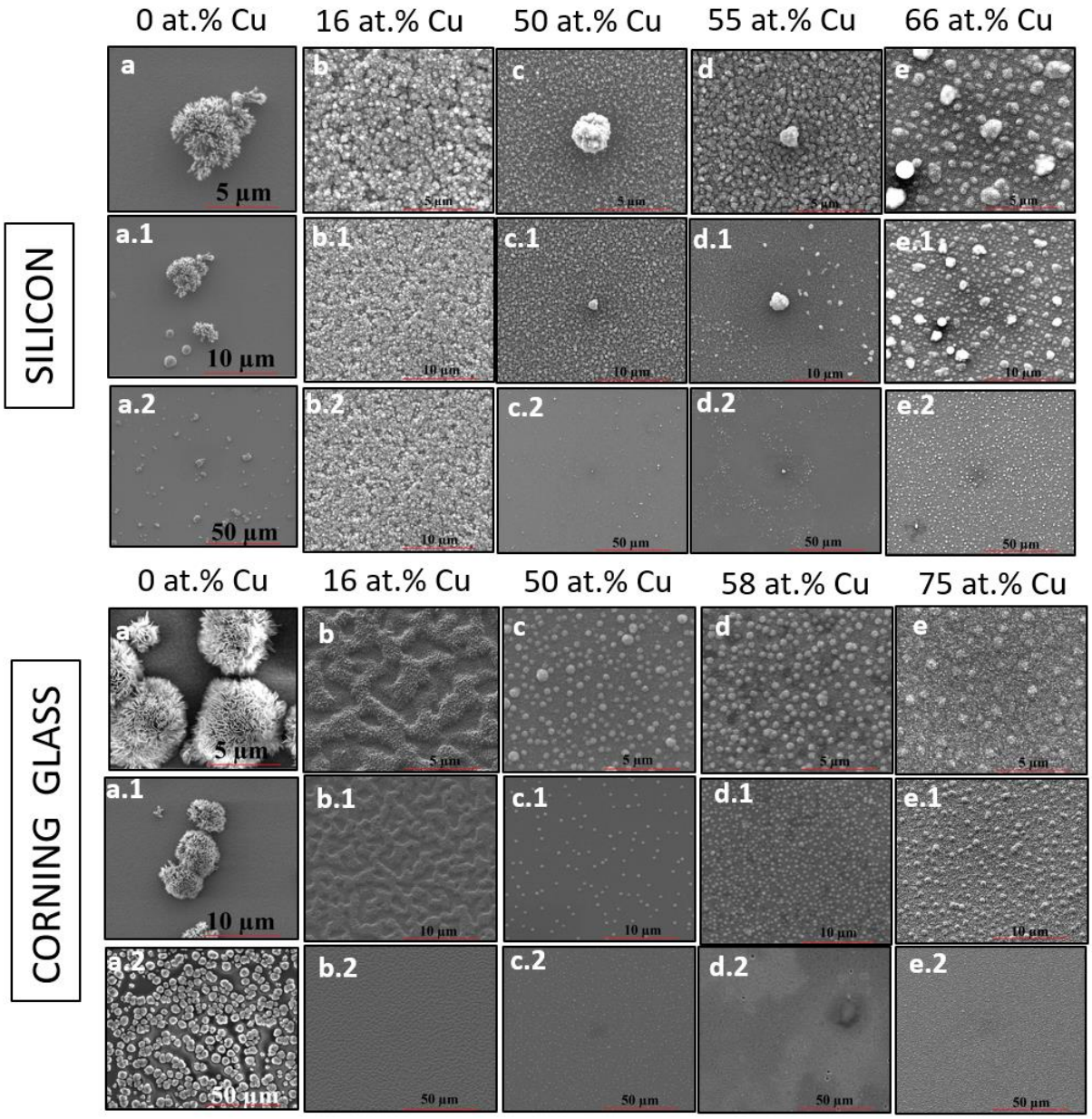

Figure V- 3. SEM images of microstructures corresponding to a) pure TiO_2 film, b) Cu-Ti-O - 16 at.% Cu film c) Cu-Ti-O - 50 at.% Cu film d) Cu-Ti-O – 55 / 58 at.% Cu film and e) Cu-Ti-O – 66 / 75 at.% Cu film deposited by AA-MOCVD on silicon and corning glass substrates.

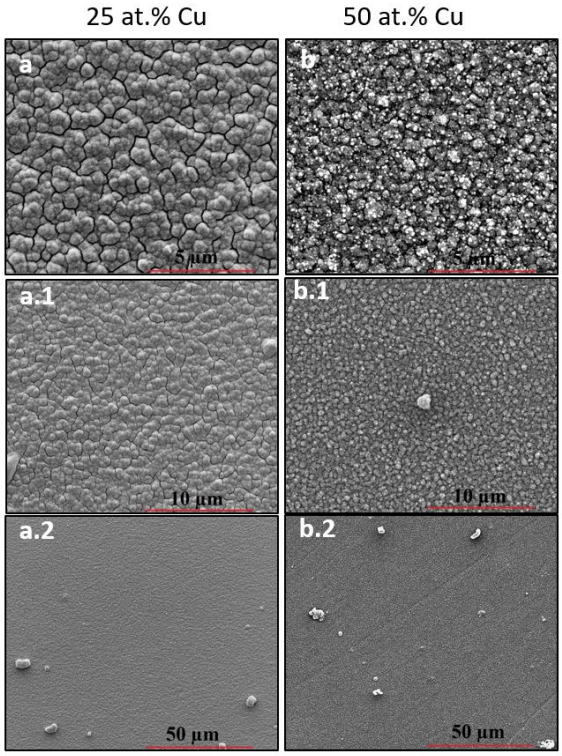

Figure V- 4. SEM images of a) Cu-Ti-O - 25 at.% Cu film and b) Cu-Ti-O - 50 at.% Cu film deposited on Al-Zr coated high speed steel substrate.

In the group of microscopy analysis, another technique used in this work was atomic force microscopy to measure the roughness of the samples. The analysis was performed in Veeco D3100 AFM with 5µm x 5µm images. Cu-Ti-O films deposited on corning glass were also characterized by AFM, which allows to quantify the roughness through the root-mean-square (RMS) of height deviation, visible in Table V. 2. This quantitative technique agrees with the SEM observation indicating higher roughness with the increase of Cu content. The images of the AFM are represented in Figure V- 5.

Table V. 2. Roughness of Cu-Ti-O thin films.

at.% Cu	R_{RMS} (nm)
16	23.77
58	30.30
75	36.90

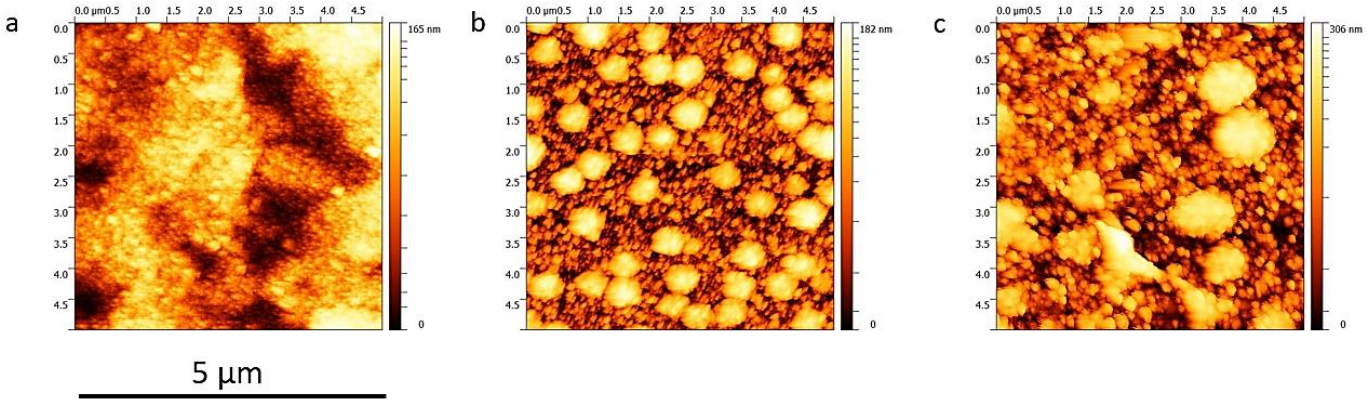

Figure V- 5. AFM images 5µmx5µm of the Cu-Ti-O films – a) CuTiO16C, b) CuTiO58C and c) CuTiO75C.

V.3. Structural properties

Wang et al. have pointed out that the addition of high concentration Cu to TiO_2 causes to phase transformation from anatase to rutile at low temperature [9]. Horzum et al. investigated the effect of Cu incorporation at a high concentration (up to 50 wt %) on the properties of TiO_2 films. They showed that Cu is incorporated homogeneously into the TiO_2 matrix until 12.5 wt% . On the other hand, for 25 wt% and 50 wt% Cu-incorporated films presented CuO in its composition [10]. Celik et al. identified the presence of anatase TiO_2, CuO, Cu_4Ti, Cu_3TiO_4 and Ti_3O_5 phases for Cu-doped TiO_2 films [11]. Saha et al. revealed the presence of anatase TiO_2 and Cu_3TiO_4 phases for a Cu-Ti composite oxide catalyst [12].

V.3.1. X-Ray Diffraction (XRD) analysis

The XRD patterns of TiO_2 film and Cu-Ti-O films with various at.% Cu were acquired using X-ray diffraction (XRD) in θ–2θ scanning mode using a Bragg–Brentano configuration between 10° and 80° at 0.011° intervals with an acquisition time of 2 s using a Bruker D8 Advance diffractometer with monochromatic CuKα1 radiation (λ = 0.15406 nm). The results are represented in Figure V- 6 a) for corning substrate and in Figure V- 7 a) for silicon. To have an increased sensibility to secondary phases, GIXRD was performed on Cu-Ti-O films and the diffraction patterns are shown in Figure V- 6 b) and Figure V- 7 b). GIXRD patterns were acquired with a Bruker C40 D8 with incidence and exit angles maintained around 0.5°. All samples exhibits diffraction peaks for the TiO_2 anatase phase. TiO_2 diffraction peaks are in agreement with JCPDS

Card No.21-1272 [13]. The presence of Cu_2O is confirmed in films presenting at.% Cu higher or equal to 50 % and diffraction peaks are in agreement with JCPDS card No. 05-0667. A small amount of CuO is detected for films deposited on both substrates for Cu content equal or higher to 50 %. This phase is particularly visible in the GIXRD diagrams, presenting CuO peaks corresponding to the crystal planes (-1 1 1) and (1 1 1) at $2\theta = 35.55°$ and 38.75° (JCPDS card No.07-1375). No other secondary phase were found in the diffraction diagrams at any composition.

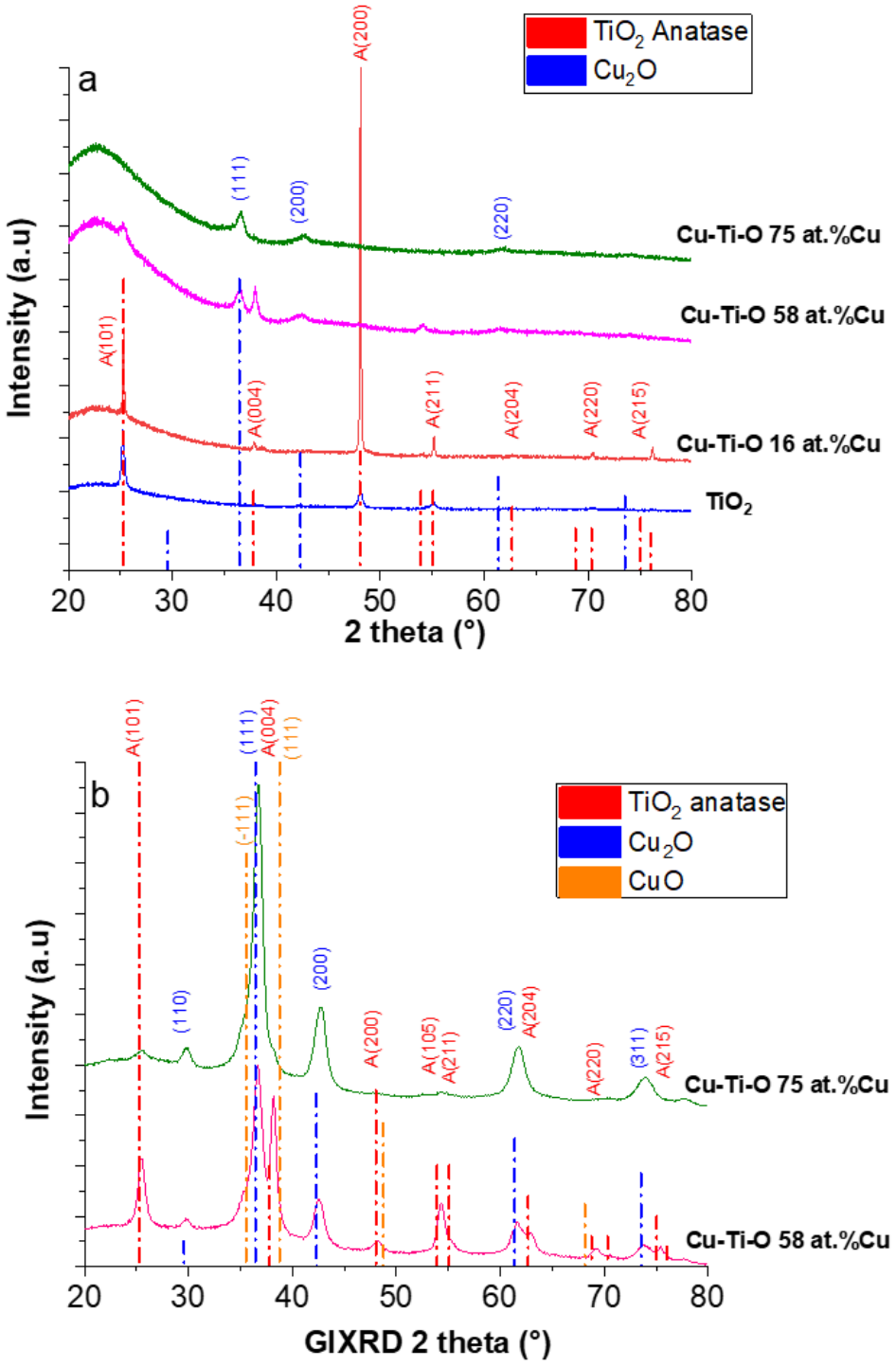

Figure V- 6. XRD diagrams of TiO_2 and Cu-Ti-O films deposited on corning glass substrates at 550°C obtained. a) in a Bragg-Brentano configuration and b) in GI-XRD configuration.

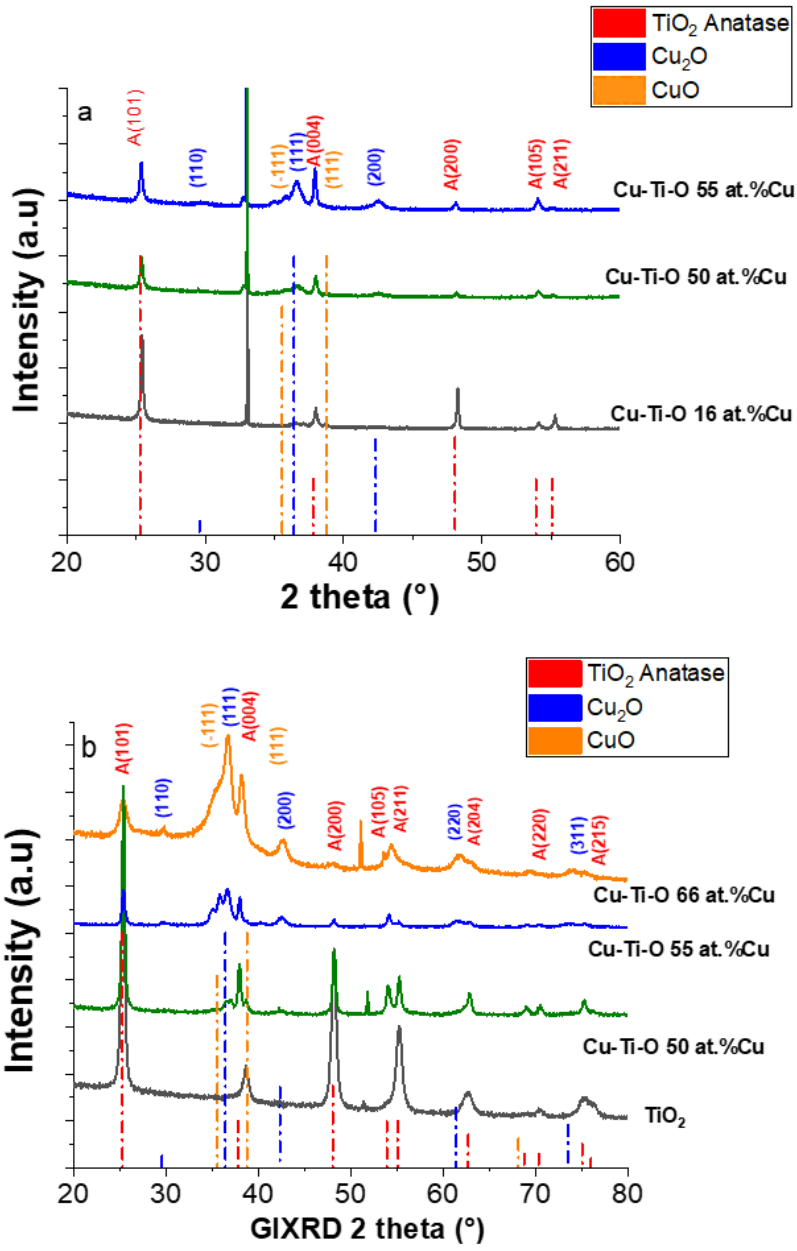

Figure V- 7. XRD diagrams of TiO_2 and Cu-Ti-O films deposited on silicon substrate at 550°C obtained. a) in a Bragg-Brentano configuration and b) in GI-XRD configuration.

V.3.2. Raman Spectroscopy analysis

Raman spectroscopy was used to clarify the early stage of phase transformation in these sets of samples. This technique is complementary to XRD analysis, but allows for a more local analysis. Raman spectra of as-deposited Cu-Ti-O thin films are represented in Figure V- 8 a), Figure V- 8 b), and Figure V- 8 c) for films deposited on corning glass, silicon and Al-Zr coated substrates, respectively.

The prominent Raman peaks observed for all samples at 144, 400, 519 and 639 cm^{-1} are related to typical anatase phase of TiO_2 as already presented in Chapter III. These peaks correspond to following Raman vibration modes: E_g modes at 143 and 639 cm^{-1}, B_{1g} mode at 400 cm^{-1} and overlapped A_{1g} and B_{1g} modes at 519 cm^{-1}. The anatase phase of Cu-Ti -O films is retained well by the incorporation of Cu in the films.

Besides, Raman spectroscopy confirmed the formation of the Cu_2O phase based on the presence of standard associated modes, which were detected in all films with at.% Cu greater than 50 as represented in Figure V- 8. Several vibrational active modes of Cu_2O are identified: $(T_{2u}) \sim 88$ cm^{-1}, $(E_u) \sim 106$ cm^{-1}, $(T_{1u}) \sim 148$ cm^{-1}, $(2E_u) \sim 215$ cm^{-1} and $(T_{1u}) \sim 625$ cm^{-1}[14].

Finally, CuO phase are barely detected for Cu-Ti-O films with at.% Cu greater than 50, independently of the substrate. 298 cm^{-1} (A_g), 346 cm^{-1} (B_g) and 632 cm^{-1} (B_g) modes are presented for this films [15,16].

Films deposited with a mixed solution of Ti and Cu are mainly constituted of TiO_2 and Cu_2O. However, as observed in Figure V- 8 a) and Figure V- 8 b), the intensity of the anatase peaks decreased and broadened for films containing more than 50 % of Cu, which indicates an increment in structural disorder [9].

The incorporation of Cu distorts the lattice structure of TiO_2 since the ionic radius of Cu^+ (0.77 Å) is slightly larger than that of Ti^{+4} (0.68 Å). Furthermore, because of the charge difference between Cu^+ and Ti^{+4}, the addition of Cu^+ into the TiO_2 matrix creates the oxygen vacancies to protect the charge neutrality in the lattice [14] and the higher concentration of Cu^+ compose more oxygen vacancies in the TiO_2 lattice. Since these oxygen vacancies are formed, the lattice distorts and the all Raman peaks shift and broaden, with increasing Cu content.

An extra peak is observed at 755 cm^{-1} for Cu-Ti-O films with a Cu content greater than 16 at.% Cu for films deposited on silicon substrate and greater than 50 at.% Cu for films deposited on Al-Zr coated high speed steel substrate and corning glass substrates.

To evaluate if this band appears only for thick films, we characterized by Raman spectroscopy a big sample of CuTiO58C film. As can be seen in Figure V- 9, the sample presents an inhomogeneous thickness. Nevertheless, the composition was confirmed at each point by EDS. The spectra obtained at the defined points are represented in the figure, and all of them are similar. The presence of TiO_2, Cu_2O and CuO bands are confirmed in all measured regions together with the absorption band at 755 cm^{-1}. We can infer that this band is not thickness dependent.

One hypothesis is that this extra peak existed with high Cu concentration can be related to A_{2u} IR active mode of anatase TiO_2 [17,18]. In our case, the A_{2u} mode (755 cm^{-1}) of anatase is more prominent when the Cu content increases. Thus frequency band corresponds to the longitudinal optical (LO) phonons. There are six Raman active modes (A_{1g} +$2B_{1g}$ +3_{Eg}) and three IR active modes (A_{2u} + $2E_u$) for anatase TiO_2. The Eg Raman modes originate from oxygen vibrations. According to M. Grujić-Brojčin et al. [18], the additional modes can be understood in terms of IR-forbidden modes [19], since the oscillator frequencies are very similar to the two strongest Eg modes in the Raman spectrum of anatase TiO_2. In our case, the addition of Cu^+ could remove the neutrality of charges in the E_g vibrational modes, causing a slight lattice distortion and appearance of IR-forbidden modes.

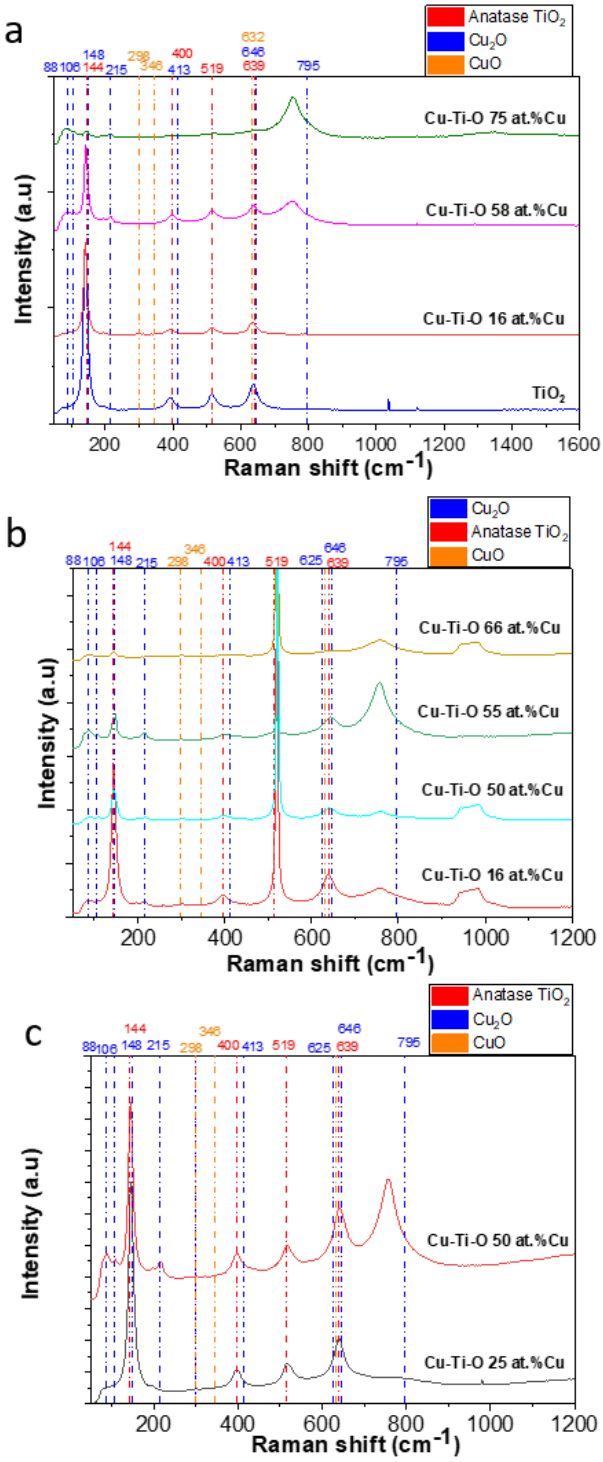

Figure V- 8. Raman spectra for Cu-Ti-O films deposited by aerosol CVD at 550°C on a) Corning glass substrate, b) Silicon substrate and c) Al-Zr coated high speed steel.

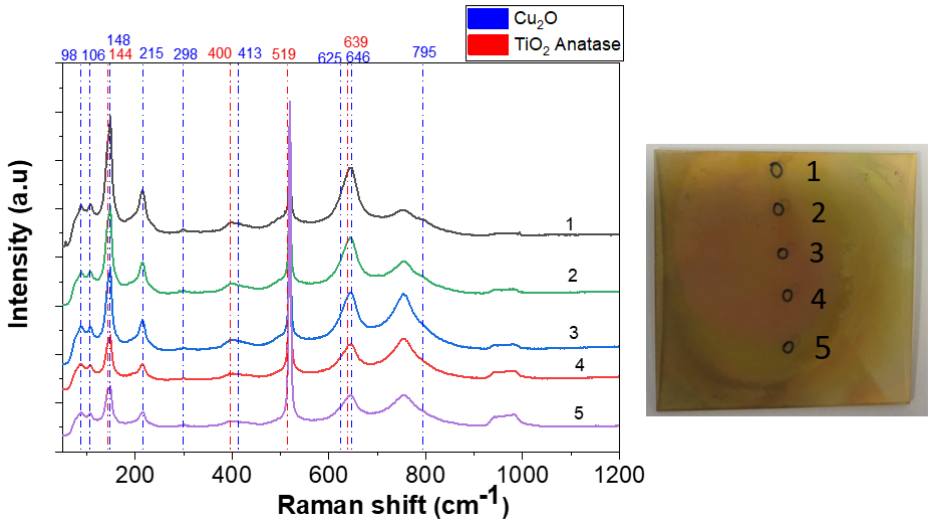

Figure V- 9. Raman spectra for CuTiO50C film measured at different points on the film surface, described on the picture on the right.

V.4. Fourier transform infrared spectroscopy (FTIR)

FTIR was used as a complementary technique to Raman, and was performed on films deposited on silicon substrates which are transparent in the Mean infrared region (MIR). The absorption spectra obtained after subtraction of silicon substrate signal are shown in Figure V- 10. The bands presented at 420 cm^{-1} and 270 cm^{-1} correspond to Ti-O bonds. These bands are characteristics of the anatase phase at 262 cm^{-1}, 435 cm^{-1} [20]. When increasing Cu content, the intensity of these bands decreases and a new band at 618 cm^{-1} appears, which corresponds to the stretching band of Cu_2O. For the highest Cu contents a band at 500 cm^{-1} corresponds to the phonon spectrum of CuO [21].

FTIR results confirm XRD interpretation that Cu-Ti-O films are composed of a mixing of TiO_2 and Cu_2O, and CuO for higher Cu contents. However, the band detected by Raman spectroscopy at 755 cm^{-1} and attributed to a FTIR forbidden band could not be confirmed in these spectra.

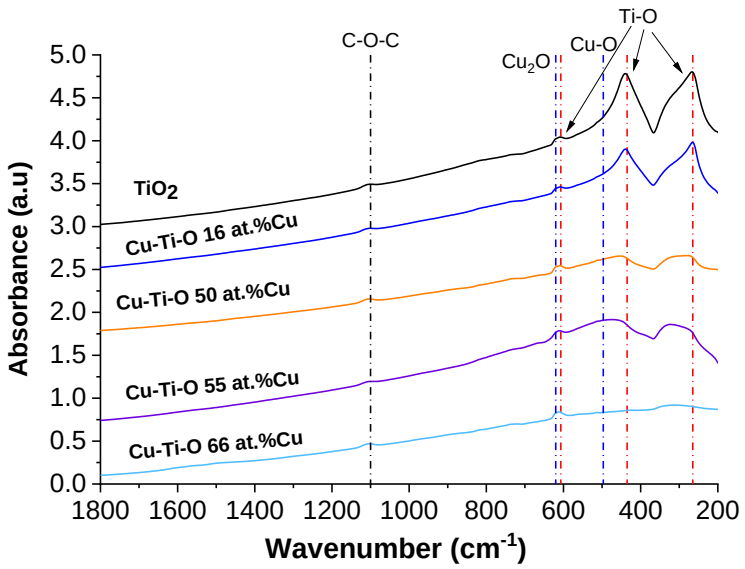

Figure V- 10. FTIR spectra of TiO_2 film and Cu-Ti-O films deposited on silicon substrate at 550°C.

V.5. UV-VIS-IR transmittance

The optical properties of the Cu-Ti-O films deposited on corning glass at 550 °C were determined by UV-Visible-Near Infrared spectrometry. These measurements were carried out in a Lambda 950 spectrophotometer from Perkin Elmer in the range of 250 nm to 2500 nm working in transmission mode. Figure V- 11 a) presents the total transmission spectra obtained for pure TiO_2, CuTiO16C and CuTiO75C films using an integrating sphere.

It is seen that for pure TiO_2 film as being colorless and transparent, the absorption starts at 390 nm in the UV-region. As the Cu atom is incorporated into the films, the color becomes darker, transmittance decreases and the absorption edge shifts to visible region.

The pure TiO_2 thin film is transparent to visible light with an expected band gap energy of 3.2 eV [22] , thus enabling the absorption of only UV light with the wavelengths shorter than 390 nm. When adding Cu in the film, a striking change is observed in the UV–vis absorption spectra of the Cu-Ti-O films. The absorption band of the Cu-Ti-O films shifted to longer wavelength region in visible light. It can be seen that the steep absorption edges shifted to the visible region obviously as the at.% Cu increases, which indicates a narrowing in the optical band gap. This behavior is correlated to the formation of Cu_2O with an indirect gap energy of 2.17 eV [23].

The spectra were employed to calculate the band gap by tracing the Tauc plot using the equation: $(\alpha hv)^n = A(hv - E_g)$ V-1 [24].

where α is the absorption coefficient, hv is the photon energy (eV), A is the proportionality constant, Eg (band gap energy) while n stands for the type of transition, which may be direct or indirect. In this case, the transition was indirect and as such n = 2. The bandgap of Cu-Ti-O films deposited on corning glass was determined by calculating the value of the intercept of the straight line at α = 0, as deduced from the Tauc plot of $(\alpha hv)^2$ versus photon energy . The Tauc representation and curves fittings are shown in Figure V- 11 b).

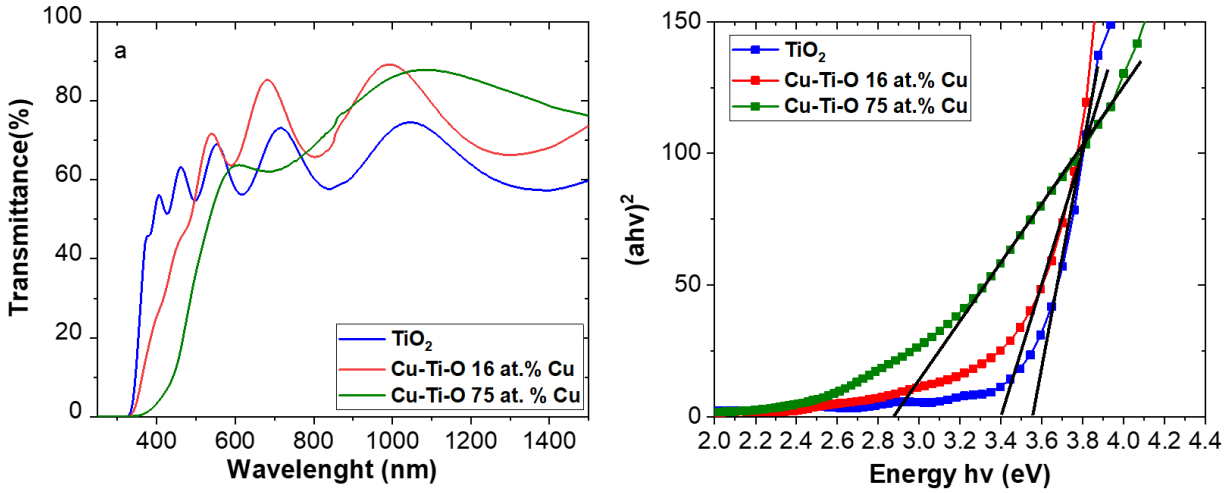

Figure V- 11. a) Total transmittance of TiO_2 and Cu-Ti-O films deposited at 550C° on corning glass substrate. b) Optical band gap calculated using Tauc plot of pure TiO_2 and Cu-Ti-O films.

We obtained a gap energy of 3.55 eV for pure TiO_2. The optical band gap energy shifted toward a visible regime with increasing Cu content, being of 3.4 eV for CuTiO16C and 2.88 eV for CuTiO75C. This last value is still higher than values reported for Cu_2O films, probably to the effect of TiO_2 mixing structure. Navas et al.[25] reported greater band gap reduction with increases in copper concentration due to the covalent character of the Cu-O interaction leading to new states at the valence band maximum.

V.6. X-ray Photoelectron Spectroscopy (XPS)

XPS is chemical sensible method widely used to study the composition and the oxidation state of elements at the surfaces, probing the top 10 nm of a film. The surface of the as-deposited films deposited by AAMOCVD at 550°C on silicon substrate were investigated by XPS in order to determine the possible changes induced in Ti oxidation state by the Cu incorporation in the film, together with the determination of the Cu oxidation state.

XPS (X-ray Photoelectron Spectroscopy) analyses were carried out in Thermo Scientific™ K-Alpha™ XPS spectrometer. Sample surfaces were irradiated with Al Kα radiation at 15 kV for a current of 20 mA. To correct for any charging effect, all the binding energies were calibrated to the C-C component of the C1s core spectrum at 285.0 eV. Peak deconvolutions were performed using ThermoAvantage software using Gaussian-Lorentzian functions

The energy windows used for the analyses of the elements were 448 - 475 eV for Ti2p, 925-965 eV for Cu2p, 525 - 545 for O1s, and 279 - 298 eV for C1s. The XPS spectra for three compositions are presented Figure V- 12. The samples are pure TiO_2, CuTiO50S and CuTiO66S.

The $Ti2p_{1/2}$ and $Ti2p_{3/2}$ spectra were analysed using two components at binding energy of 464.7 eV and 459 eV, respectively, with a separation of 5.7 eV between the two peaks. These energy values were close to those reported in the literature for the TiO_2 films at 458.9 and 464.6 eV [26]. When adding Cu to the films the area of the Ti2p components decrease and the FWHM values slightly increases, but not shift in energy is detected. We can so deduce that the oxidation state of Ti doesn't change with Cu incorporation and the Ti is in the Ti^{4+}state [27,28].

The O1s spectrum (second column in Figure V- 12) shows a main peak at 530.3 eV, indicating Ti−O and Cu−O bonds , and a second component at 531.7 eV could be ascribed to hydroxyl groups on the surface [28]. The intensity of the main peak, and so the total intensity of the O1s band, decreases with Cu content. This can be explained by the decrease in the oxygen ration when replacing TiO_2 by Cu_2O.

Concerning Cu2p spectra presented in the third columns of Figure V- 12, any curve is presented for the pure TiO_2 sample because, as expected, Cu signal was not detected. The main issue in the Cu2p spectra is the absence of satellites around 945 eV, which are the signature of the CuO presence. The main peak in the $Cu2p_{3/2}$ band is located at 933 eV, attributed to reduced copper species, Cu^{1+}or Cu^0 [29]. In our case, taking into account the phase identification by other techniques, we can assume that this peak is related to Cu^{+1}. The intensity of the Cu2p peak increases

when at.% Cu is increased from 50 to 67 % Cu, but the formation of Cu2p satellites is only distinguished for the highest Cu content. As the presence of CuO was detected by Raman and XRD; we can infer that the CuO formation takes place inside the film and not essentially at the surface.

C1s bands are characteristics of surface contamination, mainly C=C at 285 eV, and small contribution around 289 eV is also detected, attributed to C=O or C-O ligands, but not specific trends were found with Cu content. This contribution can be associated to a less efficient decomposition of the organic precursors. As in previous results, no evidence of the formation of a ternary phase was detected in the Cu-Ti-O films.

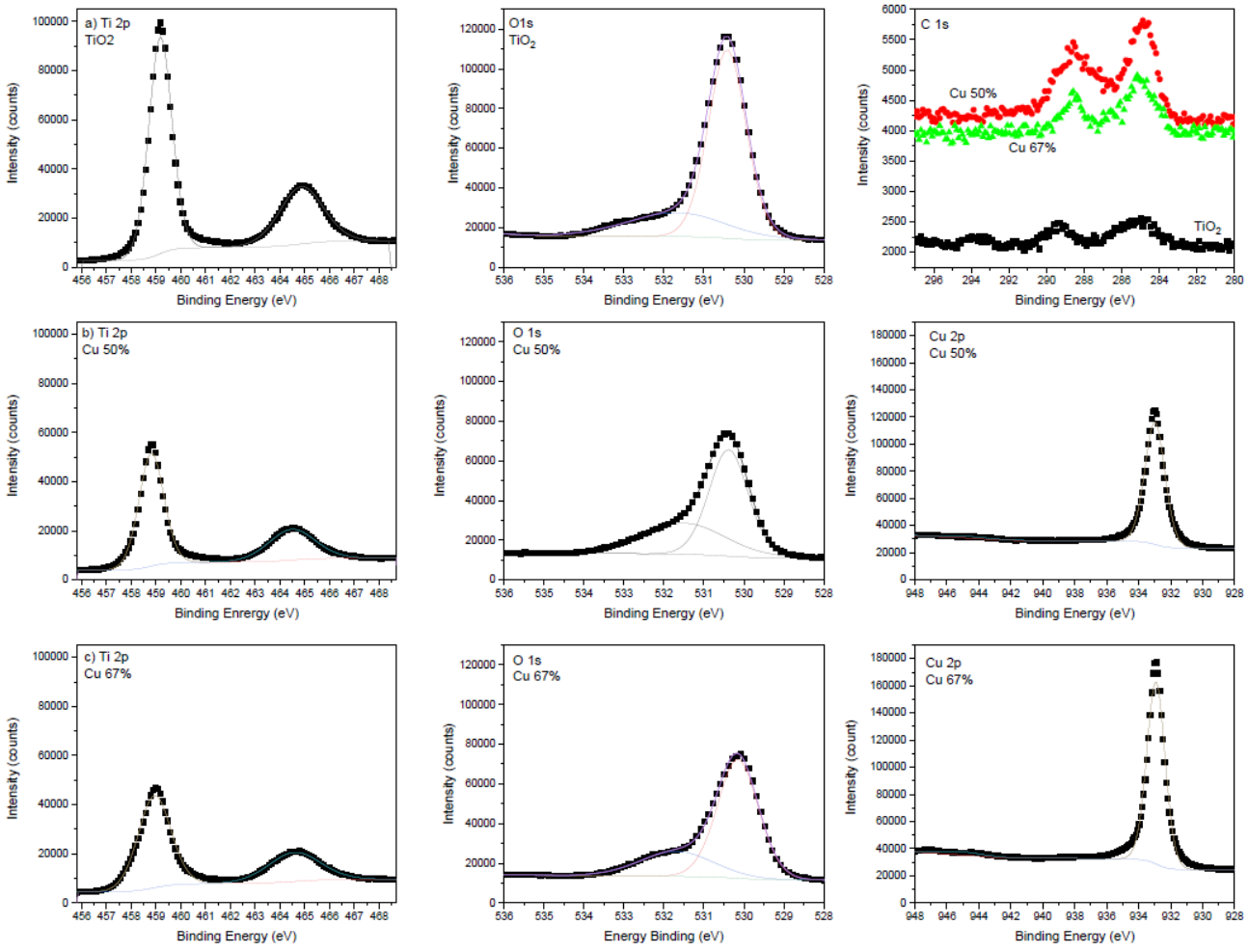

Figure V- 12. XPS spectra of Ti2p and O1s in the left and center columns respectively, and C 1s and Cu 2p in the right column. Three compositions are presented: the first row corresponds to pure TiO_2 (except last one), the second to CuTiO50S film and third row to CuTiO66S film. C1s spectra compares in the same graph the signal for the three samples.

V.7. TEM Analysis

In order to assess the location of Cu_2O and TiO_2 within the film structure (complete mixing or a two phase compound), CuTiO55S film was prepared in cross section by grating and by the tripod method for TEM observation. The equipment used for TEM imaging was a JEOL JEM 2010 microscope, operating at 200 kV (0.19 nm resolution), provided with an EDS system, INCA Energy TEM 100 X-Max 65T. Cross-section samples were prepared from films deposited on silicon.

The cross section of the sample can be seen in Figure V- 13a), and confirms the roughness of the film. The film is formed by a dense structure of around 150 nm covered with an open structure of around 300 nm. These rough structures at the top-layer are indeed agglomerates of smaller crystals with sizes ranging from 10 to 30 nm, as visible in Figure V- 13 b).

The diffraction pattern obtained from this region can be interpreted as a mixing of Cu_2O in Figure V- 13 c) and TiO_2 anatase in Figure V- 13 d).

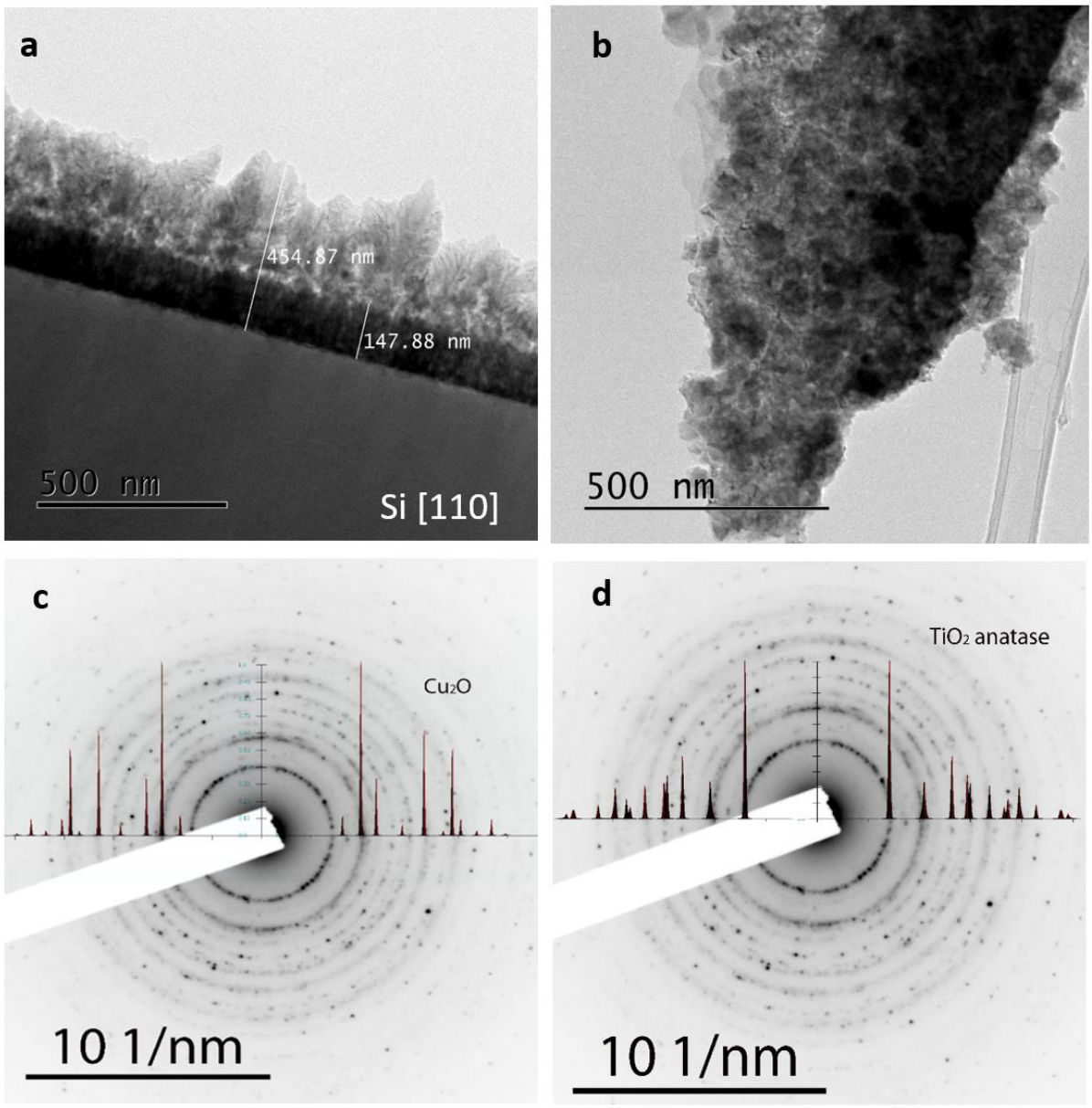

Figure V- 13. HRTEM image of a Cu-Ti-O film with 55 at.% Cu: a) cross section view on the silicon interface region, b)) detail of the film top part removed by scratching ; c) same diffraction pattern showing the presence of Cu_2O structure and d) corresponding diffraction pattern identified as TiO_2 anatase .

STEM was used to analyse the composition of the CuTiO55S film in cross section. Moreover, EDS was performed punctually using spot analysis in STEM to identify the local distribution of Cu and Ti. Mappings for each element obtained from the CuTiO55S as deposited film are presented in Figure V- 14. This analysis confirms the presence of Cu and Ti through all film without significant segregation in the grain boundaries.

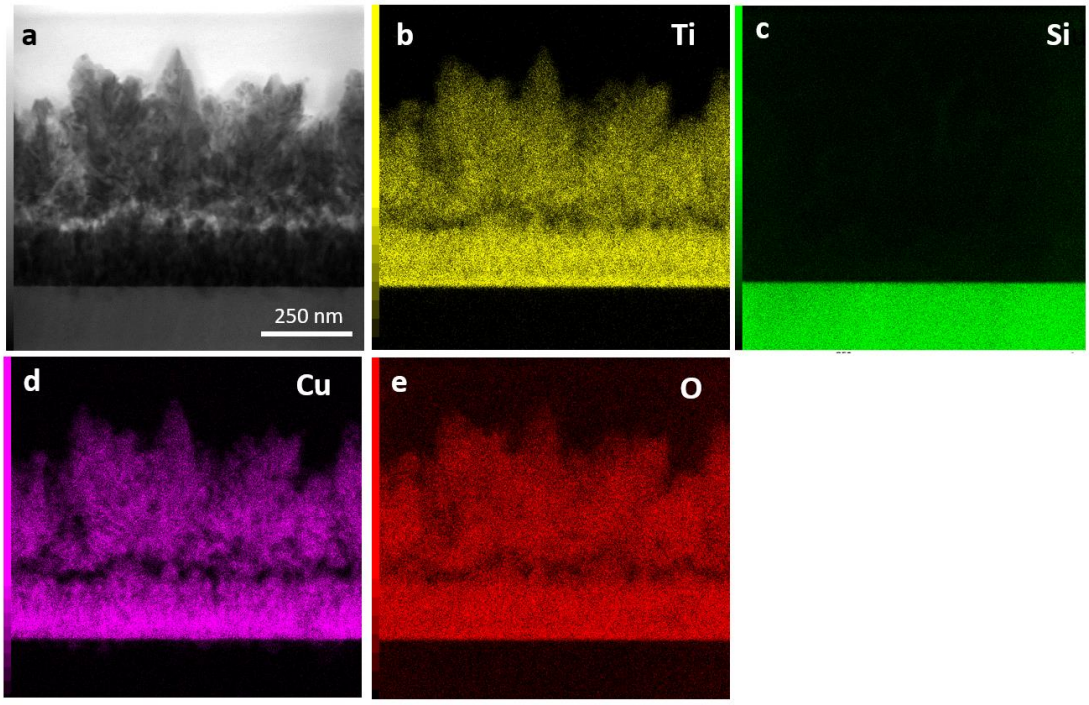

Figure V- 14. a) Bright-field STEM image of Cu-Ti-O film with 55 at.% Cu deposited on silicon, b-e) Corresponding EDS-STEM elemental mapping of the b) Ti, c) Si, d) Cu, and e) O elements, respectively. The 250 nm scale bar is valid for all images.

V.8. Contact angle measurements of TiO_2 and copper-doped films

Wettability measurements were performed for films deposited on corning glass substrate using a goniometer KRÜSS G10 equipped with an image analysis system consisting of a CCD video camera, a card of acquisition connected to a PC computer and DROP SHAPE image processing software ANALYSIS (DSA), as explained in chapter IV. As presented in chapter IV, pure TiO_2 as deposited films shows a contact angle of 15°, and after 2 hours under UV irradiation these films become superhydrophilic with a contact angle of about 5°. This films remains superhydrophilic after 6 months without UV irradiation.

Figure V- 15 shows the contact angle for Cu-Ti-O films as deposited on corning glass before and after 2 hours of UV irradiation. Cu-Ti-O films, behave in a completely different way; they are hydrophobic as deposited (angle contact of ~100 °) and remain hydrophobic after 2 hours under UV irradiation.

It has been already reported that copper oxides, such as Cu_2O and CuO exhibit hydrophobicity [30]. The hydrophobic behavior can be so attributed to the presence of Cu_2O in Cu-Ti-O films, in accordance with the XPS and XRD results.

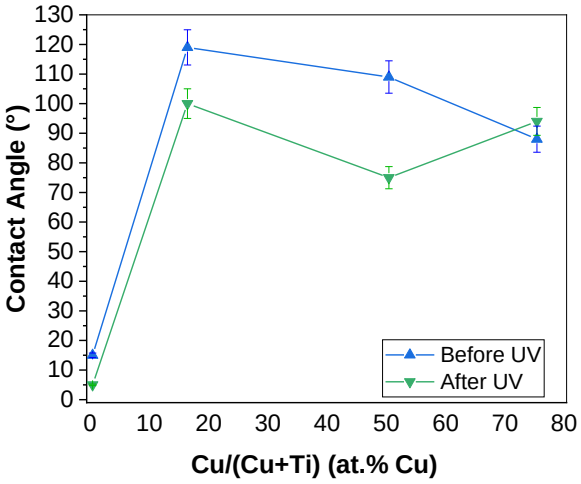

Figure V- 15. Variation of water contact angle for the Cu-Ti-O and TiO_2 films deposited on corning glass at 550°C as deposited and after 2 hours of UV irradiation.

V.9. Photocatalysis properties

The photocatalytic activity of each samples was performed using the same protocol explained in chapter III, measuring the decomposition of Orange G dye under UV visible light.

Pure TiO_2 films was used as our internal reference. We remind that the high photocatalytic activity of these films was explained by the formation of microflowers with nanopetals that increase the efficient surface and decrease the crystal size.

The photocatalytic activity was tested on Cu-Ti-O films deposited on silicon substrates with different compositions. The degradation kinetics with UV irradiation are represented in Figure V-16 a). CuTiO50S and CuTiO55S films presented the best performance in photocatalytic decomposition of Orange G dye. Figure V- 16 b) presents the evolution of the k constant for Orange G degradation calculated from the slope of the degradation rate as a function of copper content in films.

CuTiO50S film presents a maximum k value of 0.00168 min^{-1} compared to pure TiO_2 film and CuTiO55S film that present a value of k equal to 0.00144 min^{-1}. Nevertheless, the difference is very small so we can consider that both films shows photocatalytic response comparable to our

best TiO_2 films. The photocatalytic activity decreases for CuTiO66S film that presents a higher copper content. The film with low Cu content (16 at.% Cu) shows an intermediate value.

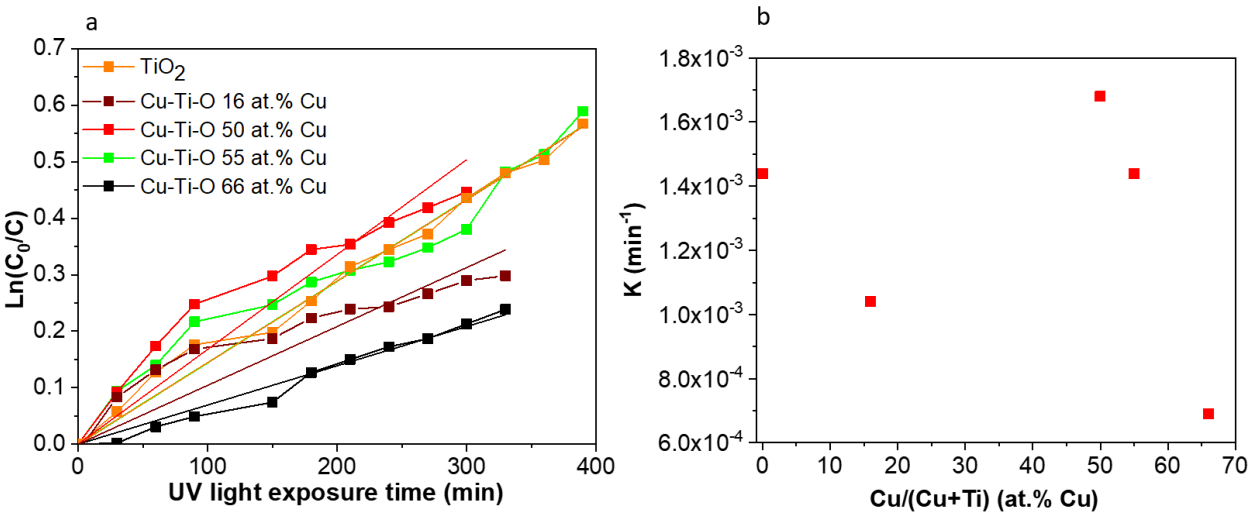

Figure V- 16. a) Kinetics of orange G degradation by the TiO_2 and Cu-Ti-O films with different Cu content under UV light (371 nm) irradiation. b) Evolution of the k constant for Orange G degradation calculated from the slope in figure a as a function of Copper content.

This result indicated there is an optimal value for the copper content and that the presence of a greater content of Cu is detrimental to the photocatalytic ability. It has been reported in the literature that loading with copper on TiO_2 particles can lead to about twice higher photocatalytic activity than pure TiO_2. Nevertheless most of the references concerned low loading values of Cu in TiO_2 nanoparticles [31,32]. Nevertheless, they also found a decreases of photocatalytic activity with Cu content and they proposed two possible reasons for this decrease. Firstly, the active sites on the catalyst are covered with the excessive Cu. Secondly, the charge-recombination rate increases with the increase in the amount of Cu. Furthermore, these phenomena may be related to the formation of recombination center of CuO which accelerate the recombination of electron-hole pairs; because the conduction band of (CuO/Cu_2O) is lower than that of TiO_2. Hence, the excited electrons in TiO_2 will be inclined to transfer to CuO instead of staying in TiO_2 to recombine with holes[33]. This last explanation is maybe the most adapted to our case.

V.10. Marine biofouling field test

Immersion in seawater enables the most authentic test to evaluate antibiofouling efficacy providing a propitious site to the development of different successive colonisers. In this work, biofouling tests were carried out in order to compare coatings with different compositions.

V.10.1. Evaluation of antifouling activity following standard test

The antifouling activity of pure TiO_2 films and Cu-Ti-O films deposited on corning glass substrates was tested by exposing the coatings in natural seawater and observing the degree of fouling by visual inspection after several months of immersion (ASTM D 3623)[34]. Fay et al.[35] reported that the Kernevel Harbour seems to be extremely favorable to the settlement of biofouling. All of the species, which are considered as representative of biofouling can be observed. In addition, the degree of fouling, determined by visual inspection, distinguishes microfouling, barnacles, tubeworms, etc. Almeida et al.[36] also reported that the adhesion of the main kinds of macroorganism species can be evaluated by visual inspection.

Confocal laser scanning microscopy (CLSM) and SEM were used as complementary analytical tools in order to study microfouling behavior. The purpose is to link the observations of the marine microfouling with the macrofouling activity of samples. Scanning electron microscopy (SEM) has become an usual method to visualize and identify organisms directly attached to coated surfaces[37]. Nevertheless, SEM can be a laborious method that demands complicated sample preparation protocols, comprising the chemical fixation and dehydration of the sample accompanied by freeze drying with the purpose of conserving the 3D-structure of micro-foulers.

CLSM is a computerized microscope that produces three-dimensional images of microorganisms. This technique, combined with the use of fluorescent probes has proven to be useful for the analyses of the three-dimensional distribution of the total and active cells in solid structures such as biofilm [38].

Three different films were tested: pure TiO_2 films, CuTiO16C and CuTiO50C films. Samples with two differ rent sizes were prepared: Square samples of 1.5 x 1.5 cm^2 for microfouling tests and 5 x 5 cm^2 for macrofouling. To take into account the variability of the experience, three samples were prepared for each composition on the large substrate and 12 samples for each compositon on small substrates. These samples were pasted on polycarbonate panels, which were stuck onto a

support, and then they were immersed in natural seawater in April 2019, at a depth of 50 cm (Atlantic Ocean, Kernevel Harbour, France), as represented in Figure V- 17.

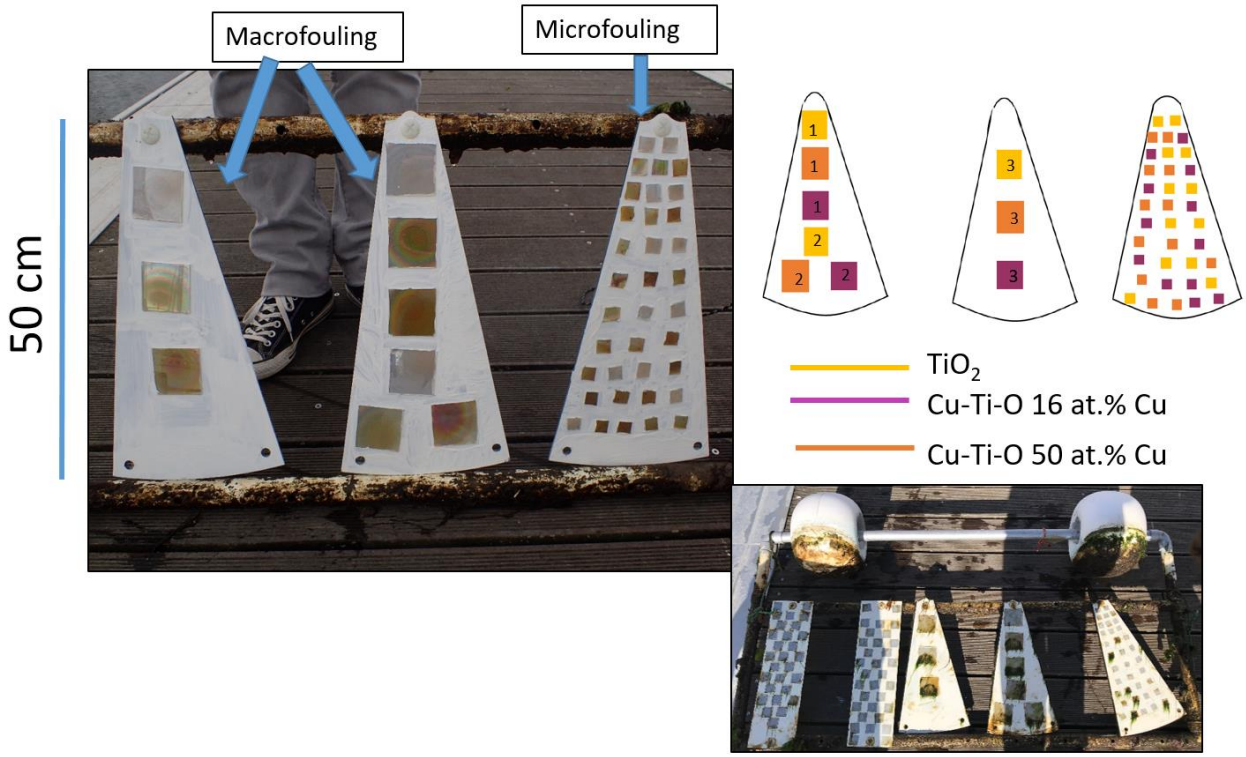

Figure V- 17. Pure TiO_2 films, CuTiO16C and CuTiO50C samples pasted on polycarbonate panels and immersed in natural seawater (Atlantic Ocean, Kernevel Harbour, France). We can identify the three kind of samples by the colors as represent on the diagram.

In this work, the estimated percentage of the sample area covered by biofouling is obtained after using ImageJ image processing program.

V.10.2. Evaluation of microfouling adhesion by microscopy

Microfouling was evaluated after 38 days of immersion on small size coated substrates. Samples were taken out and the observations were conducted by two interdependent microscopic methods: SEM and CLSM.

Regarding the microfouling analysis, four samples for each type of films were observed by SEM on a JEOL 6460LV microscope and eight others by CLSM on a Zeiss LSM 710 microscope using the oil immersion 40× objective.

Samples for SEM observations were prepared using a protocol adapted from Coy et al.[39]. Initially, samples were immersed in 3% glutaraldehyde solution during all the night and then dehydrated by several washings: phosphate buffer (10 min, 3 times); ethanol 70% (10 min, 3 times); ethanol 90% (10 min, 3 times) and absolute ethanol (10 min, 3 times). Therefore, the samples were dried by the carbon dioxide critical point method. Finally, a gold deposit is done in order to make samples conductive [35]. Images were obtained with a magnification of 500×, under an acceleration voltage of 7 keV, from secondary electrons. A representative area of the coating was chosen to be analyzed by microscopic methods.

As a representative example of the overall nature and degree of fouling found on films, SEM of both films after 1–5 weeks of immersion is shown in Figure V- 18. All coatings were subjected to the same immersion conditions. Consequently, variations in microfouling communities indicates differences in the coating performances.

1. After 10 days of immersion just a few diatoms were observed for all the films.
2. After 25 days a diverse community of microorganisms, which included bacteria and diatoms, is observed in all the films, especially in CuTiO50C films. This composition presented a greater amount of microorganisms compared to the other coatings.
3. A few diatoms were observed after 38 days of immersion for pure TiO_2 films and CuTiO16C films, which is in contrast with films containing higher Cu content. CuTiO50C films were almost totally covered by diatoms and bacteria. It is important to notice that the presence of microflowers on the surface is observed even after 38 days of immersion for pure TiO_2 films deposited at 550°C. It confirms that the TiO_2 microflowers are resistant to seawater and are also mechanically stable, which is quite important since microflowers are responsible for ensuring a better photocatalytic activity, as showed in chapters III and IV.

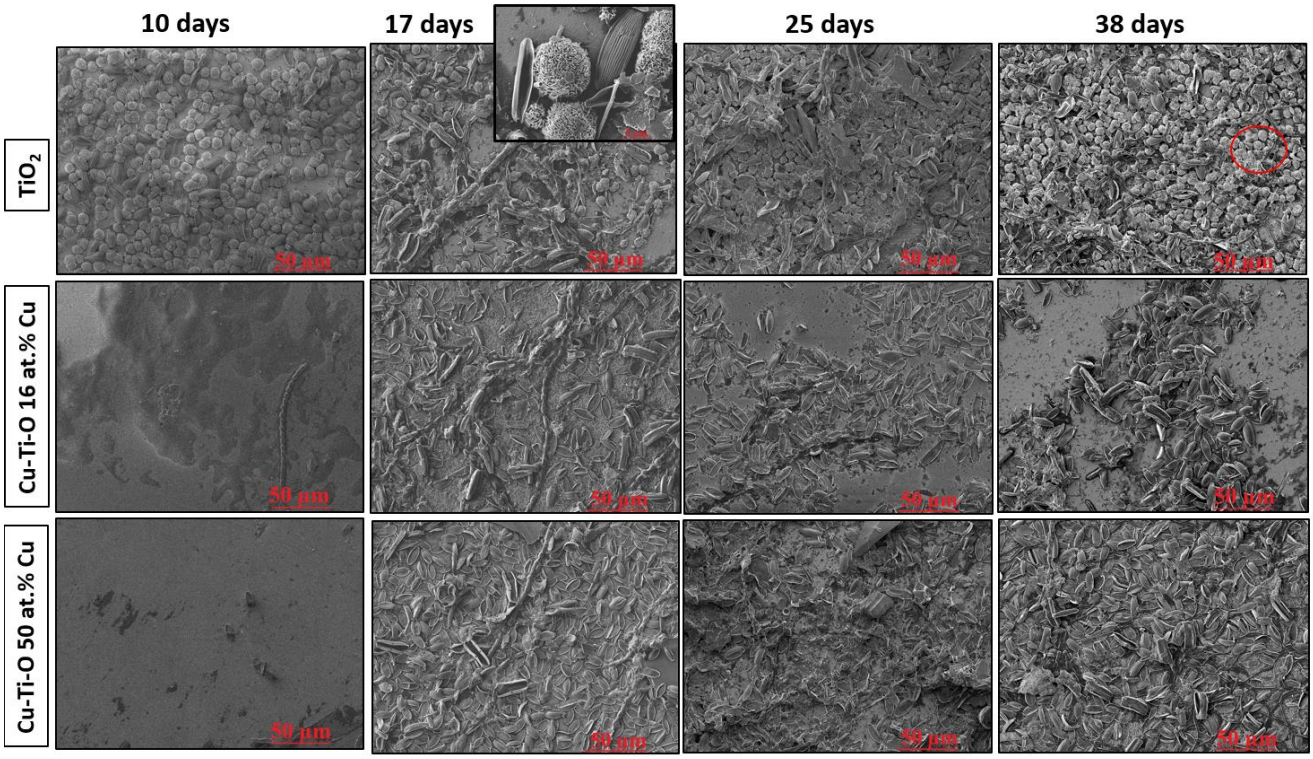

Figure V- 18. Observation of coatings colonisation by SEM after 38 days of immersion in the Atlantic Ocean.

Figure V- 19 presents the film's surface covered by diatoms in red after 38 days of immersion. The number of diatoms was counted for each sample and the TiO_2 pure film presents approximately 133 diatoms on surface. Besides, CuTiO16C and CuTiO50C films presents approximately 183 and 260 diatoms, respectively.

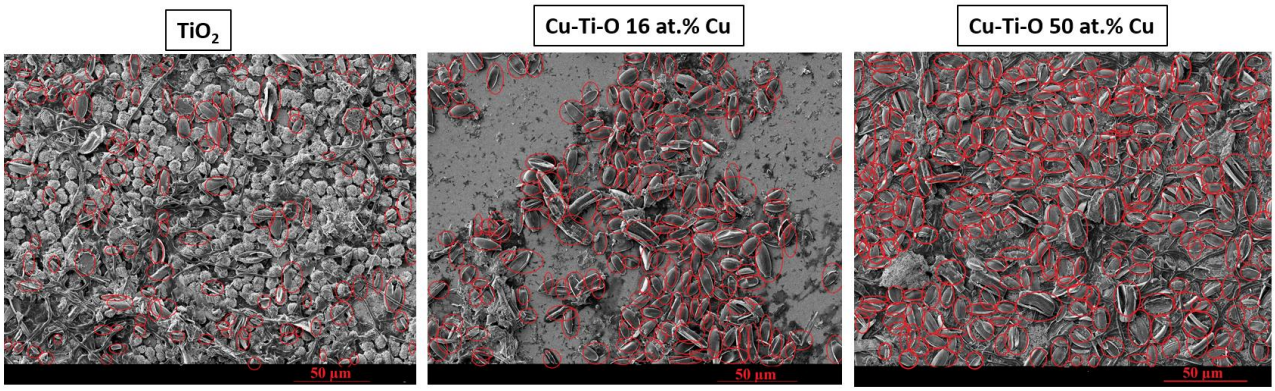

Figure V- 19. SEM images of pure TiO_2 films and Cu-Ti-O films covered by diatoms in red.

These results were confirmed by CLSM. For CLSM experiments, adherent cells on coatings were stained by inserting Syto 9 stains (Molecular Probes. They are noted after 10 min of incubation. Syto 9 (5 µM) was employed as a nuclear stain for live cells. It was excited at 488 nm, and the emission was gathered at 498–550 nm (red fluorescence). Microalgae were observed by their fluorescence at 633 nm, and the emission was collected at 638-720 nm.

Figure V- 20 presents micrographs of the different coatings taken at different immersion time. After 4 weeks of immersion in seawater, the microfouling present on coatings with different compositions was clearly different.

After 10 days of immersion bacteria are presented in all the films. Indeed pure TiO_2 films and CuTiO16C films presented a small amount of bacteria on the surface compared to CuTiO50C films. After 17 days of immersion all the coatings developed a biofilm composed of bacteria, diatoms and micro-algae. Additionally, the presence of micro-algae on the surface are better noticed for CuTiO50C films.

In our case, CuTiO16C showed a clearly better resistance to biofilm and micro-algae development since SEM and CLSM observations presented a smaller growth potential.

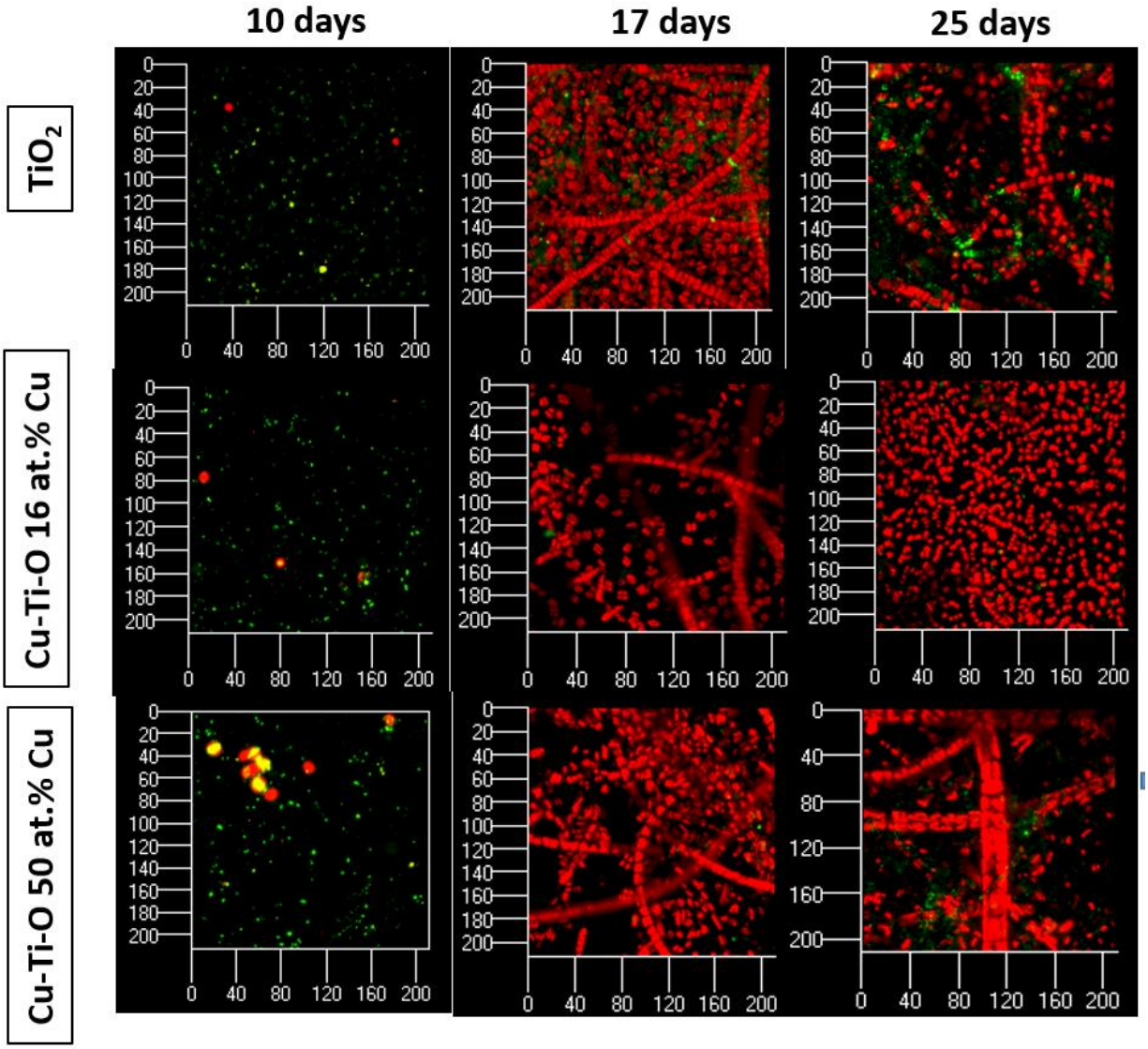

Figure V- 20. Observation of coatings colonisation by CLSM after 10, 17 and 25 days of immersion in Atlantic Ocean. Bacteria were stained with Syto 61 red/Sytox green allowing live and dead cells to appear in red and green, respectively. Micro-algae were observed in red by autofluorescence.

Cassé and Swain showed that, an understanding of the development of microfouling is an important feature concerning the choice of new antifouling coatings 40]. Some authors have demonstrated that the microbial film may boost macro-organism colonization [41,42].Additionally, they forward better understanding of the microfouling (bacteria and diatoms) development on the coatings particularly by examination of colonisation kinetics. Therefore, the microscopic methods and the tests in natural seawater can give complementary information on antifouling activity.

V.10.3. Evaluation of macrofouling adhesion by visual inspection and image analysis

The percentage of surface covered by different fouling types was visually assessed at periodical time during 13 weeks after the static immersion. Figure V- 21 summarizes the macroscopic observations of surfaces after 7, 8, 9, 10 and 13 weeks of immersion in natural seawater.

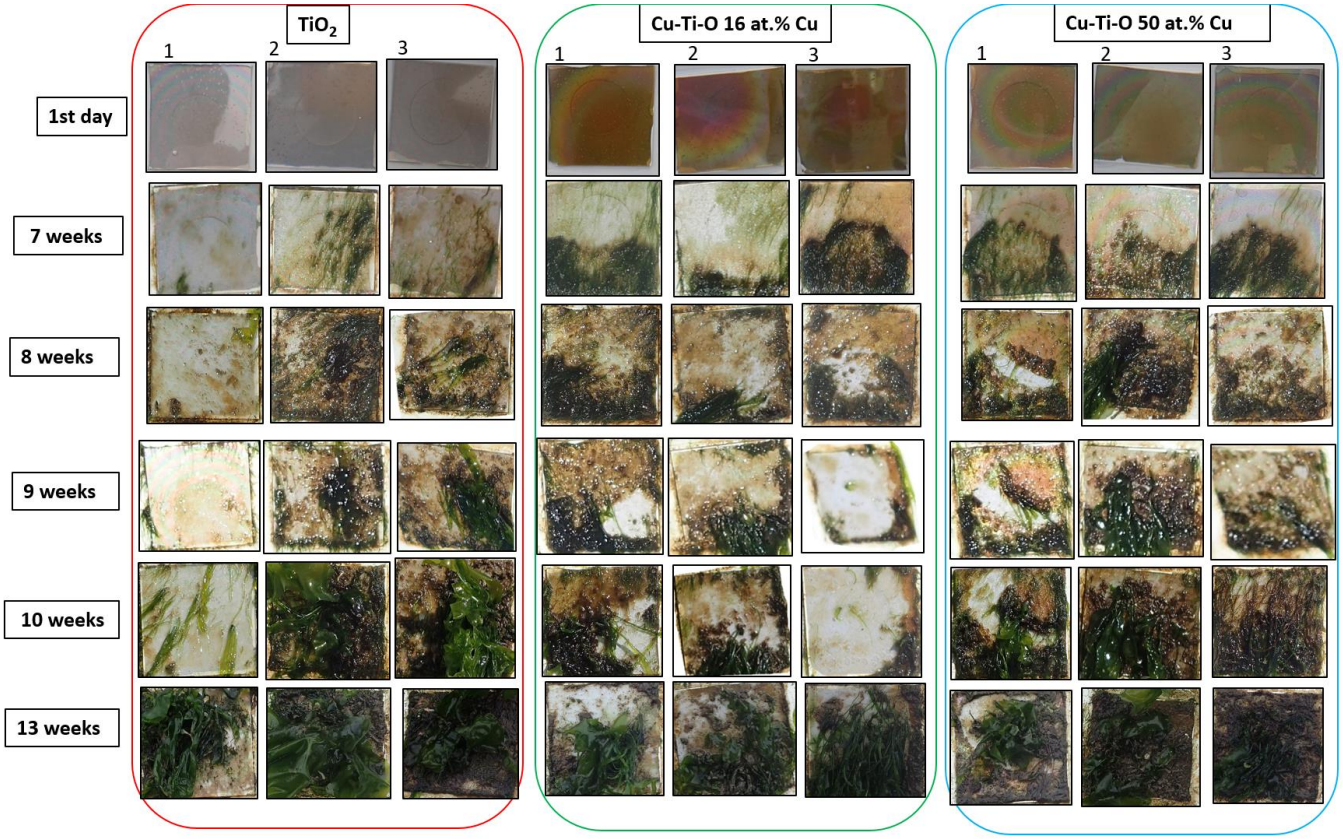

Figure V- 21. Images showing the evolution of biofouling of the sample surfaces on TiO_2 and Cu-Ti-O films deposited on corning glass at different immersion time during a tota immersion of 13 weeks in Kernevel Harbour.

Figure V- 22 presents the evolution of fouling development with immersion time by quantifying with ImageJ software the surface area of sample covered by biofouling.

After 4 weeks pure TiO_2 films shows the best performance, presenting the smallest percentage of surface area covered by biofouling, with an average value of 20 %. On the other hand, CuTiO16C and CuTiO50C films presented an average value of 27 % and 29 %, respectively. It is

importance to notice that TiO_2 sample placed on the top of the panel showed a better performance compared to samples placed on the bottom of the panel as represented in Figure V- 22 a). It can be explained by the fact that the sample are closer to the water surface allowing it to receive more UV/VIS radiation and then to be more photocatalytic active.

On the contrary, CuTiO16C presented a best performance for the samples placed on the bottom during the first 10 weeks. After 13 weeks all the samples showed an important growth of algae on the surface (Figure V- 22 b).

For CuTiO50C films, all the samples presented almost the same performance independently of the location, as shown in Figure V- 22 c.

Some particular numbers have to be given:

- After 8 weeks pure TiO_2 films presented an average value of 46% against 52% and 60% for CuTiO16C and CuTiO50C films, respectively.
- After 10 weeks, it is observed a self-cleaning effect in one of CuTiO16C films which show clearly a decrease of biofouling from 54 % to 24 % of surface area covered.
- After 10 weeks CuTiO16C films showed better performance compared to the other compositions with an average value of 50 %. One of pure TiO_2 coatings presented a good performance after 10 weeks showing 29 % of surface area covered by biofouling.
- After 10 weeks CuTiO50C presented a higher average percentage of surface covered with an estimated value of 80 % due to the growth of macro and micro-algae on the surface.

Figure V- 22 shows that after static immersion for 13 weeks all the coatings tested presented a percentage of surface covered by fouling higher than 70 %, which is dominated by macro-algae. Actually, juvenile barnacles and a calcareous tubeworms were not settled on coatings.

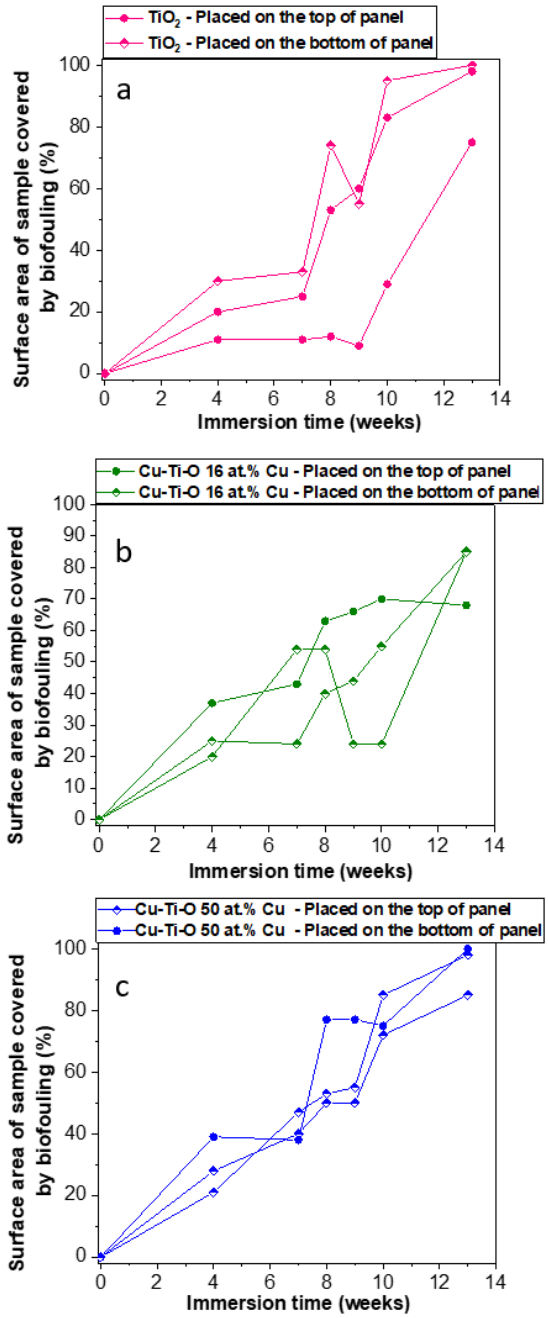

Figure V- 22. Evolution of surface area of samples covered by biofouling with immersion time obtained from pictures shown in Figure V- 21 for a) TiO_2 films, b) CuTiO16C films and c) CuTiO50C films.

Comparison of macro and microfouling

In this experiment, the observation of biofilms on antifouling coatings revealed a good correlation between microscopic observation (microfouling observation) and visual inspection following ASTM standard testing (macrofouling observation).

In particular, CuTiO16C films showed a better resistance to the development of biofilms and micro-algae and also a lower percentage of the area covered by macroorganisms after 13 weeks of immersion. Pure TiO_2 films are also coherent in the observation and the macrofouling results indicate a possible influence of photocatalytic activity. Nevertheless, CuTiO50C films present the worst resistance to microfouling and macrofouling activities.

These results revealed that TiO_2 films and CuTiO50C films that presented a good performance in photocatalysis under UV radiation do not show the same resistance to the development of biofouling in seawater after 13 weeks. On the other hand, TiO_2 films show better behavior up to 8 weeks of immersion, which can be explained by a higher photocatalytic activity in these films since the sample placed at the top of the panel showed better performance. The CuTiO16C films with a lower photocatalytic activity seems to enhance self-cleaning properties after 10 weeks of immersion. These results are encouraging but they are only a preliminary study that needs further investigation. Nevertheless, they allow to propose a not toxic approach to the marine biofouling problem.

V.11. Conclusions

New Cu-Ti-O films with high contents of copper were deposited by AAMOCVD at 550 °C with a deposition time of 40 minutes in order to develop an efficient visible-light-active photocatalyst material, presenting a high surface area for adsorption of targeted species, high conductivity, long-charge lifetimes, direct pathways to carry photogenerated charge, and good chemical stability in water.

$Cu(AcAc)_2$ solutions with a concentration of 0.01 M and 0.03 M were prepared and then mixed with a $TiO(AcAc)_2$ solutions dissolved in ethanol at a concentration of 0.03 M. For Cu-Ti-O films deposited using $Cu(AcAc)_2$ as a start solution at a concentration of 0.03M, the Cu content in film varies between 50 and 66 at.% Cu for films deposited on silicon, between 50 and 75 at.% Cu for films deposited on corning glass and between 25 and 50 at.% Cu for Al-Zr coated high speed steel (HSS). Cu-Ti-O films deposited using $Cu(Acac)_2$ as a start solution at a concentration of 0.01M, the Cu content in film is 16 at.% Cu for films deposited on Si and corning glass substrates.

XRD and Raman spectroscopy revealed that films with at.% Cu greater than 50 present Cu_2O, TiO_2 anatase and CuO phases on its composition. The UV-Visible study showed that the optical band gap energy decreases with increasing Cu content. CuTiO75C film presented a lower band gap of 2.88 eV.

Cu-Ti-O films remain hydrophobic after 2 hours under UV irradiation, contrary to pure TiO_2 films which presents a superhydrophilic behavior.

CuTiO50S and CuTiO55S films present a good performance on photocatalytic activity compared to CuTiO16S and CuTiO66S films. CuTiO50S film presents a maximum k value of 0.00168 min^{-1} compared to pure TiO_2 film and CuTiO55S film that present a value of k equal to 0.00144 min^{-1}. Nevertheless, the difference is very small so we can consider that both films shows a photocatalytic response comparable to our best TiO_2 film.

Marine biofouling field tests reveals that pure TiO_2 films show better behavior up to 8 weeks of immersion, which can be explained by a higher photocatalytic activity in these films since the sample placed at the top of the panel showed better performance. CuTiO16C films showed a lower percentage of the area covered by macroorganisms after 13 weeks of immersion. This composition also presented a better resistance to the development of biofilms and micro-algae compared to other

films. These preliminary studies propose a non- toxic approach to the marine biofouling problem and encourage a further investigation in order to check the reproducibility.

References

[1] L.G. Devi, S.G. Kumar, Influence of physicochemical–electronic properties of transition metal ion doped polycrystalline titania on the photocatalytic degradation of Indigo Carmine and 4-nitrophenol under UV/solar light, Appl. Surf. Sci. 257 (2011) 2779–2790. doi:10.1016/J.APSUSC.2010.10.062.

[2] M.-C. Wu, P.-Y. Wu, T.-H. Lin, T.-F. Lin, Photocatalytic performance of Cu-doped TiO_2 nanofibers treated by the hydrothermal synthesis and air-thermal treatment, Appl. Surf. Sci. 430 (2018) 390–398. doi:10.1016/J.APSUSC.2017.09.035.

[3] H. Zhang, X. Yu, J.A. McLeod, X. Sun, First-principles study of Cu-doping and oxygen vacancy effects on TiO_2 for water splitting, Chem. Phys. Lett. 612 (2014) 106–110. doi:10.1016/J.CPLETT.2014.08.003.

[4] W. Xie, R. Li, Q. Xu, Enhanced photocatalytic activity of Se-doped TiO_2 under visible light irradiation, Sci. Rep. 8 (2018) 8752. doi:10.1038/s41598-018-27135-4.

[5] M. Nasr, L. Soussan, R. Viter, C. Eid, R. Habchi, P. Miele, M. Bechelany, High photodegradation and antibacterial activity of BN-Ag/TiO_2 composite nanofibers under visible light, New J. Chem. 42 (2018) 1250–1259.

[6] P. Basnet, E. Anderson, Y. Zhao, Hybrid Cu_xO–TiO_2 Nanopowders Prepared by Ball Milling for Solar Energy Conversion and Visible-Light-Induced Wastewater Treatment ,

ACS Appl. Nano Mater. 2 (2019) 2446–2455. doi:10.1021/acsanm.9b00325.

[7] J. Resende, Copper-based p-type semiconducting oxides : from Joao Avelas Resende To cite this version : HAL Id : tel-01793013, (2018).

[8] T. Ikenoue, S. Sakamoto, Y. Inui, Fabrication and characteristics of p-type Cu_2O thin films by ultrasonic spray-assisted mist {CVD} method, Jpn. J. Appl. Phys. 53 (2014) 05FF06. doi:10.7567/jjap.53.05ff06.

[9] H. Wang, Y. Li, X. Ba, L. Huang, Y. Yu, TiO_2 thin films with rutile phase prepared by DC magnetron co-sputtering at room temperature: Effect of Cu incorporation, Appl. Surf. Sci. 345 (2015) 49–56. doi:10.1016/j.apsusc.2015.03.106.

[10] S. Horzum, S. Gürakar, T. Serin, Investigation of the structural and optical properties of copper-titanium oxide thin films produced by changing the amount of copper, Thin Solid Films. 685 (2019) 293–298. doi:10.1016/j.tsf.2019.06.052.

[11] E. Celik, Z. Gokcen, N.F. Ak Azem, M. Tanoglu, O.F. Emrullahoglu, Processing, characterization and photocatalytic properties of Cu doped TiO2 thin films on glass substrate by sol-gel technique, Mater. Sci. Eng. B Solid-State Mater. Adv. Technol. 132 (2006) 258–265. doi:10.1016/j.mseb.2006.03.038.

[12] S. Saha, S.B.A. Hamid, T.H. Ali, Catalytic evaluation on liquid phase oxidation of vanillyl alcohol using air and H_2O_2 over mesoporous Cu-Ti composite oxide, Appl. Surf. Sci. 394 (2017) 205–218. doi:10.1016/j.apsusc.2016.10.070.

[13] H.E. Swanson, E. Tatge, R.K. Fuyat, Standard X-ray diffraction powder patterns, (1953).

[14] M. Sahu, P. Biswas, Single-step processing of copper-doped titania nanomaterials in a flame aerosol reactor, Nanoscale Res. Lett. 6 (2011) 441. doi:10.1186/1556-276X-6-441.

[15] T. Maruyama, Copper oxide thin films prepared by chemical vapor deposition from copper dipivaloylmethanate, Sol. Energy Mater. Sol. Cells. 56 (1998) 85–92. doi:10.1016/S0927-0248(98)00128-7.

[16] F.A. Akgul, G. Akgul, N. Yildirim, H.E. Unalan, R. Turan, Influence of thermal annealing on microstructural, morphological, optical properties and surface electronic structure of copper oxide thin films, Mater. Chem. Phys. 147 (2014) 987–995. doi:10.1016/j.matchemphys.2014.06.047.

[17] M. Mikami, S. Nakamura, O. Kitao, H. Arakawa, Lattice dynamics and dielectric properties of (formula presented) anatase: A first-principles study, Phys. Rev. B - Condens. Matter

Mater. Phys. 66 (2002) 1–6. doi:10.1103/PhysRevB.66.155213.

[18] M. Grujić-Brojčin, M.J. Šćepanović, Z.D. Dohčević-Mitrović, I. Hinić, B. Matović, G. Stanišić, Z. V. Popović, Infrared study of laser synthesized anatase TiO_2 nanopowders, J. Phys. D. Appl. Phys. 38 (2005) 1415–1420. doi:10.1088/0022-3727/38/9/014.

[19] F. Gervais, B. Piriou, Temperature dependence of transverse-and longitudinal-optic modes in TiO_2 (rutile), Phys. Rev. B. 10 (1974) 1642.

[20] C. Pecharromán, F. Grac\ia, J.P. Holgado, M. Ocana, A.R. González-Elipe, J. Bassas, J. Santiso, A. Figueras, Determination of texture by infrared spectroscopy in titanium oxide--anatase thin films, J. Appl. Phys. 93 (2003) 4634–4645.

[21] N. Serin, T. Serin, S.Horzum, Y. Celik, Annealing effects on the properties of copper oxide thin films prepared by chemical deposition, Semicond. Sci. Technol. 20 (2005) 398.

[22] C. Dette, M.A. Pérez-Osorio, C.S. Kley, P. Punke, C.E. Patrick, P. Jacobson, F. Giustino, S.J. Jung, K. Kern, TiO_2 anatase with a bandgap in the visible region, Nano Lett. 14 (2014) 6533–6538.

[23] M. Cheon, B. Jung, S.J. Kim, J.I. Jang, S.Y. Jeong, High-quality epitaxial Cu_2O films with (111)-terminated plateau grains obtained from single-crystal Cu (111) thin films by rapid thermal oxidation, J. Alloys Compd. 801 (2019) 536–541. doi:10.1016/J.JALLCOM.2019.06.152.

[24] J. Tauc, A. Menth, States in the gap, J. Non. Cryst. Solids. 8–10 (1972) 569–585. doi:10.1016/0022-3093(72)90194-9.

[25] J. Navas, A. Sánchez-Coronilla, T. Aguilar, N.C. Hernández, M. Desireé, J. Sánchez-Márquez, D. Zorrilla, C. Fernández-Lorenzo, R. Alcántara, J. Martin-Calleja, Experimental and theoretical study of the electronic properties of Cu-doped anatase TiO_2, Phys. Chem. Chem. Phys. 16 (2014) 3835–3845.

[26] B. Bharti, S. Kumar, H.N. Lee, R. Kumar, Formation of oxygen vacancies and Ti^{3+} state in TiO_2 thin film and enhanced optical properties by air plasma treatment, Sci. Rep. 6 (2016) 1–12. doi:10.1038/srep32355.

[27] P. Sangpour, F. Hashemi, A.Z. Moshfegh, Photoenhanced Degradation of Methylene Blue on Cosputtered M:TiO_2 (M = Au, Ag, Cu) Nanocomposite Systems: A Comparative Study, J. Phys. Chem. C. 114 (2010) 13955–13961. doi:10.1021/jp910454r.

[28] B. Moongraksathum, J.Y. Shang, Y.W. Chen, Photocatalytic antibacterial effectiveness of

Cu-doped TiO_2 thin film prepared via the peroxo sol-gel method, Catalysts. 8 (2018). doi:10.3390/catal8090352.

[29] C. Wang, Q. Hu, J. Huang, C. Zhu, Z. Deng, H. Shi, L. Wu, Z. Liu, Y. Cao, Enhanced hydrogen production by water splitting using Cu-doped TiO_2 film with preferred (0 0 1) orientation, Appl. Surf. Sci. 292 (2014) 161–164. doi:10.1016/J.APSUSC.2013.11.105.

[30] Y. Xu, J. Li, L. Yao, L. Li, P. Yang, N. Huang, Preparation and characterization of Cu-doped TiO_2 thin films and effects on platelet adhesion, Surf. Coatings Technol. 261 (2015) 436–441. doi:10.1016/J.SURFCOAT.2014.09.031.

[31] T. Morikawa, Y. Irokawa, T. Ohwaki, Enhanced photocatalytic activity of $TiO_{2-x}N_x$ loaded with copper ions under visible light irradiation, Appl. Catal. A Gen. 314 (2006) 123–127. doi:10.1016/J.APCATA.2006.08.011.

[32] C.S. Kim, J.W. Shin, Y.H. Cho, H.D. Jang, H.S. Byun, T.O. Kim, Synthesis and characterization of Cu/N-doped mesoporous TiO_2 visible light photocatalysts, Appl. Catal. A Gen. 455 (2013) 211–218. doi:10.1016/j.apcata.2013.01.041.

[33] Z. Jin, X. Zhang, Y. Li, S. Li, G. Lu, 5.1% Apparent quantum efficiency for stable hydrogen generation over eosin-sensitized CuO/TiO_2 photocatalyst under visible light irradiation, Catal. Commun. 8 (2007) 1267–1273. doi:10.1016/J.CATCOM.2006.11.019.

[34] W. Conshohocken, Standard Test Method for Testing Antifouling Panels in Shallow Submergence 1, Order A J. Theory Ordered Sets Its Appl. (1998) 1–8. doi:10.1520/D3623-78AR04.2.

[35] F. Faÿ, D. Carteau, I. Linossier, K. Vallée-Réhel, Evaluation of anti-microfouling activity of marine paints by microscopical techniques, Prog. Org. Coatings. 72 (2011) 579–585. doi:10.1016/j.porgcoat.2011.04.002.

[36] E. Almeida, T.C. Diamantino, O. de Sousa, Marine paints: The particular case of antifouling paints, Prog. Org. Coatings. 59 (2007) 2–20. doi:10.1016/j.porgcoat.2007.01.017.

[37] S.M. Jackson, E.B.G. Jones, Fouling film development on antifouling paints with special reference to film thickness, Int. Biodeterior. 24 (1988) 277–287. doi:10.1016/0265-3036(88)90012-7.

[38] F. Joux, P. Lebaron, Use of fluorescent probes to assess physiological functions of bacteriaat single-cell level, Microbes Infect. 2 (2000) 1523–1535. doi:10.1016/S1286-4579(00)01307-1.

[39] W.F. McCoy, J.D. Bryers, J. Robbins, J.W. Costerton, Observations of fouling biofilm formation, Can. J. Microbiol. 27 (1981) 910–917.

[40] F. Cassé, G.W. Swain, The development of microfouling on four commercial antifouling coatings under static and dynamic immersion, Int. Biodeterior. Biodegrad. 57 (2006) 179–185. doi:10.1016/j.ibiod.2006.02.008.

[41] J.R. Henschel, P.A. Cook, The development of a marine fouling community in relation to the primary film of microorganisms, Biofouling. 2 (1990) 1–11. doi:10.1080/08927019009378125.

[42] P.Y. Qian, V. Thiyagarajan, S.C.K. Lau, S.C.K. Cheung, Relationship between bacterial community profile in biofilm and attachment of the acorn barnacle Balanus amphitrite, Aquat. Microb. Ecol. 33 (2003) 225–237. doi:10.3354/ame033225.

Conclusions and future works

The rising demands for eco-friendly materials presenting antibiofouling and anticorrosion properties for marine applications present a challenge to develop advanced coatings. Two different coatings, Al-Zr and TiO_2, were successfully prepared in order to develop a potential bifunctional Al-Zr/TiO_2 bilayer coating combining anticorrosion and photocatalytic properties using high-speed steel (HSS) as substrates.

First, the anticorrosion performance of Al-Zr films was studied. Al-Zr films with different Zr contents were deposited on HSS, glass and silicon substrates by direct current magnetron sputtering. Al-Zr films having Zr content below 10 at. % present well-defined diffraction peaks, which correspond to fcc structure, indicating a supersaturated solid solution of Zr in Al. Al-Zr (4 at.% Zr) was chosen to be used as an underlayer since it presents the best compromise between intrinsic corrosion resistance, sacrificial character/steels and mechanical reinforcement.

Secondly, TiO_2 films proposed as photocatalysts were deposited by AACVD using $TiO(AcAc)_2$ as precursor under optimized conditions to develop a microstructure characterized by the presence of TiO_2 microflowers physically attached to TiO_2 film surface. Formation of this microstructure occurs at a specific thermal window that depends on the precursor concentration; more precisely when working with a 0.03 mol L^{-1} concentration solution and an aerosol feeding rate of 3 ml min^{-1}. The maximum flowers density was achieved for films deposited at 550 °C, presenting an area fraction coverage of about 40 %.

TiO_2 with different structural and morphological characteristics were deposited on Al-Zr (4 at.% Zr) as a second layer in order to produce multifunctional Al-Zr/TiO_2 bilayer films. X-ray diffraction and Raman spectroscopy show that the TiO_2 micro-flowers as well as the TiO_2 thin film crystallize

in the anatase phase. This TiO_2 phase presents higher charge mobility and consequently a better photocatalytic response.

Photocatalytic performance of bilayer films was evaluated by means of degradation of Orange G dye under UV illumination. The presence of TiO_2 microflowers having a size of about 7 µm and a crystallite size of 20 nm plays a crucial role in photocatalysis. The photoefficiency of TiO_2 films, quantified in terms of kinetic rate constant increases with microflowers area fraction coverage. This behavior was clearly noticed for TiO_2 samples deposited at 550 °C, showing a higher decomposition rate of Orange G (780×10^{-10} mol L^{-1} min^{-1}) under UV light as compared to other films obtained at lower deposition temperatures (500 and 540 °C).

TEM analysis revealed that after the AA-MOCVD process performed at 550 °C, Al-Zr (4 at.% Zr) presented precipitates, which are more rich in zirconium than the matrix. The structure formed after deposition at 550°C is clearly biphased; an FCC solid solution of zirconium in aluminum and an ordered metastable Al_3Zr compound. Literature shows that these particles are an important grain refiner in commercial structural of Al-based alloys and present a minimal impact on corrosion properties.

Electrochemical tests were carried out in an aerated and stirred chlorine solutions (5 wt.% NaCl). They revealed that Al-Zr/TiO_2 bilayer coatings is an attractive alternative for preserving the sacrificial protection of steel structures in saline environments. These films offer good protection thanks to the preferential oxidation of the bilayer presenting a lower corrosion current density of 4.01×10^{-7} A/cm^2. TiO_2 as a second layer reduces the electrochemical activity of the films through the formation of a dense passive film and also increases the pitting resistance when the cathodic reaction kinetic is lower.

In order to improve the properties of TiO_2 wide band gap semiconductor, the incorporation of transition metals such as Cu was proposed as an efficient method. The influence of incorporation of copper into TiO_2 thin films on structural, optical, photocatalytic activity and antibiofouling properties was studied. New Cu-Ti-O films with high copper contents were deposited by AAMOCVD at 550 °C in order to develop an efficient visible-light-active photocatalyst material. TiO_2 and Cu_xO mixtures reveal great potential due to their low toxicity and their suitable energy band positions.

Cu-Ti-O films were deposited on corning glass, silicon and Al-Zr coated substrates. Cu-Ti-O films are composed of Cu_2O, TiO_2 anatase and for films with a Cu content higher than 50 at.% the

CuO phase also appear. Besides, band gap decreased for Cu-Ti-O films starting from a Eg TiO_2 value of 3.55 eV, to the lowest value near to 2.88 eV with the higher Cu content (75 at.% Cu).

Cu-Ti-O films showed hydrophobic behavior even after 2 hours under UV irradiation, contrary to superhydropilic TiO_2 films. Hydrophobic surfaces are known to show good 'fouling release' properties, whereas the hydrophilic surfaces show resistance to protein adsorption and cell adhesion.

Photocatalysis activity was evaluated using the decomposition of Orange G dye under UV visible light. The photocatalytic activity of Cu-Ti-O film with 50 at.% of Cu is remarkable high and presents a maximum k value of 0.00168 min^{-1} compared to 0.00144 min^{-1} for pure TiO_2 film and Cu-Ti-O film with 55 at.% Cu. Cu-Ti-O films a very promising materials for the photocatalytic degradation of organic compounds under visible light. Indeed, photocatalytic oxidation processes using TiO_2 based catalysts appear to be a very useful technique for the antifouling properties, leading to the mineralization of the pollutants or to their conversion to more biodegradable compounds.

Marine biofouling field tests were carried out in Lorient's Harbor in order to evaluate the antifouling properties of pure TiO_2, Cu-Ti-O (16 at.% Cu) and Cu-Ti-O (50 at.% Cu) films deposited on corning glass. Pure TiO_2 films showed better behavior until 8 weeks of immersion, which can be explained by a higher photocatalytic activity while the sample placed at the top of the panel showed better performance. SEM images showed that TiO_2 microflowers were present even after 38 days of immersion, which confirms that microflowers are resistant to seawater and mechanically stable. This fact is quite important since TiO_2 microflowers are essential for ensuring a better photocatalytic activity.

Biofouling tests revealed that after 13 weeks of immersion in seawater, Cu-Ti-O (16 at.% Cu) films presented a better resistance to the development of biofilms, microalgae and macroalgae on the surface confirmed by SEM and CLSM analyzes, and also the visual observations.

New biofouling tests are in progress in order to validate the reproducibility of the anti-fouling behavior of these coatings. Pure TiO_2 films with different densities of micro-flowers on the surface are being test in order to check the real role of flowers on anti-fouling properties since this films have shown a good performance on photocatalysis. Moreover, the chemical stability of Cu-Ti-O films and TiO_2 films in sea water needs to be evaluated in order to know if these films degrade when they are immersed.

Additionally, more understanding of coatings surface properties in the immersed condition, rather than in dry is necessary, as immersion changes the dynamics of self-assembly and surface organization. When the coated samples are immersed in the natural marine environment, their properties might change further as a result of surface conditioning by adsorption of macromolecules and microorganisms, which will also change according to the season and geographic location. The anti-fouling behavior of novel Cu-Ti-O and TiO_2 films for fouling-release needs to be tested more times in order to understand the adhesion mechanisms of micro and macro-organisms. Interdisciplinary studies combining chemistry, biology and advanced physical techniques for interfacial characterization will be crucial for advancing this research work.

The control of biofouling of surfaces in the marine environment is a challenge: the fouling organisms present the capability to attach and proliferate on the material surfaces in the highly turbulent marine environment. Regarding this aspect, dynamic test system is necessary to check the efficacy of coatings.

Moreover, the HSS/Al-Zr/TiO_2 bilayer coatings combining both corrosion and antifouling properties need to be tested in real conditions.

Other antifouling approaches range from biocidal and self-cleaning coatings to various disinfecting techniques. For instance, medical devices use antimicrobial coatings to inhibit biofilm formation. Developing non-toxic foul-release films for medical, marine and industrial applications is the particular appeal of this thesis. Future research could focus on gathering the best properties from each coating and combining them to produce an effective antifouling surface resistant to a variety of foulers.

Finally, regarding the scalability, the development of low cost, non-vacuum CVD-based techniques like aerosol assisted CVD offers the potential to be scaled up for large area or mass production. This can widen the scope of engineering applications of CVD technique.

Appendix

A. PDF X-Ray File

Pattern : 00-021-1272 *Radiation =* 1.540598 *Quality :* High

TiO_2

Titanium Oxide
Anatase, syn

Lattice : Body-centered tetragonal
S.G. : I41/amd (141)

a = 3.78520
c = 9.51390
Z = 4

Mol. weight = 79.90
Volume [CD] = 136.31
Dx = 3.893
I/Icor = 3.30

Color: Colorless
Additional pattern: See ICSD 9852 (PDF 01-071-1166).
Sample source or locality: Sample obtained from National Lead Co., South Amboy, New Jersey, USA.
General comments: Anatase and another polymorph, brookite (orthorhombic), are converted to rutile (tetragonal) by heating above 700 C.
General comments: Pattern reviewed by Holzer, J., McCarthy, G., North Dakota State Univ, Fargo, North Dakota, USA, *ICDD Grant-in-Aid* (1990). Agrees well with experimental and calculated patterns.
Additional pattern: Validated by calculated pattern.
Temperature of data collection: Pattern taken at 25 C.
Data collection flag: Ambient.

2th	i	h	k	l
25.281	100	1	0	1
36.947	10	1	0	3
37.801	20	0	0	4
38.576	10	1	1	2
48.050	35	2	0	0
53.891	20	1	0	5
55.062	20	2	1	1
62.121	4	2	1	3
62.690	14	2	0	4
68.762	6	1	1	6
70.311	6	2	2	0
74.031	2	1	0	7
75.032	10	2	1	5
76.020	4	3	0	1
80.727	2	0	0	8
82.139	2	3	0	3
82.662	6	2	2	4
83.149	4	3	1	2
93.220	2	2	1	7
94.181	4	3	0	5
95.143	4	3	2	1
98.318	2	1	0	9
99.804	2	2	0	8
101.221	2	3	2	3
107.448	4	3	1	6
108.963	4	4	0	0
112.840	2	3	0	7
113.861	2	3	2	5
114.909	2	4	1	1
118.439	4	2	1	9
120.104	2	2	2	8
121.725	2	4	1	3
122.336	2	4	0	4
131.035	2	4	2	0
135.998	2	3	2	7
137.391	4	4	1	5
143.887	2	3	0	9
150.039	4	4	2	4
152.633	2	0	0	12

Appendix

Pattern : 00-021-1276 ***Radiation =*** 1.540598 ***Quality :*** High

TiO_2

Titanium Oxide
Rutile, syn
Also called: titania

Lattice : Tetragonal
S.G. : P42/mnm (136)

a = 4.59330
c = 2.95920
Z = 2

Mol. weight = 79.90
Volume [CD] = 62.43
Dx = 4.250
Dm = 4.230
I/Icor = 3.40

General comments: No impurity over 0.001%.
Vickers hardness number: VHN_{100}=1132-1187.
Sample source or locality: Sample obtained from National Lead Co., South Amboy, New Jersey, USA.
General comments: Pattern reviewed by Syvinski, W., McCarthy, G., North Dakota State Univ, Fargo, North Dakota, USA, *ICDD Grant-in-Aid* (1990). Agrees well with experimental and calculated patterns.
General comments: Two other polymorphs, anatase (tetragonal) and brookite (orthorhombic), converted to rutile on heating above 700 C.
General comments: Additional weak reflections [indicated by brackets] were observed.
Optical data: A=2.9467, B=2.6505, Sign=+
Additional pattern: Validated by calculated pattern.
General comments: Optical data on specimen from *Dana's System of Mineralogy, 7th Ed.*, I 555.
General comments: Naturally occurring material may be reddish brown.
Color: White
Reflectance: Opaque mineral optical data on specimen from Sweden: $R_3R\%$ =20.3, Disp.=Std.
Temperature of data collection: Pattern taken at 25 C.
Data collection flag: Ambient.

2th	i	h	k	l
27.447	100	1	1	0
36.086	50	1	0	1
39.188	8	2	0	0
41.226	25	1	1	1
44.052	10	2	1	0
54.323	60	2	1	1
56.642	20	2	2	0
62.742	10	0	0	2
64.040	10	3	1	0
65.480	2	2	2	1
69.010	20	3	0	1
69.790	12	1	1	2
72.410	2	3	1	1
74.411	1	3	2	0
76.510	4	2	0	2
79.822	2	2	1	2
82.335	6	3	2	1
84.260	4	4	0	0
87.464	2	4	1	0
89.557	8	2	2	2
90.708	4	3	3	0
95.275	6	4	1	1
96.017	6	3	1	2
97.176	4	4	2	0
98.514	1	3	3	1
105.099	2	4	2	1
106.019	2	1	0	3
109.406	2	1	1	3
116.227	4	4	0	2
117.527	4	5	1	0
120.059	8	2	1	3
122.788	8	4	3	1
123.660	8	3	3	2
131.847	6	4	2	2
136.549	8	3	0	3
140.052	12	5	2	1
143.116	2	4	4	0
155.869	2	5	3	0

Pattern : 00-004-0787 ***Radiation =*** 1.540598 ***Quality :*** High

Al

Aluminum
Aluminum, syn

2th	*i*	*h*	*k*	*l*
38.473	100	1	1	1
44.740	47	2	0	0
65.135	22	2	2	0
78.229	24	3	1	1
82.438	7	2	2	2
99.081	2	4	0	0
112.045	8	3	3	1
116.573	8	4	2	0
137.462	8	4	2	2

Lattice : Face-centered cubic
S.G. : Fm-3m (225)

Mol. weight = 26.98
Volume [CD] = 66.40

a = 4.04940

Dx = 2.699

Z = 4

I/Icor = 3.62

Color: Light gray metallic
Sample preparation: The material used for the NBS sample was a melting point standard sample of aluminum prepared at NBS, Gaithersburg, Maryland, USA.
Analysis: The chemical analysis (%): Si 0.011, Cu 0.006, Fe 0.007, Ti 0.0001, Zr 0.003, Ga 0.004, Mo 0.00002, S 0.0001, Al 99.9+ (by difference).
Temperature of data collection: Pattern taken at 25 C.
General comments: Mineral species of doubtful validity, *Am. Mineral.*, **65** 205 (1980).
Additional pattern: See ICSD 64700 (PDF 01-085-1327).
Data collection flag: Ambient.

Pattern : 04-007-1375 **Radiation =** 1.540600 **Quality :** High

CuO

Copper Oxide
Tenorite, syn

Lattice : Base-centered monoclinic
S.G. : C2/c (15)

a = 4.68370
b = 3.42260
c = 5.12880
a/b = 1.36846
c/b = 1.49851

beta = 99.54
Z = 4

Mol. weight = 79.55
Volume [CD] = 81.08
Dx = 6.516
I/Icor = 3.90

ANX: AX. LPF Collection Code: 1251099. Sample Preparation: STARTING MATERIALS:CuO. Compound Preparation: melted at 1173 K for 20 h in induction furnace (1), slowly cooled to 773 K, air-quenched, flux dissolved in hot water;powder prepared by hydrothermal recrystallization at 873 K and 180 kPa. CRUCIBLE: platinum. SOLVENT: Na_3CO_3 flux (1). Temperature of Data Collection: 293 K. Unit Cell Data Source: Powder Diffraction.
Data collection flag: Ambient.

Calculated from LPF using POWD-12++
anstrom sbrink S., Norrby L.J., Acta Crystallogr., Sec. B, volume 26, page 8 (1970)

2th	i	h	k	l
32.534	68	1	1	0
35.468	385	0	0	2
35.559	818	-1	1	1
38.754	999	1	1	1
38.968	240	2	0	0
46.276	20	-1	1	2
48.754	284	-2	0	2
51.403	14	1	1	2
53.503	98	0	2	0
56.744	8	0	2	1
58.359	141	2	0	2
61.570	190	-1	1	3
65.844	140	0	2	2
66.284	138	-3	1	1
66.543	8	3	1	0
67.973	88	1	1	3
68.144	124	2	2	0
68.927	4	-2	2	1
71.727	3	-3	1	2
72.472	63	3	1	1
73.010	2	2	2	1
75.062	53	0	0	4
75.282	55	-2	2	2
79.789	2	0	2	3
80.214	18	-2	0	4
82.408	40	-3	1	3
83.145	37	2	2	2
83.685	33	3	1	2
*83.685	33	4	0	0
86.609	13	-4	0	2
86.801	2	-2	2	3
88.081	1	1	1	4
*88.081	1	1	3	0
89.825	47	-1	3	1
91.754	20	1	3	1
95.707	9	2	0	4
98.169	2	-3	1	4
98.479	22	2	2	3
*98.479	22	0	2	4
99.845	30	3	1	3
102.137	8	4	0	2
103.442	22	-1	1	5
103.606	30	-2	2	4
105.918	1	-4	2	1
107.171	17	4	2	0
109.534	13	-1	3	3
110.247	24	-4	2	2
111.273	15	-4	0	4
113.631	24	1	1	5
114.095	13	-3	3	1
*114.095	13	4	2	1
115.811	25	1	3	3
117.009	15	-5	1	1
119.467	1	5	1	0
120.308	23	2	2	4
120.616	47	-4	2	3
*120.616	47	3	3	1
123.107	1	3	1	4
124.399	1	0	2	5
127.987	20	4	2	2
128.499	21	5	1	1
*128.499	21	0	4	0
131.061	20	-5	1	3
132.067	6	0	0	6
132.714	22	-3	3	3
133.666	12	-2	0	6
136.544	1	-1	1	6
140.178	12	-4	2	4
143.752	16	0	4	2
147.501	16	2	4	0
148.883	1	-2	4	1

Pattern : 04-007-9767 **Radiation =** 1.540600 **Quality :** High

Cu_2O

Copper Oxide
Also called: copper(I) oxide, Cuprite

Lattice : Cubic
S.G. : Pn-3m (224)

a = 4.26850

Z = 2

Mol. weight = 143.09
Volume [CD] = 77.77
Dx = 6.110
I/Icor = 7.94

ANX: A2X. LPF Collection Code: 1503192. Polymorphism: Room temperature phase. Sample Source or Locality: Canada. Temperature of Data Collection: 295 K. Unit Cell Data Source: Single Crystal.
Data collection flag: Ambient.

Calculated from LPF using POWD-12++
Kirfel A., Eichhorn K., Acta Crystallogr., Sec. A: Found. Crystallogr., volume 46, page 271 (1990)

2th	i	h	k	l
29.572	51	1	1	0
36.428	999	1	1	1
42.314	343	2	0	0
52.468	11	2	1	1
61.384	254	2	2	0
65.556	1	2	2	1
69.594	3	3	1	0
73.528	184	3	1	1
77.384	39	2	2	2
84.944	2	3	2	1
92.415	21	4	0	0
96.158	1	3	2	2
99.926	1	4	1	1
103.740	45	3	3	1
107.617	32	4	2	0
111.579	1	4	2	1
115.653	1	3	3	2
124.276	34	4	2	2
133.904	1	5	1	0
139.340	31	5	1	1

Résumé: Développement de revêtements multifonctionnels combinant les propriétés anti-corrosion et antisalissure

Introduction

Une fois qu'un métal est immergé dans l'eau de mer, les interactions entre le métal, les organismes vivants et l'environnement marin provoquent un bio-encrassement et une corrosion des composants métalliques, presque simultanément. Le développement de micro et macroorganismes à l'origine de la bio-salissure est un problème industriel important qui touche au secteur des transports maritimes, à la purification de l'eau, à l'industrie automobile, aux produits pharmaceutiques, à la microélectronique et aux industries alimentaires. Afin de développer un système antisalissure, il faut prendre en compte l'environnement, le revêtement et le substrat, comme montré sur la Figure 1, proposée par R.Holland et al [1].

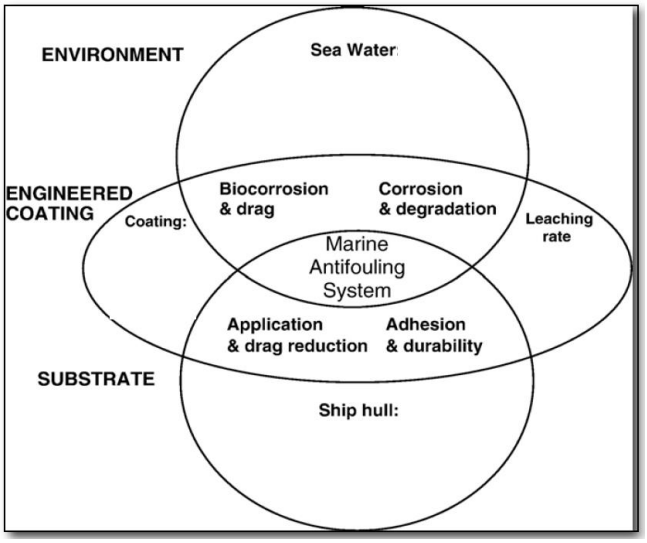

Figure 1. Paramètres affectant un système de revêtement antisalissure [1].

En même temps que les changements biologiques donnent lieu à l'accumulation de biofilms, une séquence de changements inorganiques se produit instantanément à la surface du métal après l'immersion dans un milieu aqueux agressif. Cette séquence induit un processus de dissolution du métal et la formation de produits réactionnels liés à la corrosion. Alors que la corrosion et l'accumulation de produits se développent de la surface métallique vers la solution, le développement de biofilms est un procédé inverse qui se développe de la solution vers la surface métallique.

Dans cette thèse, nous proposons un nouveau revêtement multicouche multifonctionnel composé d'une première couche d'Al-Zr et une deuxième couche de TiO_2. Il combine ainsi deux fonctionnalités : une couche antisalissure, le TiO_2, déposé sur une couche anticorrosion Al-Zr, qui protège le substrat en acier.

En effet, les alliages d'aluminium-métal de transition sont des candidats potentiels pour la protection contre la corrosion. Les métaux de transition sont ajoutés pour compenser les faibles caractéristiques mécaniques de l'aluminium pur. Un alliage d'aluminium optimisé avec une microstructure homogène a été utilisé dans ces travaux de thèse.

Le dioxyde de titane (TiO_2), candidat prometteur pour son activité photocatalytique et son comportement hydrophile/hydrophobe, ralentit le processus de bio-salissure dans les structures marines.

Le dépôt physique en phase vapeur (PVD) et le dépôt chimique en phase vapeur (CVD) sont des méthodes appropriées pour le dépôt de couches minces fonctionnelles et protectrices. Ces

méthodes permettent de contrôler les paramètres de dépôt afin d'obtenir les meilleures performances en fonction de l'application visée. Les techniques de dépôt par pulvérisation cathodique magnétron et CVD assistée par aérosol (AAMOCVD), également appelée pyrolyse d'aérosol, ont été sélectionnées pour le dépôt de films bicouches TiO_2/Al-Zr. Les films ont été caractérisés en termes de morphologie, structure cristallographique, texture, rugosité, mouillabilité de la surface, comportement électrochimique à la corrosion, l'activité photocatalytique et les propriétés antisalissures.

La demande croissante de matériaux écologiques présentant des propriétés antisalissure et anti-corrosion pour les applications marines fait face à un défi pour le développement de revêtements avancés. Dans ce contexte, l'objectif principal de cette thèse est d'utiliser des techniques de pulvérisation cathodiques magnétron à courant continu et dépôt chimique en phase vapeur afin de déposer un nouveau revêtement bicouche Al-Zr/TiO_2 combinant les deux propriétés. Al-Zr est connu pour la protection des structures métalliques contre la corrosion et les films de TiO_2 pour ses propriétés photocatalytiques sous radiation UV. Compte tenu des caractéristiques prometteuses des films Al-Zr/TiO_2, ces travaux porteront sur l'élaboration et la caractérisation des films bicouches TiO_2 et Al-Zr, afin de développer un revêtement multifonctionnel permettant d'éviter la corrosion et les biosalissures des structures utilisées en milieu marin. De plus, des essais de bio-encrassement en eau de mer naturelle, à une profondeur de 50 cm (océan Atlantique, port de Kernevel, France) ont été effectués afin d'évaluer la performance des films de TiO_2 dans l'environnement réel.

Le manuscrit de thèse est organisé en cinq chapitres.

I Etat de l'art

Ce chapitre présent un état de l'art sur les matériaux choisis et leurs fonctionnalités. Tout d'abord, l'utilisation des alliages d'aluminium-métal de transition, comme anodes sacrificielles, et la corrosion d'alliages d'aluminium dans des solutions aqueuses sont discutées en détail. Le choix du revêtement Al-Zr pour les applications de corrosion est exposé. Dans une seconde partie, les discussions portent sur les mécanismes et les applications de la photocatalyse par les semi-conducteurs en dioxyde de titane. Les principaux aspects de l'encrassement biologique et de la corrosion dans les structures marines est également présentée.

La salissure marine est définie comme la croissance et l'accumulation de micro et macroorganismes sur des surfaces mouillées dans un environnement salin. C'est un problème mondial qui affecte les industries aquatiques car cela peut réduire la vitesse des navires, augmenter la consommation de carburant et stimuler la corrosion, ce qui provoque la détérioration mécanique des structures statiques [2].

Le développement de la salissure a lieu sur presque toutes les surfaces. Ce processus commence par la fixation de molécules organiques. Il se poursuivit ensuite par l'adhérence de bactéries, diatomées et de microalgues afin de créer un biofilm qui est suivi de l'adhésion de macro-organismes, tels que les balanes, les bivalves et les macro-algues, comme indiqué sur la Figure 2.

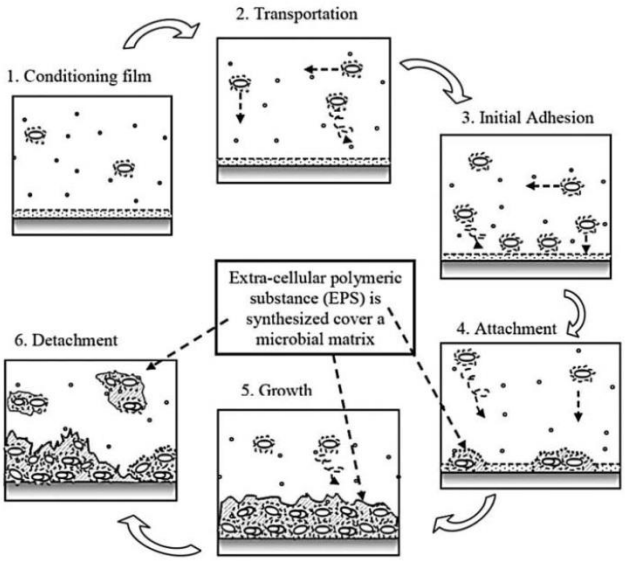

Figure 2. Étapes dans la formation de biofilms. *(Reproduit de M. Tiranuntakul,2011 [3]).*

Priyanka et al.[4] ont démontré que les matériaux photocatalytiques peuvent prévenir la bio-salissure biologique en générant des espèces réactives à l'oxygène sous irradiation par la lumière visible. Dans un environnement marin, ce mécanisme peut entraîner la mort cellulaire de nombreux contaminants [5,6].

Le titane est le métal de transition le plus abondant sur Terre et son oxyde métallique TiO_2 est un semi-conducteur à large bande interdite offrant une stabilité chimique élevée, un coût abordable, une toxicité faible et une productivité de conversion photoélectrique élevée. Au cours des dernières années, le dioxyde de titane (TiO_2) a fait l'objet de recherches approfondies pour ses remarquables propriétés photocatalytiques aux UV et autonettoyantes, qui peuvent, par exemple, favoriser la

décomposition des substances organiques présentes en produits inoffensifs, grâce aux rayons UV[7]. L'étendue de la photoactivité dépend d'une grande variété de propriétés, telles que la morphologie, la cristallinité et la surface.

Le TiO_2 possède des propriétés électroniques uniques combinées à la possibilité d'une nanostructuration et d'une stabilité chimique. En règle générale, lorsque la surface d'un matériau semi-conducteur est exposée à des photons ayant une énergie supérieure ou égale à son énergie de bande interdite, des photo-électrons e^- et des photo-trous h^+ sont produits [8]. Le photocatalyseur étant à la fois capable d'adsorber les réactifs et d'absorber les photons, les e^- et h^+ photogénérés peuvent alors réduire et/ou oxyder les polluants adsorbés à la surface du photocatalyseur [9], comme illustré sur la Figure 3.

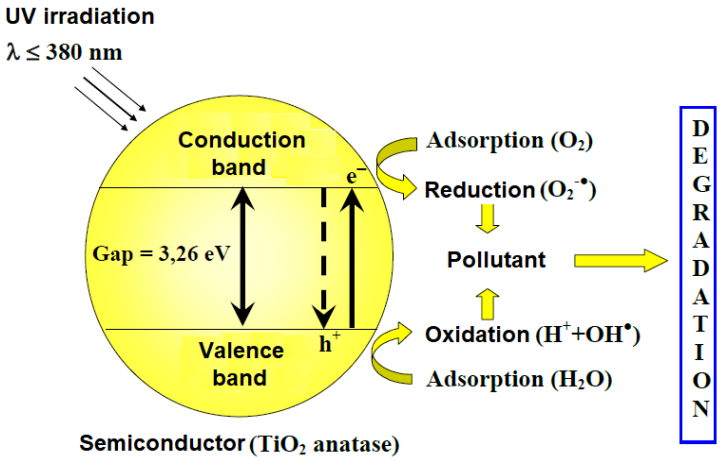

Figure 3. Schéma réactionnel simplifié de la photocatalyse.

Les nanostructures et les microstructures jouent un rôle important dans l'amélioration des performances des dispositifs, principalement en raison de l'augmentation de la surface spécifique [10], comme dans le cas des réactions photocatalytiques. Les structures de TiO_2 qui ont une mésoporosité et une surface spécifique élevées sont attractives, car elles augmentent l'efficacité des phénomènes de photocatalyse qui se produisent en surface. La morphologie, la structure, la phase et la dimensionnalité ajustent les propriétés physiques et chimiques des nanostructures de TiO_2. Tian [10] a démontré que le TiO_2 en forme de fleur 3D présentait la plus grande absorption de la lumière UV lorsqu'il était intégré dans des cellules solaires à pigment photosensible comparé à des nanosphères et à des structures de nanorodes. L'activité photocatalytique (efficacité de dégradation de 97%) pour les fleurs était supérieure à celle des sphères ou des structures en forme de bâtonnets

(respectivement 60% et 55%). Celles-ci sont principalement dues au fait que les structures 3D en forme de fleurs hiérarchiques sont facilement accessibles à la lumière et aux réactifs grâce à une surface effective accrue.

Zhu et al.[10] ont également démontré que les matériaux de TiO_2 anatase ayant des morphologies en forme de fleur avec une surface spécifique élevée présentaient d'excellentes performances lors d'essais en photodégradation du bleu de méthylène.

Il a déjà été démontré que le procédé dépôt chimique en phase vapeur assisté par aérosol (AA-MOCVD) permettait de déposer des films de TiO_2 composé des micro-feuilles hiérarchisées de TiO_2. Biswas et al.[11] ont montré que ce procédé de dépôt, fonctionnant à la pression atmosphérique, permettait la synthèse de micro-fleurs de TiO_2 liées physiquement à un film mince de TiO_2. Nous proposons d'utiliser ces microstructures en tant que couche active de TiO_2 dans le revêtement bicouche.

L'aluminium et ses alliages sont largement utilisés dans de nombreuses applications industrielles comme matériau sacrificiel pour la protection de l'acier, car leur potentiel en circuit ouvert est plus négatif. Les revêtements en alliage à base d'aluminium ont fait l'objet de nombreuses études et ont été proposés comme candidats potentiels à la protection contre la corrosion galvanique des pièces en acier mécaniques [12–15]. Par exemple, des métaux de transition (TM) peuvent être ajoutés pour renforcer mécaniquement l'aluminium. La faible solubilité des métaux de transition dans l'aluminium permet le dépôt d'une solution solide sursaturée dans l'aluminium. De plus, une bonne stabilité thermique due à la faible diffusivité du métal de transition dans l'aluminium est attendue. L'ajout d'une teneur élevée en métal de transition conduit généralement à des propriétés mécaniques élevées par rapport à l'aluminium pur, mais au détriment des propriétés sacrificielles[16,17]. La solution idéale en matière de protection des aciers doit être un compromis entre propriétés mécaniques et propriétés anticorrosion.

Le zirconium est un métal de transition connu comme raffineur de gros grains dans les alliages d'aluminium traditionnels[18]. Il renforce les propriétés mécaniques [18] et améliore considérablement la résistance à la corrosion dans une solution désaérée d'acide borate-borique contenant du Cl^- [19]. Contrairement aux méthodes traditionnelles où la solubilité solide du Zr est très faible (la solubilité maximale est de 0,083 at.% dans la réaction péritectique[20]), les méthodes de traitement hors équilibre telles que la solidification rapide[21], l'alliage mécanique et les

technique de pulvérisation cathodique [19,22,23] offrent la possibilité d'obtenir une solution mono-solide sursaturée à haute teneur en Zr.

Afin d'améliorer l'efficacité des anodes en aluminium, celles-ci sont généralement alliées à d'autres éléments pour favoriser le retrait de la couche de passivation (rupture du film d'oxyde) et /ou déplacer le potentiel de fonctionnement du métal dans une direction plus négative. L'ajout d'éléments comme Zr engendre une augmentation du potentiel de corrosion. De plus, l'augmentation de la teneur en Zr dans Al permet également de réduire la densité du courant de corrosion, ce qui est associé à une meilleure résistance à la corrosion.

Creus et al. ont [24] présenté la classification du potentiel en circuit ouvert de métaux et d'alliages à base d'Al déposés par PVD dans une solution saline comme représenté à la Figure 4. Les potentiels de corrosion du revêtement Al – Zr sont plus négatifs que le seuil de potentiel nécessaire pour obtenir la protection cathodique des aciers en solution saline. Il a été signalé que l'ajout d'éléments tels que V, Mn, Cr, Ti, Mo, Si ou Zr induit un ennoblissement du potentiel de corrosion par rapport à celui de l'Al pur lorsque la teneur en éléments d'alliage est augmentée.

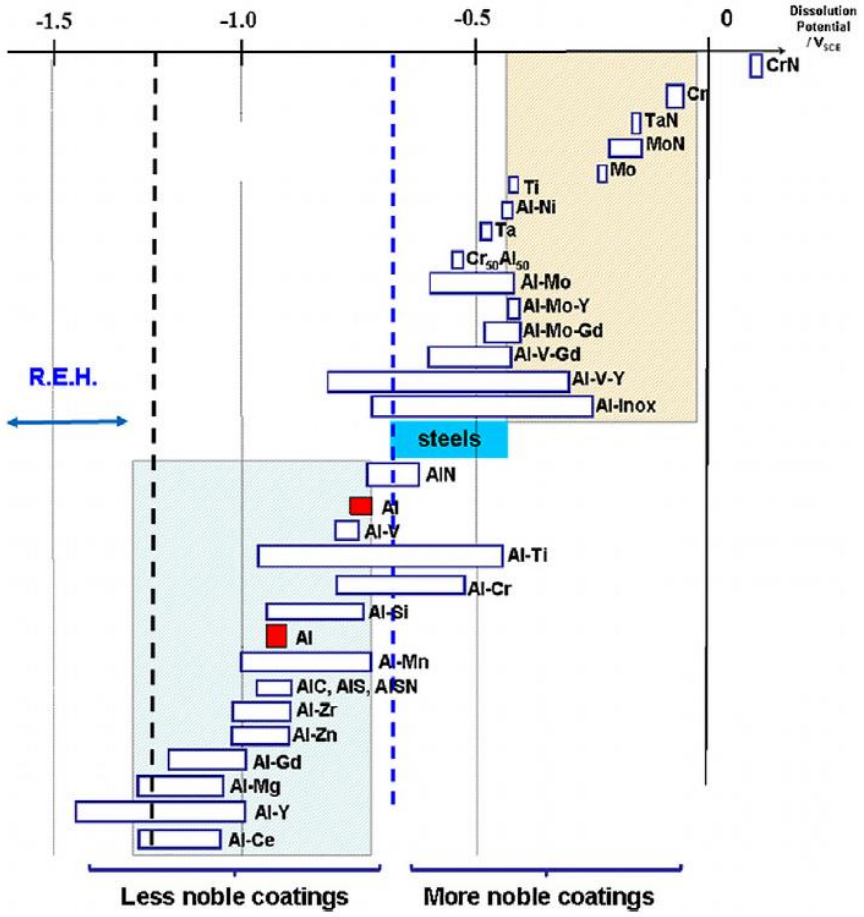

Figure 4.Classification du potentiel en circuit ouvert de métaux et des alliages à base d'Al déposes par PVD dans une solution saline (Reproduit de J. Creus et al., 2012 [24]).

II Dépôt et caractérisation des films d'Al-Zr

Les technologies de dépôt physique en phase vapeur (PVD) sont largement utilisées pour la synthèse de couches minces.

Dans les procédés physiques en phase vapeur, le revêtement est déposé par condensation à partir d'un flux d'atomes neutres ou ionisés de métaux. Les différents processus PVD peuvent être distingués par le type d'évaporation des espèces métalliques et les conditions de plasma utilisées lors du processus de dépôt [1].

La pulvérisation magnétron est une technologie PVD couramment utilisée en raison de sa vitesse de dépôt élevé et de ses bonnes performances (reproductibilité, homogénéité, etc.). Cette technique est compatible avec la synthèse de films sur de grandes surfaces. Le procédé de

pulvérisation utilise des ions argon pour bombarder une cible composé du matériau de revêtement. Les atomes cibles pulvérisés se déposent à la surface du substrat, ce qui entraîne la croissance de la couche.

Des alliages Al-Zr ont été déposés à partir de cibles métalliques en Al et Zr dans une atmosphère d'argon pur à une température de flottement (< 80 °C). Le débit massique total d'argon et la pression de travail ont été maintenus constants à 50 sccm et P_{ar} = 0,33 Pa, respectivement. Le système de dépôt est illustré à la Figure 5.

Les substrats ont été placés sur un porte-substrat rotatif (10 tours par minute) assurant une bonne homogénéité d'épaisseur et de composition des revêtements.

Une gravure ionique (puissance de 500W, pression d'argon de 0,3 Pa, durée de 30 min) est systématiquement réalisée avant chaque dépôt pour améliorer l'adhérence du film.

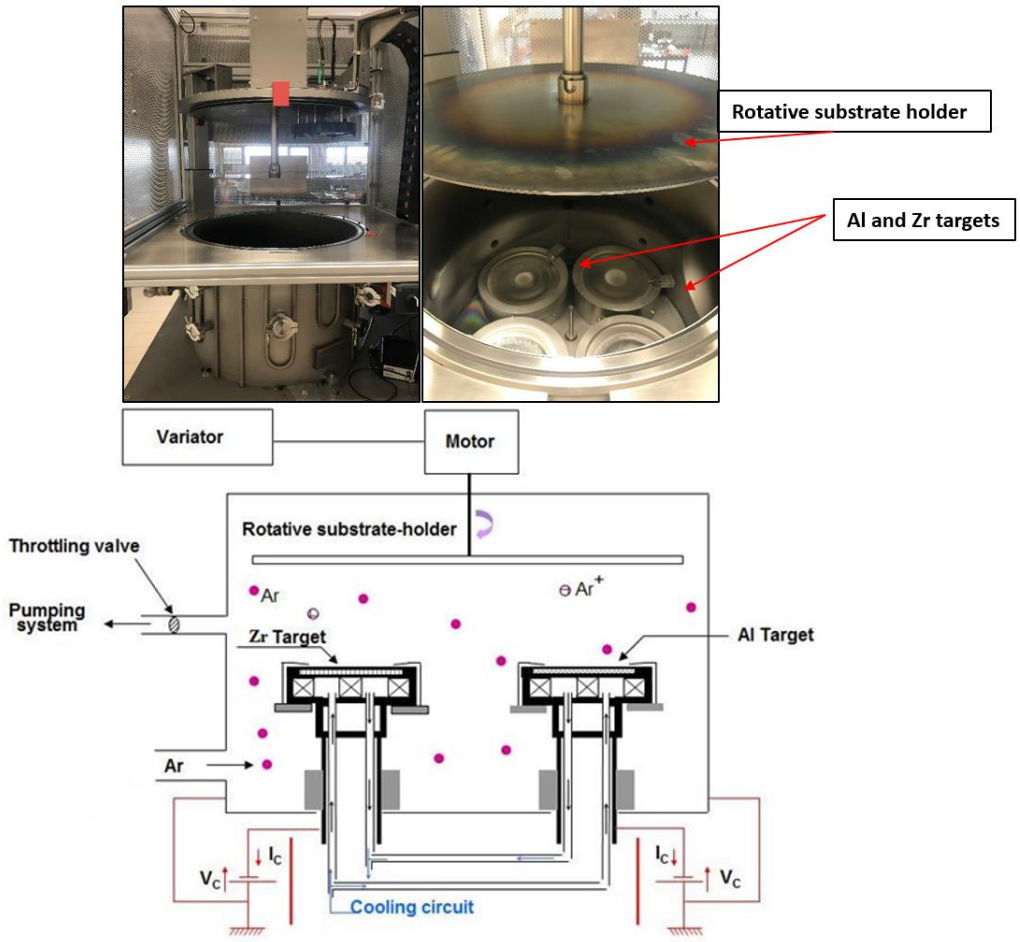

Figure 5. Schéma de la machine pulvérisation cathodique magnétron Delphis 4.

L'évolution de la quantité en Zr a été assurée en fixant le courant de décharge de l'aluminium à 2,0 A et en ajustant celui du Zr entre 0 et 1,3 A.

Afin de développer de nouveaux revêtements Al-Zr en tant qu'anodes sacrificielles, nous avons d'abord étudié l'effet de la teneur en zirconium sur les propriétés des alliages Al-Zr déposés par pulvérisation cathodique magnétron en courant continu.

Des films Al-Zr avec des teneurs en Zr comprises entre 0 et 27 at.% ont été déposés sur des lames de verre et sur des substrats en acier rapide (HSS) par pulvérisation cathodique magnétron.

Des films Al-Zr ayant une teneur en Zr inférieure à 10 at. % ont présenté des pics de diffraction bien définis correspondant à la structure cubique à faces centrées. Cela indique que c'est une croissance d'une solution solide sursaturée de Zr dans Al. Pour les contenus supérieurs à 10 at. %, les pics de diffraction deviennent plus larges. L'élargissement du pic résulte d'un raffinage du grain lorsque la teneur en Zr augmente. La morphologie des alliages Al-Zr confirme que les revêtements deviennent plus compacts à mesure que la teneur en zirconium augmente.

L'évolution de la nanodureté avec la teneur en Zr est due à un effet combiné de la diminution de la taille moyenne des grains (effet Hall-Petch), ainsi qu'à l'effet de durcissement en solution solide.

Le film d'Al-Zr déposé sur du verre contenant une teneur en zirconium de 4 at. % présente une résistance optimale à la corrosion après 1 heure d'immersion dans l'eau salée, car elle présente une densité de courant plus basse et un potentiel de corrosion plus élevé. Pour cela, Al-Zr (4% at. Zr) a été choisi comme première couche afin d'apporter des propriétés anticorrosion.

III Dépôt et caractérisation de couches minces de TiO_2

La première partie de ce chapitre est consacrée à l'étude de l'influence des paramètres de dépôt chimique en phase vapeur sur le processus de croissance des films de TiO_2 sur silicium. La microstructure, les propriétés physiques et l'activité photocatalytique seront traitées dans la deuxième partie. L'objectif est de définir les paramètres de dépôt pour faire croître des films de TiO_2 en phase anatase, correspondant aux conditions optimales du photocatalyseur. Le dépôt de films de TiO_2 sur un substrat en acier rapide (HSS) est présenté à la fin du chapitre à des fins de comparaison.

Le dépôt chimique en phase vapeur assisté par aérosol est basé sur le transport du précurseur en phase liquide en générant un aérosol à partir d'une solution source. Des petites gouttelettes sont transportées par un gaz vecteur dans la zone de réaction. La zone de réaction est chauffée, provoquant dans une très petite région l'évaporation du solvant et des précurseurs, ainsi que la réaction sur le substrat. Le précurseur de titane utilisé dans ces travaux de thèse est le titanyl (bis) acetylacetonate $(TiOAcAc)_2$. Ce précurseur se dissout facilement dans les alcools.

Dans ce travail, nous avons utilisé du butanol ou de l'éthanol comme solvant. Pour préparer une solution de précurseur avec une concentration de 0,03 $mol \cdot l^{-1}$, 4,71 g de précurseur sont ajoutés dans 600 ml de solvant alcoolique (butanol-01 ou éthanol). Le mélange est agité jusqu'à dissolution complète à l'aide d'un barreau magnétique à une vitesse de 300 cycles/min. Une fois que la solution de précurseur devient jaune claire après 30 minutes d'agitation, elle est prête pour le dépôt. Elle est alors stable pendant plusieurs mois.

Les substrats utilisés pour le dépôt de films de TiO_2 étaient des substrats en Si (100), en verre de corning (référence C1737-S111) et des substrats en acier à haute vitesse. Avant chaque dépôt, les substrats ont été nettoyés par ultrasons dans une solution d'éthanol pendant 10 minutes.

Nous avons utilisé pour ce travail un réacteur AAMOCVD fait maison, présenté en Figure 6 . La Figure 6a illustre un schéma du réacteur et la Figure 6b représente l'image du système réel. La solution de précurseur est placée dans un pot de pulverisation. Les ultrasons sont générés par une membrane piézoélectrique, avec une certaine puissance et fréquence. En conséquence, un brouillard blanc contenant des gouttelettes de la solution de précurseur est créé à la surface de la solution. Le générateur de fréquence a été fourni par la société RBI et permet de produire des fréquences comprises entre 640 kHz et 870 kHz.

Deux boutons règlent la fréquence et la puissance sur une échelle arbitraire entre 0 et 10 unités. La fréquence optimale est déterminée en observant la surface de la solution tout en changeant le potentiomètre. Lorsque nous approchons de la fréquence de résonance, la surface est recouverte d'ondes concentriques d'intensité maximale au centre du pot. La fréquence optimale est atteinte lorsque la déformation de la surface est maximale. Durant ces travaux, le potentiomètre est réglé sur 2,0, ce qui correspond à une fréquence de 800 kHz.

Le brouillard est ensuite transporté par un flux de gaz utilisé comme gaz vecteur (CG # 1) vers la chambre de réaction. Dans notre cas, le gaz vecteur est un flux de gaz oxydant constitué d'air (20% de dioxyène) avec un débit de 3 $L.min^{-1}$. Avant d'entrer dans la zone de réaction, un gaz

constitué d'air et avec un débit de 3 $L.min^{-1}$ (CG # 2) est ajouté au flux de précurseur. Ce second flux est introduit à partir de la partie centrale pour des raisons de sécurité et accélère le précurseur sur la plaque chauffante supérieure, où se déroule la réaction. Un entonnoir au sommet du substrat permet d'étendre le flux de précurseur sur une plus grande surface. La plaque chauffante de 20 x 20 cm^2 permet de chauffer jusqu'à 550 °C.

Un système d'extraction est placé en bas à droite sous la plaque chauffante. Dans ce travail de thèse, nous avons utilisé une pression d'extraction égal à 3 mmH_2O. Les sous-produits de la réaction et le solvant évaporé sont ainsi extraits et passent par un piège à solvant refroidi à l'azote liquide.

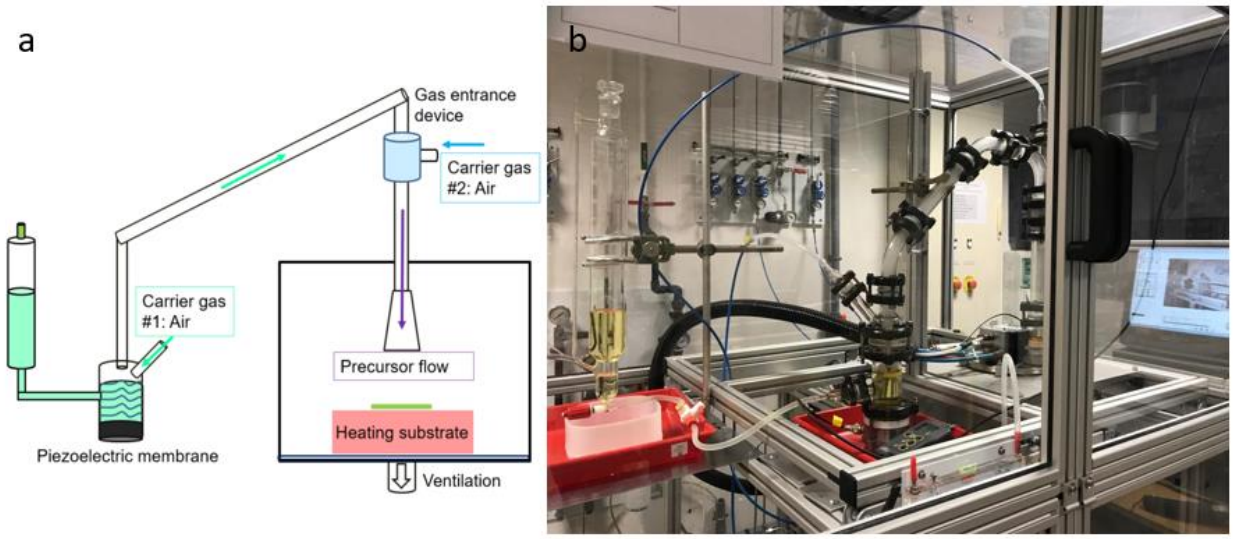

Figure 6. Schéma de la machine dépôt chimique en phase vapeur.

L'optimisation des paramètres de dépôt permet le développement et la croissance de micro-fleurs de TiO_2, de phase anatase, dispersées sur une couche mince de TiO_2. Les conditions de croissance optimales ont été obtenues en ajustant la température de dépôt et le débit de précurseur (vitesse de consommation de la solution).

Les paramètres optimaux de dépôt sont : le précurseur titanyl (bis) acétylacétonate avec une concentration de 0,03 M, une gamme de température comprise entre 500 °C à 550 °C, une vitesse de consommation de solution supérieure à 3 mL/min et une durée de dépôt de 40 minutes. Pour ces températures, des micro-fleurs de TiO_2 d'environ 7 à 8 µm de diamètre sont formées. La diffraction des rayons X confirme la phase anatase des films de TiO_2. Il est important de noter que la formation des micro-fleurs est très sensible à la température de dépôt. À des températures inférieures, telles que 400°C, aucune fleur n'est créée.

Les mesures d'activité photocatalytique de nos échantillons en couche mince ont été faites afin de comparer et comprendre le comportement photocatalytique des différents films. La molécule modèle étudiée dans ce travail est un colorant azoïque nommé orange G (***OG***, commercialisé par Aldrich et de formule brute : $C_{16}H_{10}N_2Na_2O_7S_2$). Pour nos mesures d'activité photocatalytique, 100 ml d'une solution aqueuse d'OG (de concentration 5.10^{-5} M) sont versés dans un bécher. L'échantillon est inséré dans un support en verre, à une distance de 8 mm par rapport au bas du porte échantillon. Ensuite, l'échantillon et son support sont disposés au fond du bécher. La face recouverte par la couche TiO_2 (face active) est orientée vers le fond du bécher. Le bécher est ensuite positionné sur un support permettant de le maintenir à 20 mm au-dessus de trois lampes UV (Philips PLS 11W). Ces lampes émettent un spectre continu dans le domaine des UV-A (émission UV-B et UV-C négligeable), avec un maximum d'émission situé à 365 nm, et fournissent une intensité lumineuse au niveau de l'échantillon d'environ 5 mW/cm^2. Le tout est placé dans une étuve régulée en humidité (RH = 40%) et température (T = 20 °C). La solution est agitée continuellement via un barreau aimanté et un agitateur magnétique fixé à 500 tr/min.

Une faible quantité de solution (environ 3 ml), comparée au volume total, est prélevée toutes les trente minutes afin de mesurer par spectrométrie UV-Visible l'évolution de la concentration d'OG, puis réinjectée dans la solution.

La loi de Beer-Lambert montre que la concentration d'OG (***C***) est une fonction de l'absorbance mesurée ***A*** (Équation 1) :

$$A = \alpha \, .l.C \qquad \textit{Équation 1}$$

où α est le coefficient d'absorption molaire à la longueur d'onde mesurée et **l** le trajet de lumière dans la solution (1 cm dans notre cas). Dans cette étude, la mesure de A est effectuée à 480 nm, ce qui correspond au maximum d'absorption de l'OG. Dans nos conditions, les paramètres l et α sont constants ce qui signifie que A est directement proportionnel à C.

La vitesse de dégradation du réactant r est écrite par l'équation 2 où la constante k décrit une constante cinétique apparente du système. Etant donné la faible concentration en OG des solutions aqueuses utilisées lors de ce travail (5.10^{-5} M), le terme K_{ads}.C est très inférieur à 1 et peut donc être négligé dans l'équation 2 qui devient :

$$r = -\frac{dC}{dt} = k_c \, . K_{ads} \, . C = k.C \qquad \textit{Équation 2}$$

Par intégration de l'équation 2 on obtient l'équation 3, responsable pour déterminer la constante cinétique k.

$$ln\left(\frac{A_0}{A}\right) = \left(\frac{C_0}{C}\right) = k.t_{UV} \qquad \textit{Équation 3}$$

où C_0 représente la concentration en OG déduite d'une mesure de l'absorbance A_0 à 480 nm au début de l'irradiation (après la période de maintien dans le noir) et C est la concentration mesurée à partir de l'absorbance A après une exposition de durée t_{UV}. La représentation de ln(A0/A) = f(t_{UV}) doit donc donner une droite passant par l'origine dont la pente permet de déterminer la constante cinétique k.

Les films de TiO_2 déposés à 550 °C montrent une meilleure performance photocatalytique, avec une valeur de k supérieure (0,00153 min^{-1}), comparés aux films déposés à des températures de dépôt plus basses (500 et 400 °C). Le niveau de minéralisation du colorant Orange G est de 30% après 240 min sous lumière ultraviolette p, comme illustré par la Figure 7. Ces films présentent une plus grande densité des micro-fleurs sur la surface du film, qui génèrent une surface rugueuse et une plus grande surface spécifique. Ces caractéristiques sont importantes pour assurer une photoactivité.

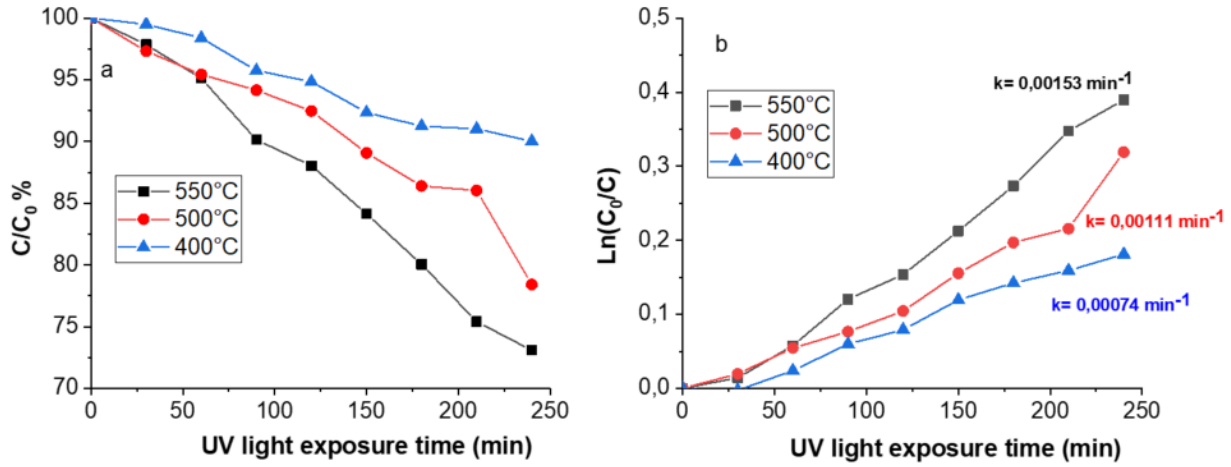

Figure 7.a) Activité photocatalytique relative de différents films de TiO_2 déposés sur du silicium (d'une épaisseur d'environ 250 nm). b) Cinétique de décomposition photocatalytique de l'orange G mesurée pour différents films de TiO_2 sous radiation UV.

Ce chapitre confirme le rôle fondamental des micro-fleurs d'une taille moyenne de 7 µm et de sa densité sur la surface du film dans le processus de photocatalyse.

IV Caractérisations de bicouches Al-Zr / TiO_2

Ce chapitre présente les propriétés fonctionnelles d'un revêtement bicouche associant l'alliage Al-Zr (4 at. % Zr) déposé pulvérisation cathodique magnétron et le TiO_2 déposé par dépôt chimique en phase vapeur assisté par aérosol sur des substrats d'acier rapide. Le film Al-Zr (4 at.% Zr) a été utilisé pour apporter des propriétés anticorrosion destinées à assurer une protection sacrificielle de l'acier. Le film TiO_2 a été ajouté en tant que seconde couche pour induire une activité photocatalytique et un comportement hydrophile pouvant générer des propriétés antisalissure afin de ralentir processus de bio-encrassement.

Dans un premier temps les propriétés microstructurales et physiques des films bicouches sont analysées. Dans un deuxième temps, les propriétés fonctionnelles telles que le comportement électrochimique et les propriétés de photocatalyse de films bicouches sont traitées.

La morphologie des films d'Al-Zr, observée par MEB, est illustrée sur la Figure 8 (a-b) avec un grossissement faible et élevé, respectivement. Une coupe transversale est représentée sur la Figure 8c. Pour une faible teneur en Zr, les revêtements se développent avec une morphologie en colonne formant de gros grains d'environ 500 nm de diamètre. L'épaisseur d'Al-Zr est de 3 µm.

Lors du dépôt de TiO_2 par AACVD sur le revêtement Al-Zr, deux types de caractéristiques sont apparus. D'une part, un film constitué de petits grains de 50 nm en forme d'aiguille (microsphères dendritiques) recouvre les grains d'Al-Zr de manière conforme. Cette morphologie peut être observée sur la Figure 8 (e-h-k), pour les trois températures de dépôt utilisées.

Les grains d'Al-Zr peuvent encore être identifiés même si l'épaisseur du film de TiO_2 est d'environ 400 nm. D'autre part, les micro-fleurs ont commencé à croître à une température de dépôt supérieure à 500 °C. Sur la Figure 8 (d-f), on peut observer que les micro-fleurs obtenues à 500°C sont beaucoup plus petites que celles obtenues à 540-550°C (Figure 8 (g-i) et (j-l)). Par ailleurs, pour les films déposés à 540 ° C et à 550 ° C une densité de micro-fleurs assez élevée est observée à la surface. Les films de TiO_2 déposés à 500 °C, 540 °C et 550 °C ont un pourcentage de surface couverte par micro-fleurs égal à 8 %, 23 % et 43 %, respectivement.

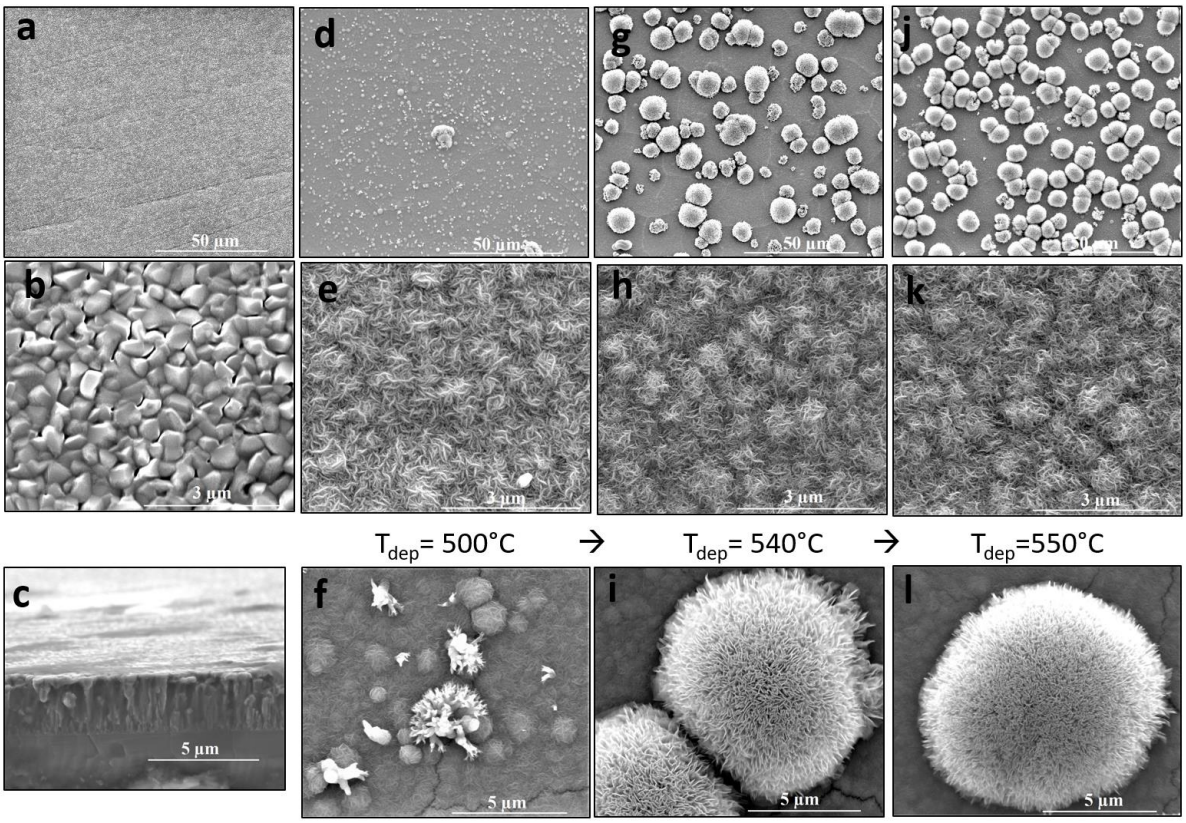

Figure 8. Clichés MEB des films: a-b-c) Al-Zr (4 at.% Zr) et bicouche Al-Zr/TiO_2 déposé à d-e-f) 500 °C, g-h-i) 540 °C and j-k-l) 550 °C.

Les fleurs ayant un diamètre moyen d'environ 7 µm peuvent être décrites par une association homocentrique de nano pétales de TiO_2 formant une corolle comme si elle poussait dans le réceptacle d'une fleur. Ces pétales ont une épaisseur nanométrique (~ 5 nm) et sont formés par des nanocristaux d'anatase.

La diffraction des rayons X et la spectroscopie Raman confirment que les micro-fleurs de TiO_2 et les films sont constitué d'une phase d'anatase pure pour les films déposés dans une gamme de température comprise entre 500 °C et 550 °C.

Concernant l'activité photo catalytique, la température de dépôt a une influence sur le taux de dégradation du colorant pour les films contenant des micro-fleurs de TiO_2. Elle a une valeur maximale dans le cas du film déposé à 550 °C, qui montre 50% de minéralisation après 400 min d'exposition aux rayons ultraviolets. Pour le film déposé à 540 °C, la valeur est de 30% de minéralisation pour le même temps d'exposition et le film déposé à 500 °C montre 20% de minéralisation du colorant Orange G. Pour les films sans la présence de micro-fleurs déposées à

500 °C et à 550 °C la constante k est inférieur d'un ordre de grandeur à celle des films contenant des micro-fleurs déposées à la même gamme de températures. Les micro-fleurs, constituées d'une petite taille de cristallites, augmentent grandement la surface spécifique et renforcent ainsi l'activité photocatalytique. En effet, elles améliorent le taux de dégradation des polluants organiques en multipliant les sites actifs d'absorption dans TiO_2. Par ailleurs, l'augmentation de la surface spécifique permet également l'absorption des réactifs sur le photocatalyseur et une augmentation de l'absorption de la lumière.

Les films bicouches Al-Zr /TiO_2 ont été irradiés avec une lumière UV pendant 4 heures et l'angle de contact avec l'eau a été mesuré à différentes durée d'exposition. Pour tous les films, l'angle de contact a fortement diminué avec le temps d'environ 60° à 0° après 4 heures, indiquant un caractère superhydrophile photo-induit. Il est intéressant de noter que, même après six mois sans aucune irradiation UV, les échantillons restent superhydrophiles avec un angle de contact d'environ 5°.

Afin de tester la résistance à la corrosion des films, des mesures électrochimiques ont été effectuées dans une solution saline aérée et agitée. Les courbes de polarisation des aciers revêtus avec Al-Zr, TiO_2 et bicouche Al-Zr /TiO_2sont présentées à la Figure 9 et comparées à celles de l'acier nu.

Les revêtements bicouches Al-Zr/TiO_2 se sont révélés être une alternative intéressante pour préserver le caractère sacrificiel de la protection des structures en acier en milieu salin, montrant un potentiel de corrosion de -0,61 V vs Ag/AgCl. Ces revêtements bicouches Al-Zr /TiO_2 déposés sur des substrats en acier offrent une bonne protection grâce à l'oxydation préférentielle de la bicouche. Ces échantillons présentent une faible densité de courant de corrosion avec une valeur égale à 4,01 x 10^{-7} A /cm^2. L'échantillon formé par une bicouche d'Al-Zr/TiO_2 réduit l'activité électrochimique des films par la formation d'un film passif et dense, et augmente également la résistance aux piqûres lorsque la cinétique de la réaction cathodique est plus basse.

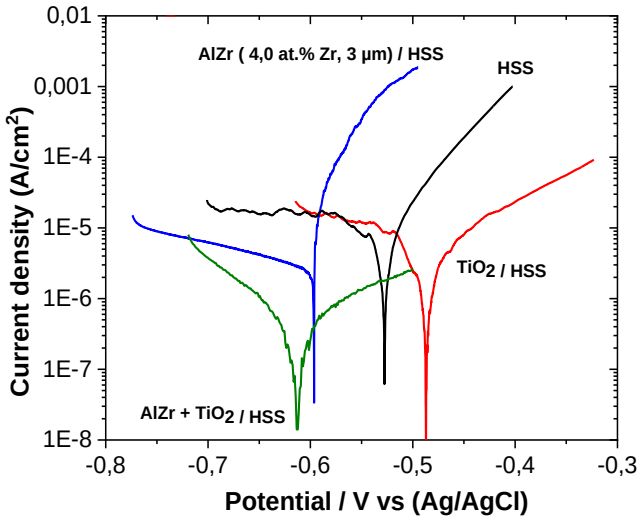

Figure 9. Courbes de polarisation des films Al-Zr (4 at. % Zr), TiO_2 et TiO_2/Al-Zr déposés sur acier rapide après 1h d'immersion dans une solution 5 wt.% NaCl.

V Nouveaux films de Cu-Ti-O pour des applications photocatalytiques et anti-encrassement

Dans ce chapitre, l'influence de l'incorporation de cuivre dans des couches minces de TiO_2 sur l'activité structurelle, optique, photocatalytique et les propriétés antisalissure des films TiO_2 a été étudiée. Les films Cu-Ti-O avec des différentes teneur en cuivre ont été déposés par dépôt chimique en phase vapeur assisté par aérosol en utilisant les mêmes paramètres que ceux utilisés pour le dépôt des films de TiO_2, mais à partir de solutions qui contenaient une mélange de précurseurs. Les propriétés des composés obtenus ont été évaluées par diffraction des rayons X, spectroscopie Raman, XPS, spectromètrie UV- Visible et MET, ainsi que par des tests de dégradation photocatalytique d'Orange G. Les tests de biossalisure in-situ ont été réalisés sur le port de Lorient en France afin d'évaluer les performances antisalissure des revêtements.

Cu(II) acetylacetonate ($Cu(AcAc)_2$) a été utilisé comme précurseur de cuivre et des solutions de départ avec une concentration de 0,01M et 0,03M ont été préparées en utilisant de l'éthanol comme solvant. Ethylène diamine à 0,01M a été ajouté en tant que dispersant. La solution préparée de $Cu(AcAc)_2$ (0,01M ou 0,03M) est ensuite mélangée à une solution de $Ti(AcAc)_2$ dissoute dans de l'éthanol à une concentration de 0,03M.

La spectroscopie de rayons X à dispersion d'énergie (EDS) a été utilisée afin de quantifier la quantité de Cu présent dans les films (Tableau 1). Les solutions contenant 33% de cuivre produisent

des films avec une quantité de cuivre égal à 16 at.% Cu lorsqu'ils sont déposés sur des substrats de silicium et verre.

De plus, les solutions contenant 50 % de cuivre produisent des films avec un teneur en cuivre comprise entre 50 at.% Cu et 66 at.% Cu pour le substrat de silicium, entre 50 at.% Cu et 75 at.% Cu pour le verre et entre 25 at.% Cu et 50 at.% Cu pour les substrats d'acier rapide revêtus d'Al-Zr.

Tableau 2. Cu-Ti-O films déposes sur Si, verre et Al-Zr/HSS.

Solutions	**% Cu dans solution**	**Cu/(Cu/Ti) pour films déposés sur Si (at.% Cu)**	**Cu/(Cu/Ti) pour films déposés sur verre (at.% Cu)**	**Cu/(Cu/Ti) pour films déposés sur Al-Zr /HSS (at.% Cu)**
Solution 1 Ti(AcAc)2 **0.03 M** + Cu(AcAc)2 **0.01 M**	33	16	16	-
Solution 2 Ti(AcAc)2 **0.03 M** + Cu(AcAc)2 **0.03 M**	50	50	50	25
		55	58	50
		66	75	

La morphologie est assez différente pour les films contenant du cuivre. Les micro-fleurs ne sont plus présentes et lorsque la teneur en cuivre augmente, la morphologie devient granuleuse et rugueuse.

La Figure 10 montre que tous les échantillons présentent des pics de diffraction pour la phase anatase, comme en témoignent les pics dominants à 2θ = 25.5°, 37.9°, 47.9 °, 54.1° et 55.1° correspondant au (1 01), (0 0 4), (2 0 0), (1 0 5), (2 1 1), (2 0 4), (2 2 0) et (2 1 5) plans respectifs de diffraction.

Cu-Ti-O films avec un teneur en cuivre égal ou supérieur à 50 at.% Cu ont montré la présence de Cu_2O par des mesures de diffraction des rayons X dans la configuration Bragg-Brentano et en incidence rasante. Le spectre a montré des pics de Cu_2O correspondant aux plans cristallins (110), (1 1 1), (2 0 0), (2 2 0) et (3 1 1) à 2θ = 29.57°, 36.43°, 42.31°, 61.38° et 73.53°. Les films avec un avec un teneur en cuivre égal ou supérieur à 50 at.% Cu ont révélé une petite quantité de CuO correspondant aux plans cristallins (-1 1 1) et (1 1 1) à 2θ = 35.55° et 38.75°.

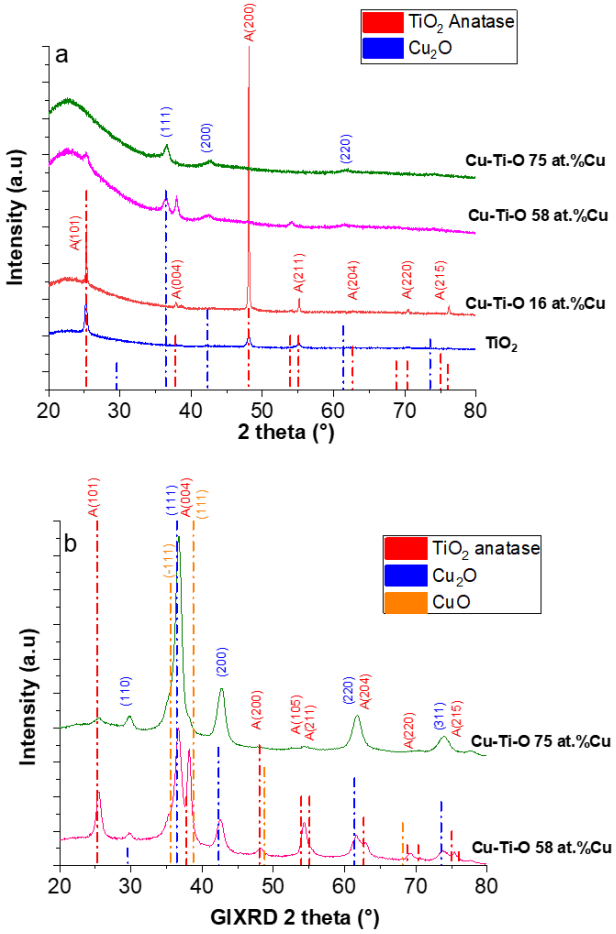

Figure 10. Spectres DRX des films de TiO_2 et Cu-Ti-O déposés sur verre à 550 °C a) en mode Bragg-Brentano. b) En incidence rasante.

La spectrométrie UV/VIS a été effectuée dans un spectrophotomètre Lambda 950 de Perkin Elmer, dans la gamme de 250 nm à 2500 nm à fin de mesurer les énergies de bande interdite.

L'étude par spectroscopie UV-Visible a montré que l'énergie de bande interdite diminue avec l'augmentation de la teneur en Cu. L'ajout de Cu a entraîné une réduction de la bande interdite de 3,55 eV pour le film de TiO_2 pur à 3,40 eV et 2,88 eV pour les films Cu-Ti-O 75 at.% Cu déposés sur un substrat de verre, respectivement. Il a également été découvert qu'une fois que la teneur en cuivre augmente, cela décalait le bord d'absorption du TiO_2 vers un régime visible décrivant la modification possible de la structure de la bande électronique.

Les mesures de photocatalyse ont montré que le film de TiO_2 pur avec des micro-fleurs sur la surface, les films Cu-Ti-O 50 at.% Cu et Cu-Ti-O 55 at.% Cu présentent les meilleures performances de dégradation photocatalytique du composé organique Orange G, comme représenté sur la Figure 11 .

Ces résultats montrent qu'une forte teneur en cuivre est préjudiciable à l'activité photocatalytique.

Cela peut être expliqué par le taux de recombinaison électron-trou qu'augmente une fois l'augmentation de la concentration en Cu[25,26].

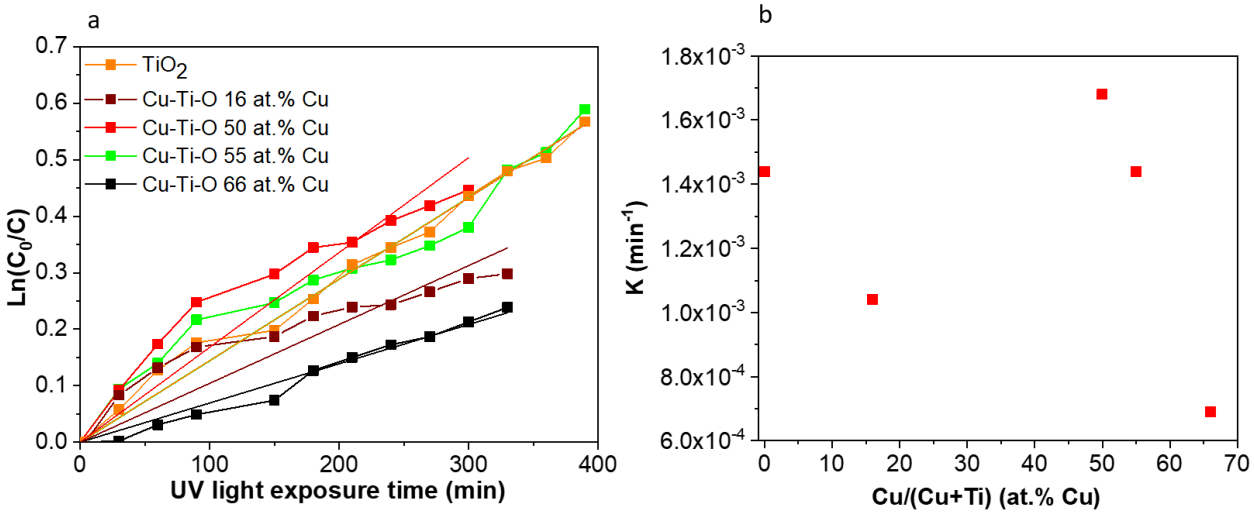

Figure 11. a) Cinétique de décomposition photocatalytique de l'OG à la surface des films TiO_2 et Cu-Ti-O avec différentes teneurs en Cu sous irradiation UV (371 nm). b) Evolution de la constant k avec la teneur en Cu.

L'immersion dans l'eau de mer permet d'avoir le plus authentique test afin d'évaluer l'efficacité antisalissure, offrant un site propice au développement de différents micro et macro-organismes. Dans ce travail, des tests d'encrassement biologique ont été réalisés afin de comparer des revêtements avec différentes compositions.

Des films de TiO_2 purs et les films Cu-Ti-O ont été déposés sur un substrat de verre (Corning glass reference C1737-S111) puis immergés dans de l'eau de mer. Pendant les trois mois d'immersion, le degré de salissure par inspection visuelle a été estimée chaque semaine (ASTM D 3623) [27].

Trois films différents ont été testés : TiO_2 pur, Cu-Ti-O 16 at.% Cu et Cu-Ti-O 50 at.% Cu.

Des échantillons de 1,5 x 1,5 cm et de 5 x 5 cm ont été collés sur des panneaux de polycarbonate. Les panneaux sont d'abord collés sur un support, puis immergés dans la mer, à une profondeur de 50 cm (océan Atlantique, port de Kernevel, France), comme représenté à la Figure 12.

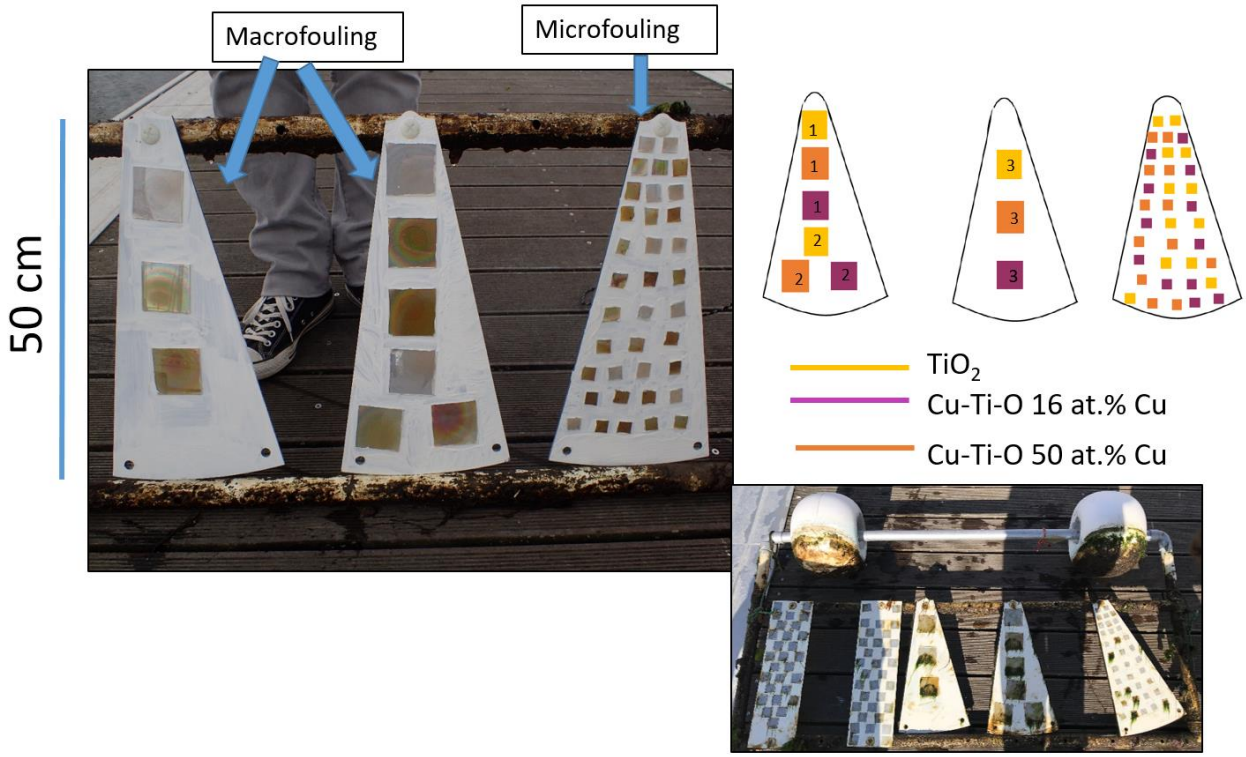

Figure 12. Films de TiO_2 pur, Cu-Ti-O 16 at% Cu et Cu-Ti-O 50 at% Cu collés sur des panneaux de polycarbonate et immergé dans l'eau de mer naturelle (Océan Atlantique, Port de Kernevel, France).

Trois échantillons pour chaque type de revêtement ont été immergés pour évaluer l'aptitude des films à empêcher la salissure par les macroorganismes. Dans un deuxième temps, douze échantillons pour chaque type pour analyser le potentiel pour empêcher la salissure par micro-organismes. L'étude a débuté en avril 2019.

Dans ce travail, le pourcentage estimé de la surface de l'échantillon couverte par l'encrassement biologique est obtenu après un traitement d'image à l'aide du logiciel ImageJ.

Microscope confocal à balayage laser (MCBL) et le Microscope électronique à balayage (MEB) ont été utilisés comme outils analytiques complémentaires pour étudier le comportement des micro-organismes. L'objectif est de relier les observations de salissure par micro-organismes marins à l'activité de macroorganismes sur les échantillons.

En ce qui concerne l'évaluation de la salissure par micro-organismes, après 10 jours d'immersion l'analyse MEB a permis de voir que seulement quelques diatomées ont été observées

pour tous les films, comme montré sur la Figure 13. Après 25 jours d'immersion, on observe dans tous les films une diversité de microorganismes comprenant des bactéries et des diatomées, en particulier dans les films Cu-Ti-O 50 at.% Cu. Cette composition a présenté une plus importante quantité de micro-organismes en comparaison avec les autres compositions. Quelques diatomées ont été observées après 38 jours d'immersion pour les films de TiO_2 pur et les films Cu-Ti-O 16 at.% Cu, ce qui contraste avec les films contenant une teneur plus élevée en Cu dont la surface était presque totalement recouvert de diatomées et bactéries.

Il est important de mentionner que la présence de micro-fleurs à la surface est observée même après 38 jours d'immersion pour des films de TiO_2 pur déposés à 550 °C. Cela confirme que les micro-fleurs de TiO_2 résistent à l'eau de mer et présentent également une bonne stabilité mécanique. C'est un résultat majeur car les micro-fleurs sont indispensables pour améliorer l'activité photocatalytique des films de TiO_2.

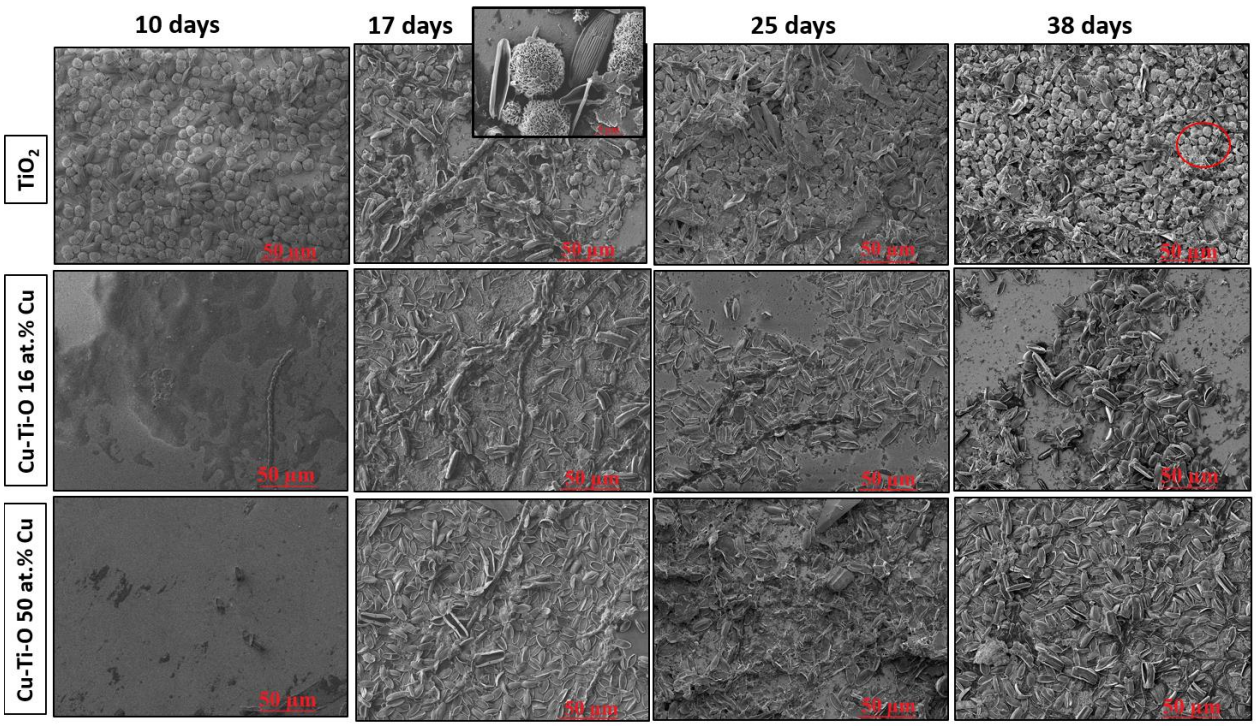

Figure 13. Clichés MEB de la colonisation des films après 38 jours d'immersion dans l'océan Atlantique.

Ces résultats ont été confirmés par le Microscope confocal à balayage laser. Après 4 semaines d'immersion dans l'eau de mer, les micro-organismes présents sur des films de compositions différentes sont clairement différents.

Après 10 jours d'immersion, les bactéries sont présentées dans tous les films. En effet, les films de TiO_2 purs et les films Cu-Ti-O 16 at.% Cu présentent une faible quantité de bactéries à la surface en comparaison avec les films Cu-Ti-O 50 at.% Cu. Après 17 jours d'immersion, tous les films ont développé un biofilm composé de bactéries, diatomées et de micro-algues. De plus, la présence de micro-algues à la surface est mieux notée pour les films Cu-Ti-O 50 at.% Cu.

Dans notre cas, les films Cu-Ti-O 50 at.% Cu ont montré une résistance nettement meilleure au développement de biofilms et de micro-algues après les observations MEB et CLSM.

Le pourcentage de la surface couverte par différents types de macroorganismes a été évalué visuellement après l'immersion statique.

La Figure 14 présente l'évolution du développement de l'encrassement avec le temps d'immersion en calculant la surface de l'échantillon couvert par l'encrassement biologique. Après 4 semaines, les films de TiO_2 purs montrent la meilleure performance, présentant le plus faible pourcentage de surface couverte par bio-encrassement, avec une valeur moyenne de 20%. En revanche, les films Cu-Ti-O 16 at.% Cu et Cu-Ti-O 50 at.% Cu présentaient une valeur moyenne de 27% et 29%, respectivement.

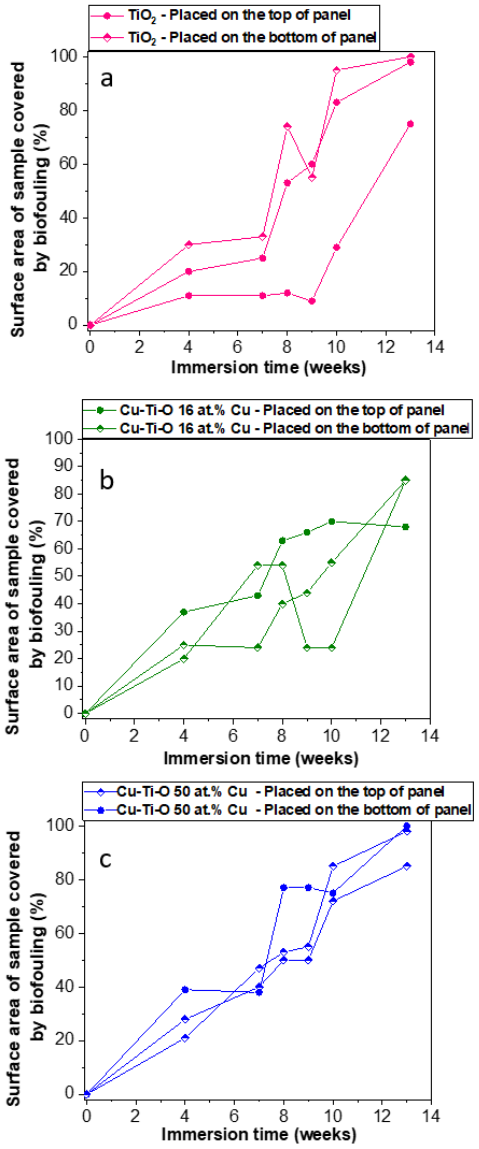

Figure 14. Evolution de la surface des échantillons recouverts de bio-encrassement avec le temps d'immersion pour a) TiO_2 films, b) Cu-Ti-O 16 at.% Cu films et c) Cu-Ti-O 50 at.% Cu films.

Le échantillon de TiO_2 placé en haut du panneau a montré une meilleure performance par rapport aux échantillons placés en bas du panneau, comme illustré à la Figure 14a. Cela peut-être expliqué par le fait que l'échantillon est plus proche de la surface de l'eau, il reçoit alors plus de rayons UV/VIS et il a donc une activité photocatalytique plus intense. Il est important de noter que, depuis le début de l'essai (soit 9 semaines plus tard), la partie supérieure des échantillons a connu une croissance plus lente des algues par rapport à la partie basse, ce qui peut être associé au phénomène précédemment expliqué.

Au contraire, les films Cu-Ti-O 16 at.% Cu ont présenté une meilleure performance pour les échantillons placés en bas du panneau pendant les 10 premières semaines. Après 13 semaines, tous les échantillons ont révélé une croissance importante d'algues à la surface (Figure 14b).

Pour les films Cu-Ti-O 50 at.% Cu, tous les échantillons montrent presque les mêmes performances indépendamment de l'emplacement, comme le montre la Figure 14bc.

Après 8 semaines, les films de TiO_2 purs présentent une valeur moyenne de 46 % contre 52 % et 60% pour les films Cu-Ti-O 16 at.% Cu et les films Cu-Ti-O 50 at.% Cu, respectivement.

Après 10 semaines, on constate un effet d'auto-nettoyage sur l'un des revêtements Cu-Ti-O 16 at.% Cu qui montre clairement une diminution de l'encrassement biologique de 54 % à 24 % de la surface couverte par bio-encrassement. Après 10 semaines, les revêtements Cu-Ti-O 16 at.% Cu ont révélé de meilleures performances par rapport aux autres compositions avec une valeur moyenne de 50 %. L'un des revêtements de TiO_2 pur placé en haut du panneau a présenté une bonne performance après 10 semaines, montrant 29% de la surface couverte par l'encrassement biologique.

Après 10 semaines, Cu-Ti-O 50 at.% Cu films présentaient un pourcentage moyen plus élevé de surface couverte d'une valeur estimée à 80 % en raison de la croissance de macro et de micro-algues à la surface.

La Figure 14 montre qu'après une immersion statique de 13 semaines, tous les revêtements testés présentaient un pourcentage de surface recouverte d'encrassement supérieur à 70 %, dominé par les macro-algues.

Cu-Ti-O 16 at.% Cu films ont montré un pourcentage plus faible de la surface couverte par macroorganismes après 13 semaines d'immersion. Cette composition a également montré une meilleure résistance au développement de biofilms et de micro-algues. De plus, dans notre cas, l'observation de biofilms sur des revêtements antisalissure a révélé une bonne corrélation entre l'observation microscopique des différents micro-organismes et l'inspection visuelle pour l'observation de macroorganismes.

Ces résultats montrent que les films de TiO_2 et Cu-Ti-O 50 at.% Cu qui ont montré une bonne activité photocatalytique sous radiation UV ne montrent pas la meilleure résistance au développement de la biosalissure dans l'eau de mer après 13 semaines. Par contre, les films de TiO_2 montrent un meilleure comportement jusqu'à 8 semaines d'immersion, ce qui peut être

expliqué par une activité photocatalytique plus élevée dans ces films vu que l'échantillon placé en haut du panneau a montré une meilleure performance.

Conclusion

La fonctionnalité potentielle d'un revêtement bicouche Al-Zr /TiO_2combinant les propriétés anticorrosion et photocatalytiques a été testée en utilisant de l'acier rapide (HSS) comme substrat. Des films Al–Zr contenant de différents pourcentages atomiques de Zr ont été déposés sur des substrats d'acier rapide, verre et silicium par pulvérisation cathodique magnétron. Al–Zr (4 at.% Zr) montre le meilleur compromis entre le la résistance à la corrosion, le caractère sacrificiel et le renforcement mécanique du revêtement.

Les films de TiO_2 ont été élaborés par déposition chimique en phase vapeur assisté par aérosol dans des conditions optimisées afin de développer une microstructure caractérisée par la présence de micro-fleurs de TiO_2 physiquement attachés au film de TiO_2. Les conditions de croissance optimales ont été obtenues par la combinaison de température de dépôt, concentration en précurseur et vitesse d'alimentation en précurseur. La diffraction des rayons X et la spectroscopie Raman confirme que les micro-fleurs de TiO_2 et le film mince sont constitués de TiO_2 en phase anatase. La présence de micro-fleurs de TiO_2 ayant un diamètre et une hauteur d'environ 7 µm et une taille moyenne de cristallite de 20 nm joue un rôle crucial dans la photocatalyse du composé Orange G. Ce comportement est amélioré sur des films de TiO_2 déposés à 550 °C qui montrent un taux de décomposition plus élevé d'Orange G sous irradiation UV par rapport aux autres films déposés à plus faible températures (500 et 540 °C).

Les revêtements bicouches Al-Zr /TiO_2se sont révélés être une alternative intéressante pour préserver le caractère sacrificiel pour la protection des structures en acier dans les environnements salins. Ces films déposés sur des substrats en acier offrent une bonne protection grâce à l'oxydation préférentielle de la bicouche présentant une faible densité du courant de corrosion avec une valeur

égale à 4,01 x 10^{-7} A /cm^2. La bicouche d'Al-Zr/TiO_2 réduit l'activité électrochimique des films par la formation d'un film passif et dense, et augmente également la résistance à la corrosion par piqûres lorsque la cinétique de la réaction cathodique est plus basse.

Des tests d'encrassement biologique ont été réalisés dans la mer afin d'évaluer les propriétés antisalissure des films de TiO_2 pur, Cu-Ti-O 16 at.% Cu et Cu-Ti-O 50 at.% Cu.. Les films de TiO_2 et Cu-Ti-O 16 at.% Cu ont montré dans un premier temps une meilleure résistance à la formation de biofilms, micro-algues et macro-algues à la surface des échantillons confirmés par les analyses MEB, CLSM et l'inspection visuelle en comparaison avec les films Cu-Ti-O 50 at.% Cu. Après 13 semaines d'immersion dans l'eau de mer naturelle les films Cu-Ti-O 16 at.% Cu ont montré une résistance nettement meilleure au développement de biofilms et de micro-algues et un pourcentage plus faible de la surface couverte par macro-algues.

Des nouveaux tests sont envisagés afin de valider la reproductibilité du comportement antisalissure de ces revêtements et il faudra aussi évaluer les propriétés antisalissure et corrosion des revêtements bicouche dans l'eau de mer.

References

[1] R. Holland, T.M. Dugdale, R. Wetherbee, A.B. Brennan, J.A. Finlay, J.A. Callow, M.E. Callow, Adhesion and motility of fouling diatoms on a silicone elastomer, Biofouling. 20 (2004) 323–329. doi:10.1080/08927010400029031.

[2] P.N. Sudha, T. Gomathi, J. Venkatesan, S.-K. Kim, Marine Biomaterials as Antifouling Agent, in: S.-K. Kim (Ed.), Springer Handb. Mar. Biotechnol., Springer Berlin Heidelberg, Berlin, Heidelberg, 2015: pp. 1181–1192. doi:10.1007/978-3-642-53971-8_52.

[3] M. Tiranuntakul, Evaluation of fouling in a pilot scale membrane bioreactor, (2011) 256.

[4] P. Sathe, K. Laxman, M.T.Z. Myint, S. Dobretsov, J. Richter, J. Dutta, Bioinspired nanocoatings for biofouling prevention by photocatalytic redox reactions, Sci. Rep. 7 (2017) 3624. doi:10.1038/s41598-017-03636-6.

[5] S. Baruah, M. Jaisai, J. Dutta, Development of a visible light active photocatalytic portable water purification unit using ZnO nanorods, Catal. Sci. Technol. 2 (2012) 918–921. doi:10.1039/C2CY20033C.

[6] P. Sathe, M. Tay, Z. Myint, S. Dobretsov, J. Dutta, Removal and regrowth inhibition of microalgae using visible light photocatalysis with ZnO nanorods : A green techn ...., Sep. Purif. Technol. 162 (2016) 61–67. doi:10.1016/j.seppur.2016.02.007.

[7] A. Mills, N. Elliott, I.P. Parkin, S.A. O'Neill, R.J. Clark, Novel TiO2 CVD films for semiconductor photocatalysis, J. Photochem. Photobiol. A Chem. 151 (2002) 171–179. doi:10.1016/S1010-6030(02)00190-9.

[8] A. FUJISHIMA, K. HONDA, Electrochemical Photolysis of Water at a Semiconductor Electrode, Nature. 238 (1972) 37. http://dx.doi.org/10.1038/238037a0.

[9] J.M. Herrmann, C. Duchamp, M. Karkmaz, B.T. Hoai, H. Lachheb, E. Puzenat, C. Guillard, Environmental green chemistry as defined by photocatalysis, J. Hazard. Mater. 146 (2007) 624–629. doi:10.1016/j.jhazmat.2007.04.095.

[10] G. Tian, Y. Chen, W. Zhou, K. Pan, C. Tian, X. Huang, H. Fu, 3D hierarchical flower-like TiO2 nanostructure: morphology control and its photocatalytic property, CrystEngComm. 13 (2011) 2994–3000. doi:10.1039/C0CE00851F.

[11] S. Biswas, C. Jiménez, A. Khan, S. Forissier, A.K. Kar, D. Muñoz-Rojas, J.-L. Deschanvres, Structural study of TiO $_2$ hierarchical microflowers grown by aerosol-assisted MOCVD, CrystEngComm. 19 (2017) 1535–1544. doi:10.1039/C6CE02648F.

[12] F. Sanchette, T. Czerwiec, A. Billard, C. Frantz, Sputtering of Al-Cr and Al-Ti composite targets in pure Ar and in reactive Ar-N2 plasmas, Surf. Coatings Technol. 96 (1997) 184–190. doi:10.1016/S0257-8972(97)00110-2.

[13] F. Sanchette, Tran Huu Loi, A. Billard, C. Frantz, Structure—properties relationship of metastable Al-Cr and Al-Ti alloys deposited by r.f. magnetron sputtering: role of nitrogen, Surf. Coatings Technol. 74–75 (1995) 903–909. doi:10.1016/0257-8972(94)08210-3.

[14] F. Sanchette, A. Billard, C. Frantz, amorphous aluminium alloy coatings, Surf. Coat. Technol. 98 (1998) 1162–1168. doi:10.1016/S0257-8972(97)00231-4.

[15] F. Sanchette, A. Billard, Main features of magnetron sputtered aluminium-transition metal alloy coatings, Surf. Coatings Technol. 142–144 (2001) 218–224. doi:10.1016/S0257-8972(01)01197-5.

[16] M. Reffass, C. Berziou, C. Rébéré, A. Billard, J. Creus, Corrosion behaviour of magnetron-sputtered Al1−x–Mnx coatings in neutral saline solution, Corros. Sci. 52 (2010) 3615–3623. doi:10.1016/J.CORSCI.2010.07.008.

[17] C. Berziou, K. Remy, A. Billard, J. Creus, Corrosion behaviour of dc magnetron sputtered Fe1−xMgx alloy films in 3 wt% NaCl solution, Corros. Sci. 49 (2007) 4276–4295. doi:10.1016/J.CORSCI.2007.04.008.

[18] I.G. Brodova, D. V Bashlykov, A.B. Manukhin, V. V Stolyarov, E.P. Soshnikova, Formation of

nanostructure in rapidly solidified Al-Zr alloy by severe plastic deformation, Scr. Mater. 44 (2001) 1761–1764.

[19] H. Yoshioka, H. Habazaki, A. Kawashima, K. Asami, K. Hashimoto, The corrosion behavior of sputter-deposited AlZr alloys in 1 M HCl solution, Corros. Sci. 33 (1992) 425–436. doi:10.1016/0010-938X(92)90071-A.

[20] E. Clouet, J. Sanchez, C. Sigli, E. Clouet, J. Sanchez, C. Sigli, First principles study of the solubility of Zr in Al To cite this version : HAL Id : hal-00001055, (2004).

[21] Z.A. Chaudhury, C. Suryanarayana, A TEM study of decomposition behavior of a melt-quenched Al-Zr alloy, Metallography. 17 (1984) 231–252. doi:10.1016/0026-0800(84)90060-0.

[22] J. Ho, K. Lin, The metastable Al-Zr alloy thin films prepared by alternate sputtering deposition, J. Appl. Phys. 75 (1994) 2434–2440. doi:10.1063/1.356267.

[23] M.N. Rittner, STRUCTURE-PROPERTY CORRELATIONS IN NANOCRYSTALLINE Al-Zr ALLOY COMPOSITES, 44 (1996) 1271–1286.

[24] J. Creus, C. Berziou, S. Cohendoz, A. Perez, C. Rébéré, M. Reffass, S. Touzain, C. Allely, Y. Gachon, C. Héau, F. Sanchette, A. Billard, Reactivity classification in saline solution of magnetron sputtered or EBPVD pure metallic, nitride and Al-based alloy coatings, Corros. Sci. 57 (2012) 162–173. doi:10.1016/j.corsci.2011.12.021.

[25] T. Morikawa, Y. Irokawa, T. Ohwaki, Enhanced photocatalytic activity of TiO2−xNx loaded with copper ions under visible light irradiation, Appl. Catal. A Gen. 314 (2006) 123–127. doi:10.1016/J.APCATA.2006.08.011.

[26] C.S. Kim, J.W. Shin, Y.H. Cho, H.D. Jang, H.S. Byun, T.O. Kim, Synthesis and characterization of Cu/N-doped mesoporous TiO2 visible light photocatalysts, Appl. Catal. A Gen. 455 (2013) 211–218. doi:10.1016/j.apcata.2013.01.041.

[27] W. Conshohocken, Standard Test Method for Testing Antifouling Panels in Shallow Submergence 1, Order A J. Theory Ordered Sets Its Appl. (1998) 1–8. doi:10.1520/D3623-78AR04.2.

Résumé: Développement de revêtements multifonctionnels combinant les propriétés anti-corrosion et antisalissure

List of communications

Journal Articles

[1] Bifunctional TiO_2/AlZr Thin Films on Steel Substrate Combining Corrosion Resistance and Photocatalytic Properties, *Coatings* 2019, *9*(9), 564; https://doi.org/10.3390/coatings9090564

[2] Cu-Ti-O films for photocatalysis and antibiofouling applications, article in progress.

[3] Precipitation of $L1_2$-Al_3Zr metastable phase in an Al-Zr (4 at.% Zr) layer deposited by DC magnetron sputtering, article in progress.

Oral Presentations

[1] Development of multi-functional architectured coatings combining anti-corrosion and anti-biofouling - French NTU GDRI on Renewable Energies, Dec 2017, NTU, Singapore.

[2] Multi-functional AlZr-TiO_2 bilayer coatings - Matériaux 2018, Nov 2018, Strasbourg, France. ⟨hal-01981217⟩

[3] Multi-functional AlZr-TiO_2 bilayer coatings combining anticorrosion and antifouling properties – ICMCTF, May 2019, San Diego, USA.

Poster Presentations

[1] Multi-functional AlZr-TiO_2 bilayer coatings for corrosion and antibiofouling prevention by photocatalytic reactions - EuroCVD22-Baltic ALD 16, June 2019, Luxembourg.

Caroline VILLARDI DE OLIVEIRA

Doctorat : Matériaux, Mécanique, Optique, Nanotechnologie

Année 2019

Développement de revêtements multi-fonctionnels combinant les propriétés anti-corrosion et antisalissure

Quand un métal est immergé dans l'eau de mer, les interactions entre le métal, les organismes vivants et l'environnement marin provoquent un bio-encrassement et une corrosion des composants métalliques, presque simultanément. Cette thèse est focalisée sur le développement d'un film anticorrosion basé sur un alliage Al-Zr qui a une fonction de protection cathodique de l'acier, et d'un film TiO2 qui a des propriétés photocatalytiques. La combinaison de ces deux films permet de développer un nouveau revêtement multifonctionnel capable d'éviter la corrosion et l'encrassement biologique des structures marines.

Le film d'Al-Zr (4 at.% Zr) est d'abord déposé sur acier par pulvérisation cathodique, et le film de TiO2 est ensuite déposé par CVD afin de ralentir le processus de bio-encrassement.

Le film de TiO2 en phase anatase contient des micro-fleurs spontanément générées à partir du film et présente un taux de dégradation très élevé du colorant organique Orange G. Cette performance photocatalytique est associée à la grande surface effective développée. Des tests électrochimiques en solution saline ont révélé que les bicouches Al-Zr/TiO2 offrent une bonne protection par l'oxydation préférentielle et une résistance à la corrosion par piqûres.

Finalement, films de Cu-Ti-O ont été déposés par AAMOCVD en utilisant une combinaison de deux précurseurs afin d'améliorer les propriétés photocatalytiques et anti-bioencrassement. Des tests de biossalisure in situ sur le port de Lorient en France ont été réalisés afin d'évaluer les performances antisalissure des revêtements.

Mots clés : photocatalyse – corrosion – salissures biologiques – dépôt chimique en phase vapeur – pulvérisation cathodique.

Development of Multifunctional Coatings Combining Anticorrosion and Antibiofouling Properties

Once a metal is submerged into seawater, interactions between metal, living organisms and marine environment result in biofouling and corrosion of metal components, almost at the same time.

This thesis is focused on the development of an anticorrosion Al-Zr film providing cathodic protection for steel parts and of a TiO2 film providing photocatalytic properties. The combination of both films is performed in order to develop a novel multi-functional coating able to avoid corrosion and biofouling of marine structures.

An optimized Al-Zr (4 at.% Zr) underlayer film was deposited by magnetron sputtering, and TiO2 was added as a top layer by aerosol CVD in order to slow down the biofouling process.

Anatase TiO2 films containing microflowers physically attached to the TiO2 films presents high decomposition rate of Orange G dye. The enhanced photocatalytic performance is associated with the high effective surface associated to the TiO2 microflowers. Electrochemical tests in saline solution have revealed that Al-Zr/TiO2 bilayers provide good protection through the preferential oxidation and an increased pitting resistance.

Finally, films of Cu-Ti-O were deposited by AAMOCVD using a combination of two precursors in order to improve photocatalytic and antibiofouling properties. Marine biofouling field test, in Lorient's Harbor in France, were carried out in order to evaluate the antifouling performance of the coatings.eserunt mollit anim id est laborum."

Keywords: photocatalysis – corrosion – fouling organisms – chemical vapor deposition – magnetron sputtering.

Thèse réalisée en partenariat entre :

cea

utt UNIVERSITÉ DE TECHNOLOGIE TROYES

Ecole Doctorale "Sciences pour l'Ingénieur"